SEISMIC VELOCITIES IN UNCONSOLIDATED SANDS:
MEASUREMENTS OF PRESSURE, SORTING, AND COMPACTION EFFECTS

A DISSERTATION

SUBMITTED TO THE DEPARTMENT OF GEOPHYSICS

AND THE COMMITTEE ON GRADUATE STUDIES

OF STANFORD UNIVERSITY

IN PARTIAL FULFILLMENT OF THE REQUIREMENTS

FOR THE DEGREE OF

DOCTOR OF PHILOSOPHY

Michael Andrew Zimmer

November 2003

I certify that I have read this dissertation and that, in my opinion, it is fully adequate in scope and quality as a dissertation for the degree of Doctor of Philosophy.

_____

Amos Nur, Principal Adviser

I certify that I have read this dissertation and that, in my opinion, it is fully adequate in scope and quality as a dissertation for the degree of Doctor of Philosophy.

_____

Gary Mavko

I certify that I have read this dissertation and that, in my opinion, it is fully adequate in scope and quality as a dissertation for the degree of Doctor of Philosophy.

_____

Mark Zoback

I certify that I have read this dissertation and that, in my opinion, it is fully adequate in scope and quality as a dissertation for the degree of Doctor of Philosophy.

_____

Jack Dvorkin

Approved for the University Committee on Graduate Studies.

ABSTRACT

This dissertation presents the results of compressional- and shear-wave velocity measurements on a series of unconsolidated sand and glass-bead samples over a pressure range from 100 kPa to 20 MPa (1 to 200 bars). It discusses the relationships observed between the velocities and the effective pressure, porosity, and loading history of the samples. It also compares the velocities measured in water-saturated samples at ultrasonic frequencies to the velocity dispersion predicted by Biot and squirt models, and compares the dynamic bulk moduli calculated from the velocity measurements to the static bulk moduli calculated from strain measurements. The sensitivities of the velocities to the pressure are also compiled with velocity-pressure data from consolidated clastic and crystalline rocks to demonstrate an approximately universal pressure-sensitivity versus pressure trend for all of the rocks over a wide range of pressures.

To allow the transmission of interpretable ultrasonic signals through these highly attenuating sediments, the transducers of the apparatus built to make these measurements were made with low frequency (200 kHz), broadband piezoelectric crystals and low-impedance, glass-filled polycarbonate face-plates. The average pressure dependence of the shear-wave velocities observed in measurements on 21 unconsolidated sand and glass bead samples is close to the fourth root of the effective pressure ($V_S \propto p'^{1/4}$), as has commonly been observed at low pressures. This pressure dependence is consistent over the entire pressure range. The average pressure dependence of the compressional-wave velocities in dry samples is slightly lower ($V_P \propto p'^{0.22}$), though still consistent with pressure and still greater than the dependence predicted by theoretical models based on Hertz-Mindlin contact behavior ($V \propto p'^{1/6}$). The magnitude of the velocities compares well to the contact model predictions if the grains are assumed to be frictionless. Preconsolidation produces only a slight increase in the velocities and a slight reduction in the pressure dependence.

A subset of texturally similar samples, consisting of 13 sand and glass bead samples, were prepared with controlled grain-size distributions to produce samples with initial porosities ranging from 0.25 to 0.44. Over this porosity range, the velocities measured in the dry samples at a given pressure show very little sensitivity to the porosity. For the

water-saturated case, compressional-wave velocities modeled from Gassmann fluid substitution increase significantly with decreasing porosity. For both the dry and water-saturated cases, the porosity-velocity trend at a given pressure can be roughly described by the isostress (harmonic) average between the moduli of the highest porosity sample at that pressure and the moduli of quartz, the predominant mineral component of the samples. For both the dry and water-saturated measurements there is no systematic relationship between the pressure dependences and the porosity for either the initial loading or the unloading-reloading paths for any of the moduli. The porosity dependence of the water-saturated, compressional-wave velocities is mostly contained in the initial (zero-pressure) bulk modulus.

The velocity results from four natural sands, measured at a frequency of 150 kHz in similarly prepared water-saturated and dry samples, were compared to velocity values predicted from the Gassmann, Biot, and Mavko-Jizba models. The measured water-saturated compressional-wave velocities exceed the Gassmann and Biot model predictions, but would be exceeded by the Mavko-Jizba model predictions were the model not anchored at the highest-pressure data values, indicating that the squirt mechanism must be active in these sands to produce the observed dispersion. The shear-wave velocities measured in the water-saturated samples closely match the Gassmann and Mavko-Jizba model results, but are over-predicted by the Biot model, indicating that the Biot viscous flow and inertial mechanisms do not contribute significantly to the dispersion at this frequency. The dispersion in the velocities demonstrates no significant change with compaction to higher preconsolidation pressures. It follows that the porosity reduction associated with compaction does not significantly change the features of the pore geometry responsible for the dispersion.

For the dry samples of these same four natural sands, and one glass bead sample, the dynamic modulus calculated from the ultrasonic compressional- and shear-wave velocity measurements was compared to the static modulus calculated from the volumetric strain changes observed between pressure steps. For a given sample, the static bulk modulus at a given pressure demonstrates a great deal of variation based on the loading history of the sample, while the dynamic modulus is only slightly sensitive to the loading history. The K_{dyn} to K_{stat} ratio on the initial loading path varies from between 2 and 10 for the various

samples, and decreases slightly with increasing pressure, as the dynamic modulus rises faster than the bulk modulus. On the first unloading step, the dynamic and bulk moduli are approximately equal, while with continued unloading the K_{dyn} to K_{stat} ratio rises from 1 to near 3 at zero pressure for each of the samples. The significant variability of the K_{dyn} to K_{stat} ratio with the pressure history indicates that a robust prediction of the static bulk modulus from dynamic measurements would require information on both the loading history and on the current effective pressure of the sediment. The Preisach-Mayergoyz space analysis was adapted to account for the effects of plastic strains, in addition to those of elastic hysteresis, on the relationship between the static and dynamic bulk moduli. Inaccuracies in the volumetric strain measurements lead to a quantitative mismatch between the dynamic modulus predicted from this analysis and that observed in the data. Nevertheless, this analysis does demonstrate the degree to which both the strain magnitude dependence and the occurrence of plastic strain contribute to the difference between the static and dynamic moduli.

A compilation of the velocity data from these measurements and from a number of published sources demonstrates that the sensitivity of the seismic velocities to pressure ($\partial V / \partial p'$) is a very continuous function of the effective pressure for a wide variety of rocks over a wide range of pressures. The compiled dataset includes data from unconsolidated sediments, consolidated sandstones and shales, and crystalline limestones and granites. The pressure range covered extends from below 100 kPa to above 600 MPa. All of the data are from laboratory measurements made at ultrasonic frequencies under hydrostatic pressure conditions. The pressure sensitivity data from all of these sources follow an approximately universal power-law trend over the entire pressure range for both the compressional- and shear-wave velocities, and for both dry and water-saturated rocks. These observations indicate that at pressures appropriate to the brittle crust the sensitivities of the velocities to pressure are, to the first order, independent of the porosity, density, and mineralogy of rocks and sediments.

ACKNOWLEDGEMENTS

TABLE OF CONTENTS

LIST OF TABLES

LIST OF FIGURES

CHAPTER 1:
INTRODUCTION

The assessment of the mechanical and flow properties of unconsolidated sediments from seismically-derived information is becoming more and more feasible as seismic reflection technology is increasingly used in aquifer characterization and geotechnical engineering and in support of drilling for offshore petroleum reservoirs. As seismic technology has improved over the past several decades, it has become practicable to seismically image the very shallow sediment layers that are of interest in geotechnical and geohydrologic applications. The potential exists to extract additional information from the seismic data beyond the stratigraphic geometry, including information on the spatial variability of the mechanical or flow properties of the sediments, given an appropriate survey acquisition design and an understanding of the correlations between seismically-derived properties and the properties of interest. Likewise, as offshore drilling progresses to greater and greater water depths, the successful completion of these deep-water wells requires accurate predictions of the mechanical properties of the unconsolidated sediments that overlie the exploration targets. The effective exploitation of shallow unconsolidated petroleum reservoirs also requires that their flow properties and fluid content be characterized with seismic survey techniques.

The principal objective of the research described in this dissertation has been to establish relationships that allow the interpretation of the mechanical and flow properties of unconsolidated sands from their compressional- and shear-wave velocities over a pressure range of interest for applications in geotechnical engineering, drilling engineering, and aquifer and reservoir characterization. This work focuses on sands since their properties are of primarily concern in most of these applications and since experiments on clays are significantly more complicated and time consuming, especially when working with water-saturated samples. For clean sands, the primary controls on their mechanical stability are the effective pressure and porosity; these non-cohesive sediments are more likely to experience compaction, liquefaction, or shear failure if the effective pressure is low and if the porosity is high. A larger porosity also generally corresponds to a higher permeability in clean sands. Since the porosity and pressure are the primary controls on the mechanical and flow properties in sands, and given the large

1

uncertainties observed in direct correlations of the seismic properties to the mechanical or flow properties themselves, the successfully characterizations of shallow sub-aerial soils and seafloor sediments for these properties will require the development of relationships between the seismic properties and the porosity and pressure.

In consolidated rocks, a great deal of research has been conducted to establish empirical and theoretical relationships between a number of rock properties, including the porosity and pressure, and the seismic properties, especially the compressional-wave velocity. In unconsolidated sediments, these relationships have been limited to empirical relationships established generally at pressures up to only a few hundred kilopascals (kPa), and have concentrated on the shear-wave velocity. Accurate remote characterizations of shallow unconsolidated sediments from seismic velocity measurements would require extensions of these relationships over a broader range of pressures for both the compressional- and shear-wave velocities. Likewise, the flexible granular framework of unconsolidated sediments allows for large plastic deformations and irrecoverable porosity loss on loading, and potentially leads to seismic behavior unique from that demonstrated by consolidated rocks.

The research presented in this dissertation constitutes an initial effort to develop robust relationships between the velocities and the pressure and porosity over this pressure range, concentrating on porosity variations due to different grain size distributions and compaction histories. As the seismic velocities are also very sensitive to a number of other factors, including the clay content and depositional fabric, I conducted controlled experiments on a set of 21 synthetic and natural sand and glass bead samples, most of which were reconstituted in a standardized fashion to allow the isolation of the effect of the porosity variation due to the different grain size distributions. The compressional- and shear-wave velocities of the samples were measured over a range of pressures from below 100 kPa up to 20 MPa. Each sample was subjected to a number of pressure cycles with increasing peak pressures to investigate how the porosity change from compaction affected the velocities. In addition, I compared the measured velocities to theoretical models for the velocity-pressure relationship and for the fluid-related velocity dispersion. I also compared the dynamic and static bulk moduli measured in the natural sand samples. Lastly, I compiled a dataset of velocity-pressure data from a wide

range of rock types and demonstrated that the pressure sensitivity of the velocities demonstrates a continuous, approximately universal trend with effective pressure.

CHAPTER DESCRIPTIONS

Chapter 2 describes in detail the experimental apparatus constructed to make these measurements. This unique apparatus was designed specifically to permit accurate velocity measurements on highly attenuating unconsolidated sediments over a pressure range corresponding to depths from 10 m to 2 km. This chapter also describes the sample preparation protocols used to reconstitute the samples and the methods used to measure the velocities and the static strains of the samples.

Chapter 3 presents the velocity results for all 21 sand and glass bead samples, and empirical relationships between the effective pressure and the compressional- and shear-wave velocities and shear, bulk, and P-wave moduli for each of the samples. It also compares the measured data to velocities predicted from Hertzian-contact-based effective-medium models, and discusses the implications of the misfit of the models for the mechanics of wave propagation in unconsolidated sands.

The 4th Chapter discusses the results of the velocity measurements on a subset of the samples consisting of synthetic sand and glass bead samples prepared with controlled grain-size distributions to produce a broad range of porosities. Besides the porosity variation associated with the different grain-size distributions, the porosity of each sample was also reduced during loading cycles to subsequently increasing peak pressures. This allowed measurements of the relationship between the velocities at a given pressure and the porosity as it varied due to both compaction and sorting. Besides discussing the direct velocity-porosity trends, this chapter also looks at the influence of the porosity variation on the pressure-velocity relationship. The observations made here lead to the development of a correction for the influence of the porosity on the water-saturated, compressional-wave velocity and of an approximate transform between the V_P-V_S ratio and the shear modulus.

Chapter 5 compares the velocities measured in water-saturated samples of four natural sands to theoretical model predictions based on the velocity measurements in similarly prepared dry samples. These include the Gassmann, Biot, and Mavko-Jizba

models. This chapter also demonstrates that there is no change in the magnitude of the dispersion at a given pressure with compaction of the samples.

Chapter 6 analyzes the relationship between the static and dynamic bulk moduli of five of the dry samples, including the four natural sands discussed in the previous chapter and one glass bead sample. This chapter describes an expansion of the Preisach-Mayergoyz space analysis to include the plastic strains observed in these unconsolidated samples. This analysis demonstrates the relative influences of the plastic and hysteretic elastic strains on the relationship between the static and dynamic moduli.

Chapter 7 presents a compilation of laboratory velocity-pressure data from a wide variety of rocks and sediments over a broad pressure range. The compiled dataset demonstrates a remarkable consistency in the trend of the pressure sensitivity of the velocity, $\partial V / \partial p'$, versus the effective pressure for both the compressional- and shear-wave velocities of both dry and water-saturated samples. This chapter also speculates on the reasons for the approximate universality of this trend.

The final chapter, Chapter 8, summarizes the conclusions of Chapters 2 through 7, and identifies the most significant contributions of this work. It also discusses the implications of these results for the *in situ* characterization of unconsolidated sediments, and suggests some areas for future research.

SOME DEFINITIONS

To prevent any confusion, I define here some common terminology and present some deterministic relationships assumed throughout this dissertation.

Stress and pressure

All of the experiments presented here were conducted under an isotropic stress state, where the stresses are equal in every direction. This is also often referred to as a hydrostatic stress state, which in this usage does not imply a stress magnitude, but only the isotropy of the stress state. The effective stress, σ', which is the stress that correlates to the velocities and mechanical properties of porous media, is defined as the applied stress, σ, minus the pore pressure, p_p. Since for these experiments all of the stresses are equal, the mean effective stress can be referred to as the effective pressure, p'. In this dissertation, any mention of the pressure without qualification as the pore pressure or confining pressure is referring to the effective pressure.

Preconsolidation and overconsolidation

A normally consolidated sediment is one that has not been exposed to an effective pressure greater than the pressure that it is currently experiencing. A sample that has been preconsolidated or overconsolidated has been exposed to a higher pressure than it now experiences. The preconsolidation pressure is the maximum pressure that the sample has ever experienced, and the overconsolidation ratio in defined as the preconsolidation pressure divided by the current pressure.

Porosity and void ratio

The porosity, ϕ, is the relative proportion of the pore volume to the total volume of a porous medium. The void ratio, e, is the ratio of the pore volume to the volume of solid grain material in the medium. The porosity is deterministically related to the void ratio according to:

$$\phi = \frac{e}{1+e}.$$
(1.1)

Velocities and moduli

The compressional-wave velocity, V_P, can be expressed as a function of the bulk modulus, K, shear modulus, μ, and bulk density, ρ, or of the constrained or P-wave modulus, M, and density as:

$$V_P = \sqrt{\frac{K + \frac{4}{3}\mu}{\rho}} = \sqrt{\frac{M}{\rho}},$$
(1.2)

The shear-wave velocity, V_S, is a function of only the shear modulus and the density:

$$V_S = \sqrt{\frac{\mu}{\rho}}.$$
(1.3)

The Poisson's ratio, ν, can be expressed as a deterministic function of the ratio of the compressional-wave velocity to the shear-wave velocity according to:

$$\nu = \frac{\left(\frac{V_P}{V_S}\right)^2 - 2}{2\left(\left(\frac{V_P}{V_S}\right)^2 - 1\right)}.$$
(1.4)

5

CHAPTER 2:
EXPERIMENTAL APPARATUS FOR MEASUREMENTS OF ULTRASONIC VELOCITIES IN UNCONSOLIDATED SANDS

ABSTRACT

This chapter will describe an experimental apparatus constructed to measure both compressional- and shear-wave velocities at ultrasonic frequencies through unconsolidated sediment samples at hydrostatic pressures between 100 kPa and 20 MPa. It will also discuss the experimental protocols used to prepare the samples, as well as the systems used to measure the velocities and the static strains of the samples with loading. The main innovations in the design of the apparatus include the use of low frequency (200 kHz), broadband piezoelectric crystals and low-impedance (glass-filled polycarbonate) face-plates in the construction of the ultrasonic transducers. These innovations allow the propagation of interpretable ultrasonic signals through these highly attenuating sediments, which in turn will permit accurate calibrations of empirical and theoretical expressions between the velocities and various sedimentological properties in unconsolidated sediments.

INTRODUCTION

Laboratory measurements of compressional- and shear-wave velocities are often made in earth materials to permit empirical correlations or to test theoretical expressions relating the velocities to some parameter of interest. These relations can then be used to invert *in situ* velocity measurements for the desired parameter. Parameters that have been experimentally correlated to the velocities include such things as the effective stress (Hardin and Richart, 1963; Pilbeam and Vaisnys, 1973; Domenico, 1977; Eberhart-Phillips et al., 1989), porosity (Wyllie et al., 1958; Han et al., 1986; Robertson et al., 1995), fluid saturation (Nur and Simmons, 1969; Domenico, 1977, Knight et al., 1998), clay content (Tosaya and Nur, 1982; Han et al., 1986; Marion et al., 1992), cementation (Avseth et al., 2000), and static strength (Blake and Gilbert, 1997). Using relationships calibrated with laboratory measurements on samples from the actual field site, velocity information gathered *in situ* from well log measurements, from tomographic experiments, or from velocity analysis, impedance inversion, or amplitude-versus-offset (AVO) analysis of seismic imaging data, can be interpreted for these rock or sediment properties.

The experiments to be presented here aim to extend these relationships, which have been established primarily for consolidated rocks, to unconsolidated sediments. These experiments were also intended to cover a pressure range that spanned the low pressures of interest in geotechnical engineering applications and the higher pressures applicable to drilling engineering and to the characterization of loosely consolidated aquifers and hydrocarbon reservoirs. This required an apparatus that could propagate interpretable compressional and shear signals through highly attenuating sediments at pressures below 100 kPa and that could withstand confining pressures up to several tens of MPa.

This chapter will describe the apparatus that was designed and constructed to meet these requirements. This apparatus is similar to standard, hydrostatic, through-transmission ultrasonic instruments typically used for consolidated rocks (Birch, 1960; Nur and Simmons; 1969; Domenico, 1977), with design modifications to address the challenges of preparing consistent samples, monitoring the dimensions of loose samples, and getting adequate signal strength through highly attenuating unconsolidated materials. The main innovations are in the design of the transducers used to generate and receive the ultrasonic signals. They include the use of 30% glass-filled polycarbonate (shatter-proof glass) face plates to match the acoustic impedance of the transducers and samples, and of low-frequency (200 kHz) piezoelectric crystals to reduce the amount of energy scattered or absorbed by the sample. This chapter will also discuss the sample preparation protocols used for the experiments and the error analysis performed for the velocity and static strain measurements.

OVERVIEW

The apparatus built for these experiments (shown photographed in Figure 2.1 and schematically in Figure 2.2) consists of a sample holder which is placed into a vessel that can be pressurized to hydrostatic pressures above 20 MPa. The sample holder is designed for samples 3.8 cm (1.5 in.) in diameter and up to 5 cm in length. It is instrumented to allow the measurement of both compressional- and shear-wave velocities, as well as the length and circumferential strains of the sample. The apparatus also allows for measurements on both dry and fluid-saturated sediments, and allows pressurization of the pore fluid up to a few hundred kPa.

Figure 2.1: The experimental apparatus. The electrical leads for the strain gauges and ultrasonic transducers can be seen to run from the top end cap of the vessel at the center of the pressure vessel stand (center left) to the electronics located in the stand on the right. The computer used to record the ultrasonic signals is shown on the desk. The pore pressure degassing system lies on the floor to the left of the vessel stand.

Confining Pressure System

The pressure vessel is a cylindrical steel vessel, about 70 cm in length and 10 cm in diameter. The vessel is pressurized with hydraulic oil and was pressure tested to 40 MPa, though experiments were only run to a maximum pressure of 20 MPa to prevent damage to the sample holder. The vessel has pressure fittings for twelve electrical leads in the upper end cap. The upper end cap also contains an air outlet/inlet valve to allow the air at the top of the vessel to be pushed out before pressurization, and to allow air to be pumped into the vessel to force some of the oil out before removing the upper end cap at the end of an experiment. Through-puts for the pore-pressure tubing and an inlet for the hydraulic oil are found in the lower end-cap. The oil is pumped into the vessel through this inlet with either a hand pump or a pneumatic pump. The pneumatic pump, which produces strong pressure surges, is used only to fill the vessel after the sample holder has been

placed in it, with the air outlet still open. The hand pump, which allows much more careful pressure control, is used to pressurize the vessel above atmospheric pressure once the vessel is completely full of oil and all of the air has been pushed out. The pressure is measured using analog gauges, with one gauge covering the entire pressure range and a more accurate gauge used for the lowest 200 kPa.
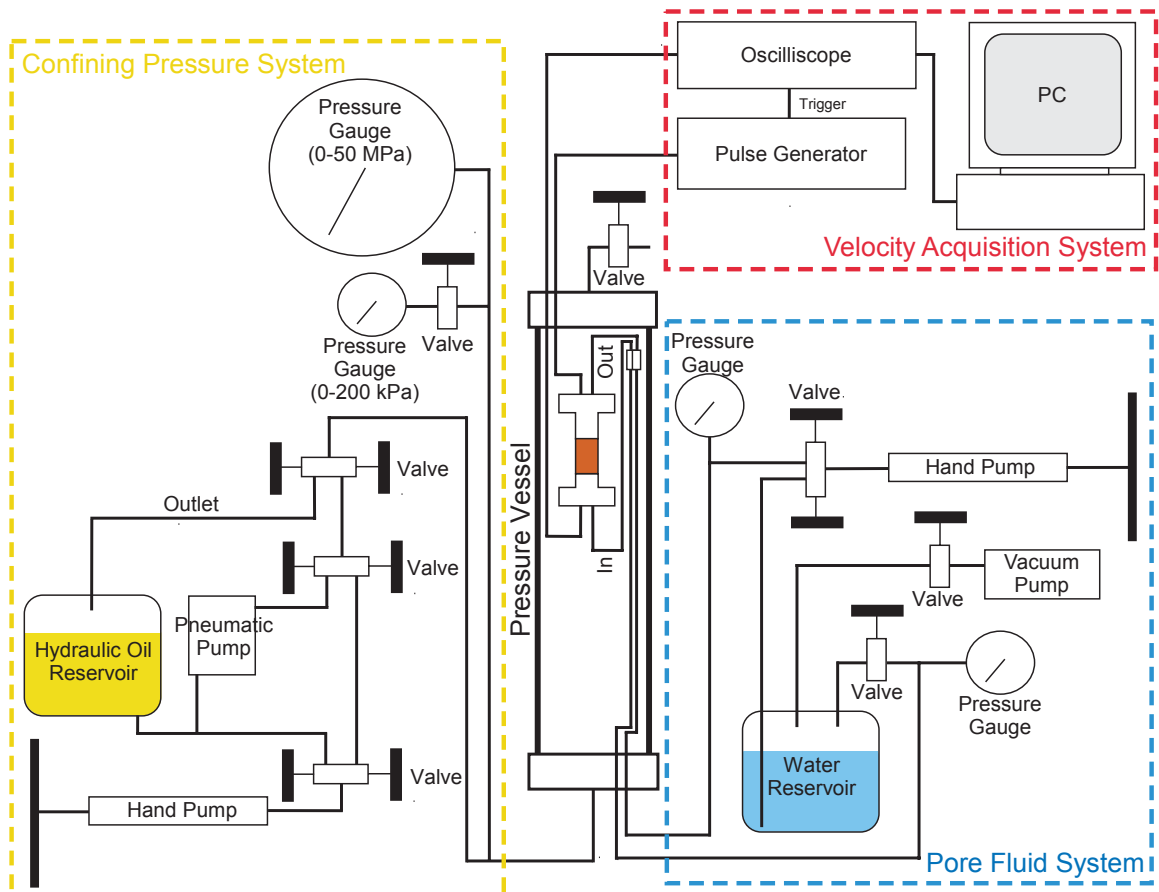
Figure 2.2: Schematic depiction of the experimental apparatus. For more detailed depictions of the ultrasonic transducers see Figure 2.4.

Pore-Pressure System

The pore-pressure system allows for measurements to be made on water-saturated samples with pore pressures up to a few hundred kPa. A hand pump is used to pump water into the sample through tubing running through the lower transducer, and the water can be drained from the sample through tubing through the upper transducer. This configuration, with the pore fluid flowing upward through the sample, allows the air in the samples to escape easily during saturation. The pore pressure is measured at both ends of the sample to ensure that the pressures are equilibrated throughout the pore-fluid

system. A pore-water degassing system keeps the water under vacuum until it is drawn into the pump.

THE SAMPLE HOLDER

The sample holder (Figure 2.3) consists of a steel and aluminum frame which supports a pair of ultrasonic transducers, the strain-measurement sensors, and the associated electronics and pore-fluid tubing. The sample holder was designed to allow the consistent preparation of unconsolidated sediment samples in that it can be easily assembled and placed in the pressure vessel with minimal disturbance to the sample. This consistent sample preparation is essential so that uncontrolled differences in the samples do not obscure the effects of the textural variations being investigated on the measured velocities.

The Ultrasonic Transducers

The ultrasonic transducers use piezoelectric (PZT) crystals to convert an electrical pulse into a compressional or shear wave (see Figure 2.4). The design of the transducers has been modified from that of the typical transducers used on consolidated rocks in two main ways: 1) they use lower-frequency (200 kHz), broadband piezoelectric crystals instead of the standard 1 MHz crystals, and 2) they use a lower-impedance face plate rather than the standard steel or aluminum face plates. The lower frequency results in less energy absorption and scattering as the signals pass through the sample. The face plates are made of a 30% glass-filled polycarbonate which has a P-impedance of 3.34×10^6 kg/m^{2}sec, while the sands have an impedance of between 0.6 and 1.2×10^6 kg/m^{2}sec when dry, and between 2.9 and 3.6×10^6 kg/m^{2}sec when water-saturated. The better impedance matching of the face plates to the samples limits the amount of energy reflected back into the transducer at its contact with the sample, and results in a much cleaner signal.

The transducers contain both compressional- and shear-wave broadband piezoelectric (PZT-5A) crystals arranged in a stack at the center of the transducer. The crystals are located in an air-filled chamber within the transducer that is sealed off from the surrounding pressure in the vessel. The shear-wave crystal is attached directly to the back of the face plate with conductive epoxy, which is grounded to the aluminum part of the transducer. The compressional-wave crystal is epoxied to the back of the shear-wave

Pore fluid inlet and outlet

Electrical leads fed to vessel endcap

Upper transducer

Sample in jacket

Circumferential gauge

Length gauge

Lower transducer
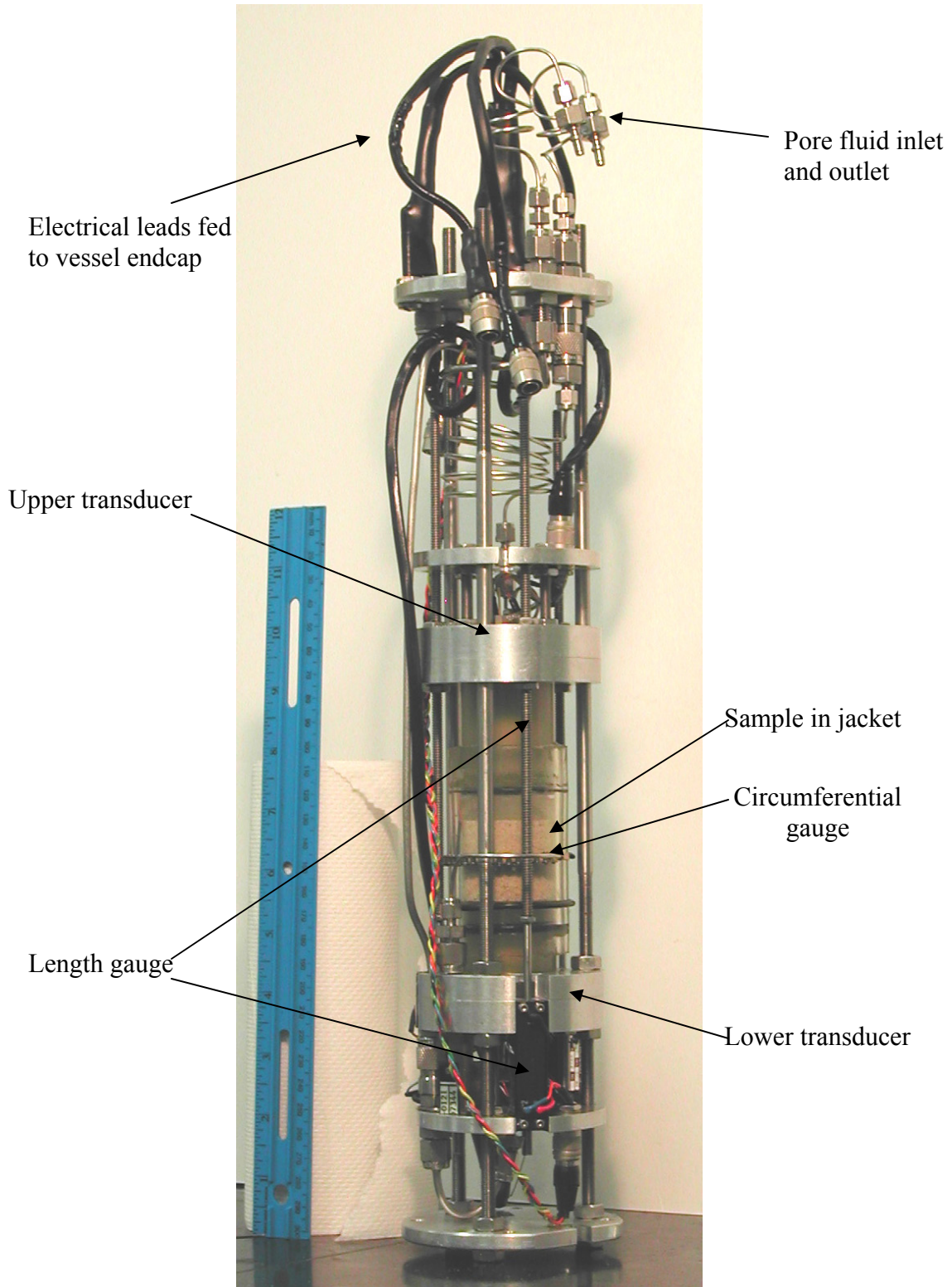
Figure 2.3: The sample holder shown holding a reconstituted sand sample in a Tygon jacket.
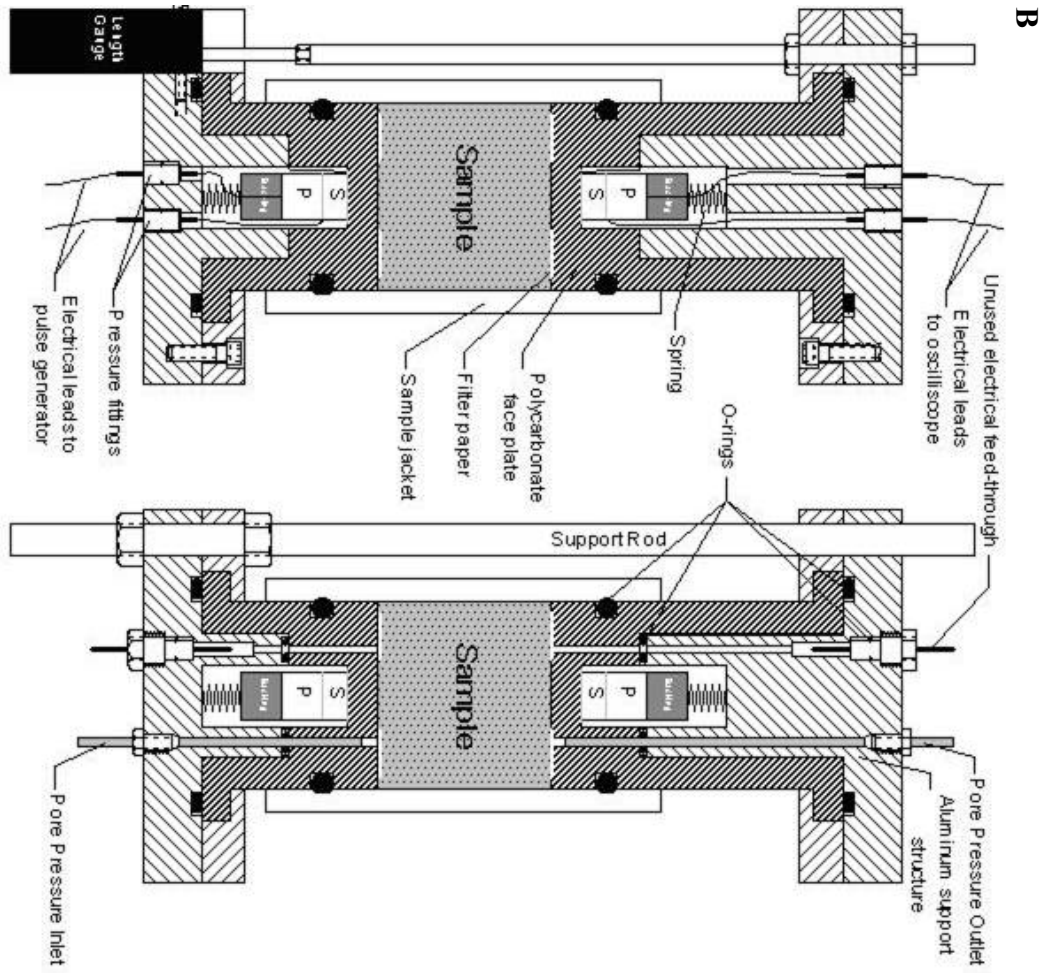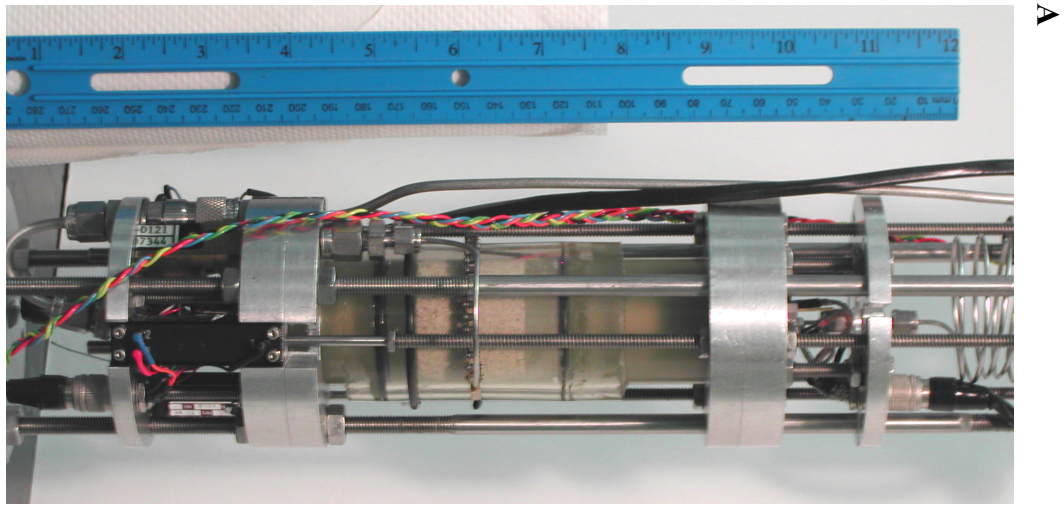
Figure 2.4: A) Close-up photograph and B) two schematic cross sections of the transducers.

crystal. Electrical leads running from between the two crystals and from the back of the compressional-wave crystal permit the crystals in the transmitting transducer to be driven independently with a high-voltage step pulse. An identical configuration in the receiving transducer allows the induced voltage in the corresponding crystals to be monitored and displayed on an oscilloscope. The stack is backed with a titanium and epoxy backing of similar impedance to the crystals to reduce the ringing of the crystals. With the stacking of the piezoelectric crystals and backing, the peak strength of the signals observed in head-to-head tests is lowered to approximately 150 kHz (Figure 2.5). With this transducer design we can produce interpretable compressional and shear signals through dry or water-saturated samples at pressures as low as 0.05 MPa. Sample signals collected at 1 MPa for both the compressional and shear waves through dry and water-saturated sand samples are shown in Figure 2.6.
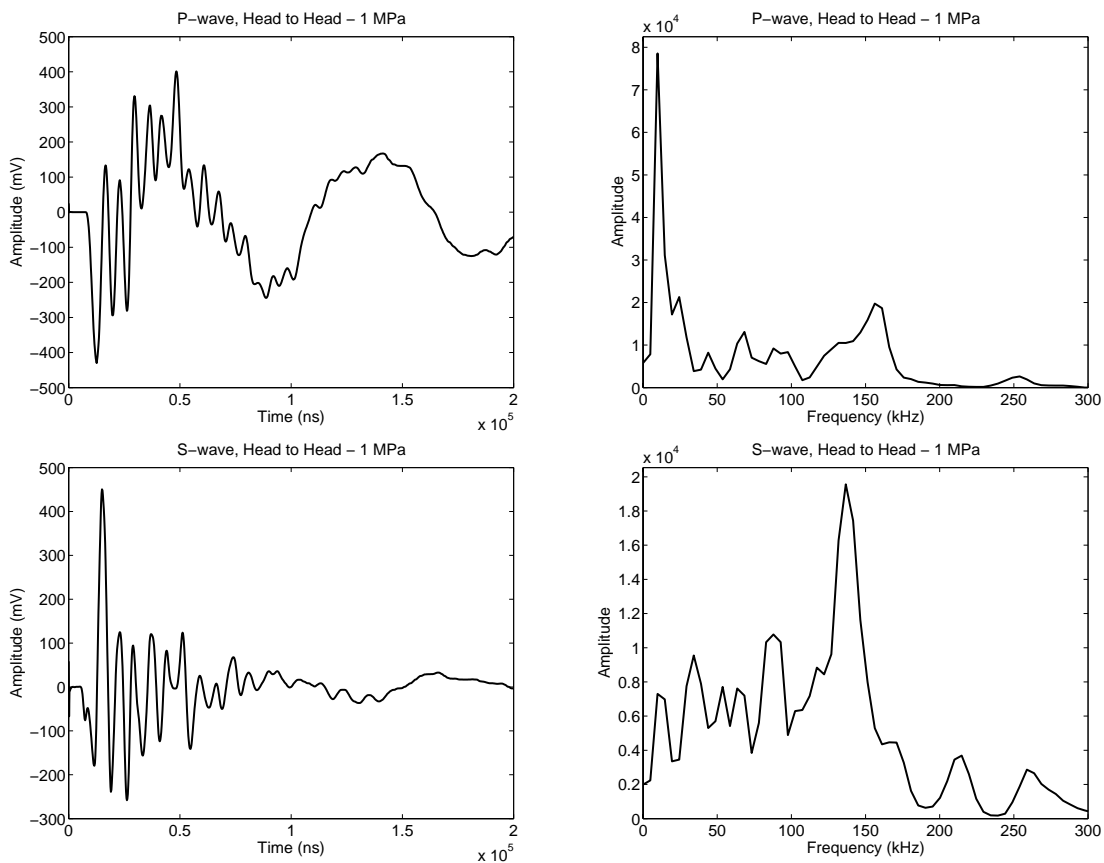
Figure 2.5: Sample signals and frequency spectra from a head-to-head test.
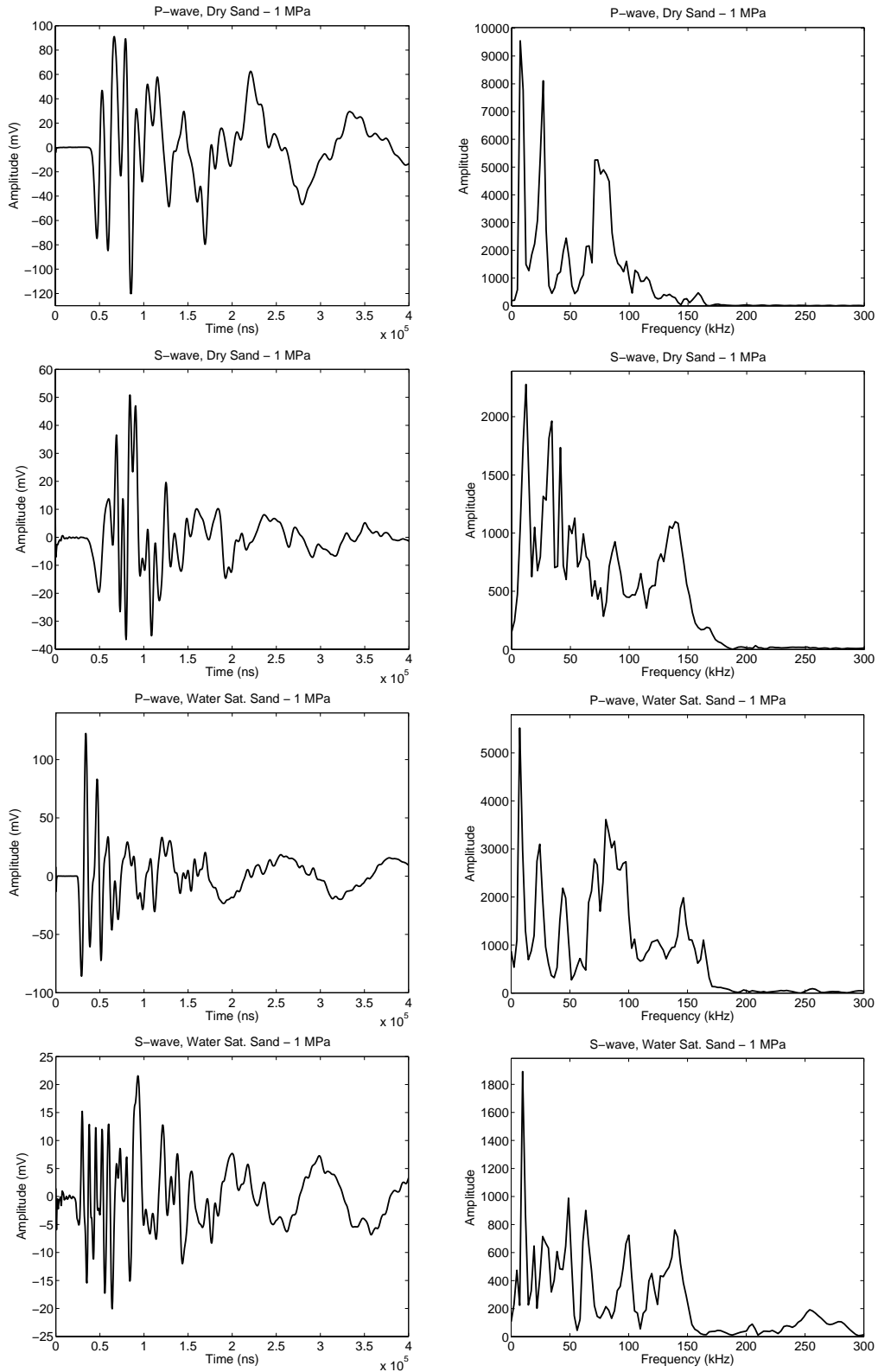
Figure 2.6: Ultrasonic compressional- and shear-wave signals and frequency spectra through dry and water-saturated samples at 1 MPa. Note the large resonance at 10 kHz visible in each of the spectra.

Strain Measurement and Porosity Monitoring

The static strains of the samples were measured using three axial gauges, and a single circumferential gauge. The axial gauges, which measure the length change between the transducers, allow an accurate determination of the length of the sample and detect any tilting of the end-caps relative to each other. The circumferential gauge, which measures the change in the circumference around the middle of the sample outside of the jacket, allows for a better estimate of the volume and porosity of the sample, as it shows how much the sample has deviated from a purely cylindrical shape.

Each length gauge consists of a linear conductive plastic (LCP) potentiometer with a 2.54 cm (1 in.) travel, anchored on the lower transducer and attached to the upper transducer by a steel rod. The circumferential gauge consists of a chain that wraps around the middle of the sample outside of the jacket, and measures the change in the circumference with a spring-loaded wire LCP potentiometer. The initial length of the sample was determined by measuring the distance between the backs of two transducers at each of the length gauges, and then subtracting the lengths of the transducers. The initial circumference was determined by averaging the diameters measured in the three accessible directions around the sample, and from this average calculating the circumference.

The initial sample volume was calculated by assuming that the outline of the sample along a vertical cross-section was described by a parabola, with the radius at the transducer faces assumed to be constant at 1.905 cm, and the radius around the center of the sample being measured after sample preparation, and corrected for the thickness of the jacket. The volume, V, is then:

$$V = \pi l \left(\tfrac{1}{5}(1.905 - r)^2 + \tfrac{2}{3} r(1.905 - r) + r^2 \right) \tag{2.1}$$

where l is the sample length and r is the radius at the middle of the sample. The initial porosity of the samples was calculated from the sample volume, grain density, and dry sample mass. The changes in the sample volume were monitored by measuring changes in the length and circumference of the samples. This allowed the porosity change to be monitored with changes in the pressure by assuming that there was a negligible change in the volume of the solid grains.

The axial strain measurements were corrected for the compression of the transducers with pressure and for the hysteresis in the potentiometers on reversals in the strain direction. The circumferential strain measurements were corrected for the compression of the sample jacket with pressure, as well as for the lack of rebound of the strain gauge on unloading, a result of the spring in the potentiometer being too strong. These corrections and their effect on the volume and static modulus measured in the samples are discussed in more detail in Chapter 6.

An error analysis of the volume measurements, taking into account all the potential errors in the initial length and circumferential measurements, in the length and circumferential strains, and in the assumption of a parabolic sample outline, estimates a potential error (2σ) of generally not more than 3%. This leads to an estimated error in the porosity of less than 3% as well. This is a conservative error estimate that can be calculated for each measurement and used to estimate errors in all the properties calculated from the sample length, volume, or porosity (e.g. density, velocities, and dynamic and static moduli).

VELOCITY MEASUREMENTS

Measurements of the compressional- and shear-wave velocities were made using the pulse transmission technique. The piezoelectric crystals in the transducers were driven with a high voltage (50 to 200V) step pulse provided by a pulse generator. A wide (1 msec) square pulse was used, since it allowed a clear signal to be recorded from the step up in the voltage without interference from the signal produced by the return step. The output of the receiving transducer was digitized with an oscilloscope and recorded by the computer. The travel time of each wave type through the sample was calculated by subtracting the delay time, measured by picking the first break of the signal when the transducers are placed together head-to-head, from the time of the first break from the signal propagated through the sample. The velocity was then calculated from this travel time and from the length of the sample as monitored with the length gauges.

Given the relatively weak signal amplitudes, especially at the lower pressures, the process of picking the first break can be the most significant potential source of error. To pick the first arrival as accurately as possible, the waveform being analyzed was compared to the waveform from the next lowest pressure step (the previous step on an

increasing pressure leg, or the following step on a decreasing leg). For the compressional-wave arrivals and the water-saturated shear-wave arrivals, the first arrival was then picked as the point where the two signals diverged. This comparison allowed me to distinguish the jacket waves from the compressional-wave arrivals, and the compressional-wave precursors from the water-saturated shear-wave arrivals. For the dry shear-wave picks, the compressional-wave precursor energy was often relatively strong and changed too much for a direct comparison of the signals from two adjacent pressure steps allow as accurate of a pick. Nevertheless, the comparison did often make it easier to locate the general area of the arrival, which could otherwise be difficult at low pressures. As the exact choice of the location of the first arrival could be relatively subjective, especially given the changes in the compressional-wave precursor energy with pressure, a pick was made of the most likely location of the first arrival, as well as the earliest and latest times that could possibly be interpreted as the first arrival. This range was then input into the error calculation to produce an error estimate for each data point.

The potential error in the velocity for each data point was calculated from the estimated potential errors in the initial length measurement, in the length change with pressure, in the delay time measurement, and in the pick of the travel time. The error (2σ) in the velocity measurements at most pressures above 1 or 2 MPa is generally less than 2% for the compressional-wave velocities and 4% for the shear-wave velocities. The difficulty in picking the shear-wave arrival from amidst the compressional-wave precursor energy led to the larger estimated errors in the S-wave velocities. Likewise, the difficulty in locating the exact time of the first arrival at low pressures generally led to larger error estimates at the lower pressures. These error estimates also varied from sample to sample, but consistently exceeded these values only for the Merritt Sand samples, which demonstrated poorer-quality signals, likely due to poor coupling of the sand to the transducer.

SAMPLE PREPARATION

In unconsolidated sediments, variations in the procedure used to prepare the samples can cause significant variations in the texture and density of the samples. The resulting velocity variations can obscure any systematic velocity trends associated with the parameters under investigation. In the experiments presented here, most of the samples

were reconstituted from completely unconsolidated sands or from synthetic mixtures of various sand or glass-bead grain sizes. Over the course of the experiments, the sample reconstitution protocol was adapted slightly to improve the repeatability of the sample preparation and to produce similar textures in the dry and water-saturated samples. Special attention was given to preparing the samples in such a way as to produce a mixing of the different grain sizes that was as homogenous as possible, and to maintain full saturation of the water-saturated samples. Experiments were also run on dry and water-saturated samples of an intact sand, for which preparation protocols were developed to produce as little disturbance in the samples as possible. The basic sample-preparation protocols used for each sample are given in Table 2.1, and each is described in more detail below.

The samples, 3.81 cm (1.5 in.) in diameter, were generally prepared to be between 2.5 and 5 cm long. For each of the samples, a very thin layer of thickened molasses was applied to each transducer face to improve coupling of the transducer to the sample. A thin ring of filter paper was also placed over the pore fluid ports on the face of the transducer to prevent grains of the sample from flowing into the pore fluid tubing. The hole in the center of this paper ring allowed direct contact of the sample with the face plate at the center of the transducer, where the piezoelectric crystals were located.

Table 2.1 – Summary of sample preparation protocols for each of the samples.

	Sample:	Dry	Sat.	Preparation Procedure:
Sands:	Sa Dry 1	X		Air pluviated, tamped.
	Sa Dry 2	X		Air pluviated, tamped.
	Sa Wet 3		X	Water pluviated.
	Sa Wet 4		X	Water pluviated.
	Sa Big	X		Air pluviated.
	Sa 35% Small	X		Mixed dry, air pluviated in sections.
	Galveston Beach	X		Air pluviated.
	Sand		X	Air pluviated, saturated once at pressure.
	Gulf of Mexico	X		Air pluviated.
	Sand		X	Air pluviated, saturated once at pressure.
	Merritt Sand	X		Intact. Dried at 65°C, cored, trimmed to size.
			X	Intact. Frozen, cored, trimmed to size, thawed in vessel.
	Pomponio Beach	X		Air pluviated.
	Sand		X	Air pluviated, saturated once at pressure.
Glass Beads:	GB Big	X		Air pluviated.
	GB Small	X		Air pluviated.
	GB 35% Small	X		Mixed dry, air pluviated in sections.
	GB Tiny	X		Air pluviated.
	GB 35% Tiny 1	X		Mixed dry, air pluviated in sections.
	GB 35% Tiny 2	X		Mixed moist, air pluviated, tamped.
	GB Broad	X		Mixed moist, air pluviated, tamped.

Figure 2.7: The air pluviation technique used to reconstitute the dry samples.

Reconstituted Samples

Dry: To prepare the dry samples, the reconstituted natural sands and single grain-size synthetic samples were simply rained through a paper funnel into a Tygon jacket placed over the lower transducer (see Figure 2.7). The upper transducer was then placed into the top of the jacket and lowered onto the top of the sample. Once the upper transducer was in place it was twisted slightly to level the top of the sample so that no gaps could be seen between the transducer and the sample. For two of the samples (Sa Dry 1, Sa Dry 2) the top of the sample was leveled by placing a 3 cm diameter, 160 g aluminum weight on top of the sand about 20 times before putting the upper transducer in place.

Similarly, the mixed grain-size samples were prepared by thoroughly mixing the grain sizes together dry, using a splitter to divide the sample into four sections, each with the same grain size distribution, and then raining each section in individually. These samples do experience some separation of the two grain sizes within each section as they

19

are poured into the sample holder, but the separation is less than if the sample was prepared in only one section.

An alternative method which produces a more homogeneous mixture of grain sizes was used on two samples (GB Tiny 2 and GB So2). They were prepared by moistening the samples with a few mL of water and mixing the grain sizes together thoroughly while moist. The samples were poured into the sample holder and tamped firmly with a weight, then allowed to dry before placing the upper transducer on. While this moist preparation method does produce a more homogenous mixture, it also produces lower velocities for both the P and S waves than observed in the other dry samples at similar pressures and porosities. In addition, it is very difficult to verify whether the sample has dried completely before beginning the experimental run.

Water Saturated: To produce similar textures in the dry and water-saturated samples, all but two of the water-saturated samples were prepared identically to the dry samples, where the dry sand was rained into the jacket, the upper transducer put in place, and the sample holder assembled and placed into the vessel. The samples were then pressurized to 200 kPa, and were saturated by pumping de-aired water up from the bottom of the sample until no more air was seen coming out of the outlet. The pore pressure was increased to 200 kPa, while the confining pressure was raised to 300 kPa, and the sample was allowed to sit for a day or two, with more de-aired water occasionally being flushed through it until the compressional-wave signals and velocities stabilized, indicating that all of the remaining air had dissolved and the sample was completely saturated, as demonstrated in Figure 2.8.

The other two samples (Sa Wet 3, Sa Wet 4) were prepared by first sliding the jacket over the lower end-cap and filling it with water, then pouring the sand slowly into the water and stirring it slightly to allow the air bubbles to escape and to level off the top of the sample. The upper end-cap was slid into the jacket above the sample until it just rested on the top of the sand, so that the sand was not at all pre-compacted. The sample holder was then assembled and placed into the pressure vessel, and the pore fluid was pressurized until any remaining air bubbles were dissolved, as describe above.

A

B
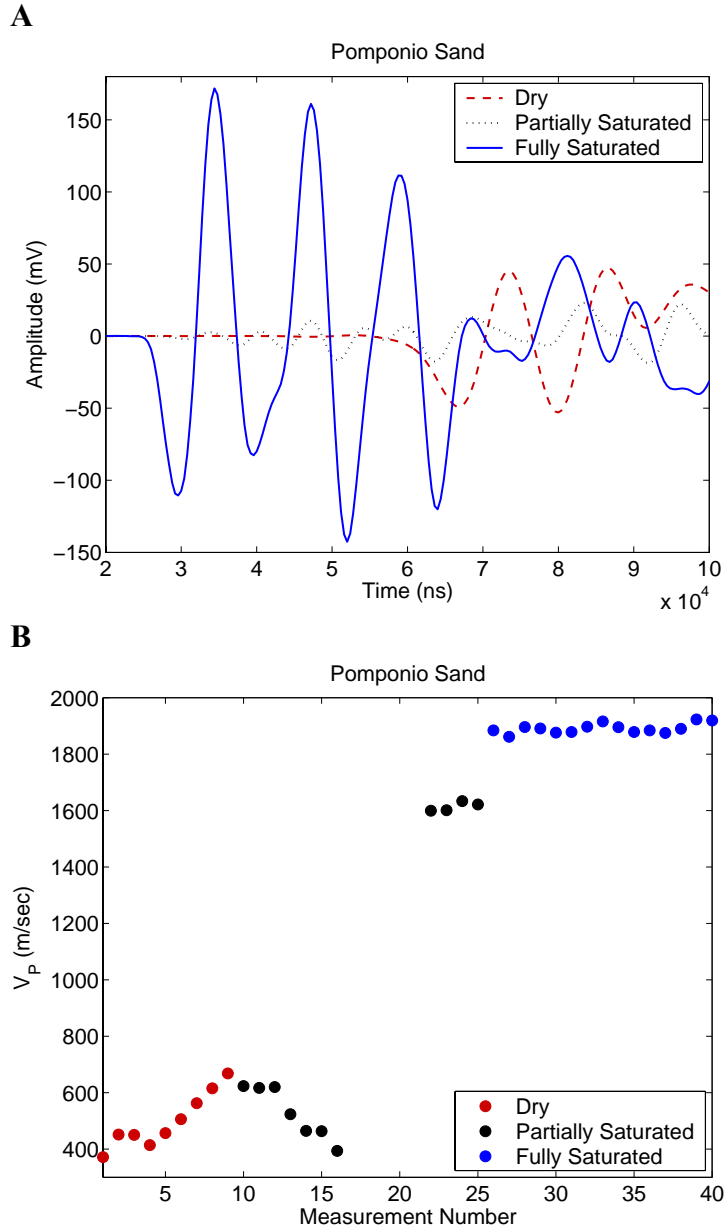
Figure 2.8: Verification of complete water saturation is demonstrated by monitoring A) the signal strength, and B) the compressional-wave velocity, both of which increase dramatically and then stabilize upon complete saturation.

Intact Samples:

Two intact samples of the Merritt sand were prepared using a 5.08 cm (2 in.) coring bit to hand core the samples out of sections of the 7.62 cm (3 in.) Shelby tube in which they were collected. For the dry sample, this was done after completely drying the Shelby tube section at 65°C. For the water-saturated sample, the Shelby tube section was frozen prior to coring. The samples were then trimmed to a 3.8 cm diameter, and the ends were

leveled by hand. The samples were placed into a rubber jacket and into the sample holder, which was then placed in the pressure vessel. The water-saturated sample was then allowed to thaw and was completely saturated as described for the reconstituted samples.

PRESSURE PATHS

Once the samples had been prepared and placed in the pressure vessel, they were each loaded through a series of 1 to 9 pressure cycles, with increasing peak pressures for subsequent cycles. The velocities and porosity were measured at the same set of pressures during each cycle (e.g. 0.1, 0.2, 0.5… MPa). This allowed the comparison of velocities and porosities measured at the same pressure for a sample that had been preconsolidated to a range of higher pressures. After each pressure step the sample was allowed to sit until the length strain and shear-wave signals had stopped changing before making the velocity and strain measurements. The length of the wait varied from sample to sample, from 20-30 minutes for the more coarse-grained and clay-free samples up to several hours for the fine-grained or clayey samples.

DISCUSSION

This apparatus has allowed accurate velocity measurements to be made in unconsolidated sands at pressures from below 100 kPa up to 20 MPa. To my knowledge this apparatus is unique, in that it can produce high quality signals over this pressure range in such highly attenuating sediments. The most dramatic improvements in the signal quality were due to the use of the lower impedance face plates. Prior versions of the transducers using the same frequencies but with stiffer, aluminum face plates did not produce interpretable signals.

This apparatus has been used to measure the velocities of a series of reconstituted natural sands, a set of synthetic sand and glass bead samples, and two intact samples. Figure 2.9 compares the velocity results from these samples to results from other measurements on unconsolidated sands in the same pressure range from Domenico (1977), Prasad and Meissner (1992), Yin (1992), Estes et al. (1994), and Robertson et al. (1995). This figure demonstrates that the velocities measured with this apparatus are in good agreement with those from other sources using a variety of different experimental apparatus.

A

Dry

B

Dry

C

Water Saturated

D

Water Saturated

▲ Galveston - Dry
▼ Galveston - Water Sat.
▲ Gulf of Mexico - Dry
▼ Gulf of Mexico - Water Sat.
▲ Merritt - Dry
▼ Merritt - Water Sat.
▲ Pomponio - Dry
▼ Pomponio - Water Sat.
▲ Sa Dry 1
▲ Sa Dry 2
▼ Sa Wet 3
▼ Sa Wet 4
▲ Sa Big
▲ Sa 35% Small
● GB Big
● GB Small

● GB 35% Small
● GB Tiny
● GB 35% Tiny 1
● GB 35% Tiny 2
● GB Broad
● Domenico (Ottawa) - Dry
♦ Domenico (Ottawa) - Water Sat.
◄ Yin (Ottawa) - Dry
► Yin (Ottawa) - Water Sat.
▼ Prasad P2 - Water Sat.
▲ Prasad P6 - Water Sat.
■ Estes - Dry
★ Estes - Water Sat.
× Robertson Dense (Ottawa) - Water Sat.
+ Robertson Loose (Ottawa) - Water Sat.

Figure 2.9: Velocity results measured with this apparatus compared to measurements made on clean sands by Domenico (1977), Prasad and Meissner (1992), Yin (1992), Estes et al. (1994), and Robertson et al. (1995): A) dry shear-wave velocities, B) dry compressional-wave velocities, C) water-saturated shear-wave velocities, and D) water-saturated compressional-wave velocities.

Potential Improvements

Potential improvements in the design of the experimental apparatus could further improve the quality of the signals produced by the transducers and allow the use of higher pore pressures. The signal strength could potentially be improved by using a stronger voltage source and by redesigning the transducers to permit the use of wider piezoelectric crystals. The small (1 cm) diameter for such low frequency crystals is probably at least a partial cause of the strong compressional-wave precursors in the shear-wave signal and the strong resonance at 10 kHz (see Figure 2.6), either of which can obscure the signal at low pressures. Space in the transducers for wide crystals could be provided by having the polycarbonate pieces machined with a ridge in them in lieu of the o-ring, or by using a larger transducer diameter. This extra space could also be used to make the pore-fluid feed-throughs capable of withstanding higher pressures. In the present configuration, the pore fluid begins to leak into the cavity that houses the piezoelectric crystals at a pressure of approximately 2 MPa. A modification of the sample preparation protocol to use thinner jackets might also improve the accuracy of the volume and porosity measurements and ensure that the sample experiences the full confining pressure at low pressures. This could be done following protocols used in the geotechnical community using thin rubber jackets supported by removable forms while the sample is being prepared. Lastly, to allow an accurate measure of the lateral rebound of the sample on unloading, the potentiometer used in the circumferential strain gauge should be replaced with one that employs less tension.

CONCLUSIONS

The apparatus described here was developed to permit the measurement of compressional- and shear-wave velocities in unconsolidated sediments over a broad range of effective pressures. The apparatus is similar to the standard isotropic stress state apparatus used at high pressures for petroleum applications and at low pressures for geotechnical applications. The main innovations are in the design of the ultrasonic transducers, which use 200 kHz, broadband piezoelectric crystals and low-impedance (glass-filled polycarbonate) face-plates to permit the transmission of high-quality signals through these highly attenuating sediments. This apparatus has enabled accurate

measurement of both the compressional- and shear-wave velocities in dry and water-saturated sediments at pressures from 100 kPa to 20 MPa.

CHAPTER 3:
MEASUREMENTS OF PRESSURE TRENDS OF COMPRESSIONAL- AND SHEAR-WAVE VELOCITIES IN SANDS

ABSTRACT

This chapter will present measurements of the compressional- and shear-wave velocities in a series of unconsolidated, dry and water-saturated sand and glass bead samples made at hydrostatic pressures from 100 kPa to 20 MPa. The average pressure dependence of the shear-wave velocities measured in these samples is close to the fourth root of the effective pressure ($V_S \propto p'^{1/4}$), as has commonly been observed at lower pressures. This pressure dependence is consistent over the entire pressure range. The average pressure dependence of the compressional-wave velocities of the dry samples is slightly lower ($V_P \propto p'^{0.22}$), but again is consistent over the whole pressure range. The pressure dependence of both velocities is reduced only slightly on preconsolidated (unloading or reloading) paths, with an average reduction of 0.01 for the pressure dependence of the shear-wave velocities and of 0.02 for compressional-wave velocities. I present empirical, power-law fits to the velocities and to the shear, bulk, and P-wave moduli for each of the samples. A comparison of the empirical results to theoretical results based on Hertz-Mindlin contact models demonstrates that the theoretical models vastly over-predict the shear moduli of granular media, and predict a lower pressure dependence of the moduli and velocities ($V \propto p'^{1/6}$). This mismatch is attributed to the inability of the models to account for grain rotation and slip at grain boundaries, and the variation in the amount of this rotation or slip with pressure.

INTRODUCTION

The pressure dependence of the compressional- and shear-wave velocities in unconsolidated sediments is an important consideration in a number of engineering applications. This pressure dependence is often used to correct or project velocities to depths or locations where measurements have not been made, especially for site-amplification predictions or liquefaction susceptibility analyses (e.g. Youd and Idriss, 1997). It also allows velocity changes to be used to monitor pressure changes in unconsolidated reservoirs or aquifers. The hazards posed to offshore drilling by unknown

overpressures at shallow depths have also prompted the use of the seismic velocities or V_P-V_S ratio to qualitatively locate regions of high pore pressure or quantitatively predict the *in situ* effective pressure.

Because of the frequent use of the dynamic shear modulus in geotechnical applications, a great deal of research has been conducted on the pressure dependence of the shear modulus and shear-wave velocity in soils. Hardin and Blandford (1989) developed a semi-empirical expression for the small-strain shear modulus, which, once calibrated for a given sediment, is meant to allow for the extrapolation of the modulus and velocity to other pressure and porosity conditions. The form for an isotropic stress state is as follows:

$$\mu_{ij} = \frac{OCR^k}{F(e)} \frac{S_{ij}}{2(1+v)} p_a^{1-n} p'^n, \tag{3.1}$$

where μ_{ij} is the shear modulus in the plane of propagation, which experiences the effective pressure p' in all directions, p_a is the atmospheric pressure, and v is the Poisson's ratio of the grain material. Equation 3.1 includes two free parameters: S_{ij}, a multiplier to account for textural factors and structural anisotropy, and n, which dictates the pressure dependence of the modulus. The void ratio function, $F(e)=0.3 + 0.7e^2$, is meant to account for the porosity differences, whether due to textural differences between samples or to the compaction of a given sample. The OCR^k term corrects the pressure dependence for the effects of compaction or preconsolidation of the sample, where OCR is the overconsolidation ratio, and k is a function of the plasticity index, with k usually assumed to be zero for clean sands. Since the overconsolidation ratio is defined as the preconsolidation pressure divided by the current pressure, the pressure dependence of the modulus for unloading or reloading paths is simply the effective pressure, p', to the quantity n-k.

A large body of work has demonstrated that the value of n for sands is generally near 0.5 (Hardin and Black, 1969; Yu and Richart, 1984; Hryciw and Thomann, 1993). Most of this work has been conducted at pressures below a few hundred kPa. Hryciw and Thomann (1993) measured the pressure dependence of a number of texturally different sands at pressures up to 300 kPa and found n to vary between values of 0.39 and 0.72, and to correlate to the compressibility of the sand. Their measurements showed

$S_{ij}/[2(1+\nu)]$ to vary from 478 to 734, and to be inversely related to n. They also recognized that k can be greater than zero for loose, compressible sands.

Direct empirical fits between the shear-wave velocity and the effective pressure have been demonstrated by Fam and Santamarina (1997) and Robertson et al. (1995). Fam and Santamarina (1997) review a number of possible empirical forms, and demonstrate that a form such as

$$V_S = OCR^k S\left(\frac{p'}{p_a}\right)^{n/2} \tag{3.2}$$

fits the shear-wave velocities, V_S, from consolidation tests on kaolinite and silica flour samples. They found $n/2$ to be approximately 0.3 for these two samples. The changes in porosity with consolidation are not strictly accounted for in this equation, but are incorporated into the pressure dependences, n and k. Robertson et al. (1995) collected shear-wave velocities through Ottawa sand samples at a number of relative densities and over a range of pressures, and fit their data with an equation of the following form:

$$V_S = (A - Be)\left(\frac{p'}{p_a}\right)^{n/2}, \tag{3.3}$$

with $n/2$ equal to 0.26 for the sand tested. Since they propose to discern the void ratio from the velocity measurement for a given vertical effective stress, they take the void ratio strictly into account, though here the coefficients A and B are not general, but must be fit to each sediment tested.

For offshore applications, compressional-wave velocities are more commonly measured than shear-wave velocities. In these applications, a local calibration of the normally pressured, compressional-wave, interval travel-time with depth is made, generally assuming that the log of the interval travel-time varies linearly when depth. Deviations above this trend are assumed to be the result of high pore pressures and low effective pressures (Hottman and Johnson, 1965; Pennebaker, 1970; Pilkington, 1988; Bowers, 1995; Sayers et al., 2000).

Hardin and Blandford (1989) also propose a semi-empirical relationship for the constrained (P-wave) modulus, M_i, similar in form to that of the shear modulus, which for an isotropic stress state can be expressed as follows:

$$M_i = \frac{OCR^k}{F(e)} \frac{S_i(1-\nu)}{(1+\nu)(1-2\nu)} p_a^{1-n} p'^n \,. \tag{3.4}$$

Experimental data collected for unconsolidated sediments to constrain the free parameters for the P-wave modulus have been more limited than for the shear modulus. Work by Hardin and Richart (1963) and Pilbeam and Vaisnys (1973) has demonstrated pressure dependences for the compressional-wave velocities between $p'^{1/3}$ and $p'^{1/6}$ for Ottawa sand, synthetic crushed sands, and glass bead samples.

A number of theoretical models (Digby, 1981; Walton, 1987; Mavko et al., 1998) have been proposed to describe the elastic moduli of granular materials. These models generally assume that the material is made up of an assemblage of perfect spheres, with the stiffness of the contacts between them described by Hertz and Mindlin solutions to the displacements of two identical spheres in contact under normal and shear forces (Timoshenko and Goodier, 1970; Mindlin, 1949). The behavior at the contacts is then used to predict the shear or compressional moduli, either by assuming a regular packing (Santamarina and Cascante, 1996), or by assuming a random arrangement of contacts (Walton, 1987). In either case these models predict both the bulk modulus, K_{eff}, and shear modulus, μ_{eff}, to have a pressure dependence of $p'^{1/3}$. For the hydrostatic stress state, Walton developed expressions for the moduli in two special cases. The first assumes that there is infinite friction between the grains in contact, such that there is no slip over the area of contact and no rotation of the grains relative to each other. These expressions are entirely equivalent to the standard Hertz-Mindlin forms given by Mavko et al. (1998), which make the same no-slip assumption:

$$K_{eff} = \sqrt[3]{\frac{C^2(1-\phi)^2\mu^2}{18\pi^2(1-\nu)^2}p'} \quad \text{and} \quad \mu_{eff} = \frac{5-4\nu}{5(2-\nu)}\sqrt[3]{\frac{3C^2(1-\phi)^2\mu^2}{2\pi^2(1-\nu)^2}p'}, \tag{3.5}$$

where p' is the effective pressure, μ and ν are the shear modulus and Poisson's ratio of the mineral making up the grains, ϕ is the porosity, and C is the coordination number, or average number of contacts between a grain and its surrounding grains. The second form given by Walton assumes that there is no friction between the grains, which is equivalent to setting the tangential stiffness to zero in the derivation of the standard Hertz-Mindlin expressions. In this case, the prediction for the bulk modulus is identical to that given in Equation 3.5, and the shear modulus is simply equal to 60% of the bulk modulus:

$$\mu_{eff} = \frac{3}{5} K_{eff} . \tag{3.6}$$

Goddard (1990) proposes two possible explanations for the discrepancy between the $p'^{1/4}$ dependence seen in velocity measurements and the $p'^{1/6}$ dependence predicted by the contact theories. He suggests that if the contacts were more similar to a cone in contact with a plane, rather than to two perfect spheres, or if the number of inter-particle contacts was allowed to vary due to the buckling of particle chains, the velocities could demonstrate a pressure dependence of $p'^{1/4}$. He also postulates that the transition from the $p'^{1/4}$ dependence at low pressure to a $p'^{1/6}$ dependence at higher pressures observed in experiments by Duffy and Mindlin (1957) on regular, close-packed spheres with varying dimensional tolerances could represent the influence of small imperfections in the spheres. The imperfections would cause the initial contacts not to be perfectly spherical, or the packing to be slightly imperfect, leaving some neighboring spheres out of contact. At low pressures, the pressure dependences would be dominated by the asperities or the changing average coordination number, while at higher pressures the area of contact would be large enough to render the asperities insignificant, and each grain's coordination number would have stabilized at its maximum possible value, producing the anticipated $p'^{1/6}$ pressure dependence.

This chapter will present the results of a series of experiments on sand and glass bead samples designed to measure the pressure dependences of both the shear- and compressional-wave velocities under both normally consolidated and overconsolidated conditions. The dataset that comprises these measurements includes 3300 independent shear- or compressional-wave velocity measurements made on a total of 21 well-characterized sand and glass-bead samples. To test the pressure dependences over the pressure range of interest in geotechnical and geohydrologic engineering, as well as in offshore drilling and reservoir characterization, the compressional- and shear-wave velocities of each sample were measured over a broader, continuous range of pressures than prior work on unconsolidated sands: from below 100 kPa up to 20 MPa. This chapter will also present comparisons of the velocity measurements to theoretical predictions from contact based models and discuss the implications of the disparities observed between the models and measurements.

EXPERIMENTAL APPARATUS AND SAMPLES

The experimental apparatus used to make the velocity measurements consists of a hydrostatic pressure vessel which holds a sample holder instrumented with compressional- and shear-wave, ultrasonic transducers and length and circumferential strain gauges. The ultrasonic transducers were made with 200 kHz piezoelectric (PZT) crystals, and plastic (30% glass filled polycarbonate) face plates to improve the impedance matching between the transducers and the sample. Velocities were calculated by picking first arrivals from pulse-transmission signals. With this arrangement we were able to get interpretable shear signals at pressures below 100 kPa, with errors generally less than 2% for the compressional-wave velocities and 4% for the shear-wave velocities. The experimental apparatus is described in more detail in Chapter 2, as are the procedures used to measure the velocities and porosity changes in the samples.

The data presented here are from a series of 7 texturally different sands and 7 glass-bead samples. Of these, four are natural sands, including two beach sands, Galveston Beach (TX) sand and Pomponio Beach (CA) sand, a Gulf of Mexico seafloor sand, and a Pleistocene dune sand (Merritt Sand) collected in Oakland, CA. The other three sands include the Santa Cruz aggregate, a quarried sand from Santa Cruz (CA), as well as two synthetic samples composed of sieve sections of this sand. For the glass bead samples, three samples (GB Big, GB Small, and GB Tiny) consisted of different narrow size ranges of beads. Three samples (GB 35% Small, GB 35% Tiny 1 and 2) were made with a "bimodal" mixture of grain sizes, with 35% of the mass made up of smaller grains and 65% of larger grains. Finally, one sample (GB Broad) was made up of a broad range of particle sizes. A summary of the principle characteristics of each of the samples is given in Table 3.1, while X-ray diffraction results for each of the sand samples are given in Table 3.2. Figure 3.1 shows the particle size distributions of each sample. The protocols used to prepare each of the samples are described in detail in Chapter 2.

The pressure path followed for each sample generally included a number of pressure cycles with increasing peak pressures for each subsequent cycle. The velocities and porosity were measured at the same set of pressures during each cycle to allow a comparison of the values measured at the same pressure for a sample that had been preconsolidated to a range of higher pressures.

Table 3.1: Sample summary

	Sample:	Saturation	Initial Porosity	D_{50} (mm)	C_U	C_C	# of cycles
Sands:	Galveston Beach Sand	Dry	0.399	0.134	1.31	1.10	3
		Water-sat.	0.397				3
	Gulf of Mexico Sand	Dry	0.430	0.0819	~3.3	~1.2	9
		Water-sat.	0.427				6
	Merritt Sand	Dry	0.364	0.225	2.63	1.34	8
		Water-sat.	0.339				8
	Pomponio Beach Sand	Dry	0.428	0.378	1.55	1.01	3
		Water-sat.	0.435				6
	Santa Cruz Aggregate: Dry 1	Dry	0.414	0.288	1.71	1.12	5
	Dry 2	Dry	0.432				1
	Wet 3	Water-sat.	0.400				2
	Wet 4	Water-sat.	0.417				4
	Sa Big	Dry	0.409	0.324	1.09	0.98	9
	Sa 35% Small	Dry	0.379	0.309	4.16	0.30	9
Glass Beads:	GB Big	Dry	0.381	0.324	1.09	0.98	8
	GB Small	Dry	0.411	0.081	1.09	0.98	8
	GB Tiny	Dry	0.422	0.040	1.09	0.98	3
	GB 35% Small	Dry	0.315	0.390	4.07	0.30	8
	GB 35% Tiny	Dry	0.296	0.390	8.14	0.15	3
	GB 35% Tiny 2	Dry	0.258				3
	GB Broad	Dry	0.339	0.150	3.62	0.90	3

Table 3.2: X-ray diffraction results for each sand sample

	Mineral components (% Wt.)					
Sand sample:	Quartz	Plagioclase	K-feldspar	Amphibole	Total Clay[1]	Other[2]
Galveston	86	6	6	0	2	0[3]
Gulf of Mexico	63	17	8	1	6	5
Merritt	59	18	7	5	11[4]	-
Pomponio	53	29	12	1	2	3
Santa Cruz	62	10	27	0	1	-

[1] – includes micas, mostly muscovite or biotite.
[2] – includes dolomite, pyrite, pyroxene, calcite
[3] – trace of calcite present.
[4] – includes a significant amount of chlorite.
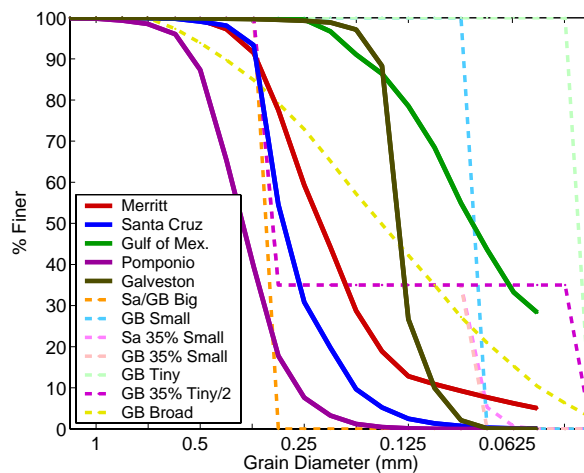
Figure 3.1: Particle-size distributions for each of the samples. The natural samples are shown in solid lines, while the synthetic samples are shown in dashed lines.

PRESSURE TRENDS

The compressional and shear velocity results from all of the sand samples are plotted against the effective pressure in Figure 2.9, along with data from similar measurements made on clean sands over this pressure range by Domenico (1977), Prasad and Meissner (1992), Yin (1992), Estes et al. (1994), and Robertson et al. (1995). In this figure, the measurements are shown to be fairly consistent from sample to sample, and to be comparable to other data collected on loose sands at these pressures. The dry compressional-wave velocity data and both the dry and water-saturated shear-wave velocity data demonstrate a power-law relationship with the effective pressure. Figure 3.2 shows all of the same data in a log-log plot, where the linear trends of the velocity data with respect to the pressure confirm this power-law relationship. The black lines in Figure 3.2 illustrate the slopes corresponding to power-laws of the velocity proportional to $p'^{1/6}$, $p'^{1/4}$, and $p'^{1/3}$. For the dataset as a whole, the shear-wave velocities for both the dry and water-saturated samples, plotted together in Figure 3.2A, run parallel to the $p'^{1/4}$ trend over the entire pressure range of the measurements. The compressional-wave velocities (Figure 3.2B) do not follow this same trend, but run along a trend intermediate between the $p'^{1/4}$ and $p'^{1/6}$ trends. Again, this trend is very continuous over the entire pressure range from below 100 kPa up to 20 MPa. The pressure trend of the water-saturated compressional-wave velocities is not linear in log-log space, but can be described by a power-law form plus a constant, as will be discussed in more detail below.

The shear- and compressional-wave velocity data from the normally consolidated sections of the loading paths and from the first unloading section from 20 MPa down of each of the dry samples are plotted against effective pressure in log-log plots in Figure 3.3. These figures also include lines showing pressure dependences of $p'^{1/6}$, $p'^{1/5}$, $p'^{1/4}$, and $p'^{1/3}$, anchored at the velocity measured at the peak pressure for each sample. These figures illustrate that while there is a fair bit of scatter in the pressure trends from sample to sample, the pressure dependence of these samples tends to remain close to $p'^{1/4}$ for the shear-wave velocities, with a slightly lower pressure dependence (shallower slope) for the compressional-wave velocities. Nevertheless, both the loading and unloading sections of any individual sample demonstrate generally continuous, straight-line slopes, indicating consistent pressure dependences over the entire pressure range.

A
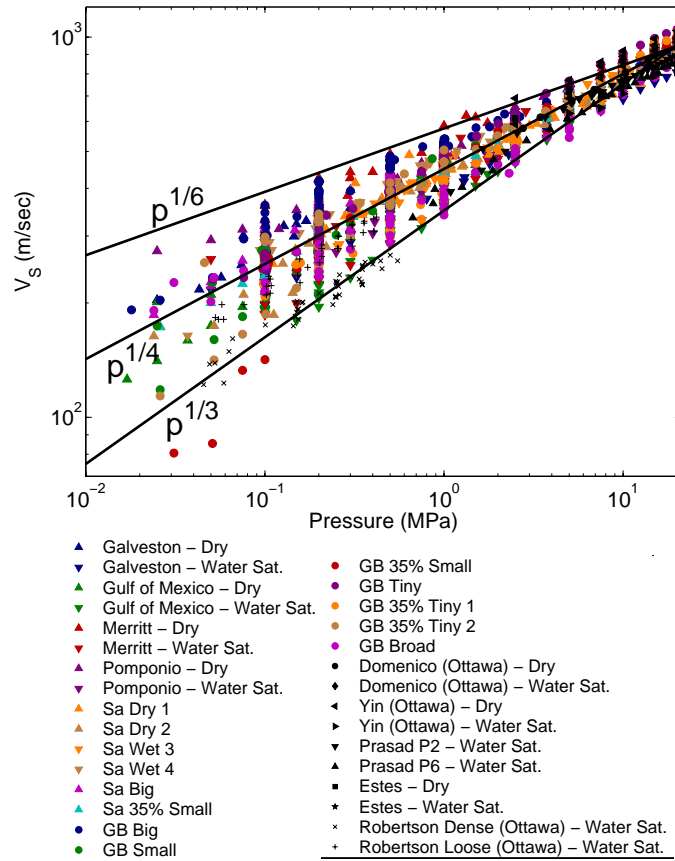
B
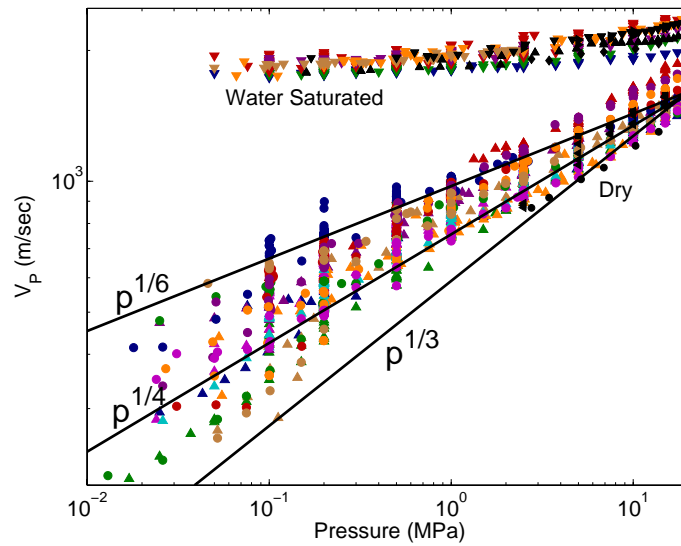
Figure 3.2: Log-log plots of A) shear- and B) compressional-wave velocities vs. effective pressure for all the samples, and for similar measurements on clean sands from Domenico (1977), Prasad and Meissner (1992), Yin (1992), Estes et al. (1994), and Robertson et al. (1995).
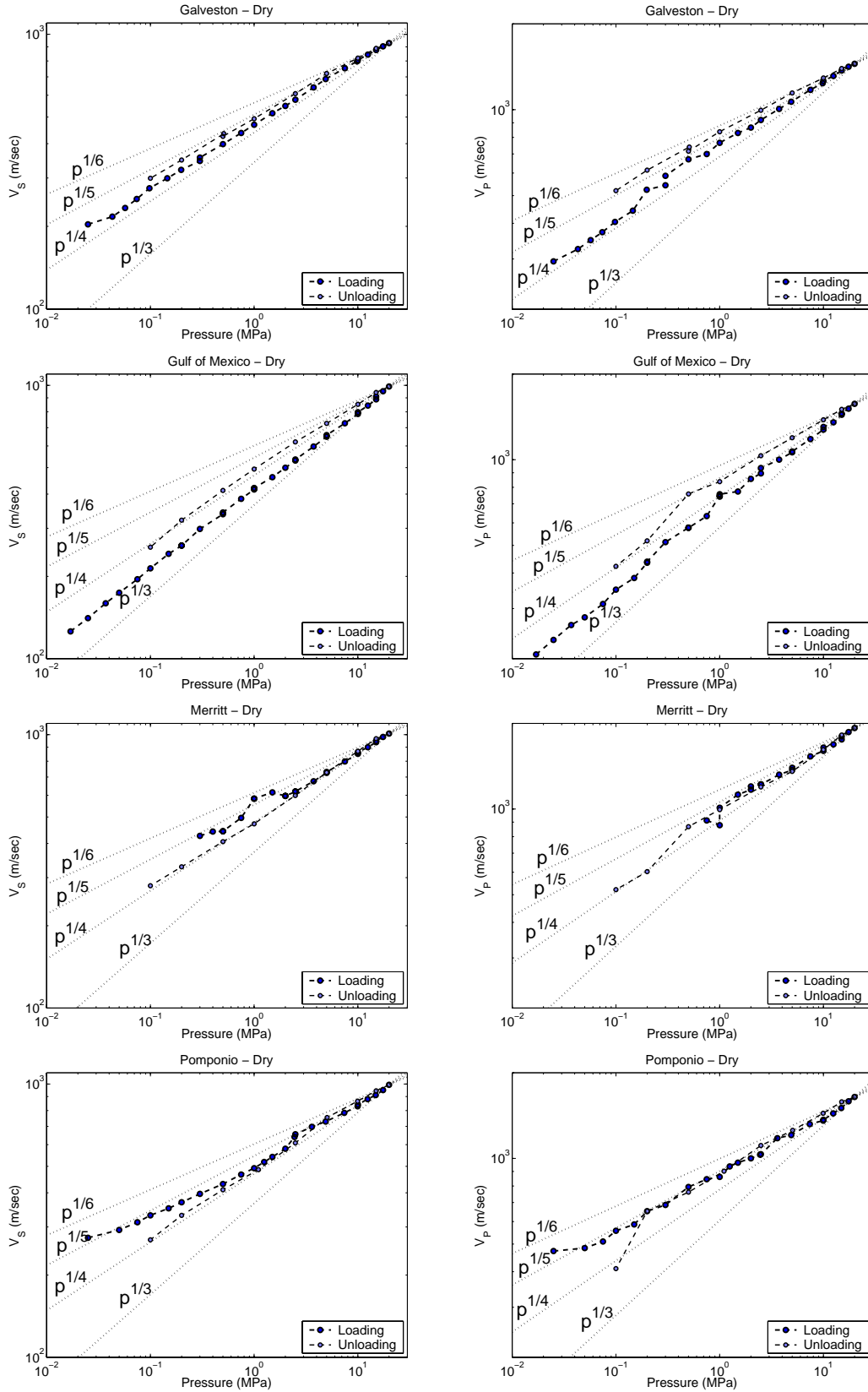
Figure 3.3: Loading and unloading path velocity data plotted against pressure in log-log plots, with slopes representing $p'^{1/6}$, $p'^{1/5}$, $p'^{1/4}$, and $p'^{1/3}$ pressure dependences.
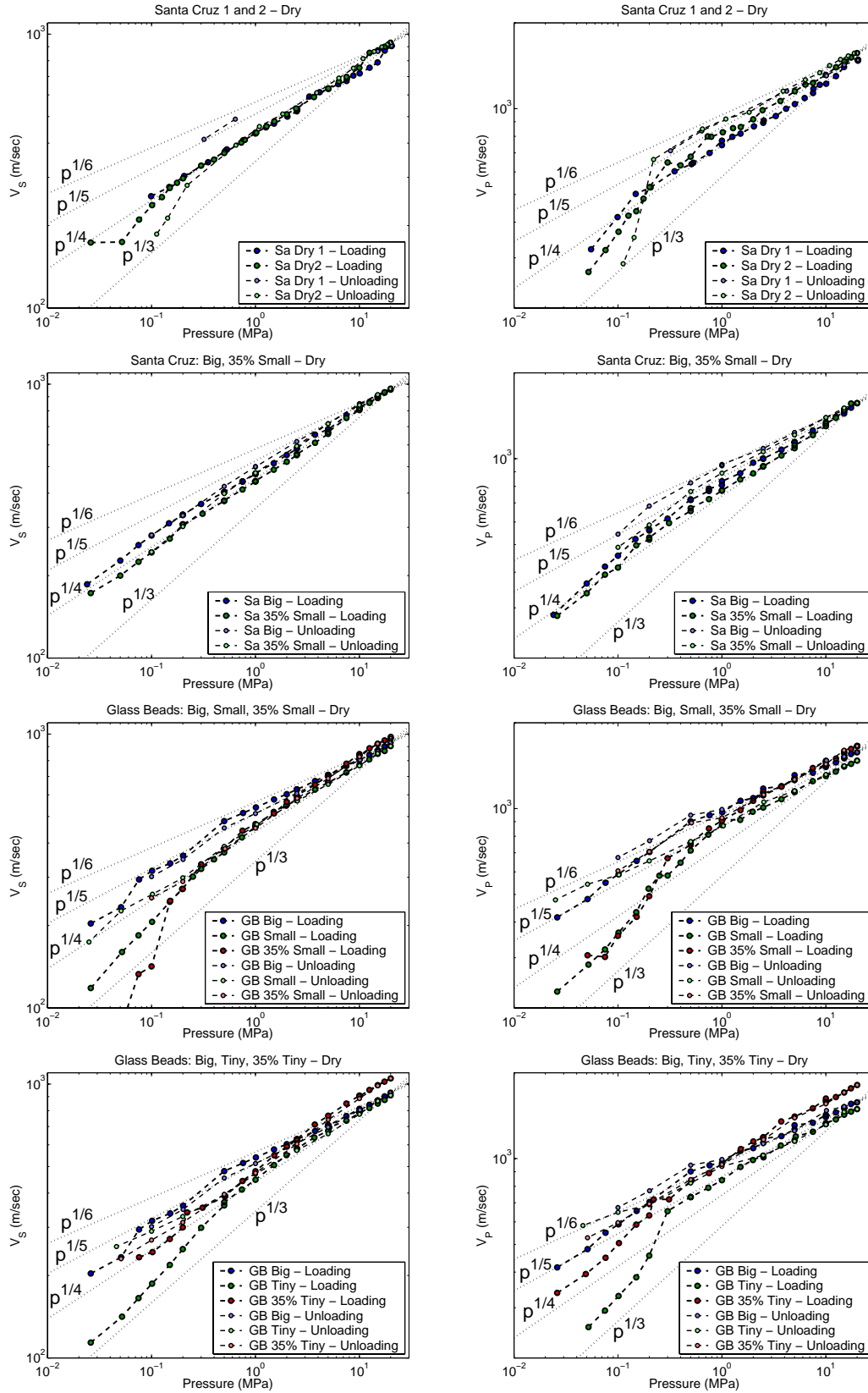
Figure 3.3: cont.

A comparison of the loading and unloading paths demonstrates that there is a very small increase in the velocities and a slight decrease in the pressure dependence of each of the velocities after consolidation to 20 MPa. The differences between the loading and unloading paths are consistently larger for the compressional-wave velocities than for the shear-wave velocities. The finer-grained Galveston Beach Sand and Gulf of Mexico Sand samples demonstrate the greatest decrease in the slope of the velocity-pressure trend upon unloading, though that difference is still relatively small.

Empirical fits of the forms proposed by Hardin and Blandford (1989), Fam and Santamarina (1997), and Robertson et al. (1995) were applied to the shear, bulk and P-wave moduli, and to the compressional- and shear-wave velocities from each sample. The forms of Fam and Santamarina and of Robertson et al. were applied directly to the dry velocity data. The Hardin and Blandford's forms, however, were simplified by lumping the void ratio function, *F(e)=0.3 + 0.7e²*, and Poisson's ratio terms, *F(ν)=2(1+ν)* for the shear waves and *F(ν)=(1+ν)(1-2ν)/(1-ν)* for the compressional waves, in with *S*, so that *n*, *k*, and *S/F(e)·F(ν)* were all treated as free parameters,. I then fit the forms of Equations 3.1 and 3.4 modified in this way to the moduli calculated from the velocity measurements. The Poission's ratio terms are constant for samples of the same mineralogy, so this term was eliminated to remove any ambiguity in the choice of an appropriate value for the various samples. Since the porosity varies with pressure, the void ratio term was removed so that the pressure dependence described by the fit parameters was independent of the porosity change. The resulting empirical forms closely resemble that of Fam and Santamarina, except that they 1) include an additional atmospheric pressure factor to make the *S* coefficient dimensionless, and 2) are fit to the moduli instead of the velocities. To allow fitting of the empirical forms to the water-saturated compressional-wave velocities and bulk and P-wave moduli, a constant, treated as a free parameter, was added to each expression. For example, the bulk modulus of the water saturated samples was fit with the following form:

$$K = K_0 + OCR^k S \ p_a^{1-n} p'^n .$$

(3.7)

Similarly, for the compressional-wave velocities the form of Fam and Santamarina (1997) was modified as follows:

$$V_P = V_{P0} + OCR^k S \left(\frac{p'}{p_a} \right)^{n/2} , \qquad (3.8)$$

and the form of Robertson et al. (1995) as follows:

$$V_P = V_{P0} + (A - Be) \left(\frac{p'}{p_a} \right)^{n/2} . \qquad (3.9)$$

Figure 3.4 shows the fit of these three basic empirical forms to the data from the Galveston Beach Sand sample. The velocity data from the dry sample are shown in linear and log-log plots against effective pressure in 3.4A and 3.4B, while the moduli are plotted against pressure in 3.4C. This figure demonstrates that each of these relations does a relatively good job of fitting the measured velocity and modulus data. The coefficients for each of the samples and the average values for each of the fit parameters are given in Tables 3.3 through 3.5.

For the shear modulus of the dry sand samples, the value of n varies from between 0.46 to 0.63, with an average value of 0.52. These values are within the range of the results of Hryciw and Thomann (1993). For these samples, the value of k for the shear modulus varied between -0.06 and 0.15, and averaged 0.06 for the dry samples, comparable to the values measured by Hryciw and Thomann (1993). These values of k are still relatively small compared to the values predicted for clays, which can be as large as 0.5 for high-plasticity clays (PI=100) and would be about 0.1 for a plasticity index of 10 (Hardin and Drnevich, 1972). The negative values of k observed for some of the samples imply a decrease in the modulus with consolidation to higher pressures. The Merritt Sand sample is the only sample to demonstrate a significantly large negative value for k. This is most likely because it was slightly cemented and had only been pre-compacted to a few hundred kPa. Pressurization to higher pressures may have broken the slight cementation, resulting in overall softening of the moduli.

The pressure dependence of the P-wave moduli of the dry sands is generally lower than that of the shear moduli, with *n* ranging from 0.44 to 0.58 and averaging 0.03 less than the *n* for the shear moduli of the dry samples. While the value of *n* was lower for the P-wave moduli, the value of *k* was almost always higher for the P-wave moduli than for the shear moduli, averaging 0.08 and ranging from -0.03 to 0.16. For the bulk moduli, the value of *n* is consistently even lower, averaging 0.46, while the value of *k* averages 0.09.
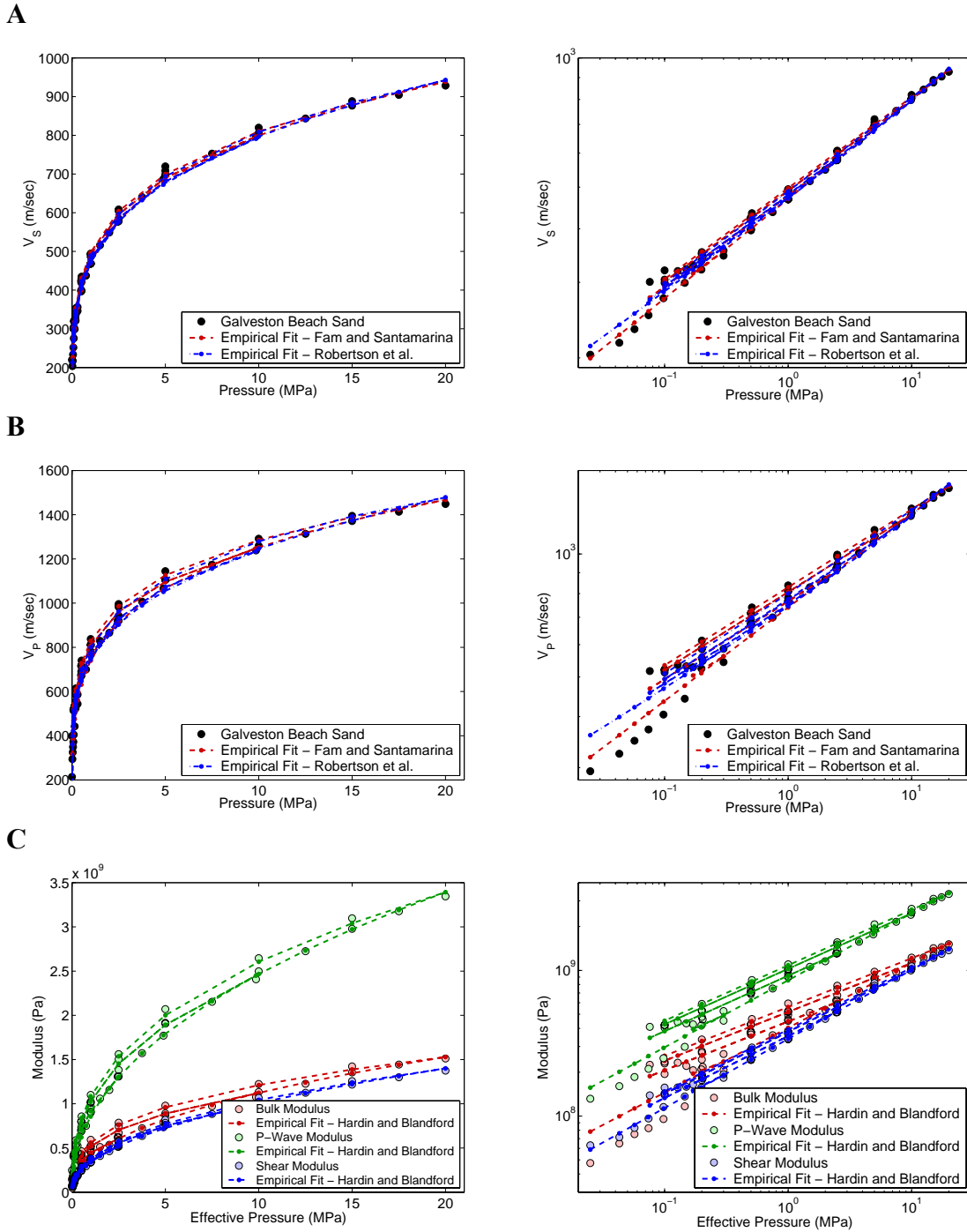
Figure 3.4: Comparison of empirical fits to the velocity and moduli data from the Galveston Beach sand: A) shear-wave velocity vs. pressure, B) compressional-wave velocity vs. pressure, and C) moduli vs. pressure. The panel of the left shows the comparison on a linear scale, while the right-hand panel shows the same data and empirical fits plotted on a log-log scale.

Table 3.3: Moduli fit coefficients – Hardin and Blandford (1989)

Sample:	G			M				K			
	S $(\times 10^3)$	n	k	S $(\times 10^3)$	n	k	M_0 (GPa)	S $(\times 10^3)$	n	k	K_0 (GPa)
Dry:											
Galveston	1.136	0.475	0.048	2.964	0.461	0.078	n/a	1.450	0.445	0.108	n/a
G. Mexico	0.572	0.634	0.150	1.962	0.576	0.123	n/a	1.226	0.524	0.101	n/a
Merritt	1.660	0.458	-0.056	5.666	0.467	-0.031	n/a	3.522	0.469	-0.019	n/a
Pomponio	1.450	0.463	-0.008	4.524	0.436	0.027	n/a	2.606	0.412	0.053	n/a
S.Cruz 1	0.815	0.520	0.151	2.532	0.500	0.157	n/a	1.459	0.482	0.156	n/a
S.Cruz 2	0.744	0.552	0.037	2.979	0.488	0.083	n/a	1.995	0.446	0.108	n/a
Sa Big	1.117	0.495	0.049	3.683	0.449	0.091	n/a	2.193	0.412	0.123	n/a
Sa 35% Sm.	0.841	0.564	0.075	2.763	0.522	0.103	n/a	1.657	0.485	0.124	n/a
Average:	1.042	0.520	0.056	3.384	0.487	0.079	n/a	2.014	0.459	0.094	n/a
Water Sat.:											
Galveston	1.038	0.480	0.021	1.384	0.503	0.090	5.893	n/c	n/c	n/c	n/c
G. Mexico	0.595	0.628	0.092	1.098	0.659	0.290	5.984	0.262	0.752	0.540	6.020
Merritt	0.534	0.696	0.222	0.678	0.844	0.534	6.905	0.265	0.902	0.709	6.824
Pomponio	0.934	0.568	0.067	1.254	0.629	0.237	7.015	n/c	n/c	n/c	n/c
S.Cruz 3	1.266	0.498	0.028	4.748	0.444	0.150	5.988	0.813	0.626	0.355	6.466
S.Cruz 4	1.508	0.476	0.032	3.888	0.480	0.147	6.129	1.091	0.621	0.326	6.234
Average:	0.979	0.558	0.077	2.175	0.593	0.241	6.319	0.608	0.725	0.482	6.386
Glass Beads:											
GB Big	1.834	0.373	-0.031	7.017	0.323	0.005	n/a	4.598	0.290	0.028	n/a
GB Small	1.019	0.470	0.008	4.020	0.398	0.047	n/a	2.729	0.344	0.068	n/a
GB Tiny	1.013	0.473	0.024	4.045	0.399	0.058	n/a	2.752	0.346	0.078	n/a
GB 35% Sm.	1.135	0.512	-0.005	5.222	0.421	0.041	n/a	3.808	0.363	0.066	n/a
GB 35% Ty.	1.300	0.520	-0.026	6.145	0.430	-0.002	n/a	4.621	0.370	0.007	n/a
GB 35% Ty. 2	0.741	0.626	-0.013	4.665	0.481	-0.026	n/a	3.962	0.400	-0.047	n/a
GB Broad	0.738	0.534	-0.041	3.279	0.456	0.001	n/a	2.319	0.410	0.022	n/a
Average:	1.111	0.501	-0.012	4.913	0.415	0.018	n/a	3.541	0.360	0.032	n/a

n/a – not applicable (assume to be zero).
n/c – fit would not converge.

For the glass bead samples and water-saturated sand samples, the fit coefficients show the same general behavior. As the fit of the water-saturated data is dominated by the constant added to the velocities, the rest of the fit parameters are more sensitive to noise in the data, so these parameters vary to a greater degree than for the dry data. The fit parameters for glass-bead samples are generally very consistent from sample to sample. The GB Big sample does stand out as the sample with the lowest pressure dependence (*n*). The two samples that were prepared by moist tamping them into the sample holder (GB 35% Tiny 2 and GB Broad) also stand out from the other glass bead samples, as they have the largest pressure dependences (*n*) and the lowest values of *S*. Several of the glass bead samples have negative values for *k*, especially for the shear moduli. The reason for this is not clear. Inspection of the glass beads in the samples

before and after loading does not reveal any damage to the beads. This implies that any changes must be a result of changes in the geometrical arrangement (i.e. texture) of the samples during the experiment.

For the velocities of the dry sands, the value of *n/2* averages 0.242 for the shear-wave velocities, and 0.233 for the compressional-wave velocities, based on the fit to the form of Fam and Santamarina (Equation 3.2). The change in the density with loading causes this value not to be exactly half of the value for the respective moduli, and also results in generally lower values of *k*. Likewise, from the fit to the form of Robertson et al. (Equation 3.3), the values of *n*, averaging 0.227 and 0.204 for the shear- and compressional-waves respectively, are lower still, due to the porosity correction that is included in the fit. The values of *A* and *B* derived from the fit to this form also demonstrate a great deal of variation and a strong correlation between the two parameters, with large values of *A* correlating to large values of *B*.

Table 3.4: Velocity fit coefficients - Fam and Santamarina (1997)

	Sample:	V_S			V_P			
		S (m/sec)	n/2	k	S (m/sec)	n/2	k	V_{P0} (m/sec)
Dry:	Galveston	275	0.232	0.020	437	0.229	0.038	n/a
	Gulf of Mexico	213	0.290	0.046	376	0.274	0.038	n/a
	Merritt Sand	341	0.204	-0.049	599	0.221	-0.031	n/a
	Pomponio	312	0.217	-0.020	548	0.206	-0.005	n/a
	Santa Cruz 1	246	0.241	0.052	433	0.230	0.062	n/a
	Santa Cruz 2	237	0.259	-0.008	441	0.244	0.017	n/a
	SC Big	282	0.233	0.010	495	0.218	0.038	n/a
	SC 35% Small	246	0.262	0.012	439	0.244	0.030	n/a
	Average:	269	0.242	0.008	471	0.233	0.023	n/a
Water Sat:	Galveston	229	0.241	0.010	25.4	0.435	0.036	1736
	Gulf of Mexico	174	0.312	0.029	18.3	0.593	0.222	1744
	Merritt Sand	169	0.333	0.090	11.8	0.745	0.444	1801
	Pomponio	218	0.278	0.016	23.4	0.530	0.148	1843
	Santa Cruz 3	258	0.244	-0.002	97.9	0.346	0.093	1708
	Santa Cruz 4	273	0.246	0.018	56.5	0.449	0.126	1775
	Average:	220	0.276	0.027	38.9	0.516	0.178	1768
GB:	GB Big	340	0.189	-0.014	663	0.164	0.009	n/a
	GB Small	248	0.248	0.013	483	0.217	0.041	n/a
	GB Tiny	242	0.255	0.034	487	0.216	0.050	n/a
	GB 35% Sm.	238	0.271	0.011	519	0.221	0.036	n/a
	GB 35% Ty.	261	0.268	-0.006	560	0.226	0.010	n/a
	GB 35% Ty. 2	198	0.312	0.006	495	0.243	-0.025	n/a
	GB Broad	236	0.239	-0.035	462	0.218	-0.009	n/a
	Average:	252	0.255	0.001	524	0.215	0.016	n/a

Table 3.5: Velocity fit coefficients - Robertson et al. (1995)

Sample:		V_S			V_P			
		A (m/sec)	**B** (m/sec)	**n/2**	**A** (m/sec)	**B** (m/sec)	**n/2**	**V_{P0}** (m/sec)
Dry:	Galveston	575	384	0.207	1340	1160	0.184	n/a
	Gulf of Mexico	526	394	0.235	776	500	0.230	n/a
	Merritt Sand	94.9	-354	0.254	280	-466	0.255	n/a
	Pomponio	270	-42.9	0.228	638	144	0.204	n/a
	Santa Cruz 1	659	547	0.185	1245	1075	0.169	n/a
	Santa Cruz 2	244	11.7	0.259	569	154	0.232	n/a
	SC Big	399	159	0.220	1209	961	0.175	n/a
	SC 35% Small	361	179	0.244	865	650	0.207	n/a
	Average:	391	160	0.229	865	522	0.207	n/a
Water Sat.:	Galveston	253	23.3	0.234	131	125	0.331	1725
	Gulf of Mexico	289	145	0.281	314	388	0.296	1729
	Merritt Sand	530	632	0.231	558	1033	0.241	1786
	Pomponio	290	95.8	0.263	347	427	0.253	1799
	Santa Cruz 3	268	18.5	0.243	546	556	0.196	1631
	Santa Cruz 4	605	468	0.227	1047	1394	0.256	1763
	Average:	372	230	0.246	490	654	0.262	1739
GB:	GB Big	-267	-961	0.221	568	-182	0.161	n/a
	GB Small	-149	-577	0.265	749	323	0.198	n/a
	GB Tiny	489	315	0.228	2562	2787	0.150	n/a
	GB 35% Sm.	146	-222	0.273	1483	2013	0.175	n/a
	GB 35% Ty.	-57.1	-745	0.295	-110	-1623	0.244	n/a
	GB 35% Ty. 2	269	202	0.303	-285	-2243	0.289	n/a
	GB Broad	199	-36.0	0.257	421	-59.9	0.224	n/a
	Average:	90.0	-289	0.263	770	145	0.206	n/a

COMPARISON TO CONTACT MODELS

Except for the bulk and P-wave moduli of sample GB Big, the moduli of all of the samples demonstrate a pressure dependence above $p'^{1/3}$, the dependence predicted by Hertz-Mindlin contact models. Figure 3.5A compares the velocities predicted by the contact model to the velocities measured for a representative sand sample. The model predictions were calculated assuming that the coordination number varies with porosity according to the trend observed by Murphy (1982) and tabulated in Mavko et al. (1998). This trend can be estimated from the following function:

$$C = 24.00 \exp(-2.547\phi) - 0.3731. \tag{3.10}$$

The velocities predicted by the no-slip contact models (Equation 3.5) vastly over-predict the magnitude of both the compressional- and shear-wave velocities of all of the samples. The zero-friction, zero-tangential-stiffness, "soft" model of Walton does a much better job of modeling the overall magnitude of the velocities, though the mismatch between the pressure dependences, illustrated by the slope of the model and data trends, is apparent in the log-log plot on the right in Figure 3.5A. A comparison of the model predictions for

the actual bulk and shear moduli (Fig. 3.5B) shows that the magnitude of the bulk modulus, which is identical for both the infinite- and zero-friction models, is predicted fairly well by the models. The shear modulus, on the contrary, is reduced dramatically in the zero-friction case, so that the modulus and velocities from the models provide a reasonable match to the magnitude of the data.

Figure 3.6A shows the comparison of the contact-model predictions to the experimental bulk and shear moduli from the normally consolidated, initial loading path and the final unloading path of sample GB Big. For this sample, the zero-friction model fits both the magnitudes of the velocities and their pressure dependence quite well. Nevertheless, the other glass bead samples do show larger pressure dependences, especially for the shear modulus, that are not matched by the contact models, as shown in Figure 3.6B for the GB Small sample.

A
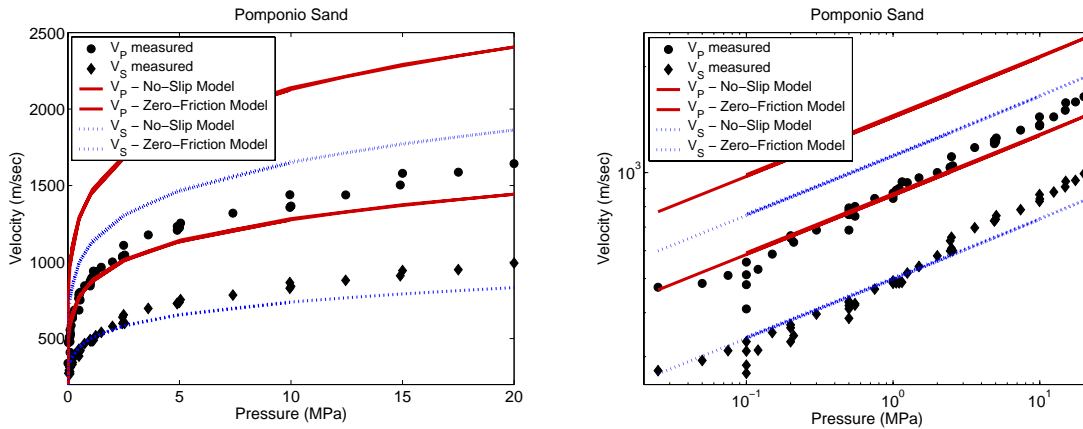
B
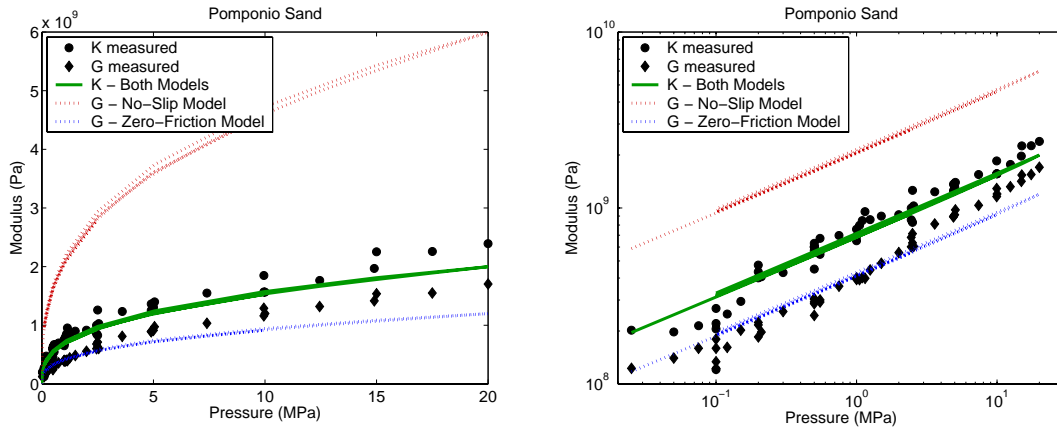
Figure 3.5: Comparison of contact model predictions to data from the dry Pomponio Beach sand:
A) the velocities in linear and log-log plots, and B) the bulk and shear moduli.

43

A

B
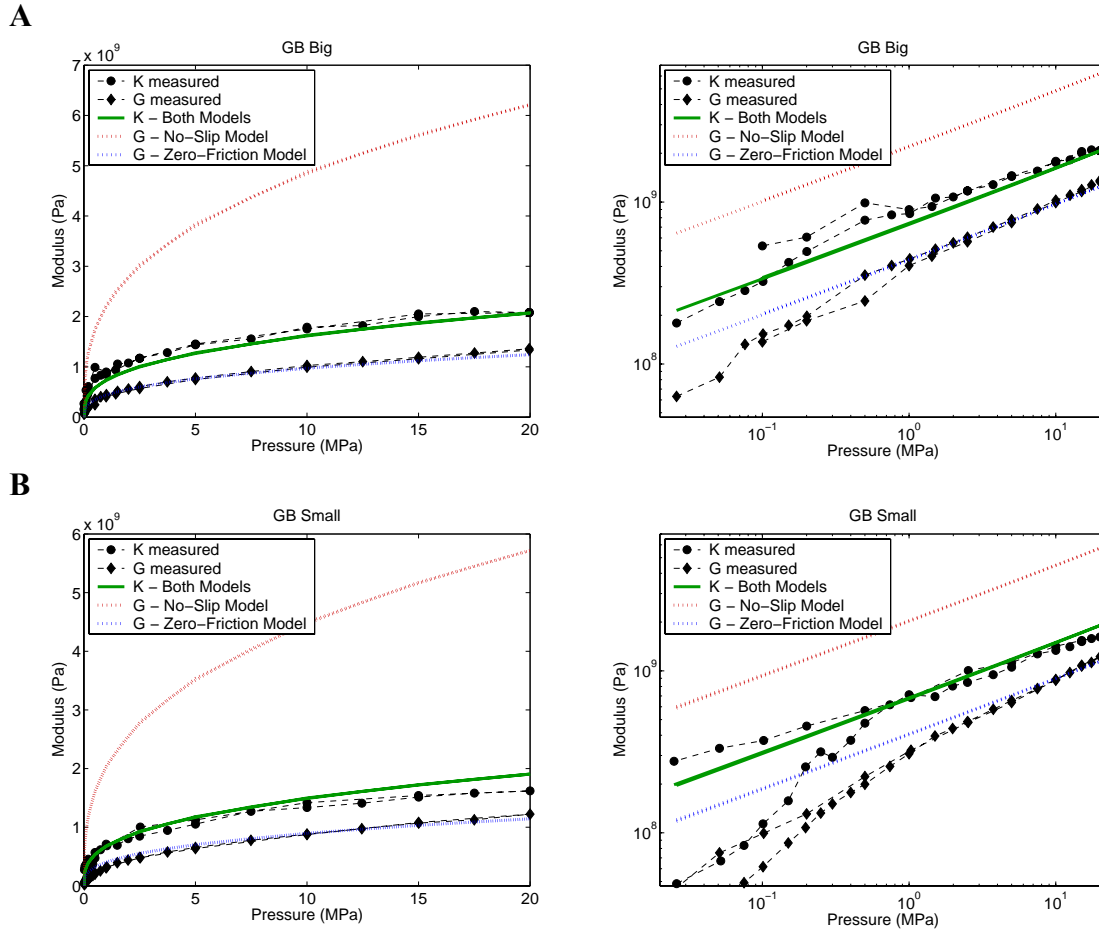
Figure 3.6: Comparison of contact model predictions to moduli data from glass bead samples A) GB Big and B) GB Small.

Allowing the coordination number to vary according to Equation 3.10 has very little effect on either the magnitude or the pressure dependence of the contact model predictions. It does result in an almost imperceptible increase in the slope of the model predictions, but not enough to match the slope observed in the data from the sand samples. This variation in the coordination number also fails to produce the significant increases in the velocity with consolidation of the samples seen in the data (e.g. Figure 3.3). Likewise, the contact model equations in Equations 3.5 and 3.6 can be used to invert for the coordination number required to match the models to the data. The results of such an inversion are shown for the dry Pomponio Beach sand, Gulf of Mexico sand, and the GB Big samples in Figure 3.7. There is a fair bit of scatter in the inverted coordination numbers at the lowest pressures, most likely because the measured moduli do not really approach zero at low pressures. The coordination numbers required to fit the no-slip

44

shear-modulus model vary from 2 to 4 for all three samples. The coordination numbers inverted from the zero-friction shear-modulus models rise with pressure from less than 6 to almost 16 for the sand samples and from 8 to 10 for the glass bead sample. The coordination numbers inverted from the bulk modulus data stay close to 10 over the entire pressure range for the sands, while they drop from near 15 to about 10 with increasing pressure for the glass bead sample.

DISCUSSION

The fact that the contact models demonstrate a power-law pressure dependence and that the zero-tangential-stiffness versions provide a good match to the magnitude of all the data and to the pressure dependence of the large-grained glass bead sample indicates that these models are probably capturing the basic mechanics controlling the wave speeds in granular materials. The significant over-prediction of the magnitudes of the velocities by the no-slip model does indicate that the no-slip and no-grain-rotation assumptions do not hold in unconsolidated materials.

The misfit between the power-law exponents observed in the data and that predicted by the contact models may be due to a number of factors. Goddard (1990) suggests that this misfit could be due either to the grains not being perfect spheres or to changes in the coordination number with pressurization of the sample. The fact that the data from the large-grained glass-bead sample fits the $p'^{1/3}$ pressure dependence predicted by the models, while the sand data do not, might indicate that the shape of the grains at the contacts is controlling the pressure dependence. On the contrary, the other glass bead samples do not display such a low pressure dependence, especially for the shear modulus, suggesting that this might not be the only factor determining the pressure dependence. Likewise, the contact geometry required by Goddard to produce a $p'^{1/4}$ dependence, namely, a cone in contact with a plane, is no more likely to be universally valid for these sands than that of two perfect spheres in contact.

For a change in the coordination number to cause the higher pressure dependence, the change in coordination number for the samples must be of the same order of magnitude as those shown for the sands in Figure 3.7. While the maximum coordination number possible for an assemblage of identical spheres is 12, mixtures of particle sizes could produce larger average coordination numbers. Thus, the coordination numbers inverted

45

A

B

C
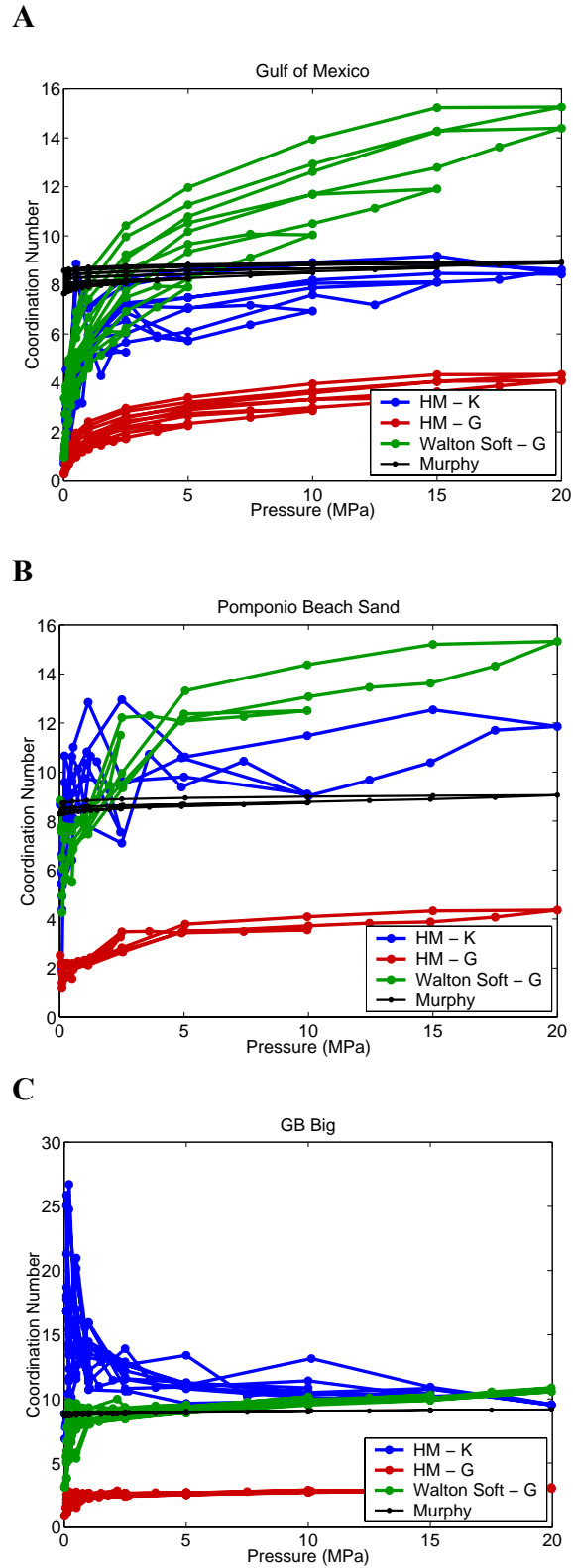
Figure 3.7: Coordination numbers predicted for the A) Gulf of Mexico sand, B) Pomponio Beach sand, and C) GB Big samples from the infinite-friction (HM) and zero-friction (Walton Soft) contact models. The black line demonstrates the contact numbers predicted by Murphy (1982) for the porosities of the samples.

from the contact models are within the range of values that might be observed in irregularly shaped granular media with a distribution of grain sizes. Nevertheless, the range of coordination numbers predicted from Equation 3.10 for the measured porosities (in black in Figure 3.7) does not match that inverted from the contact models. Likewise, the small changes in porosity observed in the samples, and the limited porosity rebound on unloading, would not be likely to produce a doubling of the coordination number on loading and an almost complete rebound of the coordination number on unloading. For these reasons the change in the coordination number does not seem likely to be a principle control on the pressure dependence.

While the non-spherical contact geometry and the change in the coordination number with pressure do not provide entirely satisfactory explanations for the differences between the measured and model-predicted pressure dependences, the fact that the zero-friction contact models roughly match the magnitude of the measured moduli suggests that changes in the slip and grain rotation behavior with pressure might contribute significantly to this difference. The friction of two grains in contact is of course neither infinite nor zero. Likewise, the prevalence of slip or grain rotation at the contacts is more likely to be free to change with pressure than is the coordination number. As the sample is pressurized, the normal force at each individual contact will increase, limiting the number of contacts that will slip. At the same time the grain framework will become more rigid, limiting the amount of sympathetic (non-slip) grain rotation that can occur at neighboring grains. Numerical modeling of stress-strain behavior of granular media has confirmed that the occurrence of slip and rotation at grain contacts can produce a significant softening of the granular framework, with the effect of grain rotation being more important than that of slip at the contacts (Jenkins, 1997). However, to my knowledge the variation in the amount of rotation or slip with pressure and its influence on the pressure dependence has not been simulated. Nevertheless, the fact that the models require that slip be occurring at the contacts to fit the magnitudes of the velocities indicates that the variation in the amount of this slip or grain rotation with pressure might be responsible for the larger pressure dependences observed in the measurements.

A number of other factors that were not systematically investigated here might also influence the pressure dependence of the velocities and elastic moduli of granular

materials. These include textural factors such as the packing, age, and mineralogy (especially clay content) of the material, as well as experimental factors such as the strain magnitude and strain rate. Likewise, at higher pressures the pressure dependence is likely to change once grain breakage begins to occur. Given the potential influence of these parameters, the application of the results presented here for predictions of the pressure from velocities measured *in situ* should be done cautiously, limiting the application to similar, very unconsolidated sands, in the pressure range from 100 kPa to 20 MPa.

CONCLUSIONS

Data from ultrasonic velocity measurements on 21 sand and glass bead samples demonstrates that for unconsolidated, non-cohesive sediments the shear-wave velocity exhibits a pressure dependence close to $p'^{1/4}$ that is consistent with pressure from below 100 kPa to 20 MPa. For the compressional-wave velocities, the pressure dependence is generally slightly lower, between $p'^{1/4}$ and $p'^{1/5}$. These sediments exhibit only a slight increase in the velocities and decrease in the pressure dependence with preconsolidation, though the effect is larger for the compressional-wave velocities than for the shear-wave velocities.

Only one of the samples demonstrates a pressure dependence close to the $p'^{1/3}$ dependence predicted by Hertz-Mindlin contact theory, and the magnitude of the velocities for all of the samples is fit by the contact theories only when zero-friction between the grains is assumed. Obviously, for truly unconsolidated granular media, the assumptions of no slip at the contacts and of no rotation of the grains are not valid. The power-law trend observed in the moduli of all of the samples indicates that the contact mechanics are the principle control on the wave speeds. The continuity of the pressure dependence over the entire pressure range of the measurements suggests that the controlling mechanics are also consistent over the entire pressure range. The fact that the sand samples and the other glass-bead samples demonstrate larger pressure dependences, especially for the shear moduli, and that the porosity changes observed in the samples are not large enough to support the coordination number changes required to produce these pressure dependences, suggests that changes in the amount of slip and grain rotation at the contacts might be responsible for the larger pressure dependences observed in the measurements.

CHAPTER 4:
INFLUENCE OF POROSITY VARIATION FROM SORTING AND COMPACTION ON THE SEISMIC VELOCITIES IN UNCONSOLIDATED SANDS

ABSTRACT

The objective of the study presented in this chapter was to investigate the influence of sorting- and compaction-induced porosity variation on the seismic velocities and their pressure dependences in unconsolidated sands. This involved preparing a set of texturally similar, unconsolidated, granular samples with initial porosities from 0.24 to 0.44 by reconstituting sand and glass-bead samples with controlled grain-size distributions. Each sample was run through a series of hydrostatic pressure cycles at pressures from 100 kPa up to 20 MPa, and the compressional- and shear-wave velocities and porosity were measured at a number of pressures on the initial loading path and on the unloading and reloading paths. This chapter will also discuss the impact of the porosity on other velocity-related parameters, including the acoustic and shear impedances and V_P-V_S ratio, which might be extracted from seismic reflection data for use in pressure prediction.

Over this porosity range from 0.24 to 0.44, the velocities measured in the dry samples at a given pressure show very little sensitivity to the porosity. In the water-saturated case, velocities modeled from Gassmann fluid substitution demonstrate a significant increase in the compressional-wave velocity with decreasing porosity. For both the dry and water-saturated cases, the porosity-velocity trend at a given pressure can be roughly described by the isostress (harmonic) average between the moduli of the highest porosity sample at that pressure and the moduli of quartz, the predominant mineral component of the samples.

I fit an empirical, power-law expression of the effective pressure to the bulk, shear, and P-wave moduli from each sample and compared the pressure dependences for the various samples. The pressure dependence was taken to be represented by the exponent of the effective pressure in this power-law fit. For the dry measurements there is no systematic relationship between the pressure dependences and the porosity for either the initial loading or the unloading-reloading paths for any of the moduli. For the water-saturated case, there still appears to be no systematic relationship between the pressure

dependences and the initial porosity, though there is a difference in the pressure dependences of the bulk and P-wave moduli of the sands and glass beads due to the larger porosity change in the sand samples with loading.

The V_P-V_S ratio, Poisson's ratio, and shear and compressional impedances were calculated from the measured velocity data and from the water-saturated velocities modeled with Gassmann fluid substitution. The V_P-V_S ratio and Poisson's ratio, which are relatively insensitive to pressure for the dry samples, demonstrate a strong pressure dependence for the water-saturated velocities. The water-saturated V_P-V_S ratio appears to be slightly porosity-dependent at a given pressure, but the systematic, porosity-dependent variation is small compared to the scatter due to sample-to-sample variation in the shear-wave velocities. The impedances demonstrate behaviors similar to those of the corresponding velocities, though the water-saturated compressional impedance demonstrates a slightly larger relative porosity dependence than does the compressional-wave velocity.

INTRODUCTION

Two of the most common parameters that are sought to be remotely evaluated in the unconsolidated section of the sedimentary column are the porosity and pressure. The porosity of the clean, unconsolidated sands that make up some shallow aquifers and reservoirs largely dictates their flow properties, as well as the volumes of fluids that they contain. Likewise, the monitoring of pressures in these aquifers and reservoirs during fluid withdrawal can indicate zones of higher permeability and make the location of bypassed sections of water or oil possible. Both the porosity and the pressure also strongly influence the mechanical behavior of the sands, with high-porosity sands or sands that experience low effective pressures being more likely to experience compaction, shear failure, or liquefaction upon additional loading. In consolidated sandstones, both the porosity and pressure have been observed to strongly influence the seismic velocities (Wyllie et al., 1958; Han et al., 1986; Eberhart-Phillips et al., 1989; Freund, 1992; Jones, 1995; Khaksar et al., 1999). These observations enable the use of the velocities, or of velocity-related parameters obtained from seismic reflection surveys, to make *in situ* estimates of the porosity of sandstones or of the pressures that they experience.

In the studies of the velocity-porosity relationships in consolidated rocks (Wyllie et al., 1958; Han et al., 1986), the basic observation is that the velocity of rocks with similar textures tends to increase with decreased porosity. Because there are so many factors that influence the velocities and porosity in clastic rocks, there is a significant amount of uncertainty in applying any general porosity-velocity relationship to field data. These factors include textural factors such as the mineralogy (especially clay content), degree of cementation, depositional environment (and associated grain shapes and packing), and particle size distribution (including sorting and mean particle size), as well as non-textural parameters such as the fluid content, stress state, and stress history. Some of these parameters influence the porosity more than the velocity, and vice versa.

In clean, unconsolidated sands, the particle size distribution, also referred to as the sorting or grading, is one of the key controls on the porosity. A well sorted or poorly graded sand has a narrow distribution of particle sizes, while a poorly sorted or well graded sand contains a wide range of grain sizes. In general, the better the sorting and narrower the particle-size distribution are, the higher the porosity of the sand (Beard and Weyl, 1973, Cumberland and Crawford, 1987). In a poorly sorted sand, many of the smaller grains can fit within the open pores between the larger grains, resulting in a lower porosity. For a sand of a given texture and sorting quality, the porosity will also be a function of the stress history that the sand has experienced. The larger the stresses the sand has been exposed to, the greater the compaction that it will have experienced, and the lower its porosity will be.

Dvorkin and Nur (1996) recognized that the velocity-porosity trends of a set of texturally similar, poorly consolidated sands (porosities 0.22 to 0.38) at a given pressure could be approximated by the Hashin-Shtrikman lower bound between the moduli of the principal mineral and the moduli predicted by Hertz-Mindlin contact models at the critical porosity at that pressure. The lower Hashin-Shtrikman bound represents the lower limit of the moduli produced by a mixture of two materials, and closely approximates the moduli measured in suspensions. Avseth et al. (2000) observed a similar relationship between the log-derived compressional-wave velocities and porosities of poorly consolidated reservoir sands from the North Sea. They attributed the porosity variation to

variation in the sorting based on particle-size distributions garnered from thin section analysis.

A number of researchers in the geotechnical community have measured the influence of the porosity and pressure on the shear-wave velocity and shear modulus in unconsolidated sands. Robertson et al. (1995) investigated the effect of porosity variation due to variations in the packing of samples and to different amounts of compaction on the shear-wave velocities in reconstituted samples of Ottawa sand. They fit empirical relations of the following form to the shear-wave velocity, V_S:

$$V_S = (A - Be)\left(\frac{p'}{p_a}\right)^{n/2},$$

(4.1)

where A, B, and n are empirical coefficients, e is the void ratio, p' is the effective pressure, and p_a is the atmospheric pressure. The parameter n dictates the pressure dependence, while the B parameter represents the effect of the porosity. Hardin and Blandford (1989) also incorporate a porosity correction in empirical forms that they developed for the shear modulus. For the shear modulus their expression is as follows:

$$\mu_{ij} = \frac{OCR^k}{F(e)} \frac{S_{ij}}{2(1+v)} p_a^{1-n} \left(\sigma_i' \sigma_j'\right)^{n/2},$$

(4.2)

where μ_{ij} is the shear modulus in the plane of propagation, which experiences the effective stress σ_i' in the direction of propagation and σ_j' in the direction of particle motion, p_a is the atmospheric pressure, and v is the Poisson's ratio of the grain material. This expression can be simplified to equation 3.4 for an isotropic stress state. Equation 4.2 includes two free parameters: S_{ij}, a multiplier to account for textural factors and structural anisotropy, and n, the exponent to the effective stress. The void-ratio function, $F(e)=0.3 + 0.7e^2$, is meant to account for the effect of porosity variation, whether the result of textural differences between samples or of the compaction of a given sample. The OCR^k term corrects the pressure dependence for the effects of compaction or preconsolidation of the sample, where OCR is the overconsolidation ratio, and k is a function of the plasticity index, usually assumed to be zero for sands. Since the overconsolidation ratio is defined as the preconsolidation pressure divided by the current pressure, the moduli for unloading or reloading paths is simply proportional to the effective stress to the power $n-k$. A large body of measurements, most made at pressures

below 700 kPa, has demonstrated that the value of n for the shear modulus in loose sands is generally near 0.5, and that the value of k for sands is generally close to zero (Hardin and Black, 1969; Yu and Richart, 1984; Hryciw and Thomann, 1993). Chapter 3 demonstrates that these values hold over pressures from 100 kPa to 20 MPa for measurements on a number of reconstituted sands of various textures.

Hardin and Blandford (1989) extend the empirical form presented in Equation 4.2 to the compressional-wave modulus, M_i, as follows:

$$M_i = \frac{OCR^k}{F(e)} \frac{S_i(1-\nu)}{(1+\nu)(1-2\nu)} p_a^{1-n} \sigma_i'^n, \tag{4.3}$$

where σ'_i is the stress in the direction of wave propagation, and all the other symbols are the same as for Equation 4.2. This form is only appropriate for the modulus in dry samples, whereas in water-saturated samples a constant free parameter (M_0) must be added to the expression (e.g. Equation 3.7). Hardin and Richart (1963) provide a detailed summary of early measurements of the compressional- and shear-wave velocities at low pressures, demonstrating that the pressure dependences of the compressional-wave velocities are similar to those of the shear-wave velocities. Pilbeam and Vaisnys (1973) measured pressure dependences of the velocities in dry and lubricated synthetic glass bead and crushed glass samples, observing the pressure dependence to vary from $p'^{1/3}$ to $p'^{1/6}$ for the various samples. Additional measurements of the compressional-wave velocities in unconsolidated sands have been made by Domenico (1977), Yin (1992), and Estes et al. (1994) at pressures above 2.5 MPa, and by Prasad and Meissner (1992) at pressures from 0.16 to 20 MPa in water-saturated sands. Chapter 3 demonstrates that Equation 4.3 is an effective empirical form for a pressure range from 100 kPa to 20 MPa, and that the value of n for the compressional-wave and bulk moduli is slightly lower than for the shear modulus, while the value of k is slightly larger than for the shear modulus.

The work presented here has two goals. The first is to investigate the effect of porosity variations due to sorting and compaction on the seismic velocities in unconsolidated sands. The second is to investigate the influence that this porosity variation has on the pressure dependences of the velocities, and on other related pressure indicators that might be extracted from seismic reflection data. In an effort to extend these relationships to unconsolidated sediments, this work will concentrate on measuring

the effect of the grain-size distribution, stress, and stress history on the porosity and velocities.

To do this, an idealized set of samples were prepared by reconstituting sand and glass bead samples with controlled grain-size distributions. This experiment was designed to standardize the samples so that it might isolate the effects of the sorting and eliminate other textural effects such as the clay content and diagenetic effects, including initial cementation. This chapter will present compressional- and shear-wave velocity measurements made on these texturally similar sand and glass bead samples over a range of porosities from 0.25 to 0.44 and at pressures from 100 kPa to 20 MPa. It will also compare these laboratory results to the porosity-velocity trends observed by Dvorkin and Nur (1996) and Avseth et al. (2000), and to the low-pressure empirical corrections of Hardin and Blandford (1989). Finally, it will discuss potential ways to reduce the uncertainty that porosity variation might introduce in pressure predictions from the velocities or velocity-related parameters.

EXPERIMENTAL METHODS AND SAMPLES

Here, data will be presented from thirteen samples: six sand samples and seven glass bead samples, with initial porosities from 0.26 to 0.44. Four of the sand samples were reconstituted samples of a fine-grained, well sorted, quartz sand called the Santa Cruz Aggregate. Two of these were run dry (Sa Dry 1, Sa Dry 2), and two were water-saturated (Sa Wet 3, Sa Wet 4). The other two sands were synthetic samples made up of sieved fractions of this sand, both of which were run dry. One sample (Sa Big) was entirely made up of 0.295 to 0.350 mm grain sizes. A second sample (Sa 35% Small) was made up of 65% by mass of the 0.295 to 0.350 mm size fraction and 35% of 0.053 to 0.088 mm grains. All seven glass bead samples were run dry. Three samples (GB Big, GB Small, and GB Tiny) consisted of different narrow size ranges of beads. Three samples (GB 35% Small, GB 35% Tiny 1 and 2) were made with a "bimodal" mixture of grain sizes, with 35% of the mass made up of smaller grains and 65% of larger grains. Finally, one sample (GB Broad) was made up of a broad range of particle sizes. Table 4.1 summarizes the grain sizes used and the initial porosities of all the samples.

Special attention was given to preparing the samples in such a way as to insure complete mixing of the different grain sizes, and to maintain full saturation of the water-

saturated samples. However, the sample preparation varied based on whether the sample was a single grain size and dry or water-saturated, or was a mixture of grain sizes. The dry single-size samples were prepared by air pluviation, while the water-saturated samples were prepared by water pluviation. Most of the mixed-size samples were mixed dry, split into four sections, and each section was air pluviated into the sample holder separately. Two samples, however, GB 35% Tiny 2 and GB Broad, were mixed after being moistened with a few mL of water, and then were tamped down in the sample holder and allowed to dry. These differences in sample preparation produced variations in the packing of the grains and led to some noticeable scatter in the data. More detailed descriptions of the sample preparation protocols are given in Chapter 2.

Table 4.1: Sample summary

	Sample Name:	Initial Porosity		Fraction	Size (μm)	Fraction	Size (μm)
Sands:	Sa Dry 1	0.414	clean, quartz sand; well sorted D_{10}=0.178 mm [1] D_{60}=0.304 mm				
	Sa Dry 2	0.438					
	Sa Wet 3	0.400					
	Sa Wet 4	0.418					
	Sa Big	0.409		1	295-350	---	---
	Sa 35% Small	0.380		0.65	295-350	0.35	53-88
Glass	GB Big	0.381		1	295-350	---	---
Beads:	GB Small	0.411		1	74-88	---	---
	GB 35% Small	0.321		0.65	295-350	0.35	74-88
	GB Tiny	0.422		1	37-44	---	---
	GB 35% Tiny 1	0.296		0.65	295-350	0.35	37-44
	GB 35% Tiny 2	0.258		0.65	295-350	0.35	37-44
	GB Broad	0.338			37-710	---	---

[1] D_{10} and D_{60} are the grain diameters below which 10%, or 60% respectively, of the mass of the sample is found.

The initial porosity of the samples was calculated from the grain density, dry sample mass, and sample volume. The strains of the sample were monitored with loading to allow the volume and porosity changes to be determined throughout the run. Each sample was loaded hydrostatically through a series of pressure cycles with subsequently increasing peak pressures up to 20 MPa. The velocities and porosity were measured at the same set of pressures during each cycle to allow the comparison of the velocities and porosities measured at the same pressure for a sample that had been preconsolidated to a range of higher pressures. Five of the samples were subjected to 8 or 9 cycles, while the rest underwent between 1 and 5 cycles. The velocities were measured by pulse

transmission based on the pick of the first arrival. Detailed descriptions of the experimental apparatus and procedures can be found in Chapter 2.

POROSITY TRENDS

Prior to being subjected to any load, the variation in the porosities of the samples given in Table 4.1 is a result of the different grain-size distributions, sample preparation protocols, and particle shapes (sands vs. glass beads) of the various samples. These initial porosities vary from about 0.26 to about 0.44; the initial porosities of the sand samples are limited to the range of about 0.38 to 0.44, with the glass bead samples covering the whole range. This is demonstrated by a plot of the velocities, color-coded by sample, shown in Figure 4.1. For either the sands or glass beads, the texture of the samples and the sample preparation protocols were similar enough that the primary control on the porosity should be the grain-size distribution.

For an individual sample, the porosity decreases with loading, and then rebounds only partially upon unloading. The pressure path and porosity observed for sample Sa 35% Small are shown in Figure 4.2, demonstrating the amount of porosity change and the limited rebound typically experienced by the sand samples. The glass bead samples tend to experience much less porosity loss with loading, and a more complete rebound of the porosity upon unloading, as can be seen by the smaller spread of the glass bead samples with porosity in Figure 4.1.

The porosity reduction of the individual samples was fit with an empirical expression of the following form:

$$\phi = \phi_0\left(1 - A\left(\frac{p'}{p_a}\right)^m OCR^l\right), \tag{4.4}$$

where ϕ is the porosity, ϕ_0 is the initial porosity of the samples, p' is the effective pressure, OCR is the overconsolidation ratio, and A, m, and l are free parameters. The fit of this expression to the porosity data for sample Sa 35% Small is shown in Figure 4.2C, where $1 - \phi/\phi_0$ is plotted against the pressure, and the fit coefficients for each sample are given in Table 4.2. The fit can be improved slightly by leaving the initial porosity, ϕ_0, as a free parameter, as the linearization of the first few normally consolidated points in the log-log plot is very sensitive to the choice of this parameter.

A
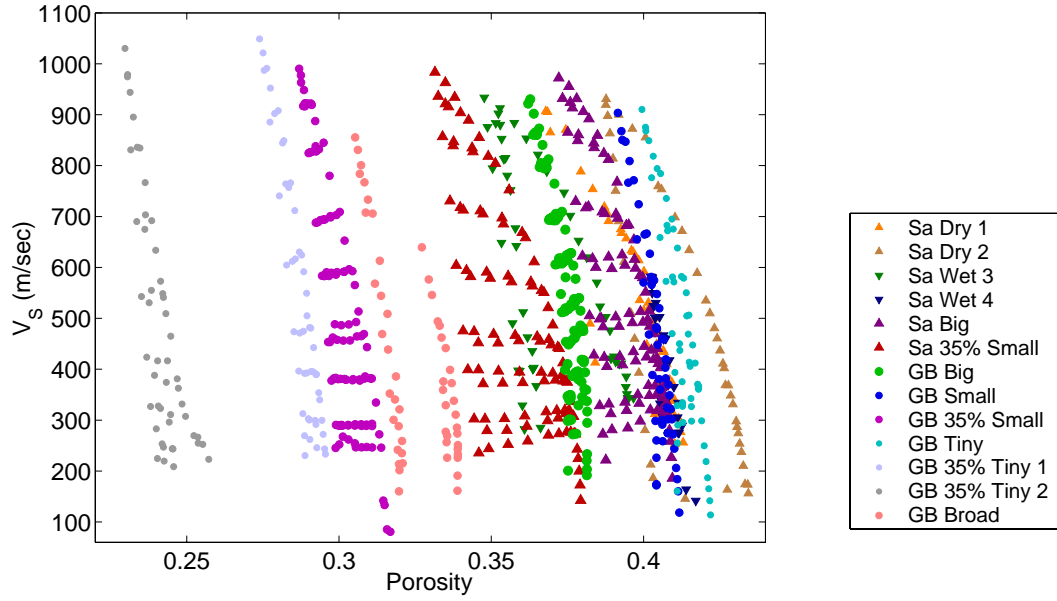
B
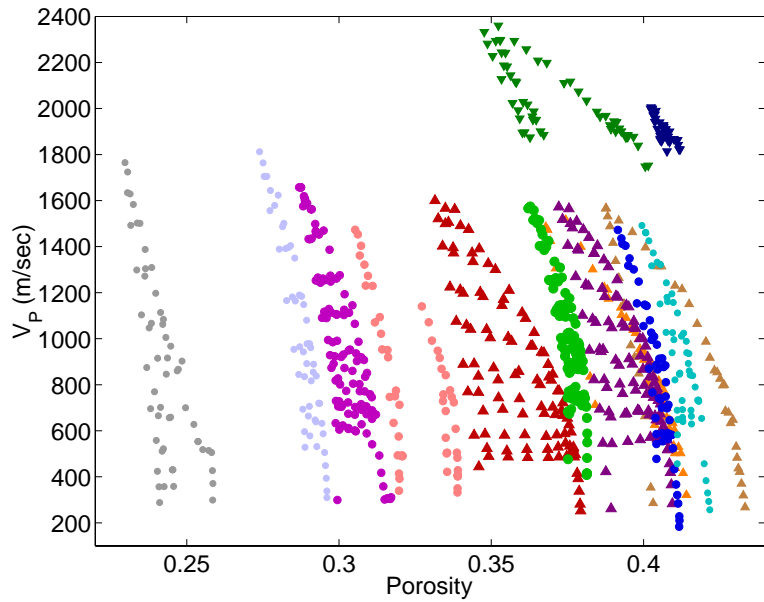
Figure 4.1: Measured velocity data plotted against the porosity, color-coded by sample: A) shear-wave velocities, and B) compressional-wave velocities.

A

B

C
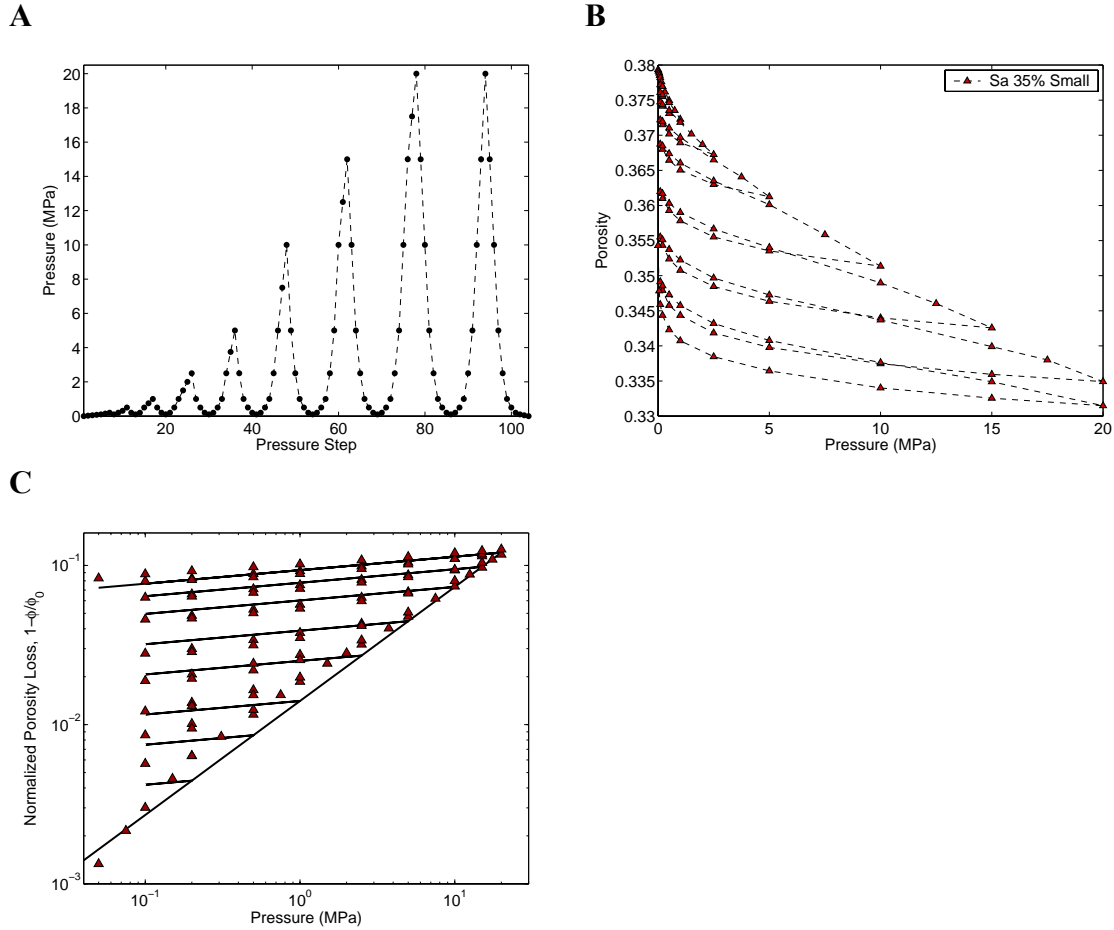
Figure 4.2: A) Pressure path and B) porosity data for each pressure step observed for a typical sand sample, Sa 35% Small. Part C) shows the empirical fit to the normalized porosity loss for the same sample.

Table 4.2: Normalized porosity loss fit parameters

	Sample:	Porosity		
		A (×10⁻³)	m	l
Dry:	S.Cruz 1	3.04	0.673	0.568
	S.Cruz 2	5.05	0.573	0.503
	Sa Big	2.02	0.704	0.583
	Sa 35% Small	2.71	0.716	0.631
	Average:	**3.20**	**0.666**	**0.571**
Glass Beads:	GB Big	1.85	0.614	0.337
	GB Small	4.35	0.453	0.256
	GB Tiny	4.83	0.451	0.294
	GB 35% Small	11.39	0.394	0.278
	GB 35% Tiny	5.23	0.505	0.259
	GB 35% Tiny 2	20.18	0.329	0.234
	GB Broad	2.60	0.700	0.591
	Average:	**7.20**	**0.492**	**0.321**
Water Sat.:	S.Cruz 3	7.53	0.528	0.465
	S.Cruz 4	11.47	0.358	0.267
	Average:	**9.50**	**0.443**	**0.366**

This section will discuss the influence of these two types of porosity variation - that due to variations in the sorting and that from compaction of the samples upon loading - on the velocities and on the pressure dependences of the velocities observed in the measurements. It will also discuss more generally the porosity trends observed in the acoustic and shear impedances, and in the V_P-V_S and Poisson's ratios, calculated from the observed velocities.

Effect of sorting on the velocities

Figure 4.1 illustrates that while the variations in the particle size distribution produce a broad range of porosities, each of the samples exhibits a similar velocity range over the full range of pressures. Figure 4.3 shows velocity data for all the dry samples, with each data point color-coded by the effective pressure at which the velocity measurement was made. This figure demonstrates that, for measurements made at a given pressure, there is only a very limited increase in the compressional-wave velocity and almost no discernable change in the shear-wave velocity with decreasing porosity. The two samples that were prepared by moist tamping, GB 35% Tiny 2 and GB Broad, do stand out from the other samples, in that the velocities measured at a given pressure are noticeably lower than the trends observed for the other samples.

The lines in Figure 4.3C and 4.3D, superimposed on the same data shown in 4.3A and 4.3B, represent the velocity-porosity trends for a given pressure predicted in three ways: the dashed lines are from the empirical porosity correction developed by Hardin and Blandford (1989), and the dotted lines and solid lines represent respectively the trends of the Hashin-Shtrikman lower bound and the Reuss bound, both of which are averages between the quartz moduli and the moduli of the highest porosity sample (Sa Dry 2) at a that pressure.

The Reuss average, the weighted harmonic average between the two end member moduli, simulates the weakest possible way to combine two distinct materials. Here the Reuss average is used to demonstrate the minimum possible effect on the velocities of mixing solid grain material, assumed to be pure quartz, and the granular framework of the highest porosity sample. This Reuss average was calculated as follows:

$$\frac{1}{M} = \frac{f_{df}}{M_{df}} + \frac{f_{Qtz}}{M_{Qtz}} \tag{4.5}$$

A
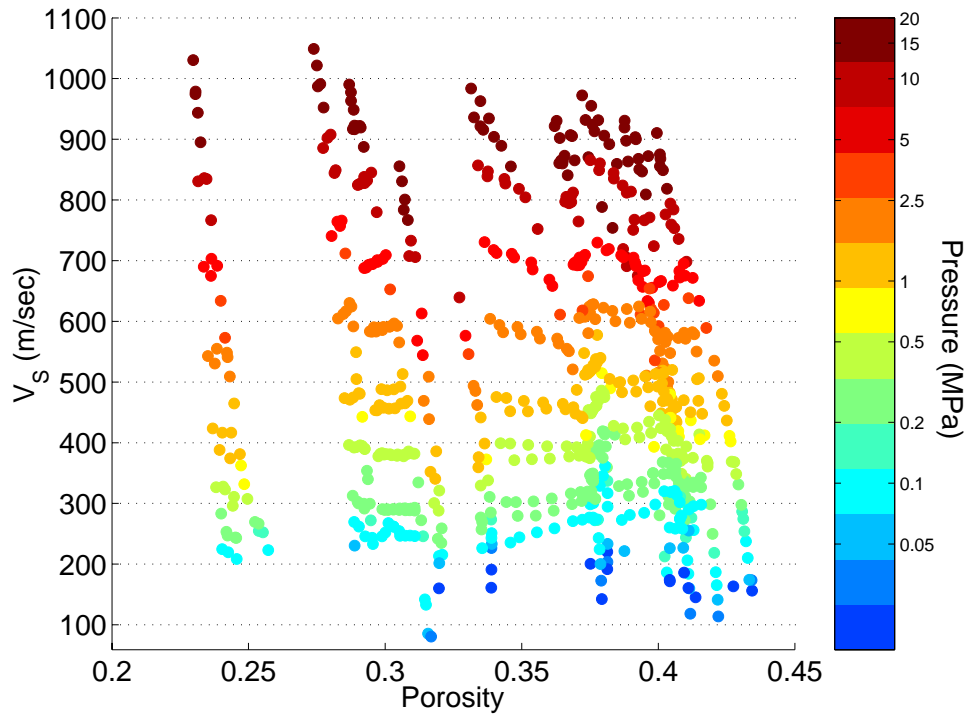
B
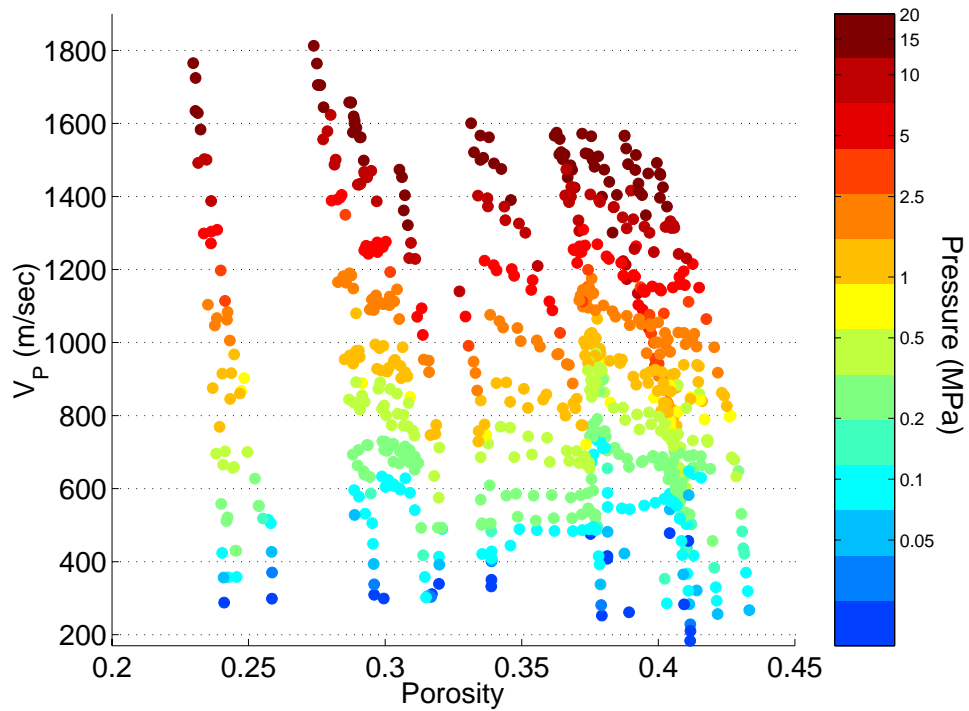
Figure 4.3: Measured velocity data plotted against the porosity, color-coded by pressure: A) shear-wave velocities, and B) compressional-wave velocities; C) and D) with Reuss average (solid), Hashin-Shtrikman lower average (dotted), and Hardin and Blandford (dashed) porosity trends.

C
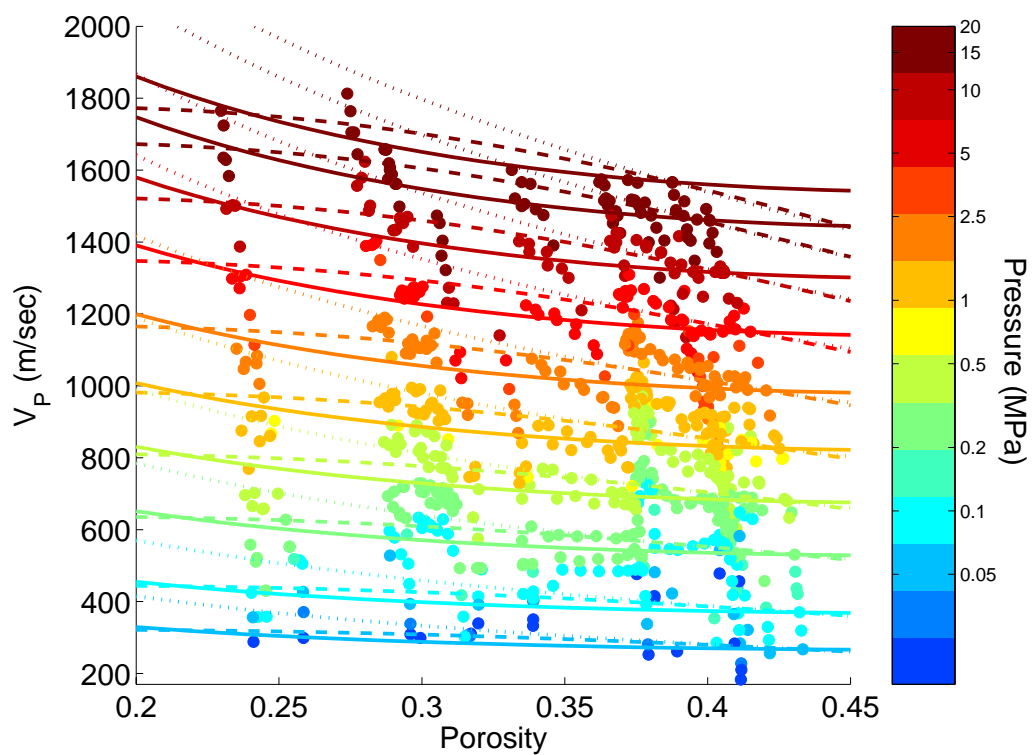
D
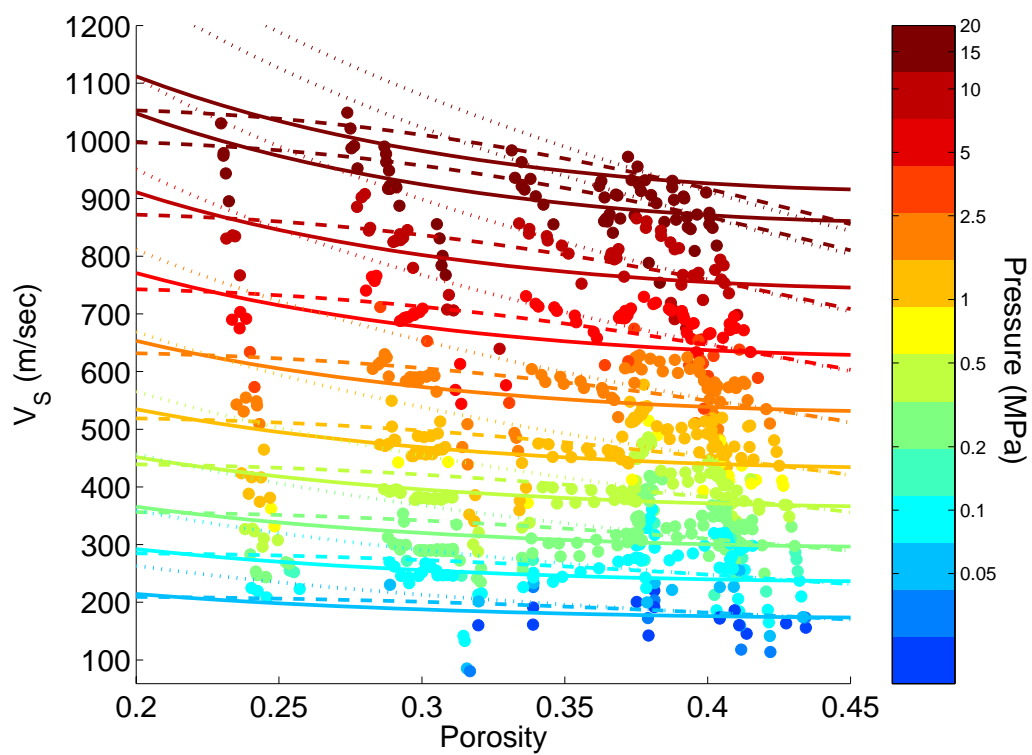
Figure 4.3: cont.

where M is the resulting average modulus, M_{df} is the modulus of the dry frame at the pressure of interest, and M_{Qtz} is the modulus of pure quartz. The fraction of dry frame, f_{df}, is simply given by $f_{df} = \phi/\phi_0$, where ϕ is the porosity, and ϕ_0 is the initial porosity at that pressure from sample Sa Dry 2. The fraction of pure quartz, f_{Qtz} is then just $1 - f_{df}$, or ($1 - \phi/\phi_0$). This average predicts a relatively flat velocity-porosity trend over porosities above 0.2. Below a porosity of 0.2 the Reuss average trend rises steeply to the velocities of the pure mineral at zero porosity.

The Hashin-Shtrikman lower bound (Hashin and Shtrikman, 1963) also represents what should be the lower limit of the mixture of the two substances, but with an idealized mixing geometry where the softer sand framework forms a shell around spheres of solid quartz. It was calculated from expression given by Mavko et al. (1998), with the fractions of the two components calculated as for the Reuss average above.

The Hardin and Blandford porosity trend was calculated by normalizing the empirically-derived void ratio function, $F(e)$ (in the denominator of equations 4.2 and 4.3), by the value of the function at the initial porosity, and then multiplying it by the high-porosity dry frame modulus for the pressure of interest as follows:

$$M = \frac{F(e_{df})}{F(e)} M_{df} = \frac{0.3 + 0.7e_{df}^2}{0.3 + 0.7e^2} M_{df} . \tag{4.6}$$

Again, M is the resulting porosity-corrected modulus, M_{df} is the modulus of the high-porosity dry frame, while e_{df} is the void ratio of the dry frame at the pressure of interest, taken from the data for sample Sa Dry 2 at that pressure, and e is the current void ratio.

Gassmann fluid substitution was performed to model the water-saturated velocities based on the velocity measurements from the dry samples. The resulting water-saturated compressional- and shear-wave velocities are plotted against pressure in Figure 4.4, with each data point color-coded by the porosity of the sample at the time of the velocity measurement. At any given pressure, the lower porosities can be seen to produce significantly higher compressional-wave velocities when fluid-substitution is performed. Figure 4.5A, showing the fluid-substituted compressional-wave velocities plotted against the porosity, demonstrates the magnitude of the porosity dependence in the water-saturated velocities. For the compressional-wave velocity, there is more than a 300 m/sec (~15%) difference between the low-porosity and high-porosity samples at a given

pressure. The shear-wave velocities, which require only a density substitution, show a much smaller porosity dependence at the higher pressures (130 m/sec, ~12%), with the low-porosity data again resulting in higher velocities. At lower pressures however, the porosity effect on the shear-wave velocities is insignificant relative to the scatter in the data, as shown by the flat trends for the lower pressures in Figure 4.3A. Figure 4.5B shows the same lines for the water-saturated compressional-wave velocities as in Figure 4.3 for the dry velocities, indicating the velocity-porosity trends predicted by Hardin and Blandford (1989), the Hashin-Shtrikman lower bound, and the Reuss lower bound.
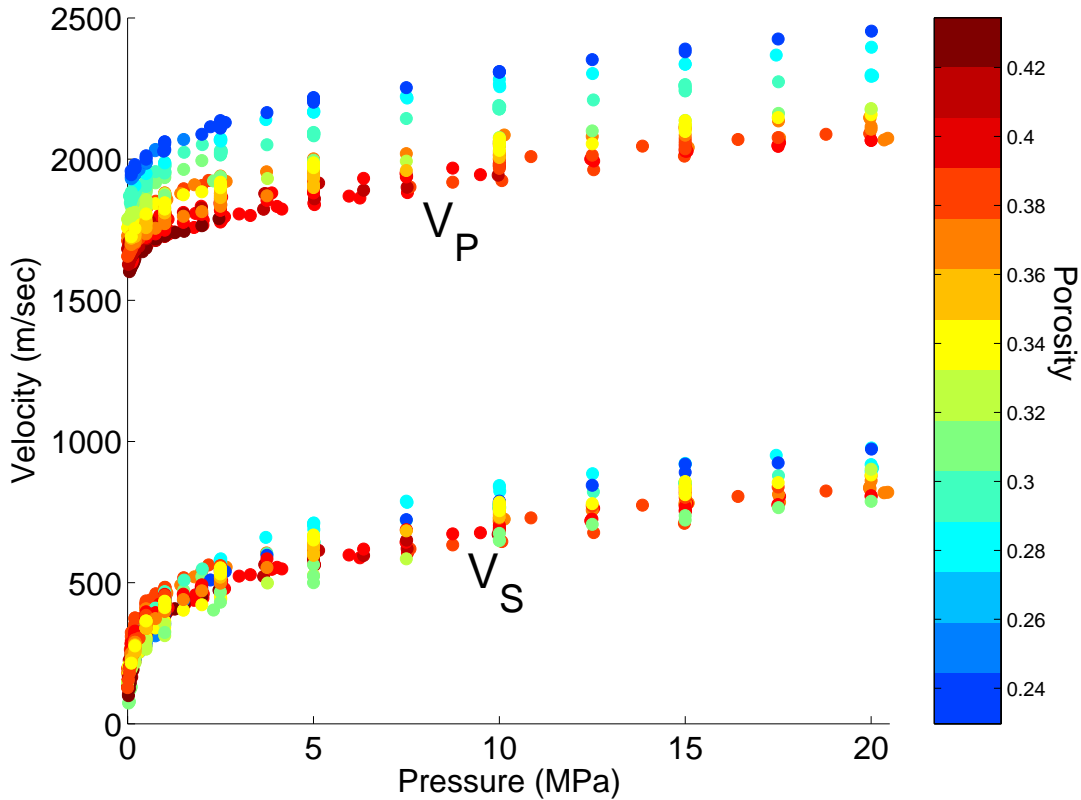
Figure 4.4: Gassmann fluid-substituted velocity data plotted against pressure, color-coded by porosity. The systematic porosity dependence of the compressional-wave velocities is easily visible.

A
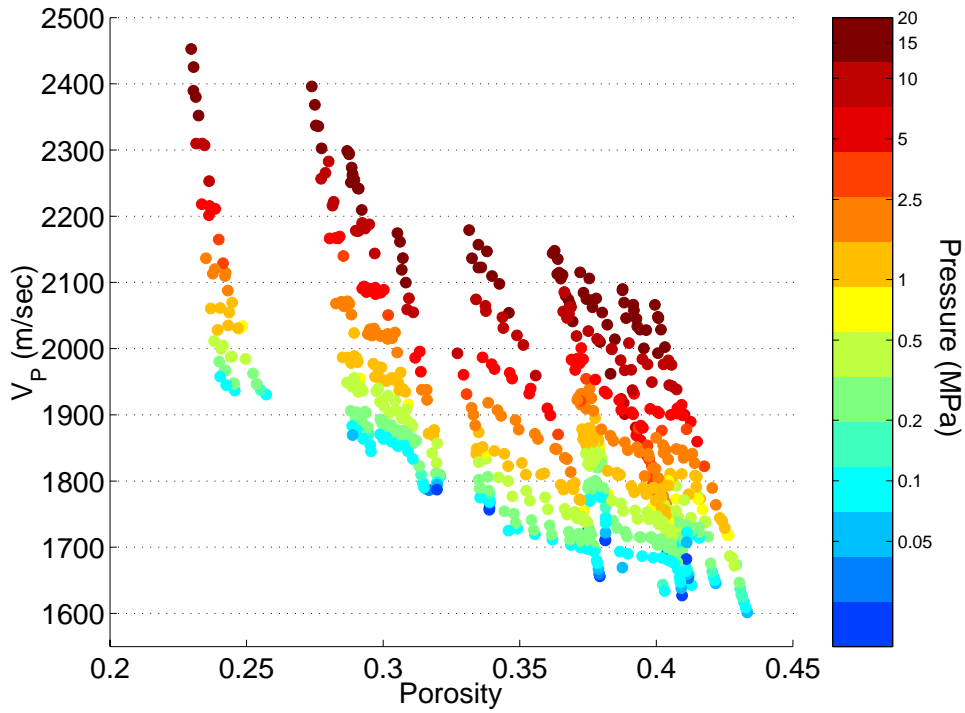
B
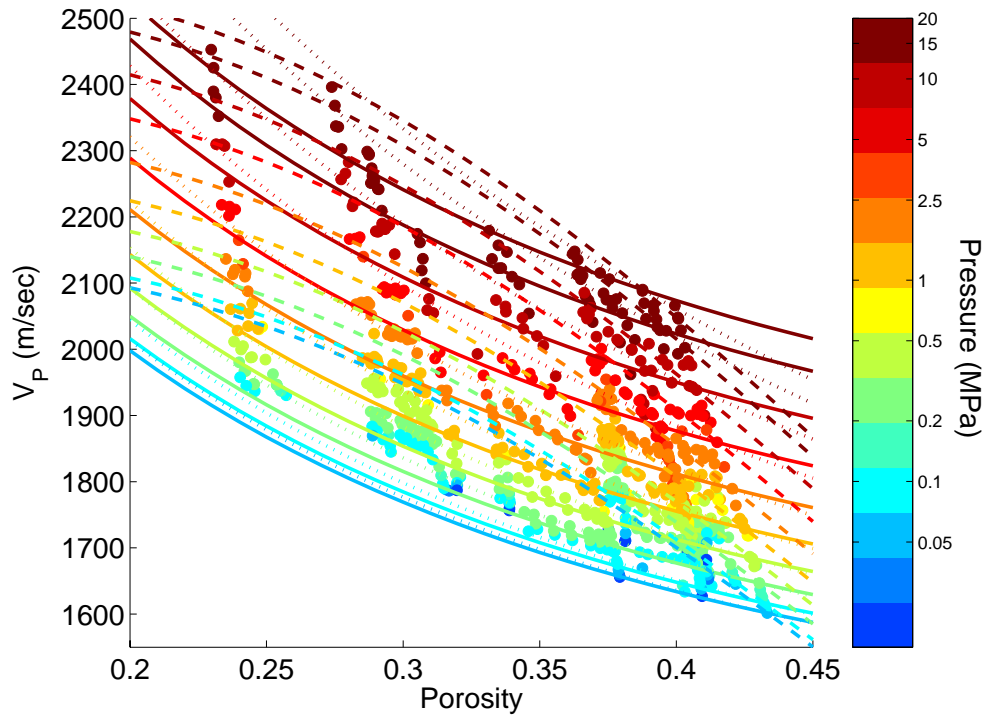
Figure 4.5: A) Gassmann fluid-substituted compressional-wave velocities plotted against the porosity and color-coded by pressure; B) with Reuss average (solid), Hashin-Shtrikman lower average (dotted), and Hardin and Blandford (dashed) porosity trends.

While there is a fair bit of scatter in the data, much of it because these data come from glass bead and sand data prepared in slightly different ways, all three trend lines approximately describe the velocity-porosity trend observed for the dry measurements. The Hashin-Shtrikman trend line does tend to over-predict the velocities at the lowest porosities, especially for the shear-wave velocities. For the water-saturated compressional-wave velocities, both the Reuss and Hashin-Shtrikman trends provide reasonable estimates of the velocity-porosity trend. On the contrary, the concave-downward trend of the Hardin and Blandford correction diverges significantly from the velocity measurements in the middle of the porosity range covered. It would also be expected to diverge from the velocity-porosity trend again at porosities below the range tested, where this empirical correction flattens, but where a continued increase in the velocities with decreased porosity would be predicted from Gassmann theory.

The Reuss and Hashin Shtrikman lower-bound averages are robust theoretical formulations that express the minimum moduli possible for mixtures of two homogenous materials. In this case, the averages are used to predict the moduli of a mixture of the high-porosity framework at a given pressure and of the pure mineral that makes up the grains. These averages represent the effect of replacing a fraction of the high-porosity framework with solid mineral. This is analogous to replacing the pore volume of that fraction of dry frame with pure mineral, assuming no change in the dry frame itself. For this dataset, the pore filling is done by the addition of smaller grains to the framework of a well sorted, high-porosity granular material. The ability of these lower bounds to describe these velocity-porosity trends implies that the addition of the smaller grains that reduce the porosity produces the minimum amount of stiffening theoretically possible. The smaller grains do not sit completely passively in the pore space, but do contribute only slightly to the stiffness of the grain framework. The scatter in the measurements, with some of the measurements lying below the Reuss bound, indicates that the samples do not truly represent a mixture of quartz and the framework that makes up the highest porosity sample, as expected given the textural variation between samples. These observations corroborate the observations by Dvorkin et Nur (1996) and Avseth et al. (2000), who found the lower Hashin-Shtrikman bound to describe the porosity-velocity trends of lab measurements on undisturbed sands and of log data from clean sand

intervals. The fact that my data generally lie slightly below the Hashin-Shtrikman lower bound could indicate that the preparation of the samples was not representative of the texture imparted by the depositional and diagenetic processes experienced by the sands of Dvorkin and Nur and Avseth et al.

Effect of compaction on the velocities

The velocity data from sample Sa 35% Small are plotted against pressure and porosity in Figure 4.6. When plotted against the pressure (Figure 4.6A,B), the velocities at a given pressure increase slightly after preconsolidated to a higher pressure. Figures 4.6C and 4.6D show the velocities plotted against porosity, demonstrating that the velocity-porosity trend steepens at higher pressures. Figures 4.6E and 4.6F also show the Reuss, Hashin-Shtrikman and Hardin-Blandford porosity trend lines superimposed, anchored at the velocity value on the initial loading path. These lines estimate the effect that the sorting-induced porosity variation has on the velocities. The preconsolidation effect for this sample is close to the sorting trends at the lower pressures, but is greater than the sorting trends at the higher pressures. This behavior is typical for the sand samples, while the glass bead samples tend to show the opposite effect (see Figures 4.1 and 4.3), with the velocity even decreasing with compaction at the higher pressures in some of the samples. Nevertheless, the total effect of the compaction of the velocities is still generally small, not exceeding a 10% change from the velocity measured on the initial loading path.

The effect of the compaction on the velocities can be captured empirically very effectively by either the relations from Robertson et al. (1995) or from Hardin and Blandford (1989), given in equations 4.1 through 4.3. The fits to the Robertson relation and a simplified form of the Hardin and Blandford equations (discussed below) are shown compared to the velocity data plotted against pressure and porosity in Figure 4.7. The implications of the velocity increases observed with compaction have been discussed for the dry velocities in Chapter 3, and will be discussed for the water-saturated case in Chapter 5. At present it is enough to say that the porosity-velocity trends from sorting and from compaction are similar, and that both are relatively small.
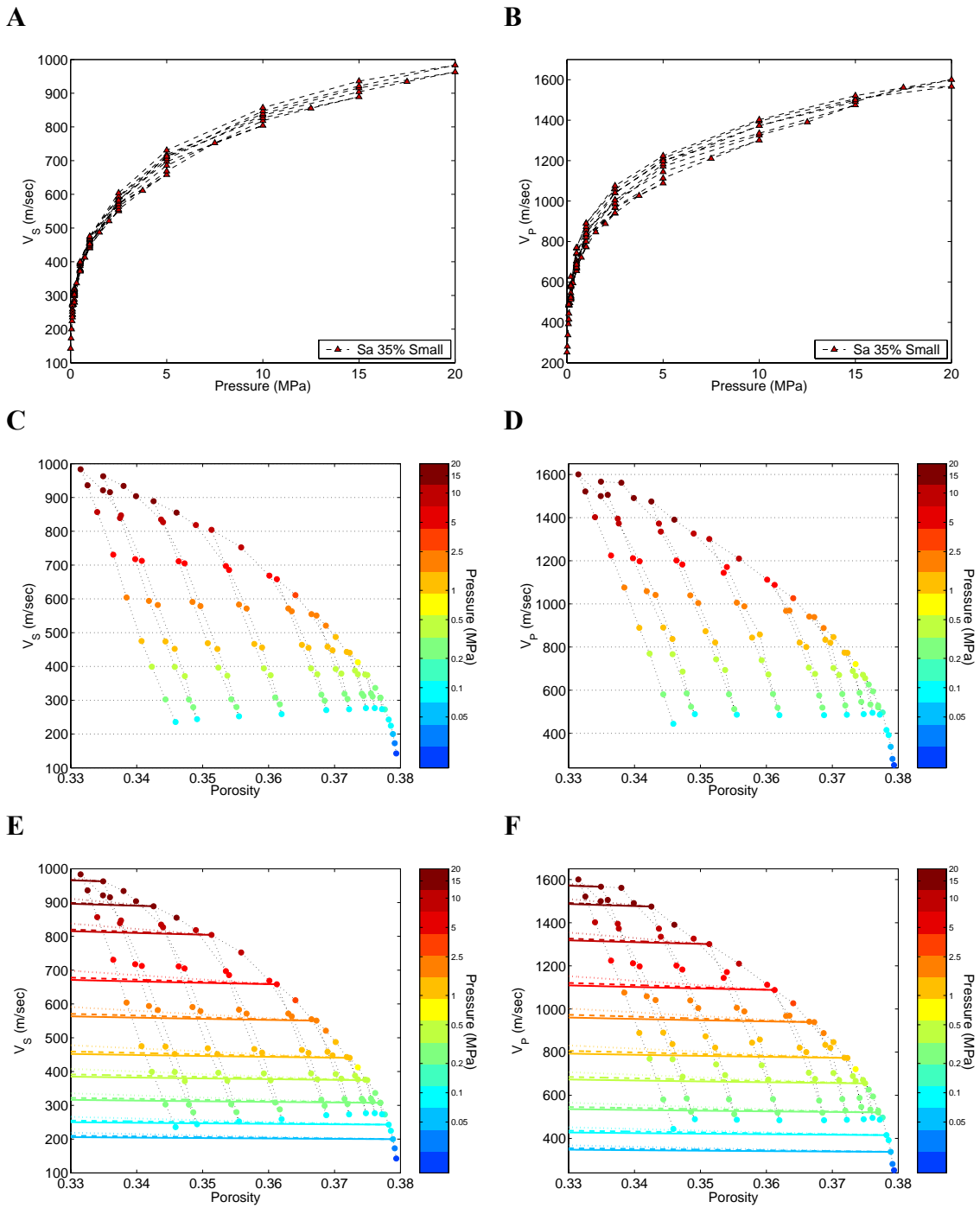
Figure 4.6: Velocity data from sample Sa 35% Small: A) shear-wave and B) compressional-wave velocity data vs. pressure, C) shear-wave and D) compressional-wave velocity plotted against porosity and color-coded for the pressure, and E) and F) the respective velocities with Reuss average (solid), Hashin-Shtrikman lower average (dotted), and Hardin and Blandford (dashed) porosity trends.

Effect of porosity on the pressure dependences of the velocities

To demonstrate the influence of the porosity on the pressure dependences of the velocities, a simplified form of Hardin and Blandford's (1989) equations (equations 4.2 and 4.3) was fit to the data from each sample. The relationships were simplified from those proposed by Hardin and Blandford so that they would apply to the hydrostatic stress state of our experiments, would be independent of the porosity, and could be applied to the water-saturated bulk and P-wave moduli:

$$M = M_0 + OCR^k\, S\ p_a^{1-n}\, p'^{\,n}\ .$$ (4.7)

Here M is the modulus being fit, OCR is the overconsolidation ratio, p' is the effective pressure, p_a is the atmospheric pressure, and S, n, k, and M_0 are free parameters. M_0 is assumed to be zero for the dry moduli and the water-saturated shear modulus. Figure 4.7 shows a comparison of the velocity data from sample Sa 35% Small to velocities calculated from the moduli fit with this relation using a non-linear least-squares method. The fit coefficients for each of the samples, along with their average values for each sample type are given in Table 4.2.

The fit coefficients are plotted against the initial porosity of the samples in Figure 4.8. As discussed in Chapter 3, the value of n is consistently smaller for the P-wave modulus than for the shear modulus, while n for the bulk modulus is consistently smaller still. Likewise, the value of k, which describes the reduction in the pressure dependence of preconsolidated samples, consistently shows the reverse, with the shear modulus demonstrating the smallest values, except for sample GB 35% Tiny 2. The generally small values of k indicate that compaction of the samples also has only a very small influence on the pressure dependence. For S, the value for the shear modulus is lower than that of the dry bulk modulus, with that for the dry P-wave modulus being the largest. For the water-saturated case, the relative values of n, k, and S for the fluid-substituted bulk and P-wave moduli for any given sample demonstrate the same patterns as in the dry case. The values of the initial bulk and P-wave moduli (M_0 or K_0) are generally similar for a given sample for both the fluid-substituted and water-saturated moduli. The values for the two water-saturated samples lie well off the trend of the fluid-substituted points as a result of frequency dispersion, since the measurements were made at high frequencies, producing higher moduli than predicted by the low-frequency Gassmann theory.
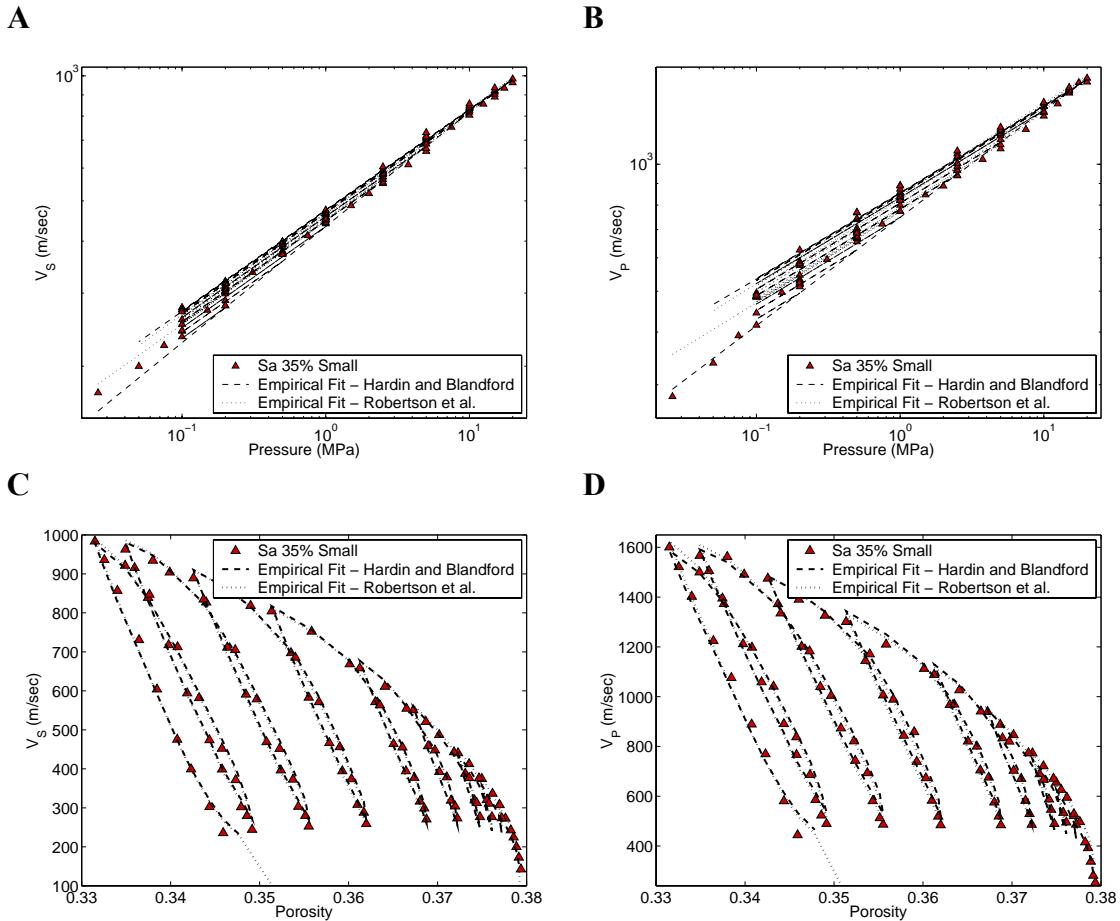
Figure 4.7: A) Shear- and B) compressional-wave velocity data from sample Sa 35% small plotted against pressure in a log-log scale, showing the fit of empirical forms from Hardin and Blandford (1989) and Robertson et al. (1995). Frames C) and D) show the same data plotted against porosity.

Figure 4.8 demonstrates that the trends of the *n* and *k* parameters for the shear modulus, and the dry bulk and P-wave moduli are relatively constant with initial porosity. A linear fit to the *n* parameters for the glass bead data are shown by the dotted lines in Figure 4.8A. If we just consider the parameters for the glass-bead samples, there might be a slight decrease in the value of *n* and a slight increase in the value of *k* with increasing porosity, especially for the bulk and P-wave moduli, but any change with porosity is very small relative to the scatter. Indeed, the trend lines for the glass beads do not fall within the error bars for most of the samples, indicating that the sample to sample variation is causing more of the variation in the fit parameter than is the sorting-induced porosity variation. For the water-saturated bulk and P-wave moduli (Figures 4.8C and D) there is a great deal of scatter in the values of *n* and *k*, though the values for the water-saturated

glass bead moduli are roughly the same as for the dry glass beads. On the contrary, the values of both *n* and *k* for the sands are significantly higher for the water-saturated case than for the dry case. This is because the porosity loss is larger for the sands, and in the water-saturated case the porosity change resulting from compaction produces a significant increase in the velocity upon Gassmann fluid substitution. This is therefore a fluid effect rather than a sediment frame effect.

There is a great deal of scatter and no noticeable trend in the value of *S* with porosity for either the dry or water-saturated moduli. This indicates that there is no causal relationship between *S* and the porosity, but that *S* is very sensitive to variations in the sample preparation that produce the scatter.

Table 4.2: Moduli fit coefficients – Hardin and Blandford (1989)

Sample:	G			M				K			
	$S (\times 10^3)$	n	k	$S (\times 10^3)$	n	k	M_0 (GPa)	$S (\times 10^3)$	n	k	K_0 (GPa)
S.Cruz 1	0.815	0.520	0.151	2.532	0.500	0.157	n/a	1.459	0.482	0.156	n/a
S.Cruz 2	0.744	0.552	0.037	2.979	0.488	0.083	n/a	1.995	0.446	0.108	n/a
Sa Big	1.117	0.495	0.049	3.683	0.449	0.091	n/a	2.193	0.412	0.123	n/a
Sa 35% Sm.	0.841	0.564	0.075	2.763	0.522	0.103	n/a	1.657	0.485	0.124	n/a
Average:	1.042	0.520	0.056	3.384	0.487	0.079	n/a	2.014	0.459	0.094	n/a
GB Big	1.834	0.373	-0.031	7.017	0.323	0.005	n/a	4.598	0.290	0.028	n/a
GB Small	1.019	0.470	0.008	4.020	0.398	0.047	n/a	2.729	0.344	0.068	n/a
GB Tiny	1.013	0.473	0.024	4.045	0.399	0.058	n/a	2.752	0.346	0.078	n/a
GB 35% Sm.	1.135	0.512	-0.005	5.222	0.421	0.041	n/a	3.808	0.363	0.066	n/a
GB 35% Ty.	1.300	0.520	-0.026	6.145	0.430	-0.002	n/a	4.621	0.370	0.007	n/a
GB 35% Ty. 2	0.741	0.626	-0.013	4.665	0.481	-0.026	n/a	3.962	0.400	-0.047	n/a
GB Broad	0.738	0.534	-0.041	3.279	0.456	0.001	n/a	2.319	0.410	0.022	n/a
Average:	1.111	0.501	-0.012	4.913	0.415	0.018	n/a	3.541	0.360	0.032	n/a
S.Cruz 3	1.266	0.498	0.028	4.748	0.444	0.150	5.988	0.813	0.626	0.355	6.466
S.Cruz 4	1.508	0.476	0.032	3.888	0.480	0.147	6.129	1.091	0.621	0.326	6.234
Average:	0.979	0.558	0.077	2.175	0.593	0.241	6.319	0.608	0.725	0.482	6.386
S.Cruz 1				1.363	0.609	0.254	5.203	0.600	0.639	0.332	5.135
S.Cruz 2		as		2.943	0.487	0.147	4.755	2.537	0.403	0.177	4.667
Sa Big		above		2.945	0.484	0.140	5.078	1.828	0.436	0.194	5.014
Sa 35% Sm.				1.901	0.588	0.209	5.480	0.938	0.587	0.309	5.443
Average:				2.288	0.542	0.188	5.129	1.476	0.516	0.253	5.065
GB Big				5.889	0.338	0.015	5.381	3.376	0.313	0.051	5.361
GB Small				5.408	0.340	0.052	4.768	4.974	0.237	0.061	4.690
GB Tiny				5.131	0.352	0.067	4.692	4.935	0.243	0.073	4.583
GB 35% Sm.		as		5.141	0.412	0.073	6.186	4.697	0.310	0.099	6.065
GB 35% Ty.		above		6.301	0.407	0.018	6.428	5.558	0.308	0.038	6.332
GB 35% Ty. 2				4.988	0.452	0.047	7.305	7.478	0.272	0.045	6.910
GB Broad				2.004	0.543	0.129	6.018	1.615	0.473	0.195	5.904
Average:				4.980	0.406	0.057	5.825	4.662	0.308	0.080	5.692

n/a – not applicable (assume to be zero).
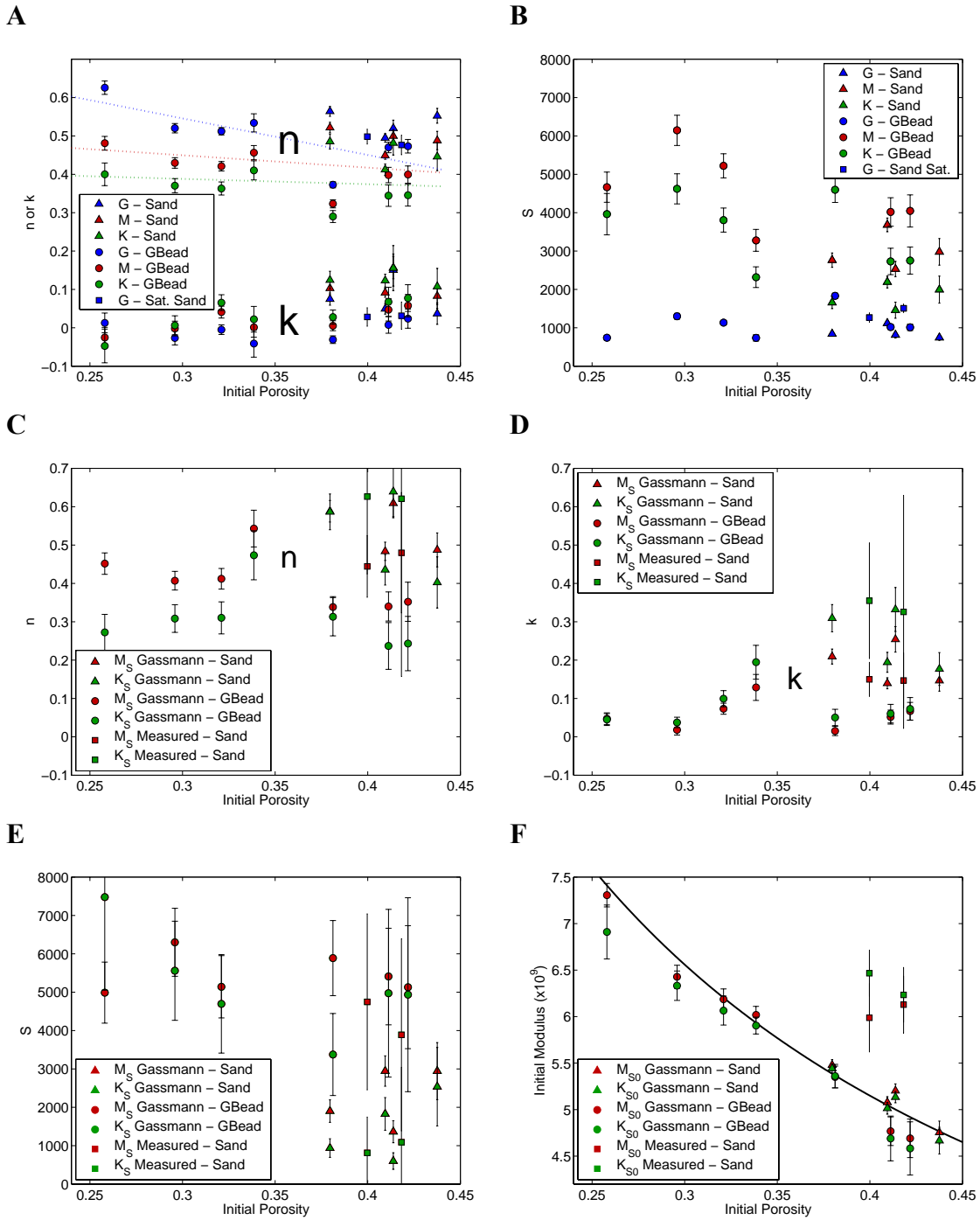
Figure 4.8: Fit parameters for each of the samples plotted against the initial porosity of the sample: A) n and k, and B) S, for the dry samples; C) n, D) k, E) S, and F) K_0 and M_0 for the water-saturated samples.

The values of the initial moduli (M_0 and K_0) do show a strong, systematic relationship to the porosity. This trend can be described by the Reuss average between water and quartz, shown in the black line in Figure 4.8E. This Reuss average is identical to the Gassmann prediction when the dry bulk modulus is zero. Since the initial modulus represents the modulus expected at zero pressure, when the dry bulk modulus is expected to be close to zero, the good fit between the Reuss average and the fit parameters implies that the fitting is fairly robust. While the pressure dependences, as represented by *n* and *k*, are mostly independent of the sorting-induced porosity variation, in the water-saturated case the porosity dependence is largely contained in the initial modulus. This result implies that a porosity correction could be applied to the moduli based on this simple Reuss average trend.

The Acoustic and Shear Impedances

The acoustic and shear impedances, values which are more easily garnered from reflection seismic data through impedance inversion than the velocities themselves, are the product of the density, ρ, and, respectively, of the compressional- and shear-wave velocities:

$$I_P = \rho \cdot V_P, \text{ and } I_S = \rho \cdot V_S, \tag{4.8}$$

where I_P is the acoustic or compressional impedance and I_S is the shear impedance. The general behavior of the impedances with the pressure and porosity is identical to that of the velocities (see Figure 4.9). However, because the density is sensitive to both the sorting and the pressure with compaction, the impedances do demonstrate a slightly larger relative sensitivity to the sorting and to the pressure. There is approximately a 25% difference in the compressional-impedances of the lowest and highest porosity samples at 1 MPa, whereas the difference in the velocities between these two samples is around 15%.

The V_P-V_S Ratio and Poisson's Ratio

Plots of the V_P-V_S ratio and Poisson's ratio of the dry samples against porosity (Figure 4.10A) illustrate a slight porosity dependence in both, with the lower porosities demonstrating slightly higher V_P-V_S ratios and Poisson's ratios. A similar slight porosity trend is observed in the water-saturated V_P-V_S ratio and Poisson's ratio shown plotted against the porosity in Figure 4.10B.
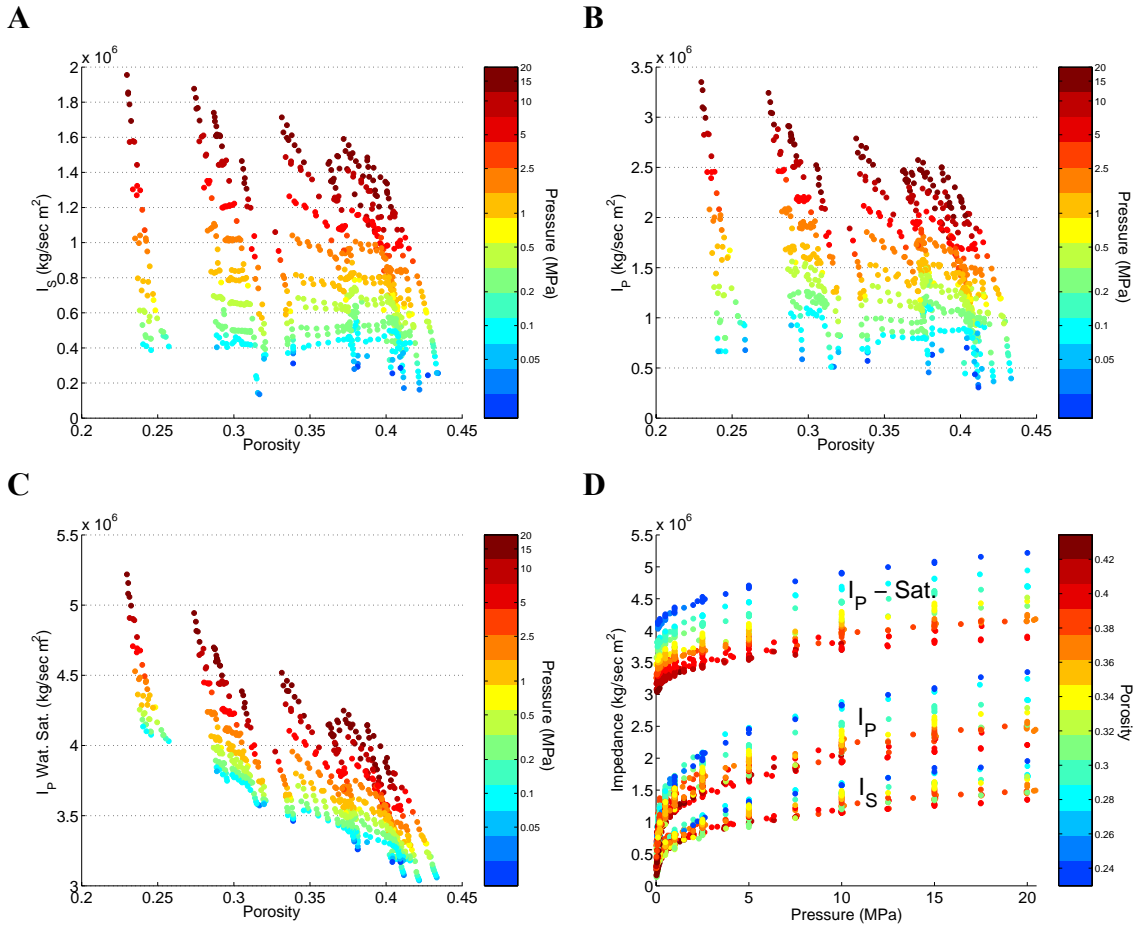
Figure 4.9: A) Shear impedance and B) compressional impedance values calculated from the dry velocity measurements, plotted against porosity and color-coded by the pressure; C) Gassmann fluid-substituted compressional impedance plotted against porosity; and D) all the impedances plotted against the pressure and color-coded by the porosity.

Plotting the V_P-V_S ratio and Poisson's ratio against the pressure, and color coding the data with the porosity (Figure 4.10C,D), demonstrates that there is a pressure dependence to both the dry and water-saturated ratios. For the dry cases, the pressure dependence is relatively small, but there is a slight decrease in the V_P-V_S ratio and Poisson's ratio as the pressure increases. Nevertheless, at pressures above about 3 MPa any variation with pressure for the dry samples is smaller than the scatter, which implies that the V_P-V_S ratio and Poisson's ratio would not serve as efficacious pressure indicators in dry sands.

This pressure dependence is much more significant in the case of the water-saturated V_P-V_S ratio and Poisson's ratio, as discussed by Huffman and Castagna (2001) and Prasad (2002). This is because the shear-wave velocity approaches zero at low pressures, while the compressional-wave velocity will not fall below the velocity of a suspension of

the sand in water of at least 1600 m/sec. The water-saturated V_P-V_S ratio increases from below 3 at 10 MPa to a mean value of about 7 at 0.5 MPa (Figure 4.10D). Similarly, the Poisson's ratio rises from 0.43 to 0.49 over this pressure range.

G

H

I
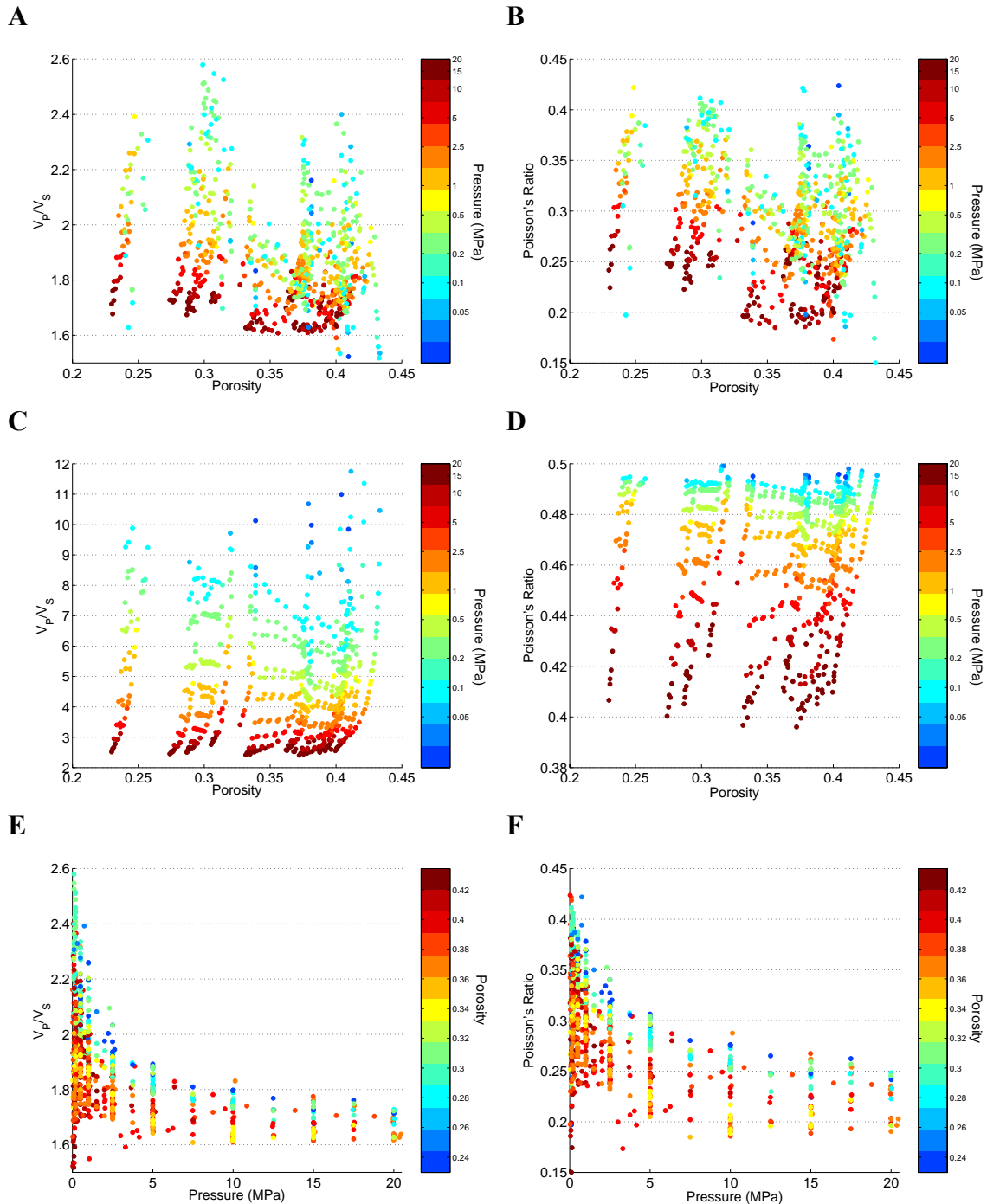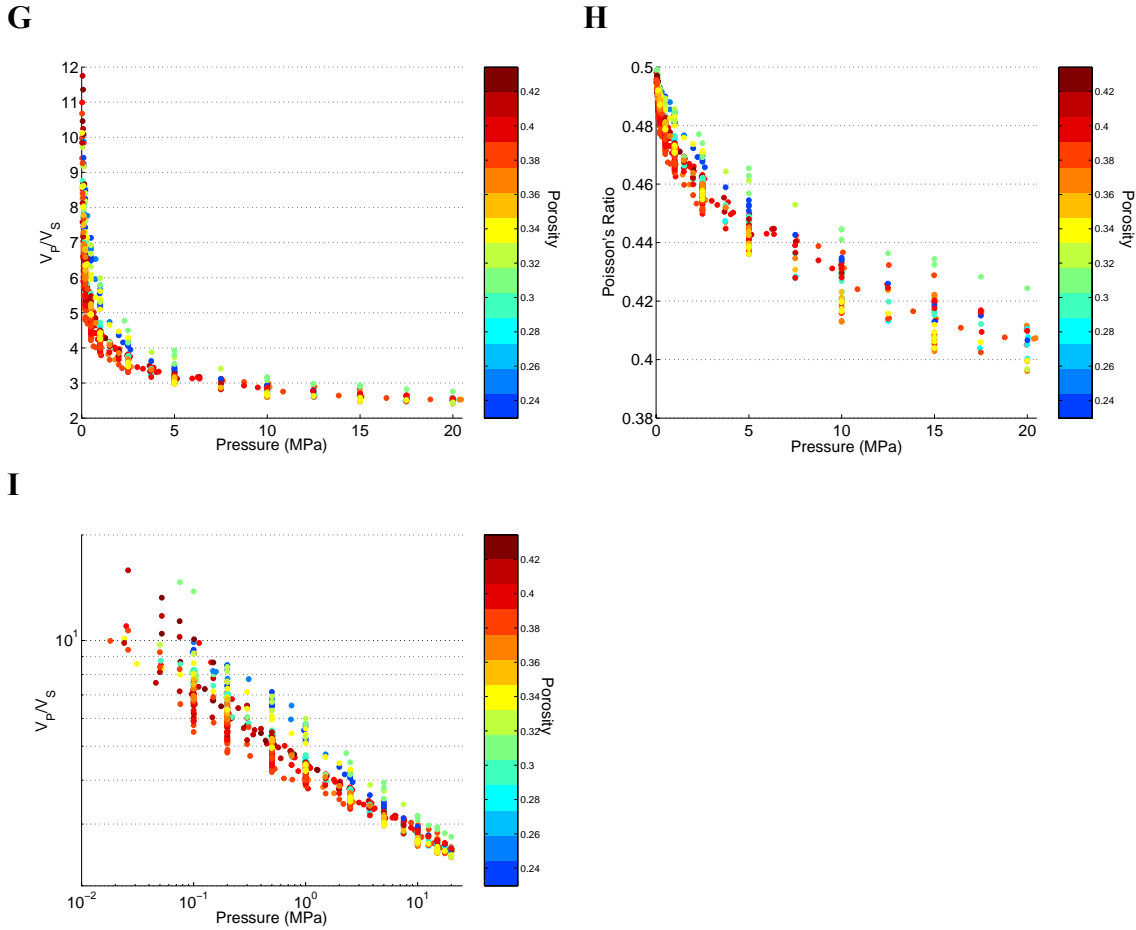
Figure 4.10: The V_P-V_S ratio and Poisson's ratio: A) and B) dry vs. porosity; C) and D) water-saturated vs. porosity; E) and F) dry vs. pressure; G) and H) water-saturated vs. pressure; and I) water-saturated V_P-V_S ratio vs. pressure in log-log scale.

Unfortunately, at the lower pressures there is a considerable amount of scatter, more easily visible in the V_P-V_S ratio, which would generate significant uncertainty in the effective pressure determined from *in situ* V_P-V_S ratio measurements. For example, if the measured V_P-V_S ratio is 5, the pressure (based on our fluid-substituted data) could vary over an order of magnitude. A fraction of this scatter correlates to the porosity with low porosities corresponding to higher V_P-V_S ratios (see Figure 4.10E). However, some of the scatter in the V_P-V_S ratio is not correlated to the porosity, but is a result of sample-to-sample variation in the shear-wave velocities, and to a lesser degree in the compressional-wave velocities. As the relative porosity effects at high pressures are more similar for the compressional- and shear-wave velocities, and because the larger shear-wave velocities do not produce as much scatter in the ratio for the same velocity scatter as at low velocities, there is less scatter in the V_P-V_S ratio above about 10 MPa. The lack of a

consistent porosity-dependence of the shear-wave velocities at lower pressures allows the porosity dependence of the P-wave velocity to show through in the V_P-V_S ratio. As the Poisson's ratio effectively compresses the low pressure values, these effects are not as visible in plots of the Poisson's ratio versus pressure (Figure 4.10F). Nevertheless, the V_P-V_S ratio and Poisson's ratio are deterministically related, so the potential inaccuracy in predicting the pressure from either parameter is the same.

POROSITY CORRECTION FOR WATER-SATURATED V_P

Since the magnitude of the porosity effect on the water-saturated compressional-wave velocities is about 50% of that of the magnitude of the pressure effect at 20 MPa, to permit accurate estimates of the pressure from the water-saturated compressional-wave velocities, or from the corresponding impedances and V_P-V_S ratio, it would be necessary to correct out the large porosity effect on these parameters. Here I will present a correction, valid for unconsolidated sands, that I developed based on the Gassmann equations and the observations of the porosity effects on the pressure dependences and initial moduli of the dry and water-saturated samples discussed above.

By assuming that the dry bulk modulus, K_{dry}, is much smaller than the bulk modulus of the pure mineral (here assumed to be quartz), $K_{dry} << K_{Qtz}$, that K_{dry} is similar from sample to sample, and that any porosity-dependent variation in K_{dry} and in the water-saturated bulk modulus at zero pressure, $K_{P=0}$, act to cancel each other out, a Gassmann-based correction for the porosity effects on the water-saturated bulk moduli can expressed as follows:

$$K_{sat, \phi=0.4} \approx \left(K_{P=0, \phi=0.4} - K_{P=0} \right) + K_{sat}. \tag{4.9}$$

This expression corrects the data to an arbitrary porosity, here chosen to be 0.4, by adding the measured water-saturated bulk modulus, K_{sat}, to the difference between the zero-pressure bulk moduli at the target porosity, $K_{P=0, \phi=0.4}$, and at the actual porosity, $K_{P=0}$. The bulk modulus at zero pressure is assumed to be the Reuss average between the bulk modulus of water and that of the average mineral components, so these moduli and the porosity are the only inputs to the correction. The derivation of this expression and a discussion of the validity of the assumptions are given in Appendix A.

A comparison of the original and porosity-corrected data for the compressional-wave velocities and the V_P-V_S ratio are given in Figure 4.11. The velocity calculation also requires that the density be corrected to the target porosity according to the following:

$$\rho_{sat,\phi=0.4} = 0.6\rho_{min} + 0.4\rho_{fl}. \tag{4.10}$$

where $\rho_{sat,\phi=0.4}$ is the corrected density, ρ_{min} is the pure-mineral density, assumed to be that of quartz (2650 kg/m^3), and ρ_{fl} is the density of the saturating fluid. This correction effectively collapses much of the compressional-wave velocity variation at a given pressure, though it is more effective at reducing the scatter at the lower pressures, while more variation in the velocities persists at the higher pressures. The remaining variation is mostly from non-systematic variation between the samples, though some might result from systematic, porosity-related variation escaping the correction when not all the porosity variation is contained in the zero-pressure bulk modulus.

A

B
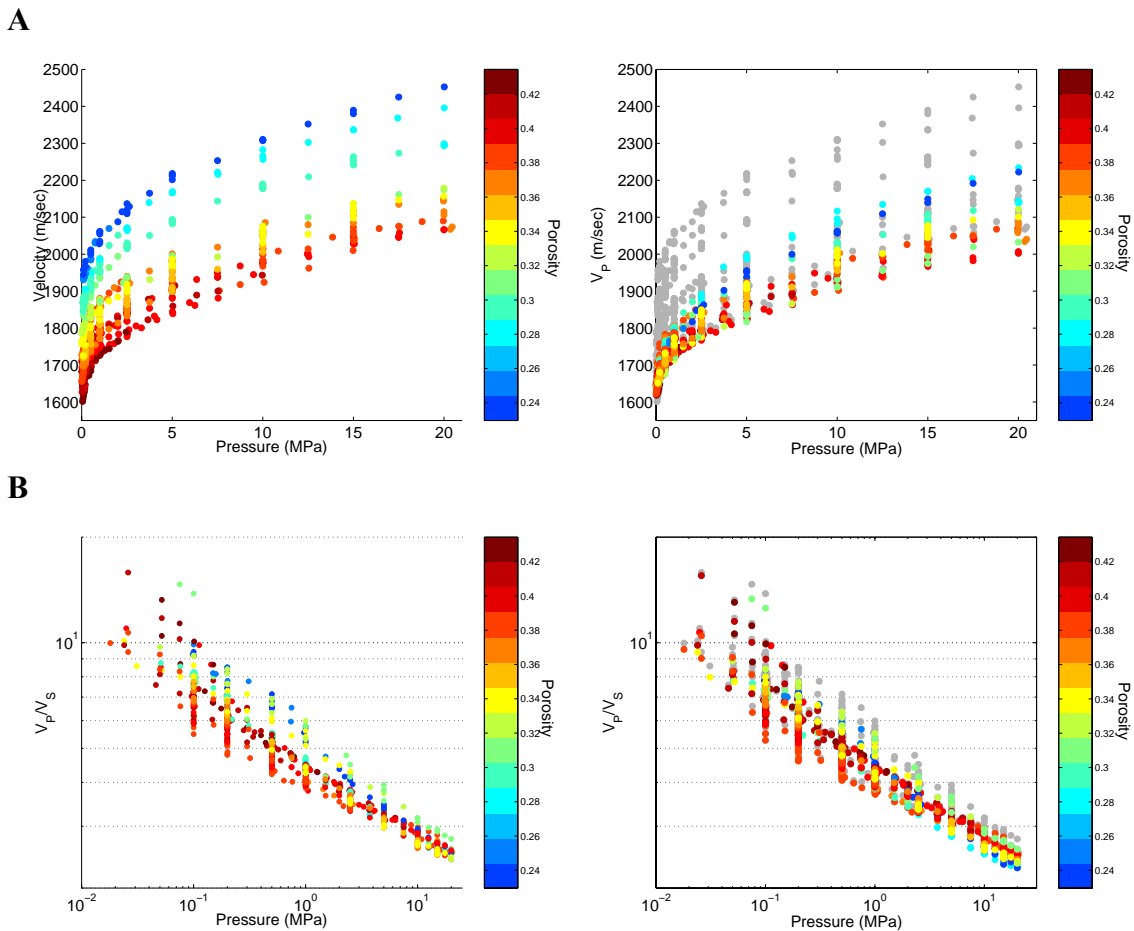
Figure 4.11: Comparison of uncorrected (left) and corrected (right) water-saturated A) compressional-wave velocity and B) V_P-V_S ratio. The gray dots in the right-hand frames are the locations of the actual data values to allow for an easier comparison.

While the correction to the compressional-wave velocities reduces the scatter by at least 50%, the corrected V_P-V_S ratio data (Figure 4.11B) demonstrate only a slight reduction in the scatter. This implies that most of the scatter in the V_P-V_S ratio does not come from the compressional-wave velocities, as discussed in the previous section, but comes from the scatter in the shear-wave velocities. As most of the scatter in the shear-wave velocities is not easily correlated to the porosity, it is unlikely that such a simple correction could be developed to reduce the uncertainty in pressure prediction from the V_P-V_S ratio.

Nevertheless, the fact that the V_P-V_S ratio is primarily sensitive to the shear-wave velocity suggests that there might exist a robust transform between the shear modulus and the V_P-V_S ratio. Such a transform could be used to approximately invert the V_P-V_S ratio, which can be derived from reflection seismic data, for the shear modulus, a primary indicator of mechanical stability, when the density of the *in situ* sediments is not known. By assuming that the ratio of the dry bulk and shear moduli is constant at about 2, approximating $K_{P=0}$ as 6×10^9 Pa, the value at about the center of the porosity range of my samples, and using the Gassmann approximation used to derive Equation 4.9, this transform can be expressed as follows:

$$\mu \approx \frac{K_{P=0}}{\left(\frac{V_P}{V_S}\right)^2 - \left(\left(1 - 2\frac{K_{P=0}}{K_{Qtz}}\right)\frac{K_{dry}}{\mu} + \frac{4}{3}\right)} \approx \frac{6\times10^9\,Pa}{\left(\frac{V_P}{V_S}\right)^2 - \frac{8}{3}}, \tag{4.10}$$

as detailed in Appendix B. A comparison of the shear modulus calculated from the shear velocity and density measurements to that calculated from Equation 4.10 is shown in Figure 4.12. While this transform produces errors of up to 20% in the shear modulus estimated from the V_P-V_S ratio, it might still serve as a first order estimate of the shear modulus in sands when the density or compressional-wave velocity data are not felt to be reliable. This transform could be improved if the porosity of the sediment were known, allowing the value of $K_{P=0}$ to be calculated more accurately.

DISCUSSION

It is important to note that to isolate the impact of sorting-related porosity variations on the velocities and their pressure dependences, these experiments used idealized, synthetic sand and glass bead samples, with mostly bimodal grain size distributions, and

with similar preparation processes (all reconstituted). Since there are many other factors that can influence the velocities in natural sediments, including textural variations or variations in the fluid content or diagenetic history, the relationships between the porosity, pressure, and velocity in natural sediments could vary quantitatively from the measurements presented here. Nevertheless, I would expect the qualitative patterns observed here to be valid for measurements made *in situ* or for lab measurements on undisturbed, natural sands. Specifically, the limited effect of the porosity variations due to sorting on the dry velocities and on the pressure dependences of the velocities and the large porosity effect in the compressional-wave velocities that were observed here should hold in natural sands.

A

B
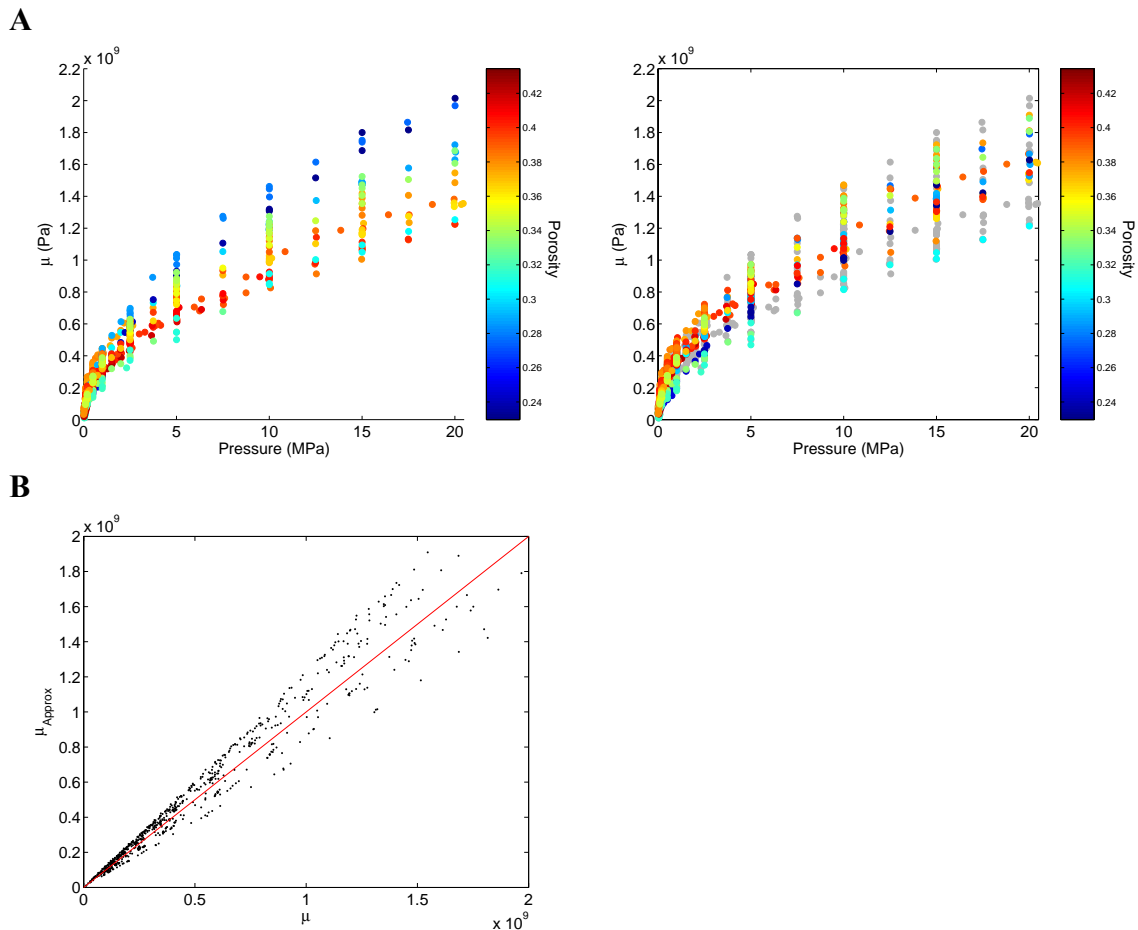
Figure 4.12: Comparison of the actual shear modulus and the shear modulus predicted from the V_P-V_S ratio transform: A) plots of the actual (left) and transform-derived (right) moduli, and B) a plot of the transform-derived modulus versus the actual shear modulus data.

CONCLUSIONS

Velocity and porosity measurements on this set of reconstituted sand and glass-bead samples with controlled grain-size distributions over pressure cycles from 100 kPa up to 20 MPa demonstrate that the sorting has a very limited effect on either the dry shear-wave or compressional-wave velocities at a given pressure in these unconsolidated sands. This limited change in the velocities with the porosity is similar to the porosity-velocity trend produced by the Reuss average between the moduli of the highest porosity sample and the moduli of quartz.

For the water-saturated velocities modeled with Gassmann fluid substitution, there is a significant increase in the compressional-wave velocity with decreasing porosity. The substitution of water for air in the pores effectively stiffens the bulk compressibility of the lower-porosity sediments more, producing higher velocities at lower porosities. As the pore fluid does not affect the shear modulus in Gassmann theory, the water-saturated shear-wave velocities show a pattern similar to the dry velocities. The porosity-velocity trend is again described by the Reuss average between the moduli of the highest porosity sample and of quartz.

Compaction of the samples results in slightly higher velocities at a given pressure for a sample that has experienced higher preconsolidation pressures. For the sand samples, this effect is slightly larger at high pressures than the sorting induced porosity effect, but is very similar at the lower pressures. The change in the pressure trend of preconsolidated samples is also relatively small, and is described effectively by the k parameter in the Hardin-Blandford empirical relations.

The sorting has no significant, systematic effect on the pressure dependences of the shear, bulk or P-wave moduli. The non-systematic scatter of these pressure dependences with the initial porosity of the samples, as measured by the exponent to the effective pressure (n) that was used as a fit parameter, is larger than any effect that might be due to the sorting. Likewise, the pressure dependence of the unloading and reloading paths (n-k) is at most only slightly dependent on the porosity. The multiplier (S) in the empirical fit between the moduli and pressure does show a significant amount of scatter, but also shows no systematic relationship with the porosity.

A significant porosity dependence is evident in the initial modulus of the bulk and P-wave moduli (M_0 and K_0) for the Gassmann fluid substituted data. An effective porosity correction for the water-saturated moduli consists of adding a porosity-dependent constant to the water-saturated modulus.

There is a slight porosity dependence in the water-saturated V_P-V_S ratio, but much more of the scatter in the V_P-V_S ratio with respect to pressure comes from non-systematic scatter in the shear-wave velocities. The primary sensitivity of the V_P-V_S ratio to the shear-wave velocity indicated by this behavior led to the development of an approximate transform between the V_P-V_S ratio and the shear modulus.

APPENDIX A: POROSITY CORRECTION

This appendix presents the derivation of a simple, approximate, porosity correction to the water-saturated bulk modulus. This correction is based on a simplification of Gassmann's fluid substitution equation applicable to unconsolidated sands at low pressures.

Gassmann's equation for the water-saturated bulk modulus, K_{sat}, is as follows:

$$K_{sat} = K_{dry} + \frac{\left(1 - \frac{K_{dry}}{K_{Qtz}}\right)^2}{\frac{\phi}{K_{fl}} + \frac{1-\phi}{K_{Qtz}} - \frac{K_{dry}}{K_{Qtz}^2}} , \qquad (A.1)$$

where K_{sat} is the bulk modulus of the dry sand, K_{Qtz} is the bulk modulus of the pure mineral (assumed to be quartz) that makes up the grains, K_{fl} is the bulk modulus of the saturating fluid, and ϕ is the porosity. For unconsolidated sediments at zero pressure, K_{dry} can be assumed to be zero, in which case Gassmann's equation reduces to the Reuss average:

$$\frac{1}{K_{sat}} = \frac{\phi}{K_{fl}} + \frac{1-\phi}{K_{Qtz}} = \frac{1}{K_{P=0}} , \qquad (A.2)$$

where $K_{P=0}$ represents the water-saturated bulk modulus for a given sample at zero pressure. This value is analogous to the initial modulus fit parameter, K_0, in the simplified Hardin-Blandford empirical form, except that it will change as the porosity of the sample decreases on compaction. By expanding the numerator in Equation A.1, we can also write Gassmann's equation as follows:

$$K_{sat} = K_{dry} + \frac{1 - 2\frac{K_{dry}}{K_{Qtz}} + \left(\frac{K_{dry}}{K_{Qtz}}\right)^2}{\frac{\phi}{K_{fl}} + \frac{1-\phi}{K_{Qtz}} - \frac{K_{dry}}{K_{Qtz}^2}} . \quad (A.3)$$

Since the maximum value of K_{dry} for our unconsolidated sand samples is more than an order of magnitude smaller than that of quartz, the primary mineral component in most sands, we can assume that $K_{dry} << K_{Qtz}$, and can discard the terms with a K_{Qtz}^2 in the denominator:

$$K_{sat} \approx K_{dry} + \frac{1 - 2\frac{K_{dry}}{K_{Qtz}}}{\frac{\phi}{K_{fl}} + \frac{1-\phi}{K_{Qtz}}} = K_{dry} + \frac{1 - 2\frac{K_{dry}}{K_{Qtz}}}{\frac{1}{K_{P=0}}} = K_{P=0} + \left(1 - 2\frac{K_{P=0}}{K_{Qtz}}\right)K_{dry} . \quad (A.4)$$

This gives us an approximate form of Gassmann, with $K_{P=0}$ equal to the Reuss average, as in A.2. Figure 4.13 compares the bulk moduli predicted from this approximate form with those predicted from the complete Gassmann equation based on the dry data from all of the samples. They compare very favorably for the low bulk moduli of this dataset.

A

B
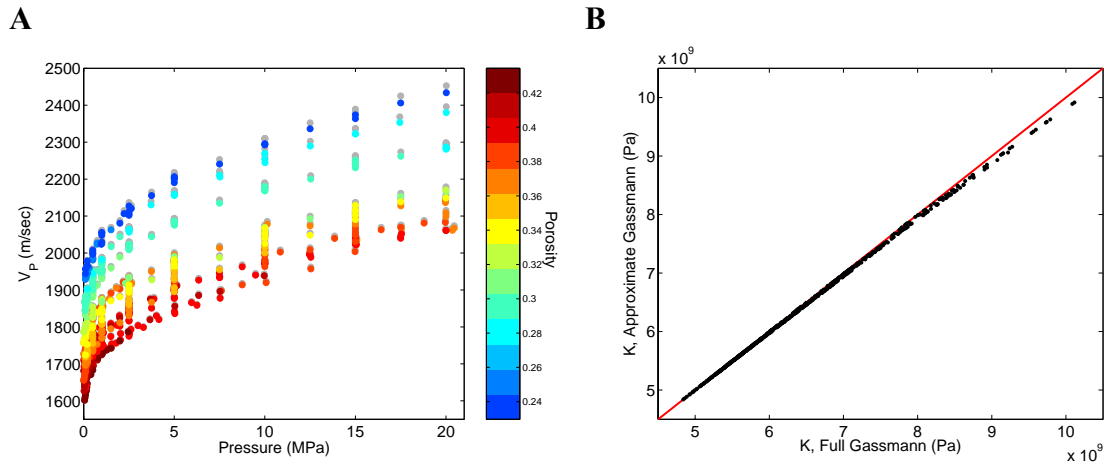
Figure 4.13: A) Estimated Gassmann fluid-substitution compressional-wave velocity values in color plotted over the full Gassmann equation values in gray; B) the estimated values of the water-saturated bulk modulus plotted against the full Gassmann values;

The expression in A.4 can be rearranged to isolate K_{dry}:

$$K_{dry} \approx \frac{K_{sat} - K_{P=0}}{\left(1 - 2\frac{K_{P=0}}{K_{Qtz}}\right)} . \quad (A.5)$$

The water-saturated bulk moduli at various porosities are all to be corrected to a common porosity, arbitrarily picked as 0.4. Rewriting Equation A.4 for the water-saturated bulk modulus at this porosity gives the following:

$$K_{sat,\phi=0.4} \approx K_{P=0,\phi=0.4} + \left(1 - 2\frac{K_{P=0,\phi=0.4}}{K_{Qtz}}\right)K_{dry,\phi=0.4}. \tag{A.6}$$

If we assume that K_{dry} is effectively constant with porosity, we can replace it in A.6 with the expression given in A.5:

$$K_{sat,\phi=0.4} \approx K_{P=0,\phi=0.4} + \frac{\left(1 - 2\frac{K_{P=0,\phi=0.4}}{K_{Qtz}}\right)}{\left(1 - 2\frac{K_{P=0}}{K_{Qtz}}\right)}\left(K_{sat} - K_{P=0}\right). \tag{A.7}$$

Figure 4.14A shows a plot of the multiplier in the second term,

$$\alpha = \frac{\left(1 - 2\frac{K_{P=0,\phi=0.4}}{K_{Qtz}}\right)}{\left(1 - 2\frac{K_{P=0}}{K_{Qtz}}\right)}, \tag{A.8}$$

against the porosity. While the variation in this parameter is relatively large, we will assume for the moment that $\alpha \approx 1$. This gives the following expression for the corrected bulk modulus:

$$K_{sat,\phi=0.4} \approx \left(K_{P=0,\phi=0.4} - K_{P=0}\right) + K_{sat}. \tag{A.9}$$

This indicates that the correction to a given porosity can be applied simply by adding the difference between the Reuss average values at a porosity of 0.4 and at the actual porosity of the sample to the measured bulk modulus. The only inputs to this correction would be the porosity of the sample and the bulk moduli of the fluid and mineral components.

The assumptions made in this approximation are 1) that $K_{dry} \ll K_{Qtz}$, 2) that K_{dry} is independent of porosity over the porosity range of the samples, and 3) that $\alpha \approx 1$, implying that the zero-pressure moduli at the two different porosities, $K_{P=0}$ and $K_{P=0,\phi=0.4}$, are close. Assumption 1 is very reasonable for unconsolidated sediments, but not necessarily for more consolidated rocks. Assumption 2 is relatively safe, given the relative independence of the fit parameters of the dry bulk modulus given in Table 4.2 and shown in Figure 4.8. Assumption 3 is not very safe, but Figure 4.14B demonstrates that, relative to a full Gassmann correction, the error introduced into the final correction by assuming that $\alpha \approx 1$ is only about twice the error introduced by the other assumptions, and counteracts those errors, most of which come from assumption 2.

A

B

C
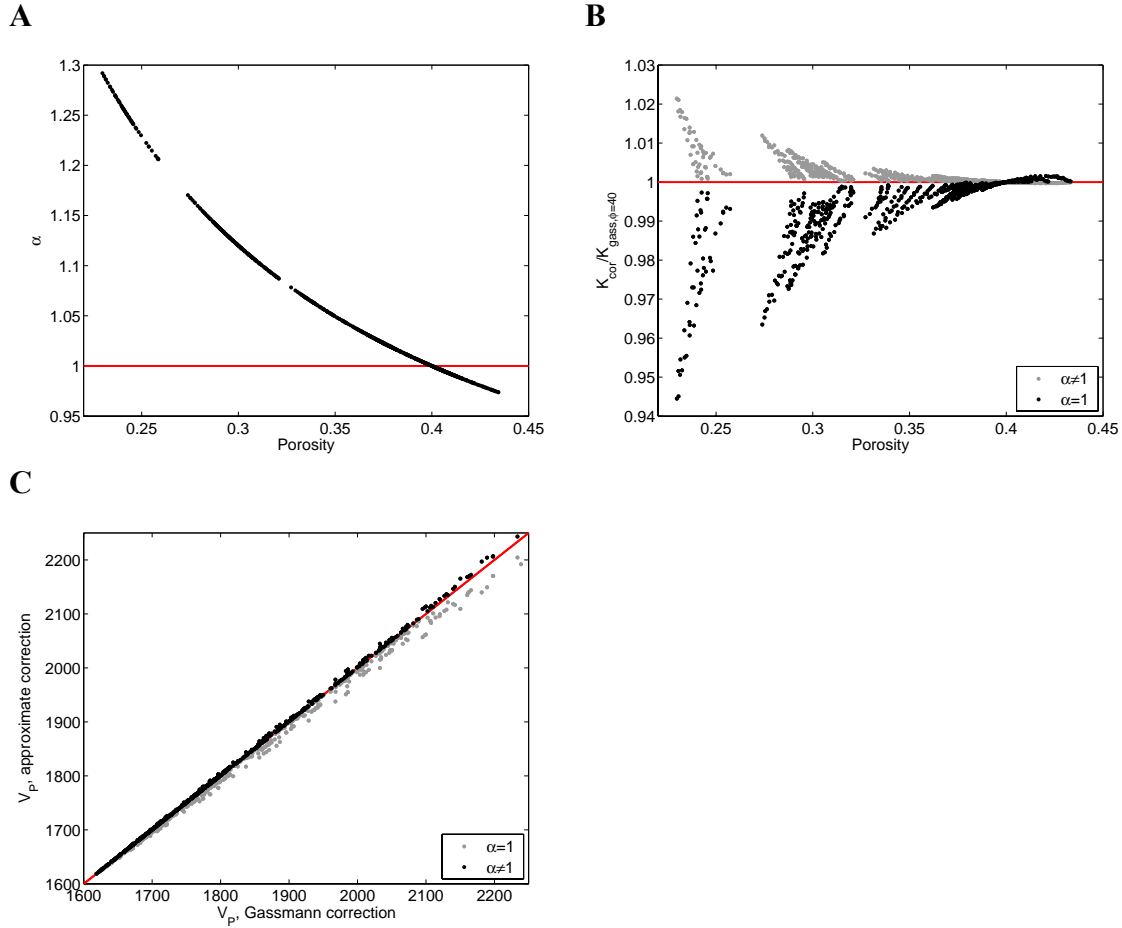
Figure 4.14: A) plot of α vs. porosity; B) plot of the corrected, water-saturated bulk modulus divided by the bulk modulus corrected with the full Gassmann's equation, and plotted against the porosity; and C) the corrected, water-saturated compressional-wave velocities plotted against the full Gassmann-corrected velocities with various assumptions for the value of α.

APPENDIX B: V_P-V_S RATIO-SHEAR MODULUS TRANSFORM

This appendix presents the derivation of an approximate transform between the V_P-V_S ratio of water-saturated samples and the shear modulus. It will take advantage of the approximate form of Gassmann's equation given in Equation A.4, so it will be based on the assumption that $K_{dry}<<K_{Qtz}$. The water-saturated V_P-V_S ratio can be expressed in terms of the shear (μ) and water-saturated bulk (K_{sat}) moduli as follows:

$$\frac{V_P}{V_S} = \sqrt{\frac{\frac{K_{Sat}+\frac{4}{3}\mu}{\rho}}{\frac{\mu}{\rho}}} = \sqrt{\frac{K_{sat}+\frac{4}{3}\mu}{\mu}} = \sqrt{\frac{K_{sat}}{\mu}+\frac{4}{3}}, \tag{B.1}$$

where ρ is the bulk density. Substituting the approximation for the water-saturated bulk modulus in Equation A.4 into Equation B.1 results in the following:
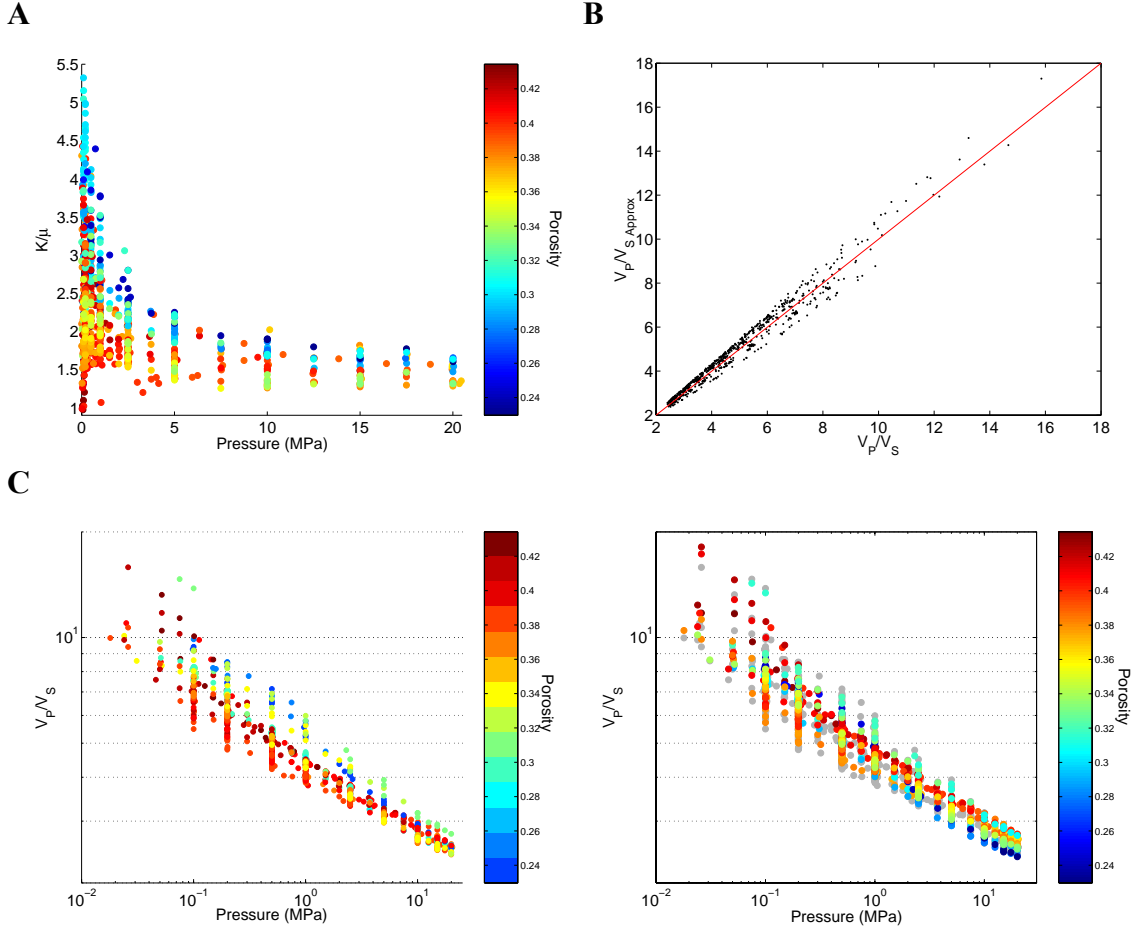
Figure 4.15: A) Plot of the K/μ ratio with pressure; B) plot of the approximate V_P-V_S ratio plotted against the actual V_P-V_S ratio data; and C) comparison of the actual V_P-V_S ratio data to the approximated V_P-V_S ratio.

$$\frac{V_P}{V_S} \approx \sqrt{\frac{K_{P=0} + \left(1 - 2\frac{K_{P=0}}{K_{Qtz}}\right)K_{dry}}{\mu} + \frac{4}{3}} = \sqrt{\frac{K_{P=0}}{\mu} + \left(1 - 2\frac{K_{P=0}}{K_{Qtz}}\right)\frac{K_{dry}}{\mu} + \frac{4}{3}} \,. \qquad (B.2)$$

$K_{P=0}$, the Reuss average between the bulk moduli of water and the pure mineral, can be estimated to be 6×10^9 Pa, the value at a porosity of 0.33, near the center of the range of porosities in this data set. I also assume that K_{dry}/μ is constant at about 2, as demonstrated in Figure 4.15A. These approximations give the following expression for the V_P-V_S ratio in terms of the shear modulus:

$$\frac{V_P}{V_S} \approx \sqrt{\frac{6\times10^9}{\mu} + \left(1 - 2\times\frac{6\times10^9}{36.6\times10^9}\right)2 + \frac{4}{3}} \approx \sqrt{\frac{6\times10^9\,Pa}{\mu} + \frac{8}{3}} \,. \qquad (B.3)$$

The quality of this estimate of the V_P-V_S ratio is compared to the measured values in Figure 4.15B. The estimated V_P-V_S ratio is generally within 10% of the actual value, and

demonstrates roughly the same amount of scatter when plotted versus pressure. Invert Equation B.3 for the shear modulus gives the following approximate transform between the V_P-V_S ratio and the shear modulus:

$$\mu \approx \frac{6 \times 10^9 \, Pa}{\left(\dfrac{V_P}{V_S}\right)^2 - \dfrac{8}{3}} . \tag{B.4}$$

The quality of this estimate is demonstrated in Figure 4.12 and discussed in the main body of the chapter. This expression assumes only that $K_{dry} \ll K_{Qtz}$ and the estimated values of $K_{P=0}$ and K_{dry}/μ are constant and valid for most samples. These values could be estimated more exactly if the porosity and/or pressure of the sediment of interest were known.

CHAPTER 5:
FLUID-INDUCED VELOCITY DISPERSION IN UNCONSOLIDATED SANDS

ABSTRACT

The compressional- and shear-wave velocities of four sands were measured at ultrasonic frequencies in similarly prepared water-saturated and dry samples. The water-saturated velocity results were compared to values predicted by Gassmann, Biot, and Mavko-Jizba models based on the dry velocity measurements. The observed water-saturated compressional-wave velocities exceed the Gassmann and Biot model predictions and are exceeded by the Mavko-Jizba model predictions over most of the pressure range of the measurements, indicating that the squirt mechanism is the primary dispersion mechanism active in these sands. The shear-wave velocities measured in the water-saturated samples closely match the Gassmann and Mavko-Jizba model results, but are over-predicted by the Biot model, indicating that the Biot viscous flow and inertial mechanisms are not significantly active in the samples at this frequency. The dispersion in the velocities demonstrates no significant change with compaction to higher pressures. It follows that the porosity reduction associated with static compaction does not significantly change the pore geometry responsible for the dispersion.

INTRODUCTION

The seismic velocities of water-saturated rocks and sediments vary significantly with the frequency of the seismic waves (e.g. Williams et al., 2002), while the velocities of dry rocks are nearly independent of frequency above a frequency of 0.1 Hz (Hagin, 2003). Since velocity measurements are conducted over a wide range of frequencies between ultrasonic laboratory measurements, sonic well-log measurements, and seismic measurements, comparisons of the velocities from the various measurement techniques require corrections for this frequency dependence. As seismic surveys are increasingly used for the imaging of unconsolidated sediments at shallower depths below the seafloor and use wider frequency bandwidths to improve the resolution of the resulting images, and as well-logs are increasingly collected in shallow unconsolidated sediments, the need for an understanding of the dispersion mechanisms active in unconsolidated sediments is becoming increasingly important.

Regardless of the frequency, the velocities of dry, porous rocks and sediments generally demonstrate an increase in the compressional-wave velocities and a decrease in the shear-wave velocities upon complete water saturation (Nur and Simmons, 1969; Domenico, 1977; Winkler, 1985). The increase in the compressional-wave velocities results from the replacement of the gas in the pore space, which has a bulk modulus approximately equal to the pore pressure, with water, which has a bulk modulus of at least 2.2 GPa. Since both water and gas have a shear modulus of zero, the replacement of the gas with water produces little change in the shear modulus of the rock while the increase in the density on saturation generally produces a slight decrease in the shear-wave velocity.

Velocity measurements on water-saturated rocks at seismic frequencies are well described by Gassmann fluid substitution theory (Gassmann, 1951). This theory, which assumes local equilibration of the pore pressure, models the water-saturated bulk modulus, K_{sat}, as:

$$K_{sat} = K_{dry} + \frac{\left(1 - \frac{K_{dry}}{K_{min}}\right)^2}{\frac{\phi}{K_{fl}} + \frac{1-\phi}{K_{min}} - \frac{K_{dry}}{K_{min}^2}} \,, \tag{5.1}$$

where K_{dry} is the bulk modulus of the dry rock or sediment (assuming low pore pressure), K_{min} is the bulk modulus of the constituent minerals, K_{fl} is the bulk modulus of the saturating pore fluid, and ϕ is the porosity. The shear modulus, μ_{sat}, is equal to that of the dry rock, μ_{dry}. The fluid-saturated density, ρ_{sat}, is determined by adding the dry density, ρ_{dry}, to the fluid density, ρ_{fl}, times the porosity:

$$\rho_{sat} = \rho_{dry} + \rho_{fl}\phi \,. \tag{5.2}$$

The water-saturated velocities are then calculated by substituting these moduli and the density into the velocity equations (Equations 1.2 and 1.3).

As the dry frame moduli of most rocks are effectively frequency independent, the frequency dispersion observed in the velocities of water-saturated samples at higher frequencies is primarily due to the interaction between the pore fluid and the porous solid. At low frequencies, the fluid pressure generally has time to equilibrate throughout a wavelength-sized volume and the viscosity of the fluid will not produce any resistance to pore compression. At higher frequencies, the pore pressure in small pores will not have

time to equilibrate with the surrounding pore volume, and the viscosity of the fluid will cause it to resist shearing, each of which could produce an effective stiffening of the pores and can result in an increase in the velocities.

Biot (1956a,b) developed a model to predict the frequency dependence of the velocities due to the fluid viscosity and the inertial interaction between the fluid and solid. These mechanisms are thought to be especially relevant in high-porosity rocks and sediments. This theory predicts compressional- and shear-wave velocities at the high-frequency limit from the dry-rock and pure mineral bulk and shear moduli, the fluid bulk modulus, the rock and fluid densities, the porosity, and the tortuosity of the pore space. The tortuosity is a quantitative measure of how much the pore structure deviates from straight tubes, and by so doing restricts the flow of the fluid through the pores. The equations for the high-frequency velocities predicted from these parameters are given by Mavko et al. (1998). The tortuosity, α, which cannot be measured independently, can be approximated by:

$$\alpha = 1 - r\left(1 - \tfrac{1}{\phi}\right), \tag{5.3}$$

where $r = \frac{1}{2}$ when the grains are spherical, and varies between 0 and 1 for other ellipsoidal grain shapes (Berryman, 1981). Biot theory predicts that the compressional-wave velocity will increase above the Gassmann prediction as the frequency increases, as the viscous pore fluid's resistance to flow on short time scales results in a stiffening of the rock frame. This theory also predicts a slightly larger shear-wave velocity than predicted by the Gassmann theory, since fluid flow relative to the sediment frame produces a lower effective density for the material displaced by the passing wave.

Mavko and Jizba (1991) developed a model that estimates the velocity increase due to the inability of the pore pressure to equilibrate throughout the pore space at high measurement frequencies. This model assumes that this "squirt" effect will be primarily due to the inability of the fluid to escape from thin, compliant pores that are compressed as the wave passes, so the pores act as if they are closed off from the rest of the pore network at high frequencies. It assumes that these pores will all be closed at high pressure, so estimates the bulk modulus of the dry rock including this "squirt" effect as the measured high-pressure, dry-rock modulus, with a small correction for the actual bulk modulus of the volume of fluid in those pores when open at lower pressures. This squirt-

influenced, dry bulk modulus is then input into the Gassmann or Biot models to predict the velocities of the water-saturated rock, producing a larger compressional-wave velocity and little change to the shear-wave velocity of the Gassmann or Biot predictions.

The objective of this study was to measure the influence of water-saturation on the ultrasonic compressional- and shear-wave velocities of a series of unconsolidated sands, and to test which of these theoretical models best describes the observed saturation effects. To do this, I prepared dry and water-saturated samples of four sands, made measurements of both the compressional- and shear-wave velocities over pressures from 100 kPa to 20 MPa, and calculated the water-saturated velocities predicted by the theoretical models based on the dry velocity measurements. I also observed how preconsolidation affected the dry and water-saturated velocities, and will discuss the implications of these observations for changes in the pore geometry with compaction in sands.

VELOCITY MEASUREMENTS

These measurements were made on four different natural sands, including samples collected from Galveston Beach (TX), from the Gulf of Mexico sea floor, from the Merritt Sand, a Pleistocene dune sand in Oakland, CA, and from Pomponio Beach (CA). The index properties and X-ray diffraction analysis results for each of the sands are given in Tables 3.1 and 3.2, and the particle size distributions of each are shown in Figure 3.1. For the velocities of the dry and water-saturated samples to be comparable, it was necessary to prepare the dry and water-saturated samples of each sand in as similar a manner as possible. To this end, the samples of the beach sands and the Gulf of Mexico sand were all reconstituted from completely unconsolidated samples by air pluviating the dry sand into the sample holder. The water-saturated samples were then saturated once the sample holder had been placed in the vessel and the sand had been loaded to a confining pressure of 200 kPa. The Merritt sand samples were prepared from intact samples collected with a 3 inch Shelby tube in such a way as to produce minimal disruption of the *in situ* texture. The dry sample was prepared by drying a section of the sample at 65°C, hand coring it with a 2 inch bit, and trimming it to size. The water-saturated sample was prepared by freezing a section of the tube sample, hand coring it while frozen, trimming it to size, and placing it in the sample holder while frozen. It was

then allowed to thaw, and completely saturated as were the other samples. A more detailed description of the experimental apparatus and the sample preparation methodologies is given in Chapter 2.

The velocity measurements were made using through-transmission of ultrasonic signals to measure both the compressional- and shear-wave velocities. The apparatus uses broad-band ultrasonic transducers optimized to produce high quality signals through unconsolidated sediments, with a center frequency of about 150 kHz for both the compressional and shear waves. Velocity measurements were made on each sample at pressures from below 100 kPa to 20 MPa over a series of between 3 and 9 pressure cycles with increasing peak pressures.

The velocities measured for each of the sands are displayed in Figure 5.1. The dry velocities are indicated by the red points, while the water-saturated velocities are shown in blue. The compressional-wave velocities are the higher set for each saturation. The dry velocities demonstrate a power-law behavior with pressure (Chapter 3), rising from near zero at low pressure to about 1000 m/sec for the shear-wave velocities and to between 1500 and 2000 m/sec for the compressional-wave velocities. The saturation of the dry samples results in a large increase in the compressional-wave velocities such that the velocities at the lowest pressures are all above 1600 m/sec. The water-saturated shear-wave velocities demonstrate a slight decrease from the dry values for all of the samples.

MODELING RESULTS

For each of the samples, the Gassmann, Biot, and Mavko-Jizba models were each used to model the velocities of the water-saturated sands based on the dry velocity measurements. The squirt-stiffened bulk modulus generated by the Mavko-Jizba model was substituted into each the Gassmann and Biot models. The result is four model predictions: the low frequency, dispersion-free Gassmann prediction, the Biot prediction, incorporating the viscous-flow and inertial mechanisms, the Mavko-Jizba with Gassmann prediction, incorporating just the squirt mechanism, and the Mavko-Jizba with Biot prediction, which includes both the squirt mechanism and the viscous-flow and inertial mechanisms. The inputs to each model where calculated as follows: the dry frame moduli were calculated from the dry velocity measurements and the bulk density; the mineral moduli were calculated as the average of the upper and lower Hashin-Shtrikman bounds

of the moduli of the various constituent minerals, based on the XRD analysis; the grain density was measured either using a pycnometer for the disaggregated samples or with a helium porosimeter for the Merritt sand; the porosity was calculated from the sample volume, grain density and dry sample mass at each measurement step; and the value of r input into Equation 5.3 for the Biot model was assumed to be ½. Figure 5.2 compares the Gassmann predicted velocities to the measured compressional- and shear-wave velocities for each sample. Figure 5.3 shows the same comparison for only the normally-consolidated values, while Figure 5.4 shows the values for the first complete unloading cycle from 20 MPa down, with the normally-consolidated values shown in gray in the background.

A

B

C

D
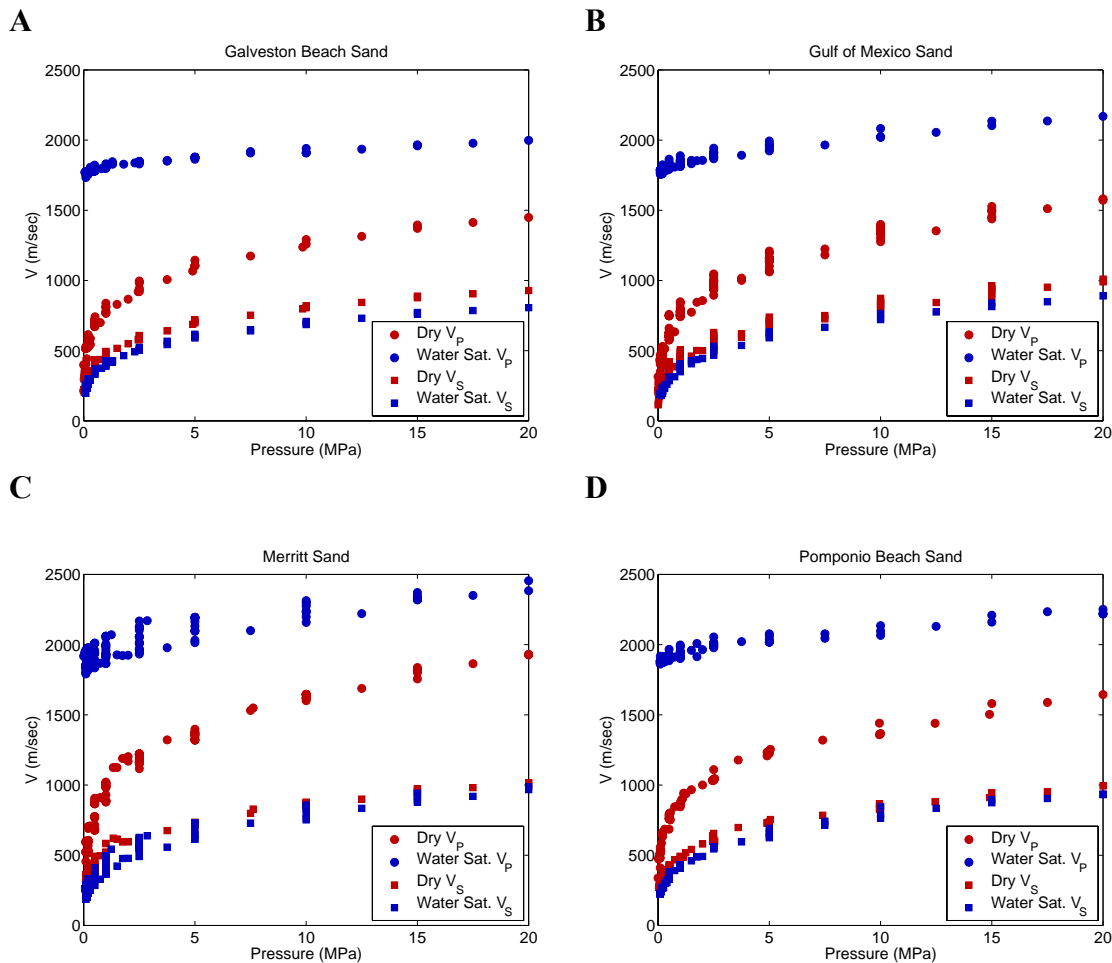
Figure 5.1: The dry and water-saturated, compressional- and shear-wave velocities measured for each sample: A) the Galveston Beach sand, B) the Gulf of Mexico sand, C) the Merritt sand, and D) the Pomponio Beach sand.

Compressional-wave velocities

A comparison of the model predictions demonstrates that the Biot model predicts the smallest increase in the compressional-wave velocities relative to the Gassmann theory, with an increase of up to 100 m/sec at the lowest pressures, and less dispersion as the pressure increases. The Mavko-Jizba squirt-flow model, combined with Gassmann, results in a larger increase in the velocity relative to the Gassmann predictions, with an increase of 200 to 300 m/sec at the lowest pressures, but produces no increase at the peak pressure. The combination of the Mavko-Jizba model with the Biot model produces only a slight increase in the predicted velocities, less than 50 m/sec, relative to the Mavko-Jizba model alone.

The compressional-wave velocities measured on the water-saturated samples of the Gulf of Mexico and Pomponio Beach sands exceed the Gassmann-predicted velocities over the entire pressure range. The magnitude of the dispersion for these samples, as measured by the difference between the measured and Gassmann-predicted velocities, is 150 to 200 m/sec at the lowest pressures and decreases with increasing pressure. The velocities of these samples also exceed the velocities predicted by the Biot model at all pressures. For the velocities predicted from the squirt-Gassmann and squirt-Biot models, the measured velocities lie below the model values at the lowest pressures, but rise above them at higher pressures. For the Biot model predictions, decreasing the value of r input into Equation 5.3 decreases the tortuosity value toward a value of 1 and increases the predicted compressional-wave velocities to better match the measured compressional-wave velocities. At the same time, however, the lower tortuosity also increases the shear-wave velocities predicted by the model, resulting in a greater misfit to the measured water-saturated shear-wave velocities, as discussed in the next section.

For the Galveston Beach sand, the measured water-saturated velocities also demonstrate a significant dispersion at the lowest pressures, but are slightly below the Gassmann-predicted values at pressures above 10 MPa. As for the Gulf of Mexico and Pomponio Beach samples, the low-pressure velocities exceed the Biot modeled velocities and are slightly below the values predicted by the squirt models, but with pressure the velocities increase less than the model predictions so that at high pressure they lie below all of the model values.
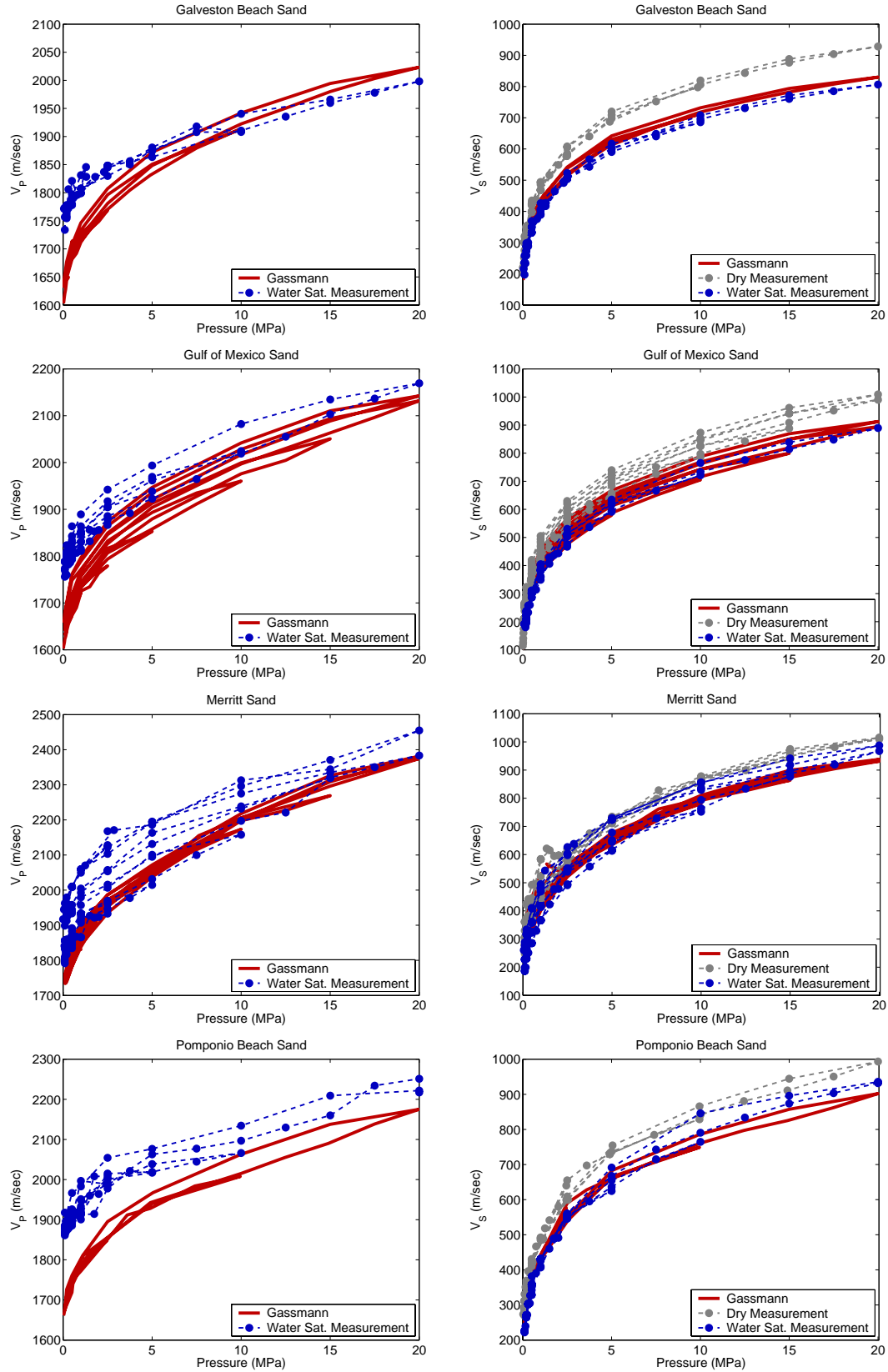
Figure 5.2: The velocity data and model predictions for the compressional-wave velocities (left) and shear-wave velocities (right) of each sample.
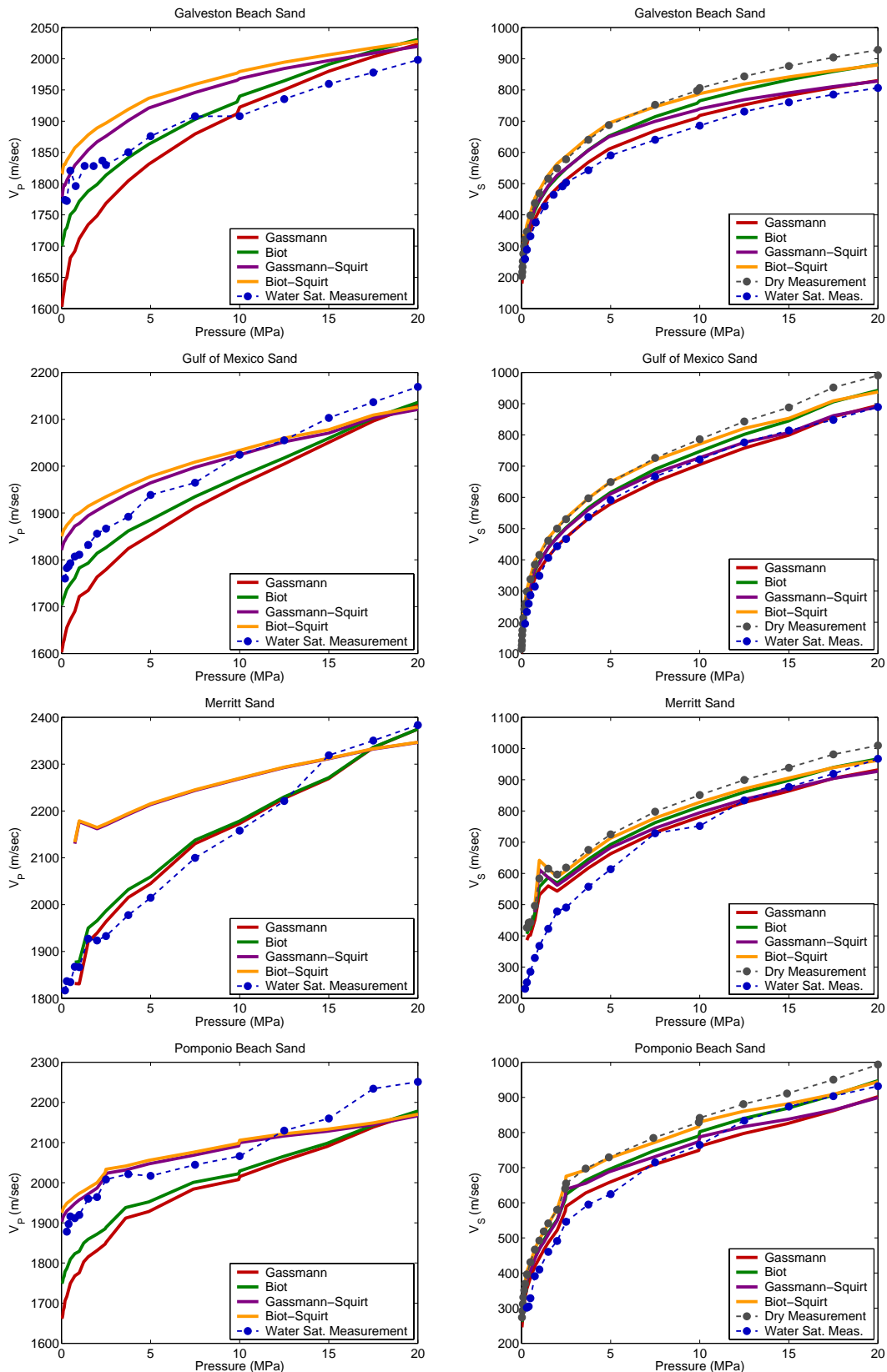
Figure 5.3: The velocity data and model predictions for the normally consolidated samples: compressional-wave velocities (left) and shear-wave velocities (right).
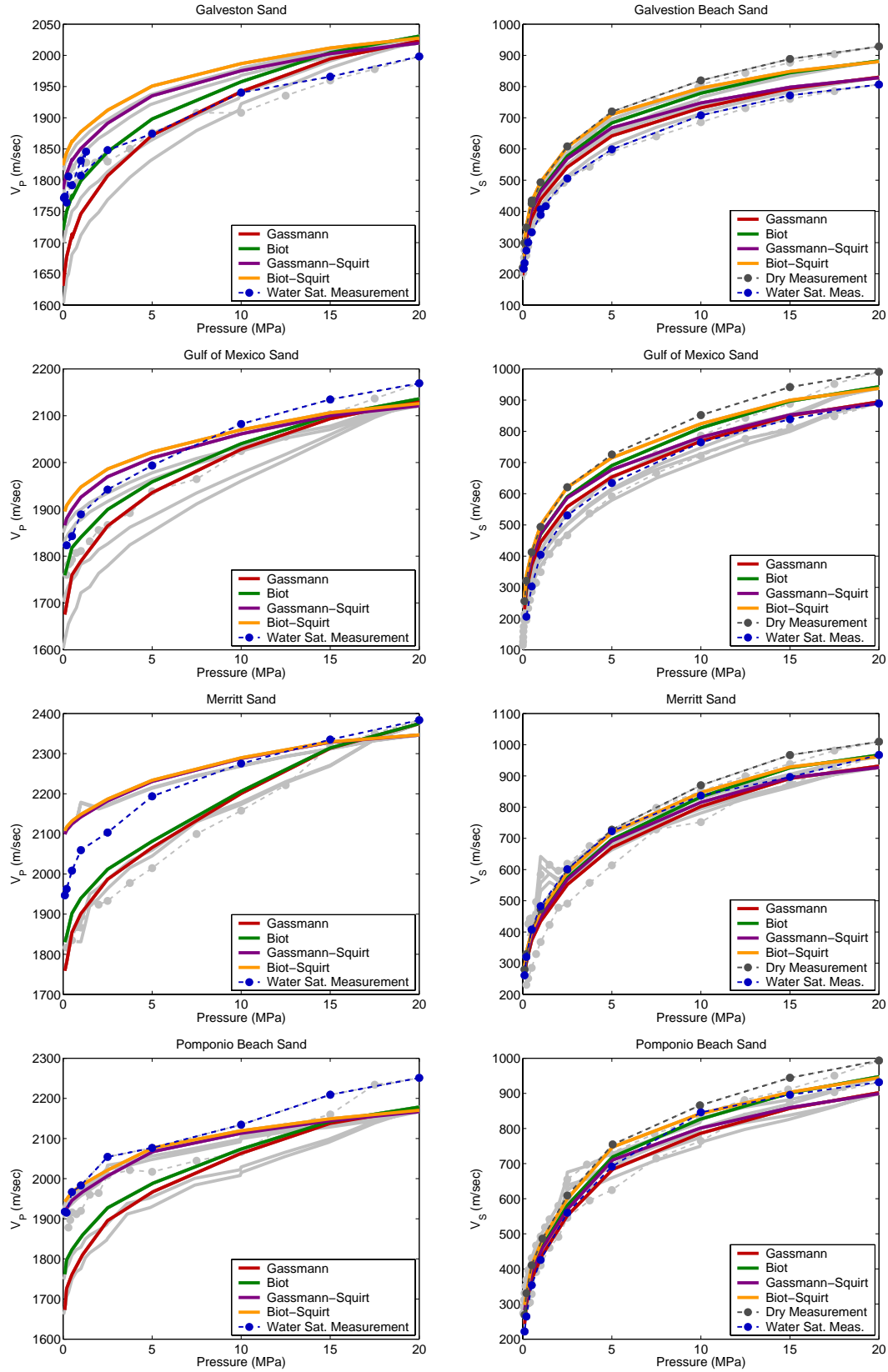
Figure 5.4: The velocity data and model predictions for the samples on the first unloading path from 20 MPa down. The normally consolidated data and model predictions are shown in gray.

On the normally consolidated portion of the loading path, the velocities of the water-saturated Merritt sand sample very closely resemble the Gassmann predicted velocities, and so lie below the values predicted by all of the dispersion models. On the contrary, on the later unloading paths, the measured velocities exceed the Gassmann and Biot predictions. By the last cycle, the measured velocities demonstrated similar behavior relative to the squirt models as the Gulf of Mexico and Pomponio Beach samples, lying below the modeled values at the low pressures, but rising slightly above them by the highest pressures.

Shear-wave velocities

The dispersion model predictions for the shear-wave velocities generally lie between the dry measured values and the Gassmann fluid-substitution values. The squirt-Gassmann model predicts only a slight increase in the shear-wave velocity above the Gassmann predictions. The Biot and squirt-Biot models, however, predict shear-wave velocity values much closer to the dry measured velocities.

The measured velocities in the water-saturated samples consistently lie close to the Gassmann, dispersion-free predictions. This implies that the dispersion mechanisms causing the increase in the compressional-wave velocities are causing an increase only in the bulk modulus and are not having any significant impact on the shear modulus. The measured values lie significantly below both the Biot model predictions and the squirt-Biot predictions, a misfit that would be worse for a lower tortuosity. The squirt-Gassmann predictions, which are similar to those of the Gassmann theory alone, are also reasonably close to the measured values.

DISCUSSION

A comparison of the model predictions for both the compressional- and shear-wave velocities to the measured data from the Gulf of Mexico and Pomponio Beach sands demonstrates that the dispersion observed in these samples at the frequency of measurement is chiefly attributable to the squirt mechanism. Both the Gassmann and Biot models under-predict the compressional-wave dispersion for these two samples, while the Biot and squirt-Biot models over-predict the shear-wave velocities. The under-prediction of the compressional-wave velocities by the high-frequency limit from the Biot model indicates that the viscous flow and inertial mechanisms are not sufficiently powerful to

produce the observed compressional-wave dispersion. Likewise, the over-prediction of the shear-wave velocities by the Biot models indicates that the inertial effects that would produce the increased shear-wave velocities are not active in these samples at this frequency. While the Mavko-Jizba model input into either the Gassmann model or the Biot model does not provide a good, overall fit to the water-saturated compressional-wave velocity measurements, the fact that it predicts more than enough dispersion at the low pressures suggests that this mechanism can produce enough stiffening of the sediment frame to explain the observed dispersion. Likewise, the Mavko-Jizba model predicts little dispersion in the shear-wave velocities, and therefore produces an acceptable match to the measured shear-wave velocities, which closely resemble the Gassmann predictions.

The imperfect fit of the squirt models, which over-predict the compressional-wave velocities of the Gulf of Mexico and Pomponio Beach sands at low pressures and under-predict them at the higher pressures, is most likely due to the model's assumptions that all of the compliant porosity is effectively isolated at high frequencies and is all closed at the highest measurement pressure. The model takes as an input the moduli from the dry sample at this highest measurement pressure, assuming that all of the squirt-causing, compliant pore volume is closed and that no dispersion occurs at that pressure. As these samples were only pressurized to 20 MPa, it is certain that there was more compliant porosity to be closed at this pressure, and that the bulk modulus of the dry sample would continue to increase with additional loading. A more accurate estimate of the dry frame when all of the compliant porosity is closed would result in higher model-predicted velocities over the entire pressure range. The model also assumes that the thin, compliant pores are effectively isolated from the rest of the pore network over the time scale of a wave period. In these high-porosity, loose sediments, this assumption is not likely to be valid, and so the model probably over-predicts the stiffening of the sediment frame due to the impeded flow of the pore fluid. If it were possible to account for these two effects – the continued occurrence of velocity dispersion at the peak measurement pressure, which causes the model to under-prediction the dispersion over the entire pressure range, and the connectedness of the pore network, which would decrease the amount of dispersion relative to when the compliant porosity is completely isolated, especially at the lowest

pressures when more of the compliant porosity is still open – the model might produce a much closer fit to the water-saturated compressional-wave velocity data of these two samples. Nevertheless, while the parameterization of the Mavko-Jizba model based on the limited pressure range of these measurements does not produce a good fit to the data, it does indicate that the squirt mechanism could produce as much dispersion as is observed in the compressional-wave velocity measurements.

While the behavior of the shear-wave velocities in the Galveston Beach sand is very similar to that of the other samples, the compressional-wave velocities behave rather erratically. The failure of the high pressure data to at least match the Gassmann predictions makes it difficult to interpret these results in terms of the dispersion mechanisms active in the sample. It is possible that this erratic behavior has an experimental cause: that the saturation process either was not successful in completely saturating the sample or disturbed the sample so that the velocities do not compare well to the dry measurements. However, since the compressional-wave velocities are consistent from cycle to cycle and the shear-wave velocities behave respectably, these do not seem to be adequate explanations for this behavior, which might also simply be a result of inaccurate first-break picks.

The Merritt sand sample demonstrates no dispersion in either the compressional- or shear-wave velocities under normally consolidated conditions, but shows more and more compressional-wave dispersion with overconsolidation. This is most likely a result of the different behavior of the dry and water saturated samples, as demonstrated by the greater porosity loss of the water-saturated sample (almost twice that of the dry sample), and the decrease in the velocity of the dry samples with overconsolidation (see Chapters 3 and 4). As the dry sample was oven dried at 65°C for several days, it is possible that the clays, which make up 11% of the sample by mass, became stiff on prolonged heating. They would therefore not permit as much porosity loss as in the water-saturated sample, and could break at the higher preconsolidation pressures, resulting in reduced velocities. The result is that the Gassmann-predicted velocities do not increase on overconsolidation even though there is some decrease in the porosity. Since the water-saturated sample was not heated, the clays retained their plasticity, continuing to permit more porosity to close and also continuing to act as contact cement after compaction. As the dry velocity data

are used to compute the inputs to the models, a heat-stiffened dry frame would lead to larger model predictions for the water-saturated compressional-wave velocities under normally consolidated conditions. Predictions based on the dry frame moduli of the actual water-saturated sample might be lower, in which case the velocities might demonstrate similar behavior to those of the Gulf of Mexico and Pomponio Beach samples.

The conclusion drawn from the Gulf of Mexico and Pomponio Beach sand results is that, since the observed compressional-wave velocities exceed the Biot model predictions, the squirt mechanism, or some other as yet unrecognized mechanism, must be invoked to explain the observed dispersion. Likewise, the lack of dispersion observed in the shear-wave velocities suggests that the Biot mechanisms are not active enough to produce dispersion in these sediments. The suggestion that the squirt model must be invoked to explain the observed dispersion, and that the inertial Biot mechanism is not active, runs counter to the conventional wisdom which suggests just the opposite: that in high porosity material with well connected pore networks the Biot mechanisms should be the principle dispersion mechanisms and that the squirt mechanism should not produce significant dispersion (Mavko et al., 1998). Winkler (1985) made a similar set of observations to those presented here in Berea sandstone samples, where the Biot model under-predicts the observed velocity dispersion. Winkler suggests that the frequency range of the Biot mechanisms is above the 400 kHz frequency used in his measurements for a rock with the permeability of the Berea sandstone. This could also be the cause of the low apparent activity of the Biot mechanisms in the measurements presented here. Winkler also attributes the larger dispersion that he observes in the water- and oil-saturated sandstone to the squirt mechanism. Theoretical work on the effect of squirt flow at grain-to-grain contacts in granular media by Palmer and Taviola (1980) indicates that fluid flow at contacts between perfect spheres would not produce significant dispersion, an assertion borne out experimentally by Winkler (1985). Palmer and Taviola do however demonstrate that lower aspect ratio contacts, where the angle between the two grains at the contact is low, could produce significant squirt-induced dispersion. This suggests that the sands measured here have enough low-angle contacts to produce squirt dispersion. At the same time, the permeability or tortuosity of the pore network appears

to prevent the inertial mechanisms modeled by Biot from acting at the 150 kHz frequencies used in these experiments.

Pore space changes with compaction

In an effort to observe how the nature of the contacts and the pore network changes with compaction, I compared the dispersion from subsequent cycles of the Gulf of Mexico and Pomponio Beach sand samples in two ways. The first way was to calculate the bulk modulus of the pore space based on both the dry and water-saturated velocity data, and to compare the difference between them for each pressure cycle. The second way was to directly compare the differences between the Gassmann-predicted velocities and the measured water-saturated velocities over each pressure cycle for both the compressional and shear waves.

The bulk moduli of the pore space, K_ϕ, or the stiffness of the pores under compression, were calculated for bulk moduli, K, measured in the dry and water-saturated samples using the following relation:

$$\frac{1}{K} = \frac{1}{K_{min}} + \frac{\phi}{K_\phi} \tag{5.4}$$

where in the water-saturated case this K_ϕ represents the stiffness of the pores when filled with water. The bulk modulus of the water-saturated pores without water, removing the Gassmann effect but not the dispersion effects, can be calculated as follows:

$$\frac{1}{K_{sat}} = \frac{1}{K_{min}} + \frac{\phi}{K_\phi + \frac{K_{min}K_{fl}}{K_{min} - K_{fl}}} . \tag{5.5}$$

A comparison of K_ϕ calculated in each of these cases is shown in Figure 5.5A. The difference between the dry K_ϕ and the water-saturated K_ϕ calculated from Equation 5.5 for the Gulf of Mexico and Pomponio Beach sand samples are shown in Figure 5.5B.

Figure 5.6 shows the difference between the water-saturated compressional- and shear-wave velocities and the Gassmann predicted velocities for both of these samples. This figure and Figure 5.5B demonstrate how the amount of dispersion occurring between the water-saturated measurements made at 150 kHz and the low-frequency prediction from Gassmann theory changes from cycle to cycle. The comparison of the pore bulk modulus, K_ϕ, from cycle to cycle in Figure 5.5B demonstrates that there is no systematic difference between the values from the different cycles. The same is true of

101

the dispersion in the compressional-wave velocities shown in Figure 5.6A, though the last cycle of the Pomponio Beach sand shows a slightly greater dispersion. The shear-wave velocity dispersion in the Pomponio Beach sand also shows a slightly larger $V_{Sat.} - V_{Gass.}$ for the last cycle, while the Gulf of Mexico sand data demonstrates a slightly smaller difference on the unloading paths of the final two cycles relative to the other cycles. As each of these values is generally very similar from cycle to cycle, the pore space does not appear to change significantly in any way that leads to greater dispersion. Since the squirt mechanism is presumably the most significant mechanism acting in these samples, this implies that most of the porosity loss on compaction occurs in the large pores rather than in the thinner, compliant porosity at the contacts. Likewise, this implies that the number of contacts does not increase significantly enough or that the close contacts that become true contacts do not contribute to the dispersion enough to produce a significantly larger dispersion.

A

B
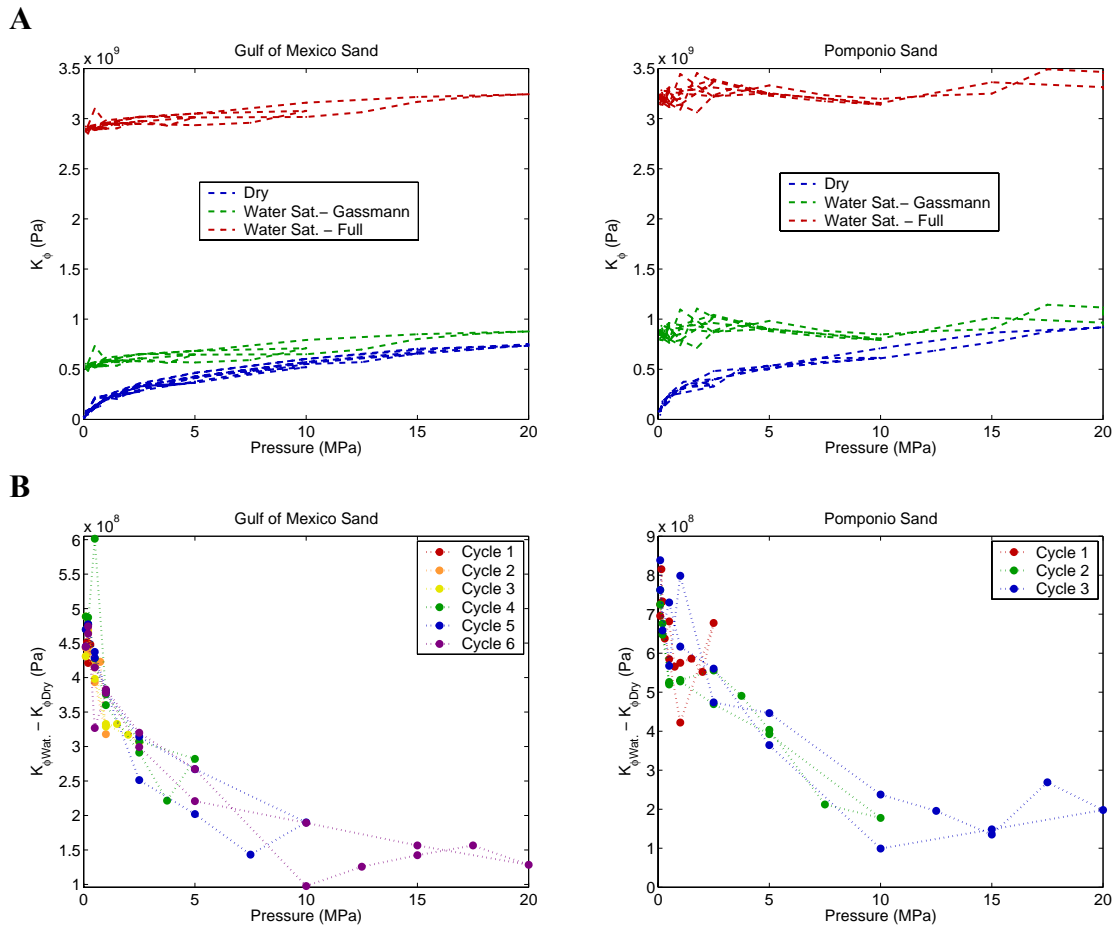
Figure 5.5: A) K_ϕ for dry and water-saturated samples of the Gulf of Mexico sand and Pomponio Beach sand, and B) the difference between the water-saturated and dry K_ϕ for each sample.

A

B
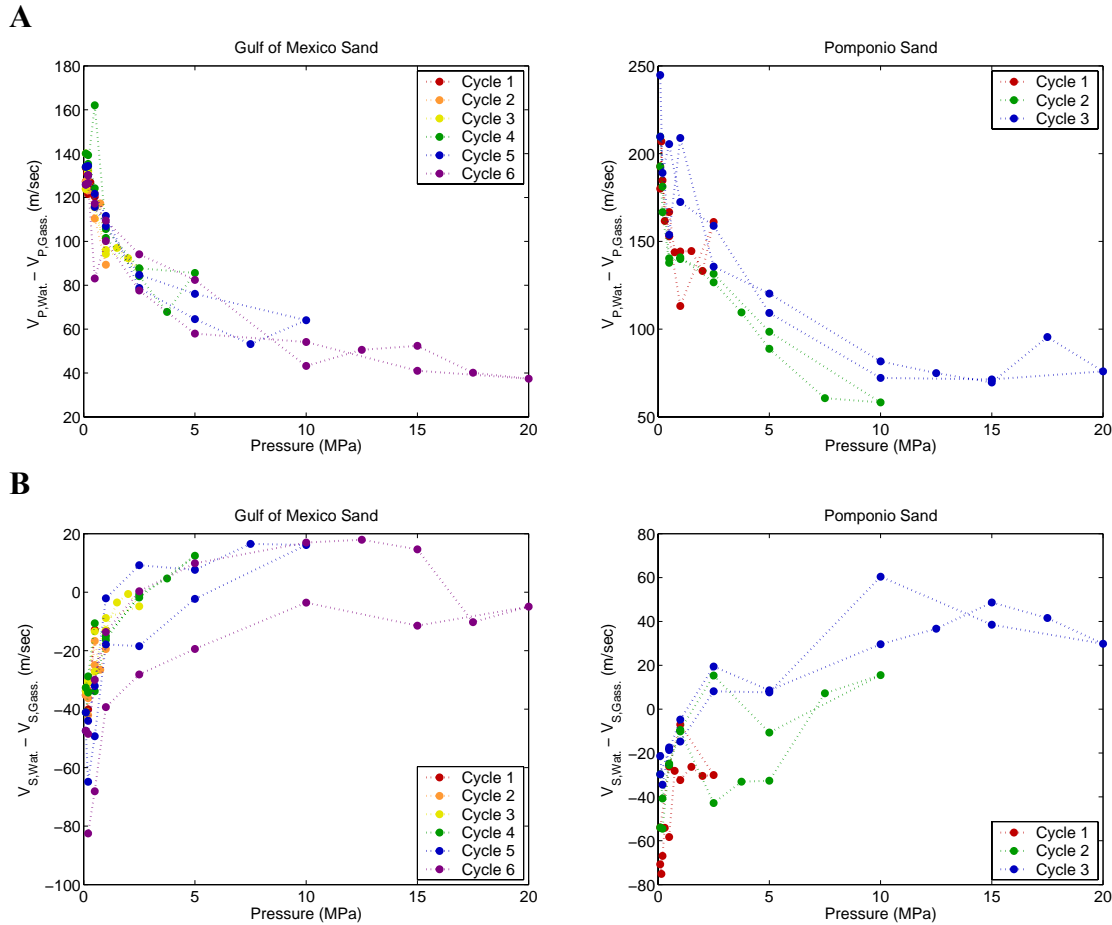
Figure 5.6: Difference between the measured water-saturated velocities and the Gassmann predicted velocities for A) the compressional waves and B) the shear waves.

CONCLUSIONS

I compared water-saturated, compressional- and shear-wave velocities measured in four unconsolidated sands at a frequency of 150 kHz to model predictions from Gassmann, Biot, and Mavko-Jizba models. The models were used to predict the water-saturated velocities from dry velocity measurements for various dispersion mechanisms. I found that the compressional-wave velocities measured in the most reliable samples exceeded the Gassmann and Biot predicted velocities. The Mavko-Jizba squirt model, used in combination with the Gassmann and Biot models, demonstrates that the squirt model could produce the magnitude of the dispersion observed in the compressional-wave velocities. For the shear-wave velocities, the water-saturated measurements were well represented by the Gassmann and Mavko-Jizba with Gassmann predictions. The Biot and Mavko-Jizba with Biot models consistently over-predicted the observed shear-

103

wave velocities. This comparison indicates that the squirt mechanism is active in these sediments at this frequency, while the Biot mechanism is not. A comparison of the dispersion in the velocities from compaction cycles to higher preconsolidation pressures demonstrates no significant change in the dispersion. It follows that the porosity reduction associated with static compaction does not significantly change the pore geometry responsible for the dispersion at this frequency.

CHAPTER 6:
COMPARISON OF STATIC AND DYNAMIC BULK MODULI IN SANDS

ABSTRACT

This chapter will present the results of dynamic and static bulk moduli measurements on reconstituted samples of four dry, natural sands and one glass bead sample over a number of pressure cycles from 0 to 20 MPa. The dynamic modulus, K_{dyn}, was calculated from ultrasonic compressional- and shear-wave velocity measurements, while the static modulus, K_{stat}, was measured from the corrected volumetric strains between pressure steps. For a given sample, the static bulk modulus demonstrates a great deal of variation based on the loading history of the sample, while the dynamic modulus is only slightly sensitive to the loading history. The K_{dyn} to K_{stat} ratio on the normally consolidated, initial loading path varies from between 2 and 10 for the various samples, and decreases slightly with increasing pressure as the dynamic modulus rises faster than the bulk modulus. On the first unloading step of any pressure cycle the dynamic and bulk moduli are approximately equal, while with continued unloading the K_{dyn} to K_{stat} ratio rises from approximately 1 at the initial unloading step to near 3 at zero pressure for each of the samples. The significant variability in the K_{dyn} to K_{stat} ratio with pressure history indicates that a robust prediction of the static bulk modulus from dynamic measurements made *in situ* would require information on the loading history of the sample and on the current effective pressure.

The Preisach-Mayergoyz space analysis was adapted to account for the effects of the plastic strains, in addition to those of the elastic hysteresis, on the relationship between the static and dynamic bulk moduli. Inaccuracies in the volumetric strain measurements lead to a quantitative mismatch between the dynamic modulus predicted from this analysis and that observed in the data. Nevertheless, this analysis does demonstrate the degree to which both the strain magnitude dependence of the static modulus and the occurrence of plastic strain contribute to the difference between the static and dynamic bulk moduli on the loading portions of the pressure path. On unloading, there is no plastic strain in the samples, so the strain magnitude dependence of the static modulus is the sole cause of the difference in the static and dynamic bulk moduli.

INTRODUCTION

The bulk modulus, *K,* of a material represents the change in mean stress, $\Delta\sigma_{avg}$, required to induce a change in volumetric strain, $\Delta\varepsilon_{vol}$:

$$K = \frac{\Delta\sigma_{avg}}{\Delta\varepsilon_{vol}}.$$ (6.1)

The bulk modulus generally describes the resistance of the material to compression. While the Young's modulus, shear modulus, and constrained modulus are more appropriate to the stress states that lead to consolidation or shear failure in rocks and sediments and so might be more easily applied to mechanical failure analyses for *in situ* materials, the bulk modulus also represents a material stiffness, is deterministically related to these parameters, and can be simpler to measure.

The bulk modulus is measured experimentally in two ways. One involves putting a sample under an isotropic stress and measuring the volumetric strain for a given change in pressure. This is generally referred to as a static measurement if the loading occurs at a low enough rate (frequency of stress cycles << 1 Hz). The second way, the dynamic measurement, involves measuring the shear- and compressional-wave velocities, generally at frequencies between a few Hz and several MHz, and calculating the bulk modulus from the velocities and the density of the sample. In a linear elastic material, the bulk modulus is related to the compressional-wave (V_P) and shear-wave (V_S) velocities as follows:

$$K = \rho\left(V_P^2 - \tfrac{4}{3}V_S^2\right),$$ (6.2)

where ρ is the bulk density. Besides the difference in the frequency of the loading, the static and dynamic measurements also tend to involve very different strain magnitudes. The static measurement may produce strains greater than 10^{-1}, while the dynamic measurement is generally limited to strains below 10^{-4}.

The relationship between the high-frequency, low-strain, dynamic measurement and the low-frequency, high-strain, static measurement is important because the dynamic measurement is easily and regularly made *in situ*, whereas it is much more difficult and expensive to retrieve a sample on which to make the static measurement in the lab. On the contrary, it is the static modulus that represents the mechanical stability under most *in situ* loading conditions. It follows that if it is possible to reliably predict the large strain

modulus from a dynamic measurement that can be made *in situ*, it would be possible to effectively use the dynamic modulus as an analog failure criterion, especially for failure due to consolidation or compaction, but also potentially for other borehole failure mechanisms, including sanding and shallow water flow.

Differences between the moduli measured with dynamic and static methods in dry rocks were initially observed by Zisman (1933) and Ide (1936), who found that the dynamic bulk and Young's moduli are nearly always larger than the static moduli, based on measurements made in a series of crystalline rocks and limestones. They recognized that this difference is due to the presence of open pores or cracks in the rocks based on the fact that no difference is observed between the static and dynamic moduli of homogenous elastic materials (Ide, 1936) and that rocks open to the confining fluid demonstrate a larger static compressibility (Zisman, 1933). They also observed that the difference between the moduli decreased at higher pressures and was smaller in rocks with larger moduli. Similar observations have been made for a wide variety of rocks and sediments for the Young's modulus (Sutherland, 1963; Cannadey, 1964; King, 1970, 1983; Eissa and Kazi, 1988; Yale and Jamieson, 1994; Plona and Cook, 1995; Fjaer, 1999), for the bulk modulus (Birch, 1961; Simmons and Brace, 1965; Cheng and Johnston, 1981; Fjaer, 1999), and for the shear modulus (Jaime and Romo, 1988; Bolton and Wilson, 1989).

Walsh (1965a) conjectured that the lower static moduli were a result of the hysteretic behavior of cracks, which slide upon static loading, resulting in an effectively more compliant rock, but which do not slide back until the rock has been unloaded to a much lower stress. He predicted that the bulk modulus would not show this behavior because bulk loading would not produce sliding on cracks. Since the dynamic measurements are essentially just very small stress or strain cycles, they do not produce enough of an unloading to reactivate these cracks and so demonstrate a greater stiffness. This supposition was corroborated by Cook and Hodgson (1965), who demonstrated that the secant moduli measured on small strain loops that were reversals of larger strain loops demonstrated a higher modulus than that of the secant or tangent moduli of the large strain loop at the same pressure. Subsequent work by Hilbert et al. (1994) and Plona and Cook (1995) showed that the dynamic (high-frequency) moduli where equal to the static

(low-frequency) moduli measured at the same strain magnitudes. They concluded that the static-dynamic difference in dry rocks is a result of differences in the strain amplitude experienced by the rock, and not of the frequency at which the measurements are made.

A quantitative formalism to predict the stain-dependent moduli of elastic rocks was developed by McCall and Guyer (1994), based on the Preisach-Mayergoyz model of hysteretic crack behavior (Preisach, 1935; Mayergoyz, 1985). McCall and Guyer assumed that the rock is made up of a large number of mechanical units, analogous to cracks, each configured such that a given mechanical unit will close or slip at one pressure, P_C, but will not necessarily open or rebound to its initial length until it has been unloaded to a lower pressure, P_O. The discretized distribution of these cracks in P_C-P_O space can be represented by a lower triangular matrix, E_{ij}, with each element representing the proportion of cracks that will be closed at points on a loading path that has exceeded P_{Ci} but that has not returned below P_{Oj}. Since each crack is assumed to produce exactly the same amount of bulk strain on closure, a knowledge of this distribution will allow a prediction of the strains associated with any given loading path; the proportion of the cracks that are closed at a given point in the path, relative to all the cracks that would be closed at the maximum pressure, gives the proportion of the maximum strain that the rock will exhibit at that point. The dynamic modulus is predicted by the proportion of units for which the opening and closing pressures are equal to the current confining pressure, $P = P_C = P_O$, represented by the elements along the diagonal of the matrix. The difference between the static and dynamic moduli predicted by this analysis comes from the fact that while the dynamic modulus only activates that strain which demonstrates equal closing and opening pressures, the static strain for an increasing pressure step will activate all the strain that has that closing pressure and that is not already activated. Likewise, on an unloading step, all the strain that has the corresponding opening pressure and that is currently closed will be activated. At the first unloading step after a loading cycle, the only strain that is already closed is that which has a closing pressure equal to the opening pressure, so the static and dynamic moduli are equal at that point. The same is true for the first loading step after an unloading cycle, where the only strain still open that has that opening pressure is that with equal opening and closing pressures. The more hysteretic (off-diagonal) strain demonstrated by a sample, the greater the difference will

be between the static and dynamic moduli. Guyer et al. (1997) describe methods to invert for the distribution of mechanical units in P_C-P_O space using a variety of underdetermined methods. This analysis allows the distribution to be developed from the static tests and to then be used to predict the dynamic moduli.

This chapter will present an analysis of the relationship between the static and dynamic bulk moduli of unconsolidated sands, based on velocity and static strain measurements on a series of sand and glass bead samples over a number of pressure cycles. It will also discuss an adaptation of the analysis developed by Guyer et al. (1997) to include plastic deformation, which constitutes a significant proportion of the strain in unconsolidated sediments. It will then discuss the implications of these results for the prediction of the static bulk modulus from dynamic measurements and for the understanding of the grain-scale mechanics of unconsolidated sediments.

EXPERIMENTAL METHODOLOGY

The static volumetric strains and compressional- and shear-wave velocities of a set of four natural sand samples and one glass-bead sample were measured at pressures from 0 to 20 MPa. The sand samples consisted of two Holocene beach sands, the Galveston Beach (TX) and Pomponio Beach (CA) sands, a Holocene sand from the Gulf of Mexico seafloor, and a Pleistocene dune sand from Oakland (CA), the Merritt sand. In addition, measurements were made on a glass bead sample with grain diameters ranging from 295 to 350 mm. Index parameters for each of the samples are given in Table 6.1, while the sample mineralogies derived from X-ray diffraction analysis are given in Table 6.2. The grain-size distributions for each of the samples are shown in Figure 6.1. In general all of the sands are relatively clean, quartz sands, and all except the very fine-grained Gulf of Mexico sand are rather well sorted.

Table 6.1: Sample summary

	Sample	Initial Porosity	Mean Grain Size (mm)	No. of Cycles	Grain Density (g/mL)	C_U	C_C
Sands:	Galveston	0.399	0.134	3	2.660	1.31	1.10
	Gulf of Mexico	0.430	0.082	9	2.640	~3.3	~1.2
	Merritt	0.363	0.225	9	2.673	2.63	1.34
	Pomponio	0.428	0.378	3	2.727	1.55	1.01
Glass Beads:	GB Big	0.381	0.325	8	2.464	1.09	0.98

Table 6.2: X-ray diffraction results

Sample	XRD (% by weight)					
	Quartz	**Plagioclase**	**K-feldspar**	**Hornblende**	**Total Clay[1]**	**Other[2]**
Galveston	86	6	6	0	2	0
Gulf of Mexico	63	17	8	1	6	5
Merritt	59	18	7	5	11	-
Pomponio	53	29	12	1	2	3
GB Big	100[3]	-	-	-	-	-

[1] Includes micas - mostly muscovite or biotite. The Merritt Sand sample also has a fair amount of chlorite.
[2] Includes pyroxene, dolomite, calcite, and pyrite. The analysis was not conducted for these minerals for the Merritt Sand sample.
[3] Silica glass.
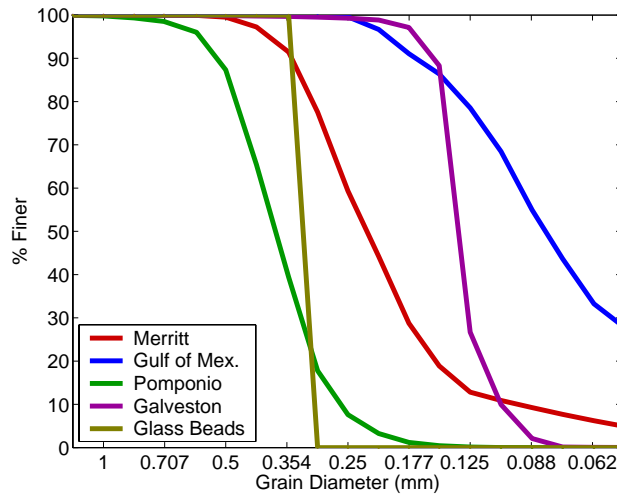
Figure 6.1: The particle size distributions for each of the samples, showing the percentage of the total mass that is finer than a given size.

The measurements were made on dry samples under isotropic loading conditions. The three Holocene sands and the glass bead sample were reconstituted from loose samples. They were prepared by raining the sand or glass beads into a Tygon sample jacket placed over the lower transducer of the sample holder. The Merritt sand sample was collected with a Shelby tube from a depth of about 5 m, cut into 10 cm lengths, dried at 65°C, hand cored, and trimmed to size to produce a sample that was minimally disturbed. It was then placed in a thin rubber jacket and put into the sample holder.

The samples were loaded hydrostatically by placing the sample holder into a pressure vessel and pumping hydraulic oil into the vessel. The samples were run through a series of up to nine pressure cycles of larger and larger peak pressures. A typical pressure path is shown in Figure 6.2. After each pressure step was applied, the samples were allowed to sit until the strain on the sample and the ultrasonic signals stabilized, at which point the volumetric stains and compressional- and shear-wave velocities were measured.
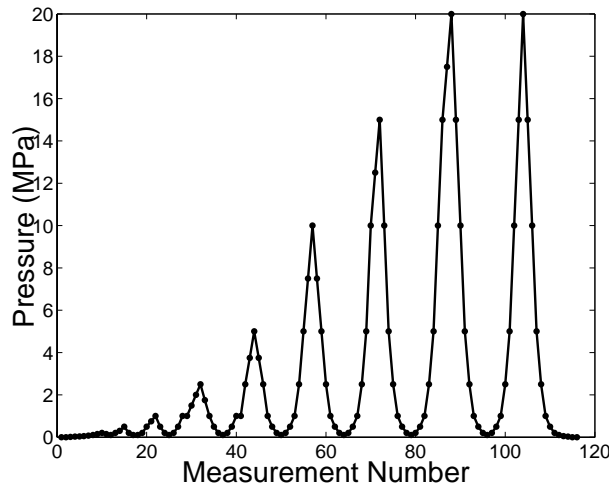
Figure 6.2: A typical pressure path for one of the samples. This sample, the Gulf of Mexico Sand, was cycled through 9 cycles of larger and larger peak pressures, up to 20 MPa. Velocity and volume measurements were made at each point.

The velocities were calculated by picking first arrivals from pulse-transmission signals. The velocity measurements are accurate to within approximately 2% for the compressional-wave velocities and 4% for the shear-wave velocities at pressures above 1 MPa, though larger errors were typical at lower pressures due to a lower signal-to-noise ratio and more ambiguity in picking the first arrival.

The volumetric strains of the samples were monitored at each pressure step using three independent axial stain gauges and one circumferential strain gauge. The volume calculation assumes that the outline of the sample between the transducers is parabolic, with the diameter at each end of the sample fixed at the diameter of the end caps, 3.81 cm (1.5 in.), and the diameter at the middle of the sample calculated from the initial circumference and the strain measured by the circumferential strain gauge. The volume, V, is then given by:

$$V = \pi l \left(\tfrac{1}{5}(1.905 - r)^2 + \tfrac{2}{3} r(1.905 - r) + r^2 \right), \tag{6.3}$$

where l is the sample length and r is the radius at the middle of the sample. The length, radial, and volumetric strains from one of the samples are shown in Figure 6.3. I applied corrections to the length strain to account for hysteresis in the strain gauges and for the compression of the end caps between the points of attachment of the strain gauges. As the spring in the circumferential gauge, which provides tension to keep the wire tight and the gauge in place around the sample, is apparently too strong, this gauge does not rebound

upon unloading. The measured radius is therefore constant over most of the unloading and reloading paths. Presumably the sample is still rebounding in the radial direction over the rest of the sample, but is constrained by the circumferential gauge at the middle. To correct for this lack of rebound, assumed to be an artifact of the gauge, the radial strain, ε_R, on the unloading and reloading paths is scaled with the length strain, ε_L, according to:

$$\varepsilon_R = \frac{\varepsilon_{RO}}{\varepsilon_{LO}} \varepsilon_L ,$$
(6.4)

where ε_{RO} is the radial strain at the last pressure step before unloading and ε_{LO} is the length strain at that same step. I also correct the radial strain for the compression of the sample jacket during loading. The resultant corrected radial and volumetric strains are shown in red in Figure 6.3.

A   **B**

C
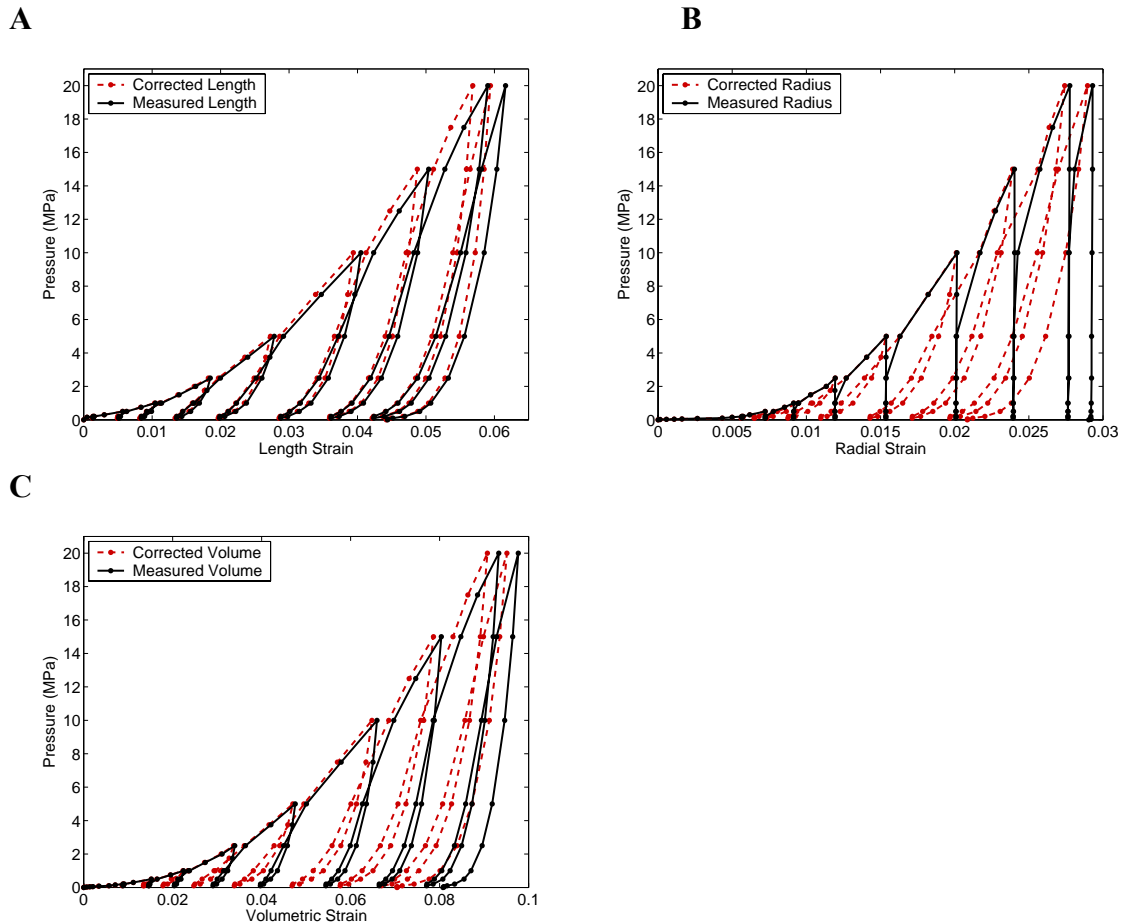
Figure 6.3: The strains measured for the Gulf of Mexico Sand sample, showing the measured strains and the strains once corrected for the hysteresis of the length strain gauges, the compression of the end caps and of the sample jacket, and the lack of rebound of the circumferential strain gauge: A) length strain, B) radial strain, and C) volumetric strain.

The static bulk moduli were calculated from the volume strain and pressure increment over each pair of consecutive measurement points, as in Equation 6.1. The dynamic moduli were calculated at each measurement point from the measured velocities, as in Equation 6.2, with the density being given by the initial mass of the sample divided by the volume at that point. An error analysis for the static moduli included errors in the change in length, due to the uncertainties from the hysteresis of the length strain gauges and from the length change in the transducers with pressure, as well as errors in the change in the radius, due to the uncertainties in the rebound correction and in corrections for the compression of the jacket. This analysis demonstrates very large relative errors (2σ), from 10 to 70% at pressure above 1 MPa, and in some cases even larger at pressures below 1 MPa. An error analysis for the dynamic moduli, which includes the uncertainty in the initial length measurements as well as in the length change measurements and in the travel time, demonstrates errors generally between 3 and 10%. The large uncertainty in the static moduli is in part a result of the small volume change measured for a given pressure step, and of the large uncertainties in the radial strain due to the lack of rebound of the circumferential gauge.

COMPARISON OF MEASURED STATIC AND DYNAMIC MODULI

Figures 6.4 through 6.8 compare the static and dynamic bulk moduli for each of the samples. The static moduli in part A of each figure are plotted against the mean of the two pressures between which the modulus is measured, while the dynamic moduli are plotted against the pressure at which the velocities are measured. To directly compare the static and dynamic moduli at the same pressure, parts B and C compare the dynamic modulus averaged between two measurement points with the static modulus measured over the same two points. The static modulus is plotted against the dynamic modulus in part B of each figure, while the ratio of the dynamic to static moduli is plotted against the average pressure of the two measurements points in part C.

The first-order observation is that for each of the samples the static bulk moduli of the initial loading, or normally consolidated, points are several times smaller than the dynamic bulk moduli. Upon unloading, the static modulus values approach or exceed the dynamic modulus on the first unloading step, and then drop back down below the dynamic modulus with continued unloading. As discussed in Chapters 3 and 4, the
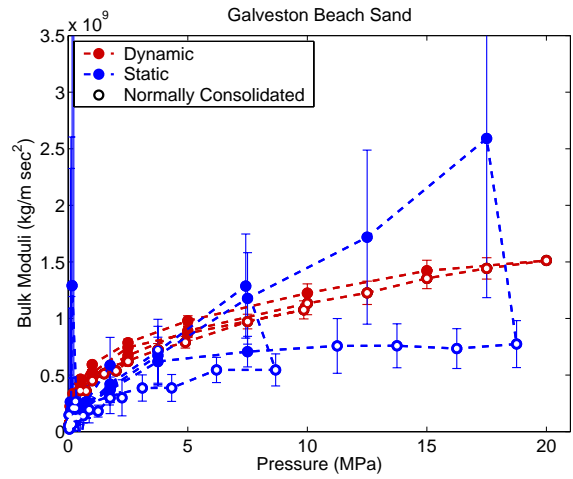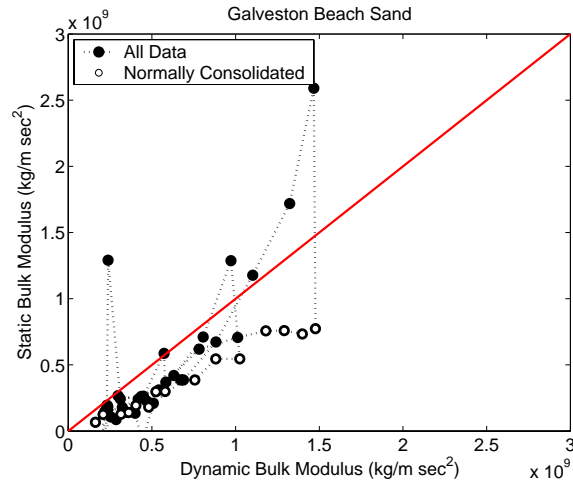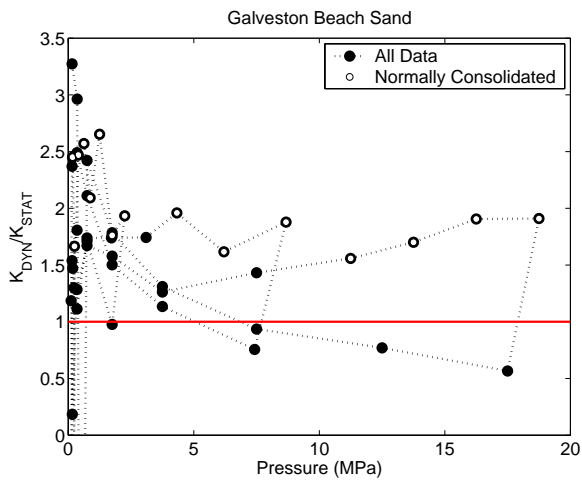
Figure 6.4: Comparisons of the static and dynamic moduli of the Galveston Beach sand sample: A) plots of moduli vs. pressure with error bars, B) plot of the static versus dynamic moduli, and C) plot of the ratio of the dynamic to static moduli vs. pressure.

114

A

B

C
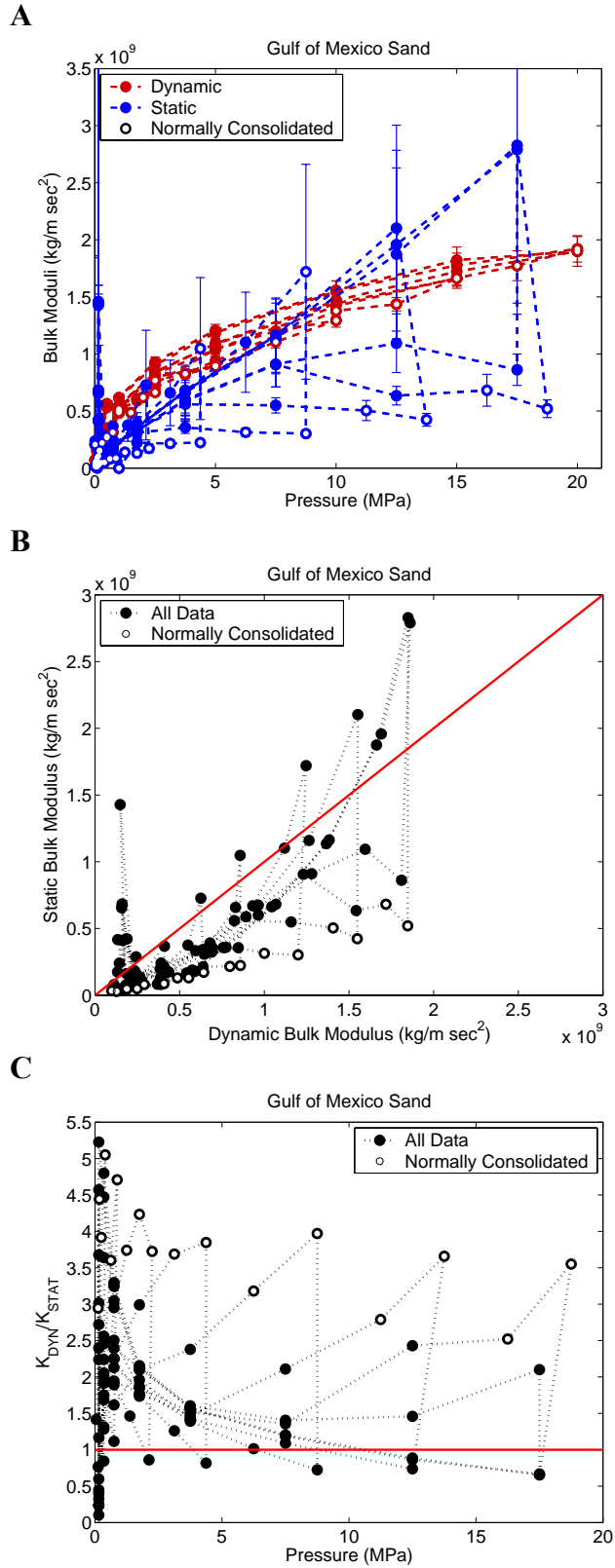
Figure 6.5: Comparisons of the static and dynamic moduli of the Gulf of Mexico sand sample: A) plots of moduli vs. pressure with error bars, B) plot of the static versus dynamic moduli, and C) plot of the ratio of the dynamic to static moduli vs. pressure.

A

B

C
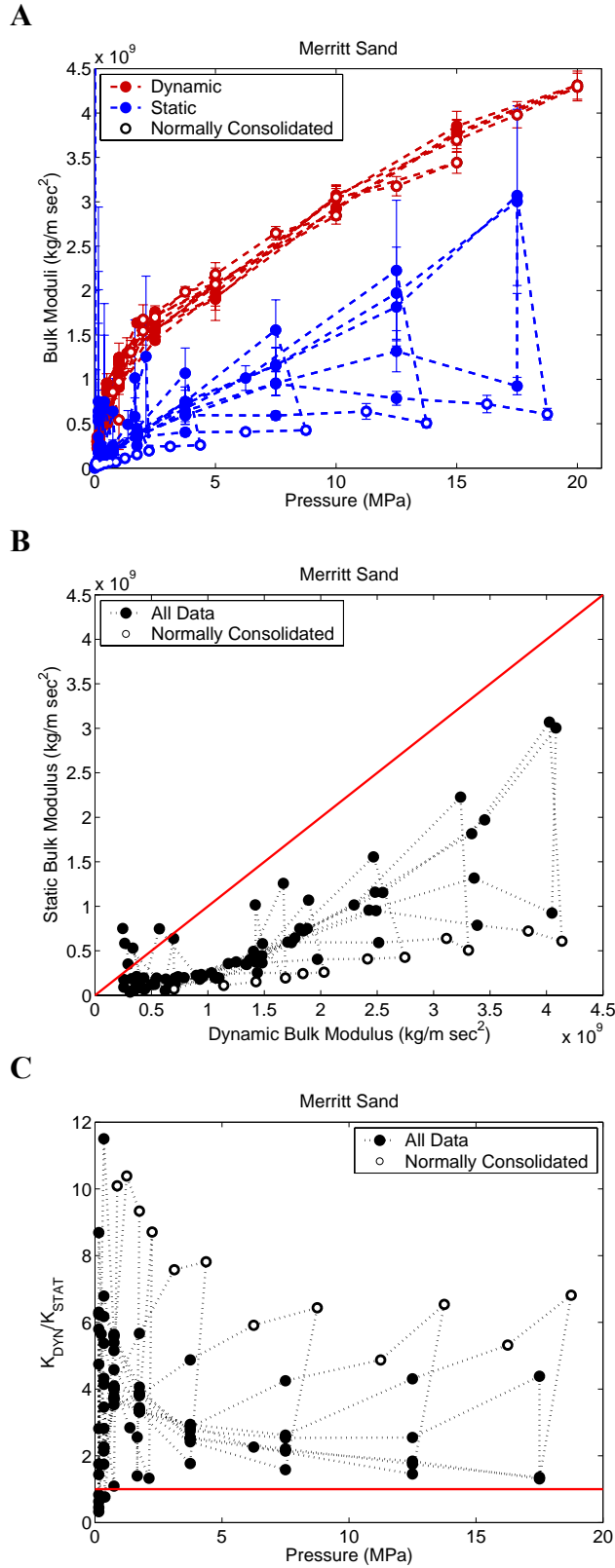
Figure 6.6: Comparisons of the static and dynamic moduli of the Merritt sand sample: A) plots of moduli vs. pressure with error bars, B) plot of the static versus dynamic moduli, and C) plot of the ratio of the dynamic to static moduli vs. pressure.

116

A

B

C
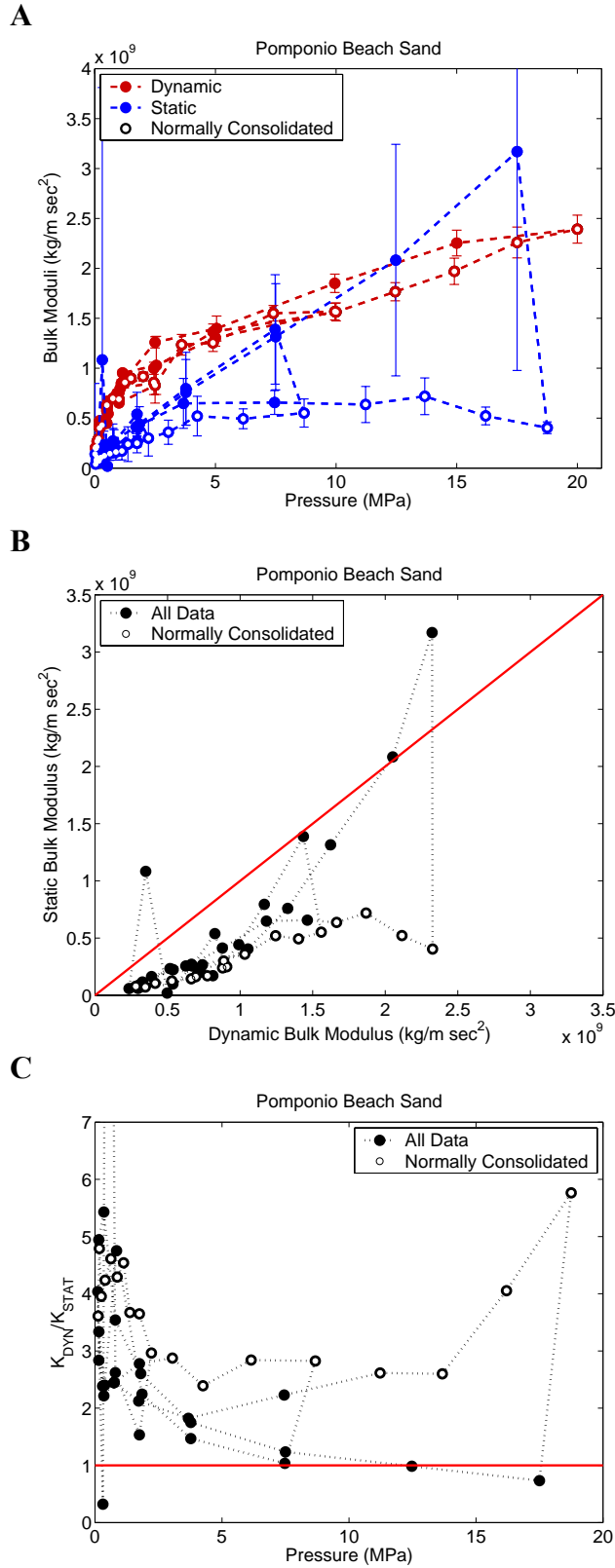
Figure 6.7: Comparisons of the static and dynamic moduli of the Pomponio Beach sand sample: A) plots of moduli vs. pressure with error bars, B) plot of the static versus dynamic moduli, and C) plot of the ratio of the dynamic to static moduli vs. pressure.

A

B

C
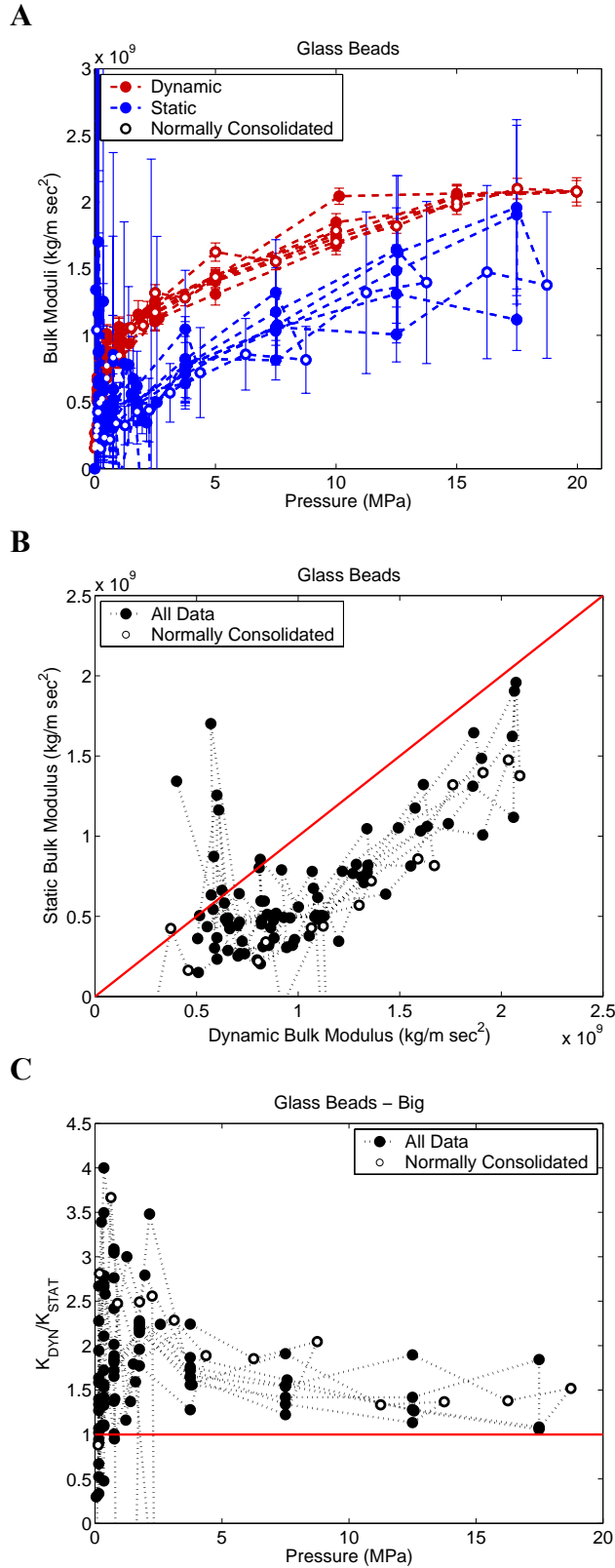
Figure 6.8: Comparisons of the static and dynamic moduli of the glass bead sample: A) plots of moduli vs. pressure with error bars, B) plot of the static versus dynamic moduli, and C) plot of the ratio of the dynamic to static moduli vs. pressure.

118

dynamic modulus increases only slightly with preconsolidation, so for a given pressure there is little difference between the values on the initial loading path and on the unloading or reloading paths. On the initial loading path, the dynamic modulus of the sand samples is between 2 and 10 times larger than the static modulus, while for the glass bead sample the ratio varies between 1.5 and 3. This ratio generally decreases with increasing effective pressure for each sample, though most of the change has occurred by a pressure of 2 or 3 MPa.

On the unloading paths, the first unloading step often demonstrates a larger static modulus than dynamic modulus, though the error bars in part A of Figures 6.4 through 6.8 extend below the dynamic modulus measured at the same pressure. The accuracy of the static modulus on that first unloading step is low, primarily because the volume change on that step is quite small, making it difficult to measure the volume strain accurately. In addition, the hysteresis in the strain measurement system, as well as the hysteresis that might result from friction of the sample jacket against the transducers or of the transducers against the support frame which is not taken into account in the error analysis, would have the largest effect at this point where the strain direction is reversing and the confining pressure is high. This implies that the values on the first unloading step are probably systematically overestimated and that, in reality, they are probably close to the values of the corresponding dynamic modulus at that pressure. However, the observation that the static modulus jumps significantly on unloading should be valid, as should the observation that with continued unloading the static modulus drops back below the dynamic modulus.

The greater scatter in the static moduli at low pressures is a result of larger inaccuracies in the volume measurements at the lower pressures. At these pressures the measurements were made over smaller pressure steps, and the hysteresis in the measurement apparatus was likely to have a larger influence on the measured volumes. In addition, at low pressures on the initial loading cycles, the strain that the sample experiences can depend on the length of time that it is allowed to sit after loading before the measurements are made, and might even show a volume loss on an unloading step if the sample is still very loose.

A

B

C

D
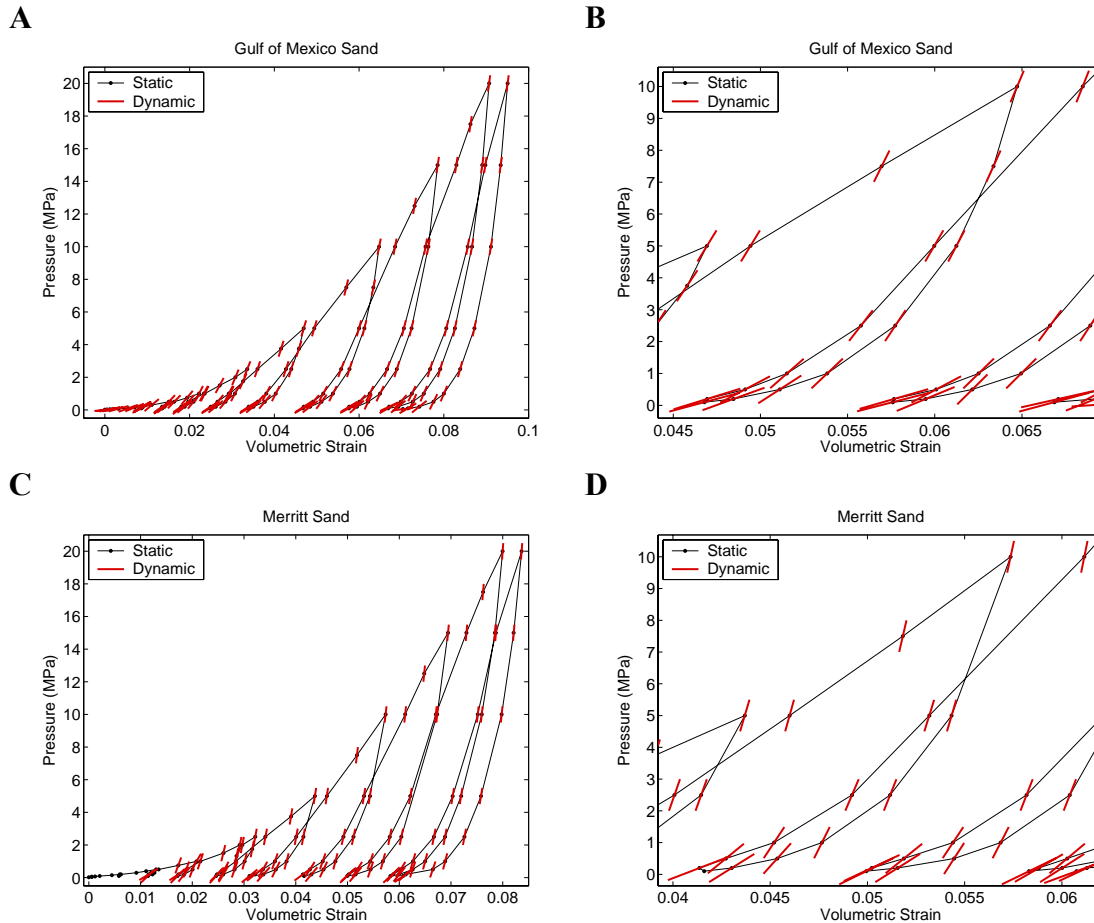
Figure 6.9: A comparison of static stress-strain path with stress-strain directions implied by the dynamic moduli for the Gulf of Mexico sand in A) and B), and for the Merritt sand, in C) and D).

The relative difference between the static and dynamic moduli is demonstrated in another fashion in Figure 6.9. It shows the volumetric stress-strain path for the Gulf of Mexico and Merritt sand samples with the black line, overlain by red lines indicating the slope of the stress-strain path implied by the dynamic bulk modulus measured at that point. The right hand panes show a closer view of one loading cycle for each sample. The dynamic stress-strain slopes are steeper than the static stress-strain path along the initial loading path, indicating a larger dynamic modulus than static modulus. On the first unloading step, the two paths are roughly parallel. With continued unloading, the static and dynamic moduli again diverge. On the first reloading step, however, the two stress-strain paths are again approximately parallel, while with continued unloading the dynamic modulus at a given pressure is very close to the dynamic modulus of the loading path at the same pressure.

PREISACH-MAYERGOYZ SPACE ANALYSIS

In an attempt to establish the relative influences of the elastic and plastic strain on the difference between the dynamic and static bulk moduli in unconsolidated sands, I adapted the Preisach-Mayergoyz space analysis of McCall and Guyer (1994) to account for the plastic strains as well as the elastic behavior. In this case, the closing of each mechanical unit was assumed to produce an identical increment of bulk strain, rather than sliding along a crack, at the corresponding closing or opening pressure. In addition to estimating the distribution of mechanical units over 100 kPa intervals of the opening and closing pressures in the elastic matrix, this analysis also estimated the relative number of mechanical units that close plastically at a given pressure on either the first or second loading cycle, and so do not re-open upon unloading. The first- and second-cycle plastic strains were each discretized at the same 100 kPa interval and were assigned to vectors with lengths equal to one dimension of the elastic strain matrix. The analysis assumed that all the plastic strain possible at a given pressure occurred by the second loading cycle to that pressure. While evidence for continued plastic strain on later cycles can be seen in the strain data, the amount of strain on later cycles was not constrained well enough to attempt to include it in the inversion.

Rather than assign an integer number of mechanical units to each element in the strain matrices, the total strain was divided into the elastic and plastic (1st and 2nd cycle) strains, and distributed throughout the elements of the elastic strain matrix and plastic strain vectors. The inversion for the distribution of the strain in the elastic matrix and the two plastic strain vectors was then performed following a procedure similar in concept to the exponential decay method presented by Guyer et al. (1997). Instead of using an exponential decay away from the diagonal of the elastic matrix, the sums of the rows of the elastic matrix, or the total strain associated with a given 100 kPa opening pressure range, were calculated from an interpolation of the last downward half-cycles. The distribution of the strain along each row (over the closing pressures) and of the plastic strain over the corresponding closing pressures was then based on a power-law relationship that was empirically derived to fit the measured static moduli. The analysis was performed according to the following steps:

Proportions of plastic and elastic strain: The first step in the analysis was to calculate the proportions of plastic and elastic strain relative to the maximum strain observed in the sample, as demonstrated in Figure 6.10. The plastic strain (red line) is equal to the portion of the maximum strain that is not recovered upon final unloading, with the remainder of the total strain being recoverable, elastic strain (blue line). The plastic strain on reloading to a given pressure for the second time (green lines in Figure 6.10) was summed over all the cycles and treated separately from the plastic strain from the first loading cycle. The relative proportions of the total strain that were made up by the elastic, plastic, and first- and second-cycle plastic strains are given in Table 6.3. The absolute values of each type of strain are given in Table 6.4.
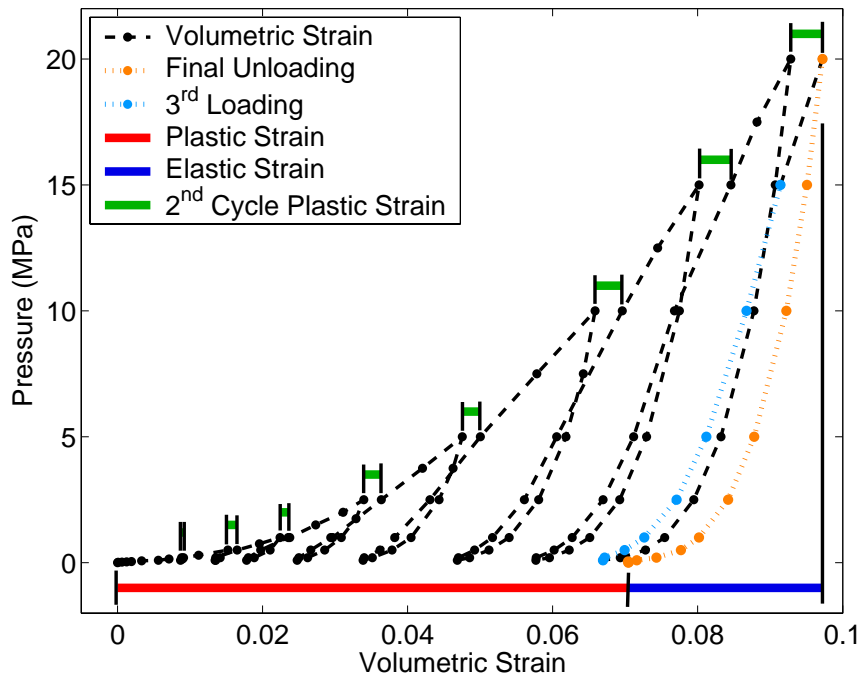
Figure 6.10: Illustration of the division of the maximum strain into elastic strain and first and second cycle plastic strains for a typical sample.

Table 6.3: Proportions of strain types

Sample:	Elastic Strains			Plastic Strains		
	Total	**Diagonal**	**Hysteretic**	**Total**	**1st Cycle**	**2nd Cycle**
Galveston	0.483	0.203 ± 0.015	0.280 ± 0.015	0.517	0.427	0.090
Gulf of Mexico	0.260	0.113 ± 0.003	0.146 ± 0.003	0.740	0.529	0.211
Merritt	0.298	0.128 ± 0.006	0.170 ± 0.062	0.702	0.466	0.236
Pomponio	0.439	0.193 ± 0.016	0.246 ± 0.016	0.561	0.463	0.098
GB Big	0.674	0.334 ± 0.014	0.340 ± 0.014	0.326	0.129	0.197
Average:	0.431	0.194	0.237	0.569	0.403	0.167
Standard Dev.:	0.165	0.087	0.080	0.165	0.157	0.068

Table 6.4: Absolute amounts of each strain type

Sample:	Elastic Strains			Plastic Strains			Maximum Strain
	Total	Diagonal	Hysteretic	Total	1st Cycle	2nd Cycle	(at 20 MPa)
Galveston	0.0227	0.00956 ± 0.00072	0.01315 ± 0.00072	0.0243	0.0201	0.0043	0.0470
Gulf of Mexico	0.0247	0.01079 ± 0.00025	0.01391 ± 0.00025	0.0704	0.0503	0.0201	0.0951
Merritt	0.0249	0.01069 ± 0.00051	0.01424 ± 0.00051	0.0587	0.0390	0.0197	0.0837
Pomponio	0.0229	0.01003 ± 0.00082	0.01284 ± 0.00082	0.0292	0.0241	0.0051	0.0521
GB Big	0.0203	0.01006 ± 0.00042	0.01027 ± 0.00042	0.0098	0.0039	0.0060	0.0302
Average:	0.0231	0.01023	0.01288	0.0385	0.0275	0.0110	0.0616
Std. Dev.:	0.0019	0.00051	0.00157	0.0252	0.0179	0.0081	0.0269

Elastic strain distribution in P-M space: The elastic strain behavior is described by a lower triangular matrix, with each element, E_{ij}, representing the portion of the maximum strain that occurs elastically at the closing pressure P_{Ci} corresponding to that row in the matrix, and that rebounds elastically at the opening pressure P_{Oj} associated with its column. Discretization in 100 kPa steps over the pressure range of the experiments from 0 to 20 MPa resulted in a 200 by 200 element matrix.

The elastic portion of the total strain was distributed over the opening pressures, P_O, based on the final unloading part of the last cycle (the orange section in Figure 6.10). As the unloading path represents completely elastic strains, the strain that is recovered over each 100 kPa interval represents all of the elastic rebound at that opening pressure, or the sum of all the strain in that column of the elastic strain matrix. Since strain measurements were not made at each 100 kPa interval, a piecewise cubic Hermite interpolation was applied to each half-cycle of the strain path (Figure 6.11A), from which the column sums can be deterministically calculated by subtracting the volumetric strain between two adjacent interpolation points. The resulting relative proportions of the total strain corresponding to each opening pressure from the Gulf of Mexico sand sample are plotted against the opening pressures in a log-log plot in Figure 6.11B.

The sum of each row of the elastic matrix, or all of the strain that occurs elastically at a given closing pressure, P_C, can be calculated from the strains measured on loading in the absence of plastic strain. By assuming that the majority of the elastic strain takes place during the first two loading cycles to a given pressure, the strains over 100 kPa increments were calculated from the interpolated strain data from the portion of the last

123

cycle that had already been loaded to that pressure at least twice (shown by the light blue line in Figure 6.10). The relative incremental strains calculated from this portion of the strain path for the Gulf of Mexico sand are plotted as the black points in Figure 6.11C. Since the sample had not been loaded above 15 MPa more than twice, the data does not cover the entire pressure range. On most of the other samples, an even smaller pressure range had been loaded at least this many times. In addition, as a result of the interpolation and of the presence of additional plastic strain occurring on later cycles, the amount of strain per increment of loading pressure is rather erratic at the higher pressures.

A

B

C
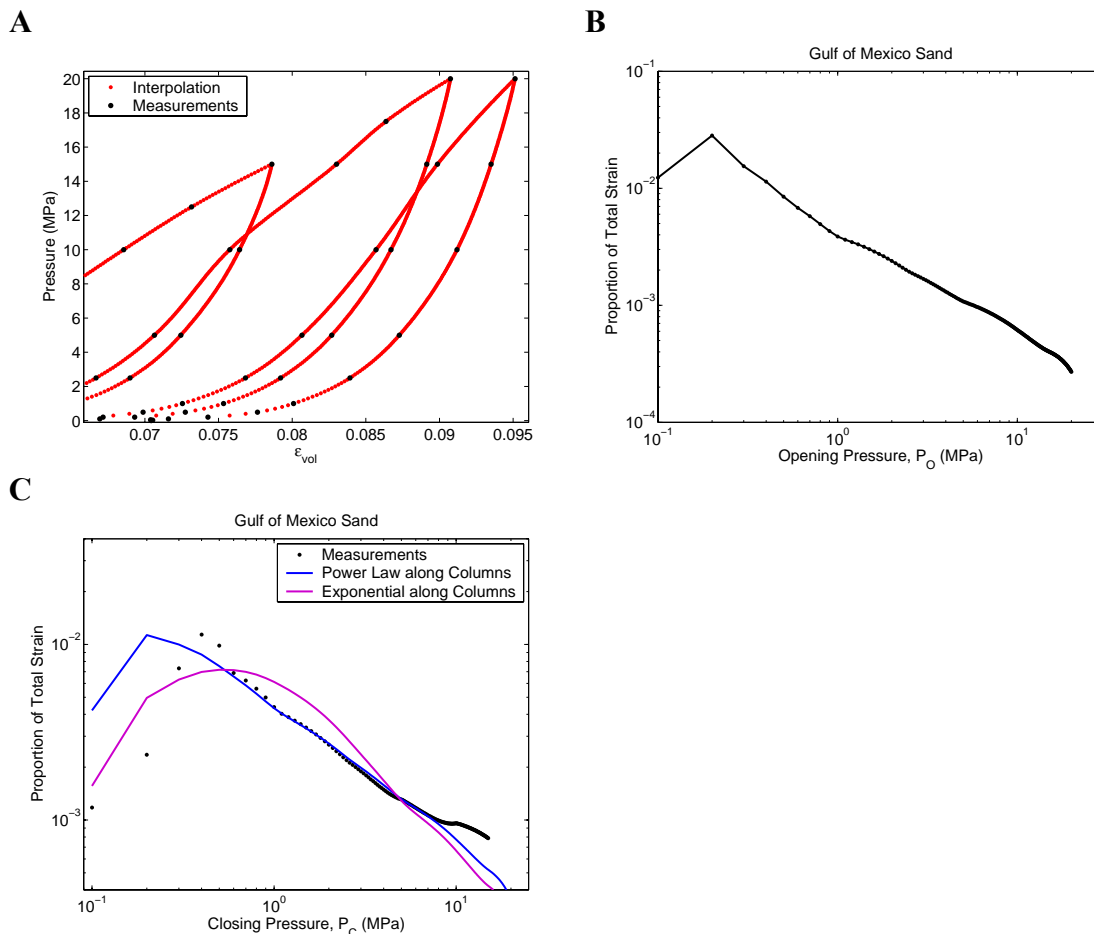
Figure 6.11: For the Gulf of Mexico sample: A) interpolation of the strain data used to calculate the distribution of strain at each 100 kPa increment of the opening pressure; B) the resultant strain distribution at each opening pressure increment plotted against pressure; and C) the distribution of strains at 100 kPa increments of the closing pressure derived from the thrice loaded portion of the strain path, compared to row sums of the elastic matrix with power law and exponential distributions along the columns. The power-law form demonstrates a better fit.

To distribute the strains throughout the elastic strain matrix, I attempted variations of two of the solution methods proposed by Guyer et al. (1997): simulated annealing and exponential decay. The incorporation of the plastic strains in the analysis required many more computations in the simulated annealing analysis. Likewise, the data was relatively sparse, especially at the larger pressures where pressure steps were as large as 2.5 MPa, limiting the real resolution of the resulting strain distributions. Therefore, a simulated annealing approach was not feasible. Instead, the strains were distributed in the elastic matrix using an approach similar in principle to the exponential decay method of Guyer et al. (1997). Their exponential decay method assumes that the density of off-diagonal mechanical units in the elastic strain matrix decreases exponentially away from the diagonal, and uses the known column and row sums to constrain the exponential coefficients. Since the values of the row sums in my analysis did not cover the whole pressure range and were not entirely reliable at the higher pressures, I modified this distribution method so that it only directly used the column sums. It then assumed a power law distribution along each column of the form:

$$E_{ij} = \left(\sum_i E_{ij} \right) \frac{P_{Ci}^{-r}}{\sum_i P_{Ci}^{-r}} , \qquad (6.5)$$

where E_{ij} is the proportion of elastic strain in element ij, corresponding to closing pressure P_{Ci} and opening pressure P_{Oj}, $\sum_i E_{ij}$ is the column sum, and r is a fit parameter that was kept constant for all the columns for a given sample. The power law of the pressure was normalized to maintain the sum of the column. A power law form was used since it provided a better fit between the P_C data and the row sums than did an exponential form (Figure 6.11C).

The distributions in each of the plastic strain vectors were created using similar forms:

$$\kappa_{1i} = \varepsilon_{pl1} \frac{P_{Ci}^{-s}}{\sum_i P_{Ci}^{-s}} , \quad \kappa_{2i} = \varepsilon_{pl2} \frac{P_{Ci}^{-t}}{\sum_i P_{Ci}^{-t}} , \qquad (6.6)$$

where κ_{1i} is the proportion of first-cycle plastic strain in element i, corresponding to closing pressure P_{Ci}, ε_{pl1} is the plastic portion of the total strain, and s is the fit parameter,

with κ_{2i}, ε_{pl2}, and t being the corresponding values for the second cycle strain. Each of the fit parameters was optimized by a largely manual grid search based on a comparison of the measured strains to the strains predicted with variations of the three parameters. The r parameter was chosen to match the amount of hysteresis in the unloading-reloading curves, while the s parameter was chosen primarily based on comparisons of the measured and predicted strains on the initial loading path. The t parameter was chosen to match the differences between the normally consolidated strains and the strains after a second loading cycle, the gap between the first and second cycles to a given pressure. The selected values of each of these parameters, and the ranges of the parameters that produced acceptable fits, are given in Table 6.5. The range of the r parameter was then used to calculate the potential variation in the division of the elastic strain into diagonal and hysteretic strains given in Tables 6.3 and 6.4. The selection of these parameters may have been made more rigorous by developing a more objective, automated fitting protocol, but the simple minimization of the square of the difference between the predicted and measured strains produced obviously inappropriate results.

The drawback of this method for distributing the stains is that it forces a given form for the distribution along each column and within the two plastic strain vectors, preventing the solution from demonstrating structure in the P-M space that might be significant. Given the sparsity of the strain measurements the analysis could not have resolved this structure. Likewise, to analyze the causes for the difference in the static and dynamic bulk moduli, this approach is adequate.

Table 6.5: Fit coefficients from the adapted Preisach-Mayergoyz analysis.

Sample:	r	s	t
Galveston	1.30 ± 0.06	0.50 ± 0.04	0.55 ± 0.05
Gulf of Mexico	1.37 ± 0.02	0.66 ± 0.02	0.19 ± 0.03
Merritt	1.36 ± 0.04	0.68 ± 0.03	0.35 ± 0.05
Pomponio	1.37 ± 0.07	0.05 ± 0.04	0.28 ± 0.07
GB Big	1.36 ± 0.04	0.92 ± 0.04	0.42 ± 0.08
Average:	1.352	0.562	0.358
Std. Dev.:	0.029	0.323	0.137

Resulting P-M space: The results of our modified analysis for each of the samples are shown in Figure 6.12, showing a comparison of the measured and modeled strains (column A), the distribution of the elastic matrix (column B), and the distributions of the plastics strains (column C). The P-M modeling generally produces a good match to the measured strains, though more in overall form than in matching all the details of the

stress-strain path. Much of the misfit would be removed with a less constrained inversion method for the strain distributions, such as the simulated annealing method described by Guyer et al. (1997), but would require a denser sampling of the volumetric deformation, with sampling at least as great as the discretization desired for the strain matrices. On the other hand, a portion of the misfit is due to deformation behavior characteristic of unconsolidated sediments, including continued plastic deformation on later loading cycles, as well as continued strain with time at a given pressure step. A more careful experiment and a more elaborate analysis might be designed to take into account these factors, but that is beyond the scope of the present work.

The elastic strain distributions produced through this analysis are all relatively similar. This is demonstrated by the similarity in the elastic strain matrices, in the choices of the *r* parameter (Table 6.5), and in the amounts of diagonal and hysteretic strain (Table 6.4). For each sample, nearly all of the elastic strain lies along the diagonal or at low opening pressures (note log color scale). The concentration of the elastic strain at low opening pressures comes directly from the shape of the strain path on the last unloading cycle, which demonstrates the greatest strains at the lowest pressures (again, note the log scale in Figure 6.11B). The amount of strain concentrated along the diagonal is a function of the *r* parameter, which is chosen to match the openness of the unloading-reloading paths. While the proportion of the elastic strain that is hysteretic is generally a little more than 50% of the total elastic strain (see Tables 6.3 and 6.4), in truth most of this strain still lies very close to the diagonal.

There is much more variability in the distributions of the plastic strains. In general, more of the plastic strain occurs at lower pressures, and there is more strain in the first cycle than in the second. Beyond these similarities there is a great deal of variation in the *s* and *t* parameters that determine these distributions. This variation is probably in part because the analysis does not capture plastic strain that occurs on repeated cycling or occurs with longer hold times at different pressure steps, features which cannot be captured with such a simple model. In addition, in some of the samples there appears to be some strain softening at high pressures (e.g. the Pomponio sand in Figure 6.12A), possibly due to the onset of grain breaking, which again cannot be captured in the current analysis which constrains the plastic strain vectors to continuous power-law trends.

127
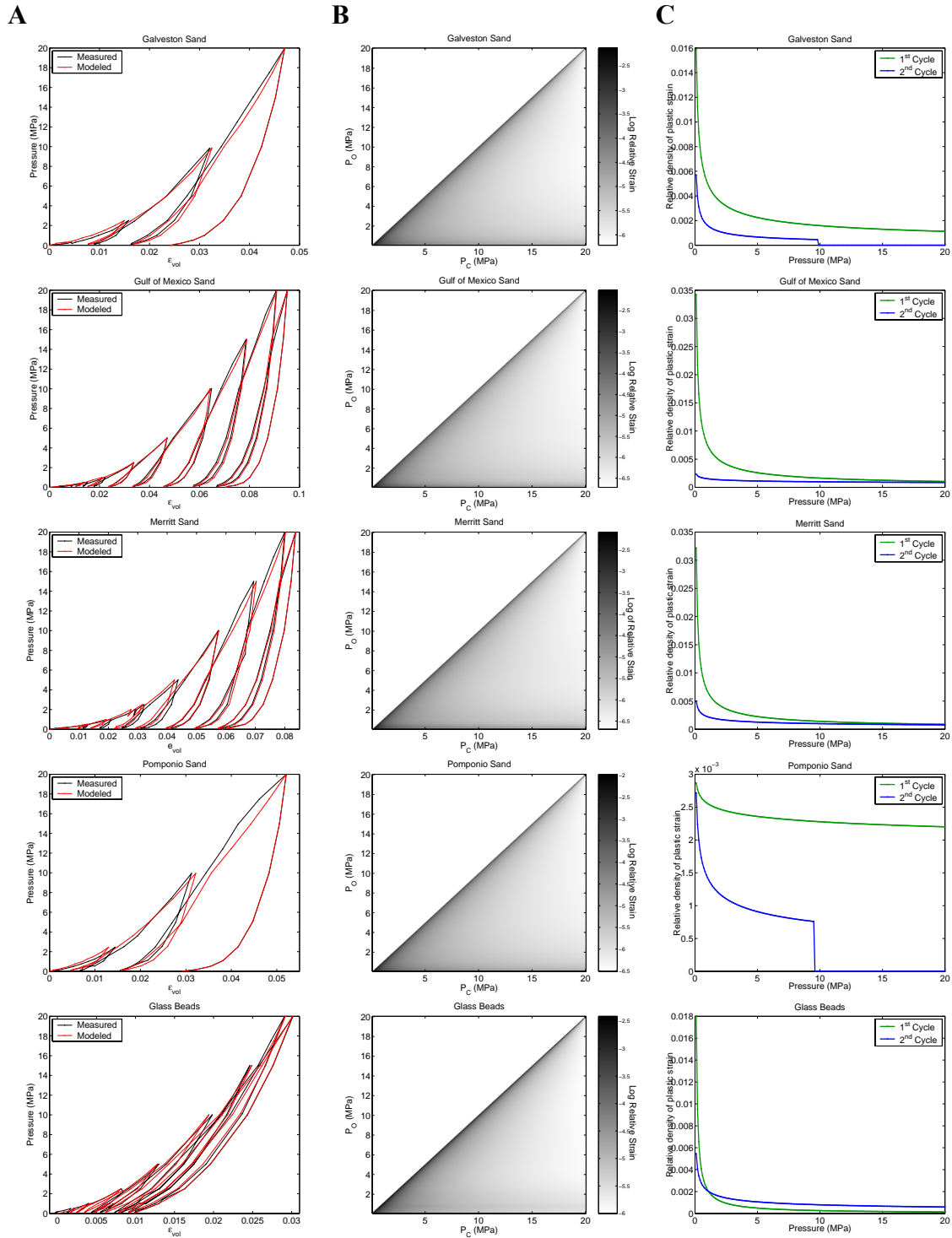
Figure 6.12: P-M space analysis results for each of the samples: A) comparison of measured and modeled strains, B) the elastic strain matrix, and C) the plastic strain vectors.

Comparison of predicted and measured moduli: Figure 6.13 shows a comparison of the static bulk moduli produced from the Preisach-Mayergoyz space analysis to the measured static moduli for each of the samples. As expected, given that the P-M space is inverted from the static behavior, the P-M space static moduli faithfully reproduce the general behavior and the magnitudes of the measured static moduli over the various pressure cycles, with some smoothing of the values between the various cycles. As for the measured data, the P-M predicted static moduli are low on the normally consolidated path, then jump dramatically on unloading to equal the P-M dynamic moduli, before dropping back off again with continued unloading.

The P-M space analysis allows the prediction of the dynamic bulk modulus, K_{di}, at pressure P_i, from the strain on the diagonal of the elastic strain matrix, $E_{ij}|_{i=j}$, according to the following relation:

$$K_{di} = \frac{dP}{E_{ij}\big|_{i=j}}, \tag{6.7}$$

where dP is the magnitude of the pressure increment, 100 kPa in this analysis. Figure 6.14 shows the dynamic moduli calculated from the measured velocities and density, compared to the dynamic moduli predicted from the P-M space analysis for each of the samples. The P-M space predictions do generally demonstrate shapes similar to the dynamic moduli, and are very similar in shape and in magnitude from sample to sample among the sands. Nevertheless, Figure 6.14 demonstrates that, with the exception of the Merritt sand, the P-M analysis significantly over-predicts the dynamic modulus of each sample.

To compare the relative effects of the elastic and plastic strains on the relationship between the static and dynamic moduli, the static moduli were calculated using both the elastic and plastic strains (blue points in Figure 6.15) as usual, and also using only the elastic strain matrix to calculate the stress-strain path while setting the plastic strains to zero (green points). Both moduli were calculated at 100 kPa pressure increments over the same pressure paths as in the actual experiments. In the case where the static moduli are reconstructed from only the elastic strain matrix, the moduli on the normally consolidated path are significantly larger than for the full strain case, so there is a smaller, but still noticeable, jump in the moduli upon unloading. The moduli predicted for the full and

elastic-only cases are identical on the unloading paths, where all of the strain is elastic. The plots of the dynamic to static modulus ratio, shown in the right hand frames of Figure 6.15, demonstrate that there is a much greater similarity between the ratios on both the normally consolidated and unloading paths for the elastic strain case than for the full strain case. Nevertheless, in both cases on the initial loading path the ratio of the dynamic to static modulus is greater than one at low pressures, and drops gradually, approaching one in the elastic-only case, and jumping to one only on unloading in the full strain case.

DISCUSSION

The over-prediction of the dynamic modulus produced by the P-M space analysis (Figure 6.14) for all of the samples except the Merritt sand is most likely a result of inaccuracies in the static measurements. The influence of this inaccuracy in the static strain measurements (~3%) on the accuracy of the analysis is similar to its influence on the accuracy of the measured static moduli, demonstrated by the large error bars in Figures 6.4 through 6.8A. Since the distribution of the strain between plastic and elastic is quite robust, this misfit essentially comes from too much of the strain being spread off the diagonal and too much of it being assigned to low opening pressures. Other possible reasons for the incorrect distribution of the elastic strain could include unaccounted-for hysteresis in the experimental apparatus and the constraint of the distributions to power-law forms. With a more accurate set of strain measurements and a finer sampling of the strain over the load path, these errors could be reduced, and the analysis might be found to produce accurate predictions of the dynamic moduli. Alternatively, the discrepancy might represent a real phenomenon: either that the dynamic modulus measurement activates more of the elastic strain than just that on the diagonal (effectively causes a greater stress variation than 100 kPa) or that the dynamic modulus measurement continues to produce minor amounts of plastic strain, resulting in a lower measured modulus.
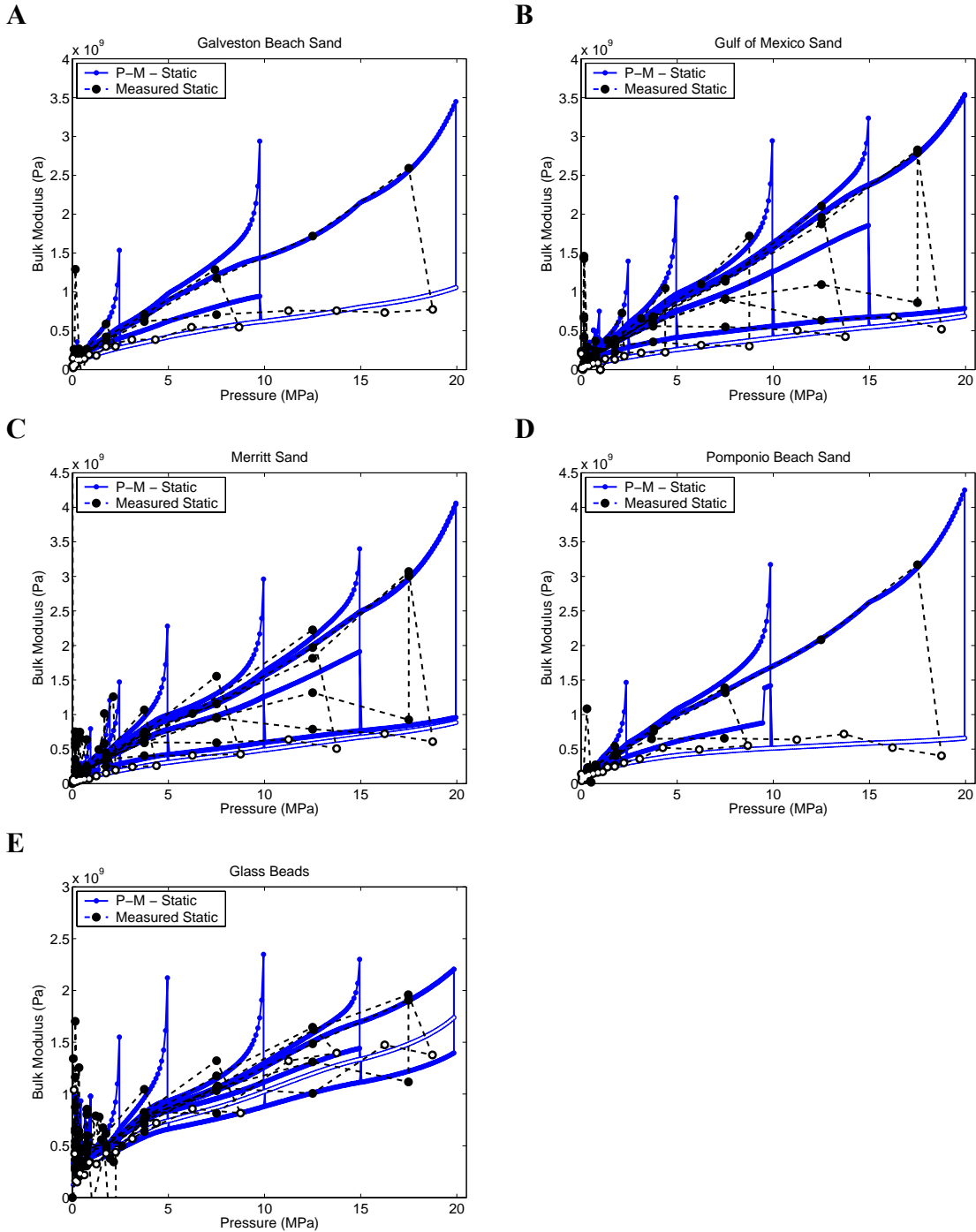
Figure 6.13: Comparison of the static moduli predicted from P-M analysis to the measured static bulk modulus for each of the samples: A) Galveston Beach sand, B) Gulf of Mexico sand, C) Merritt sand, D) Pomponio sand, and E) glass beads. The points on the normally consolidated portion of the pressure path are marked with white centers.
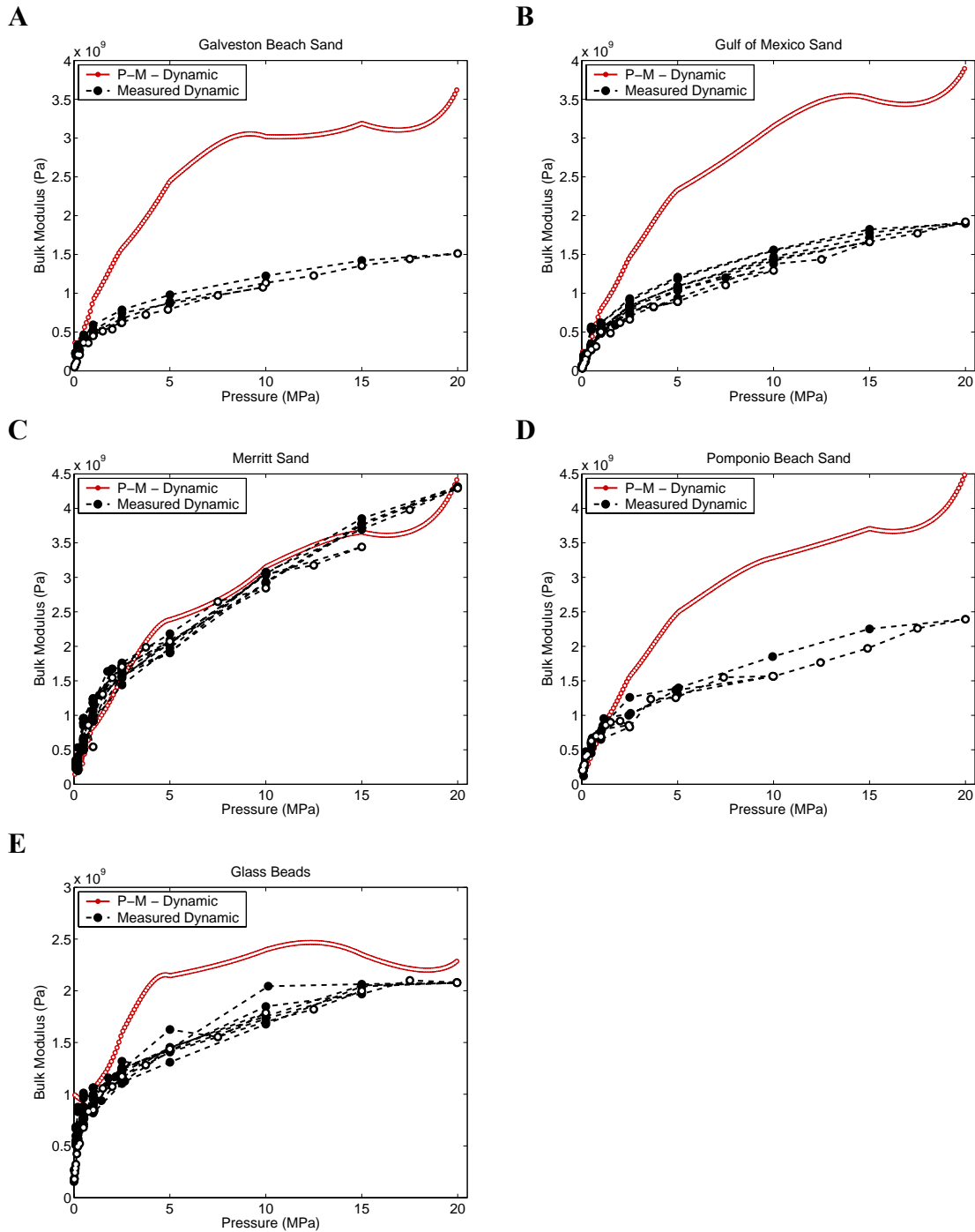
Figure 6.14: Comparison of dynamic moduli predicted from P-M analysis to measured dynamic moduli for each of the samples: A) Galveston Beach sand, B) Gulf of Mexico sand, C) Merritt sand, D) Pomponio sand, and E) glass beads. The points on the normally consolidated portion of the pressure path are marked with white centers.
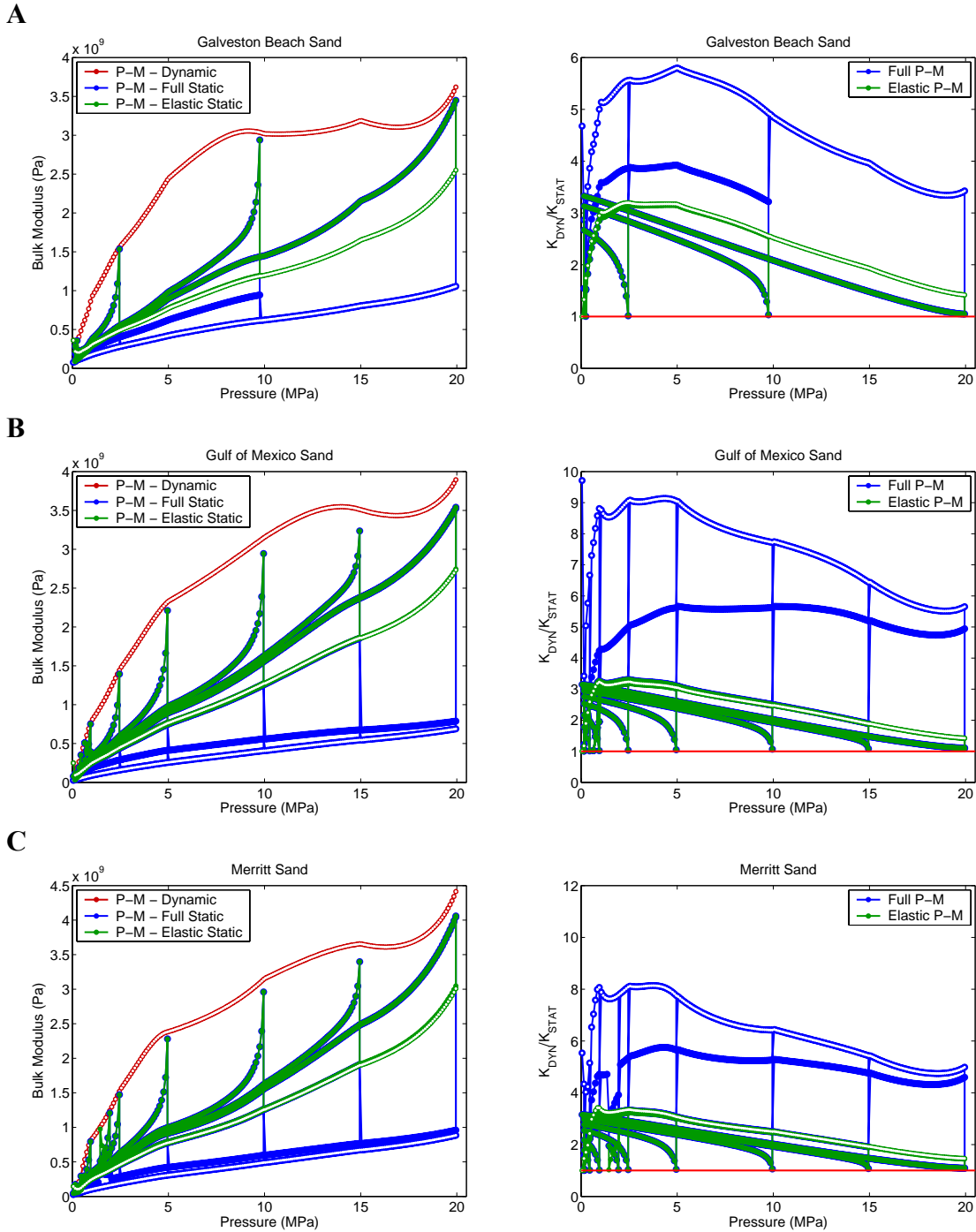
Figure 6.15: Comparison of the P-M space static and dynamic moduli for each of the samples: A) Galveston Beach sand, B) Gulf of Mexico sand, C) Merritt sand, and, on the next page, D) Pomponio Beach sand, and E) the glass bead sample The left hand panel shows the static and dynamic moduli plotted against pressure, while the right hand panel shows the ratio of the dynamic to static modulus, also plotted against pressure. The points on a normally consolidated portion of the pressure path are marked with white centers.

D
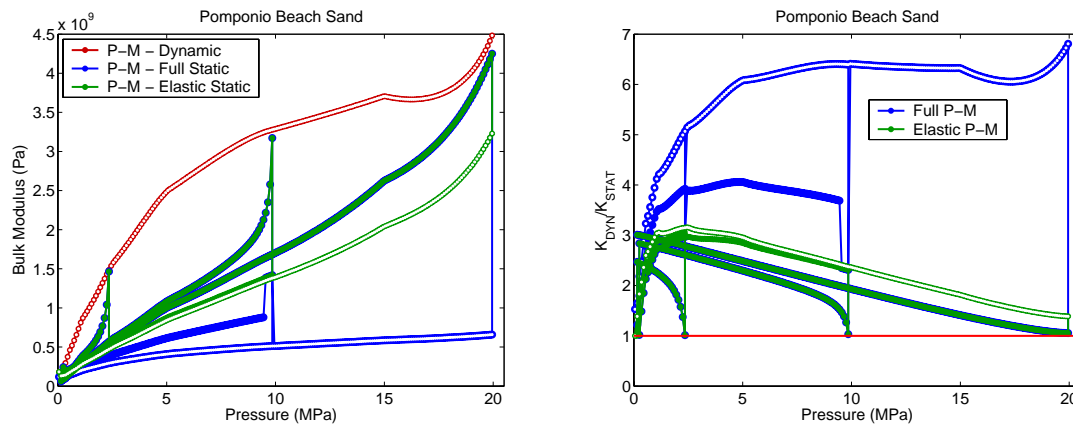
E
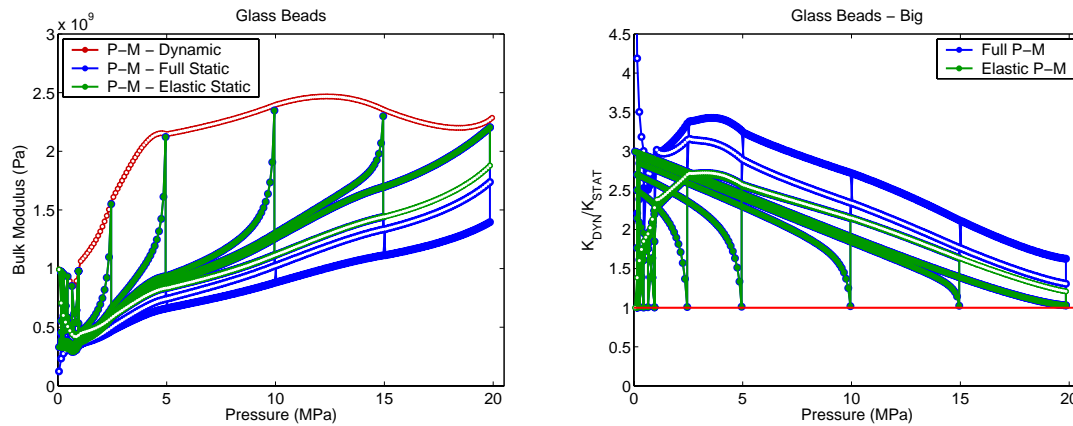
Figure 6.15: cont.

An additional weakness of this analysis is that it does not incorporate changes in the dynamic moduli with compaction. In reality, the elastic matrix would change as plastic deformation occurs, though the relatively small changes in the dynamic modulus with continued compaction indicate that these changes would be rather small. Since the elastic matrix is being developed largely based on the elastic behavior demonstrated by the last loading cycle, it is in essence a snapshot of the elastic behavior at the end of the loading regime of the experiment. At earlier stages, when the dynamic moduli are generally slightly lower, slightly more of the elastic strain lies on the diagonal of the elastic matrix (a higher *r* value).

Relative strain amounts: plastic, immediate elastic, and hysteretic

The general principle of the P-M space analysis is that the sample contains a number of mechanical units that close or compact at a given pressure and reopen or expand at a lower or equal pressure. I have expanded this analysis to include plastic strains, implying

that, once closed, those mechanical units do not reopen or re-expand at all. The fact that this expanded analysis can produce a reasonable reconstruction of the stress-strain paths and static moduli of our samples indicates that the general model can be useful for describing the stress-strain behavior of unconsolidated materials. In this case the deformation of a mechanical unit is more general than the analogy to crack sliding invoked by McCall and Guyer (1994). The deformation can represent any process that results in a bulk strain of the sample. For our unconsolidated sand samples, most of the plastic stain is likely due to the rearrangement of the sand grains, requiring them to slide or roll past each other as the sample is loaded.

The immediate elastic strain, found on the diagonal of the elastic strain matrix, is most likely due primarily to compression at the grain-to-grain contacts and small associated grain movements. This is demonstrated by the similarity between the Hertz-Mindlin effective-medium theory prediction of the bulk modulus and the measured dynamic bulk modulus for most of the samples (Figure 6.16, see also Chapter 3). The Hertz-Mindlin effective-medium theory predicts the elastic moduli based on deformation at the contacts, assuming no grain rearrangement or sliding at the grain contacts (Mavko et al., 1998, Chapter 3). For isotropic compression of a random grain packing of identically sized spheres, the bulk modulus is a function of the normal contact stiffness of a typical contact, the porosity, and the average number of contacts that a grain has with surrounding grains. The close fit between this model and the measured data indicates that compression at grain contacts can explain nearly all of the strain contributing to the dynamic bulk modulus, without any need to invoke significant sliding at the contacts.

The hysteretic elastic strain is more likely associated with sliding at grain contacts that is recovered by further sliding on unloading. As the grain framework changes with the plastic strain, the recovery of hysteretic elastic strain does not necessarily imply sliding at the same contacts that produced the strain on loading, nor a complete return to the original framework configuration. In essence this hysteretic strain involves the same mechanisms as the plastic strain, but describes that portion of this strain that is recovered on unloading through the same grain rearrangement mechanisms. The hysteretic elastic strain will also incorporate any hysteresis in the apparatus that was not corrected for,

which probably causes the analysis to predict slightly larger hysteretic strains than really occur in the sample.

A comparison of the various amounts of each type of strain in the samples (Table 6.4) reveals that the amount of elastic strain and its division between hysteretic and immediate strains is very similar for all of the samples. On the contrary, the amount of plastic strain varies dramatically from sample to sample, with the Gulf of Mexico sand demonstrating the most plastic strain and the glass bead sample the least. The plastic behavior loosely corresponds to the clay content of the samples, as the Merritt sand and Gulf of Mexico sands, which are the most clay rich at 11% and 6% respectively, show much more plastic strain than the completely clay-free glass bead sample. The large variation in plastic strain behavior might also be in part due to textural differences between the samples, including their particle size distributions, as well as the loading path that they underwent; of the sands, the Gulf of Mexico and Merritt sands were also put through the greatest number of loading cycles. Since, despite these differences in the samples and in their plastic strain behavior, the elastic behavior is all samples are very similar, we might expect similar elastic strain behavior from most unconsolidated or poorly consolidated granular media with low clay contents. The verification of this supposition would require the collection of a larger dataset than just that of the four sand samples presented here. Likewise, while the static elastic behavior of the various samples is all very similar, our measurements indicate significant differences in the dynamic behavior, especially in the Merritt sand.

A   **B**
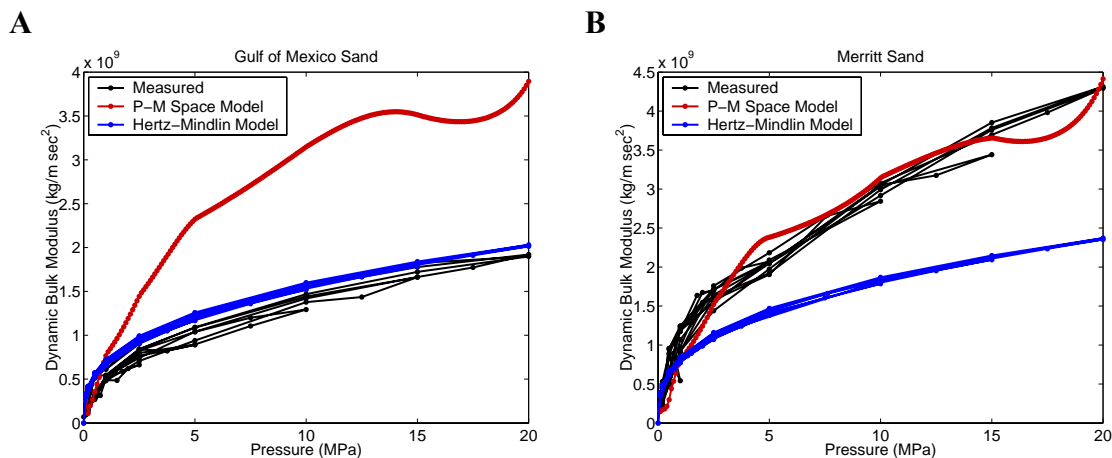
Figure 6.16: Comparison of Hertz-Mindlin prediction of the bulk modulus to the P-M space analysis prediction and the measured dynamic bulk modulus for the A) Gulf of Mexico and B) Merritt sand samples.

The results of the P-M space analysis do produce a good prediction of the dynamic modulus with pressure for the Merritt sand sample, as shown in Figures 6.14. The Merritt sand sample stands out as the one sample that was not reconstituted, but was prepared from an intact sample that was solid enough to hold together while being prepared. While the Merritt sand and Gulf of Mexico sand samples show very similar stress-strain behavior over similar loading histories, the Merritt sand demonstrates significantly higher velocities and dynamic moduli. Likewise, the measured dynamic bulk moduli calculated from these velocities exceed the Hertz-Mindlin prediction (see Figure 6.16B), indicating that consolidation from compaction and/or cementation has stiffened the sand. Upon removal of the sample from the sample holder after the experiment, the sample was found to be broken into several large pieces. This may indicate that small sections of the sample, those where the breaks occurred, accommodated most of the plastic deformation, while the rest of the sample maintained its integrity and preserved an overall large dynamic bulk modulus. The P-M space analysis may provide a good prediction only because the Merritt sand has a much higher measured dynamic modulus, while the static strains are still being over-predicted on unloading.

Influence of plastic and elastic strain on relationship between static and dynamic moduli

The initial Preisach-Mayergoyz space analysis developed by Guyer et al. (1997) assumes that the difference between the static and dynamic moduli is entirely a result of the strain magnitude dependence of the moduli resulting from hysteretic strain behavior. Unlike in consolidated rocks, in unconsolidated sediments much of the difference between the static and dynamic moduli is due to the effect of plastic strains on the static modulus. This adapted Preisach-Mayergoyz space analysis allows the modeling of the differences between the static and dynamic bulk moduli due both to the strain magnitude dependence of the modulus, and to the plastic strains experienced by unconsolidated sediments. The plastic strains, which under hydrostatic loading generally occur only on the loading path, result in much larger strains on these portions of the path and so produce a much lower static modulus. For the sand samples analyzed here, the plastic strain results in a ratio of the dynamic to static bulk modulus that is two to three times larger than the ratio resulting from the strain magnitude dependence. Nevertheless, not all of the difference between the static and dynamic moduli results from the effect of the

plastic strains. As shown in Figure 6.15, if the plastic strain is ignored, the static modulus still falls below the dynamic modulus derived from the P-M space analysis on both the loading and unloading portions of the pressure path due to the hysteretic elastic strains. On the unloading paths, where there is no plastic strain occurring, the strain magnitude dependence of the modulus is the only cause of the difference between the static and dynamic measurements (besides the measurement errors). The rise in the ratio of the dynamic to static moduli on unloading results from the activation of stored, hysteretic strain that is rebounding elastically, resulting in a lower static modulus. A comparison of the behavior predicted by this analysis to that observed in the measured relationship between the two moduli demonstrates that both these factors do have an influence; the measured dynamic to static ratio is much smaller on unloading paths and on subsequent loading paths, and rises above one with continued unloading from the reversal step.

Prediction of static moduli from dynamic measurements

The difference between the static and dynamic moduli in the P-M space analysis is an indication of how much strain is activated by a static pressure step, compared to how much is activated by the small dynamic pressure fluctuations. The difference between the two moduli varies significantly in the measurements presented in Figure 6.4 to 6.8. The result is that there is no unique relationship between a measured dynamic modulus and the corresponding static modulus (see Figures 6.4 to 6.8B). This is because this difference is a product of both the strain magnitude dependence of the modulus and of the occurrence of plastic strain during loading, both of which vary based on the pressure history of the sample prior to the pressure step in question. While the dynamic modulus for a given sample is well correlated to the pressure, and is not very sensitive to the pressure history, the static modulus is primarily a function of the pressure history. Even just considering the normally consolidated portion of the loading paths, the ratio of the dynamic to static bulk moduli varies significantly from sample to sample due to variations in both the static and dynamic moduli measured on the various samples. On the contrary, for the final unloading paths, the P-M space predictions of the ratio of the dynamic to static moduli are all very similar, with the ratio increasing from one at 20 MPa to about three at zero pressure. With some variability, similar behavior is observed in the measured data for the final unloading path. This might indicate that if a sediment

were known to be on an unloading path, with a known preconsolidation pressure and current effective pressure, a somewhat universal relationship between the static and dynamic moduli might hold. Otherwise, the large variation in the dynamic to static ratio of the normally consolidated sediments indicates that the application of any relationship between the two to *in situ* sediments would require calibration of the relationship to local samples.

CONCLUSIONS

Measurements of the static and dynamic moduli on a set of four sand samples and one glass bead sample over pressure cycles from 0 to 20 MPa demonstrate that the dynamic modulus remained several (2 to 10) times larger than the static modulus under normally consolidated conditions, but that the static modulus jumped up to or beyond the dynamic modulus on the first unloading step for all of the samples but the Merritt sand sample. An adapted Preisach-Mayergoyz space analysis permitted the segregation of the strain into hysteretic and non-hysteretic elastic strains and first- and second-cycle plastic strains. This analysis does a reasonably good job of modeling the stress-strain behavior of all of the samples. The elastic static behavior of the samples was very similar, but large variations are seen in the plastic behavior, with the Gulf of Mexico sand showing the most plastic strain and the glass bead sample showing by far the least. The P-M space analysis largely over-predicts the dynamic moduli for all of the samples except the Merritt sand sample where the prediction is (maybe coincidentally) very good. The Merritt sand sample is a more consolidated sample that demonstrates a dynamic modulus much higher than that of the other samples at all pressures.

The Preisach-Mayergoyz space analysis developed by Guyer et al. (1997) assumes that the difference between the static and dynamic modulus is a result of the strain magnitude dependence of the modulus resulting from hysteretic strain behavior. The adaptation of this analysis to include the plastic strains experienced by unconsolidated materials demonstrates that the unloading portions of the pressure path do still demonstrate differences between the static and dynamic bulk moduli as a result of this strain magnitude dependence. Nevertheless, on the loading paths, especially when the sediment is normally consolidated, a much larger proportion of the difference is due to the occurrence of plastic strain. While the P-M space analysis presented here did not

accurately predict the quantitative relationship between the static and dynamic moduli for most of the samples, it does capture the overall behavior associated with these two causes of the static-dynamic difference, and illustrates that both do influence the static-dynamic bulk modulus relationship observed in the measured data.

Because of inaccuracies in the static measurements in this study, it is difficult to discern whether a consistent quantitative relationship might exist between the static and dynamic moduli in dry sands. Nevertheless, my analysis does demonstrate consistent general behavior between the static and dynamic bulk that can be captured by the adapted Preisach-Mayergoyz space analysis. Calibration of this analysis with local samples, might permit this analysis to be used to relate the *in situ* dynamic and static bulk moduli of unconsolidated sediments as a function of the loading history and current effective stresses of the sediments.

CHAPTER 7:
APPROXIMATE UNIVERSAL TREND OF THE PRESSURE SENSITIVITY OF THE SEISMIC VELOCITIES WITH PRESSURE IN ROCKS AND SEDIMENTS

ABSTRACT

A compilation of velocity data from a number of published sources demonstrates that the sensitivity of the seismic velocities to pressure ($\partial V / \partial p'$) is a continuous function of the effective pressure for a wide variety of rocks over a wide range of pressures. The compiled dataset includes data from unconsolidated sediments, sandstones and shales, and crystalline limestones and granites. The pressure range covered extends from below 100 kPa (1 bar) to above 600 MPa (6 kbar). All of the data are from laboratory measurements made at ultrasonic frequencies under hydrostatic pressure conditions. The pressure sensitivity data from all of these sources are observed to roughly follow a single power-law trend over this entire pressure range for both the compressional- and shear-wave velocities, and for both dry and water-saturated rocks. These observations indicate that, to a first-order approximation, the sensitivities of the velocities to pressure are independent of the porosity, density, and constituent mineral moduli.

INTRODUCTION

The effective stress is a primary control on the mechanical behavior of earth materials, and so is of keen interest over a wide range of depths in the crust. One approach to making *in situ* effective stress estimates is based on the relationship between the mean effective stress or effective pressure (p') and the sensitivity of the seismic velocities to the effective pressure ($\partial V / \partial p'$). Bokelmann et al. (2003) have discussed the potential use of this relationship in concert with velocity-change measurements associated with the earth tides to estimate, or at least bound, the effective pressure. As the earth tides produce regular, but very small, pressure fluctuations in the crust of the earth, the measurement of the associated velocity changes, along with an estimation of the magnitude of the pressure fluctuation at the corresponding depths, permit an *in situ* measurement of the pressure sensitivity. This velocity change measurement can be made much more accurately than can the measurement of the velocity itself. Bokelmann et al. (2003) suggest that the relationship between the pressure sensitivity, $\partial V / \partial p'$, and the

effective pressure could also provide a more accurate and more general indicator of pressure than the direct velocity-pressure relationship. A knowledge of this relationship would then allow the use of *in situ* pressure sensitivity measurement to bound the effective pressure that the rock experiences. An estimate of the mean stress or overburden stress then allows the calculation of the pore pressure. While Bokelmann et al. (2003) were not able to see the earth tide signal in travel time data over large distances in central Europe, Reasenberg and Aki (1974) and Yamamura et al., (2002) have demonstrated the potential to observe tidally-induced velocity changes *in situ*.

The objective of this study is to test the accuracy and the generality of this relationship between the effective pressure and the sensitivity of the velocities to the effective pressure. This chapter will first review the relevant prior observations and theoretical modeling of relationships between the seismic velocities and the effective pressure. It will then present the compiled dataset of the pressure sensitivity versus effective pressure for a large number of rocks and sediments of very different characters and discuss the implications that the observed trends have for the evolution of the pore structure of crustal materials with pressure.

Empirical observations of pressure sensitivities

Measurements of the dependence of the seismic velocities on pressure have been made on a wide variety of rocks and sediments, beginning with early work by Birch and Bancroft (1938), Wyllie et al. (1958), Christensen (1965), and King (1966). This experimental work showed that on loading to higher effective pressures under hydrostatic conditions, the shear- and compressional-wave velocities of rocks and sediments increase.

For unconsolidated sediments, a large body of experimental data has demonstrated that both the compressional- and shear-wave velocities follow a power-law relationship with pressure (Hardin and Richart, 1963; Pilbeam and Vaisnys, 1973; Domenico, 1977; Roesler, 1979; Hardin, 1980; Yu and Richart, 1984; Hardin and Blandford, 1989; Hryciw and Thomann, 1993; Robertson et al., 1995; Fam and Santamarina, 1997; Chapter 3). These relationships can be most simply expressed for a hydrostatic stress state by an empirical form such as the following:

$$V = S\left(\frac{p'}{p_a}\right)^{n/2}, \qquad (7.1)$$

where V is the velocity, p' is the effective pressure, p_a is the atmospheric pressure, and S and n are empirical coefficients, with the S coefficient possibly including corrections for such things as porosity variation and overconsolidation (see Chapter 3). To fit the water-saturated compressional-wave velocity, this form requires the addition of a constant to account for the non-zero velocity at zero pressure. For the shear-wave velocities, the n coefficient is generally accepted to be around 0.5 (e.g. Hardin and Black, 1969), though for individual samples it has been reported to vary from approximately 0.34 to 0.96 (Hryciw and Thomann, 1993; Fam and Santamarina, 1997; Chapter 3). For a smaller set of measurements of the compressional-wave velocities on dry sediments, the n coefficient has been found to vary from 0.34 to 0.62 (Hardin and Richart, 1963; Chap. 3) and to be consistently lower than the value of n for the shear-wave velocity of the same sample (Chapter 3). The S parameter has been found to vary from 136 to 308 m/sec for the shear-wave velocities and between 376 and 544 m/sec for the compressional-wave velocities (Fam and Santamarina, 1997; Chap. 3), and to be roughly inversely related to the value of n (Hryciw and Thomann, 1993). This empirical form predicts the following pressure sensitivity:

$$\frac{\partial V}{\partial p'} = \frac{\frac{n}{2}S}{p_a}\left(\frac{p'}{p_a}\right)^{\frac{n}{2}-1}. \qquad (7.2)$$

The sensitivity is still a power-law function of the pressure, though the exponent will be negative, generally around -0.75, for any unconsolidated material.

Data on the velocity variation with pressure in more consolidated clastic and crystalline rocks have also been widely reported (e.g. Nur and Simmons, 1969; Christensen, 1974; Kern and Tubia, 1993; Kern et al., 2001). A wide variety of empirical forms have been used to describe the pressure dependence of these rocks. The most common form is the following:

$$V = A + Kp' - B\,e^{-Dp'}, \qquad (7.3)$$

where A, B, D, and K are empirical coefficients (Stierman et al., 1979; Moos, 1983; Eberhart-Phillips et al., 1989; Freund, 1992; Jones, 1995; Khaksar et al., 1999). The

constant, *A*, accounts for the fact that these rocks do not demonstrate vanishing velocities as the effective pressure approaches zero. The linear term, *Kp'*, is included to account for the pressure sensitivity of the constituent minerals, which becomes important once most of the porosity has closed. Ranges of the values for these coefficients found by various authors are given in Table 7.1. Alternate forms that ignore the linear term (Khaksar and Griffiths, 1998; Khaksar et al., 1999), that fit to the square of the velocities (Stiller et al., 1980; Greenfield and Graham, 1994; Meglis et al., 1996; Prasad and Manghnani, 1997), or that use power-law forms of varying complexity (Ball and Batzle, 1994; Carlson and Gangi, 1985) have also been found to provide good fits to the data. The empirical form in Equation 7.3 yields a pressure sensitivity given by:

$$\frac{\partial V}{\partial p'} = K + BD \ e^{-Dp'} . \tag{7.4}$$

This form predicts that the pressure sensitivity will decay exponentially with increasing pressure.

Table 7.1: Fit coefficients to Equation 7.3

Reference	Sat.	Vel.	A m/sec	K m/sec·MPa	B m/sec	D 1/MPa
Eberhart-Phillips et al. (1989)	Water	V_P	3110 to 5470	1.38 to 7.20	109 to 807	0.06 to 0.35
		V_S	1650 to 3440	1.07 to 7.57	123 to 1270	0.06 to 0.31
Khaksar et al. (1999)	Dry	V_P	4159 to 7298	-21.97 to 2.60	1152 to 4180	0.017 to 0.070
		V_S	2513 to 8299	-29.21 to 3.80	606 to 5631	0.010 to 0.085
Stierman et al. (1979)	Dry	V_P	5581 to 6203	1.448 to 2.665	1601 to 2939	0.0838 to 0.1210
	Water	V_P	6007 to 6308	0.5674 to 1.385	503.5 to 992	0.0381 to 0.1208
Jones (1995)	Water	V_P	3644 to 5161	0.004 to 3.583	176.8 to 868.6	0.062 to 0.181
		V_S	2195 to 3240	0 to 3.129	164.9 to 866.2	0.047 to 0.191
Freund (1992) – C_C, ϕ averages	Dry	V_P	4110 to 5600	0.433 to 0.962	2090 to 1180	0.038 to 0.130
		V_S	2720 to 3550	0.257 to 0.530	190 to 890	0.027 to 0.046

Theoretical predictions of pressure sensitivities

It has been widely recognized that the presence of open pore space results in a more compliant rock than for its pure, pore-free mineral components (e.g. Ide, 1936; Zisman, 1933; Brace, 1965; Walsh, 1965a,b). The way in which the character of this pore space influences the velocities and their pressure sensitivities has been modeled theoretically in a number of ways. For clastic rocks and unconsolidated granular media, the elastic moduli have generally been modeled based on the behavior of contacts between identical spheres, as described by Hertz-Mindlin compressional and shear contact stiffnesses

(Mindlin, 1949; Timoshenko and Goodier, 1970; Digby, 1981; Winkler, 1983; Walton, 1987; Mavko et al., 1998). The inputs to these models include the effective pressure, the porosity of the sample, and the average number of contacts per grain. They predict that the velocities of dry, granular materials will vary according to the $1/6^{th}$ power of the pressure if the other model inputs and the density are held constant. Different assumptions of contact shape or of buckling of the particle chains can lead to a $1/4^{th}$ power-dependence on the pressure (Goddard, 1990), as is generally observed in measurements of completely unconsolidated sediments. As with the empirical power-law forms, this implies that the pressure dependence of the velocities will vary with the pressure to the $-3/4^{th}$ or $-5/6^{th}$ power, with its magnitude varying with the density, porosity, and contact number chosen as inputs to the models.

The velocities of low-porosity clastic rocks and crystalline rocks are more often modeled assuming that the pore space is made up of a collection of cracks of idealized shapes (Walsh, 1965a; Kuster and Toksoz, 1974; O'Connell and Budiansky, 1974; Mavko and Nur, 1978; Hudson, 1981; Mavko et al., 1998). The most commonly assumed crack shape is the penny-shaped crack. This is an elliptical crack, circular in the plane of its widest dimension but with a very high aspect ratio in the perpendicular planes. The pressure at which a penny-shape crack will close is a function of the aspect ratio of the crack and the properties of the surrounding rock. By assuming such a crack shape it is possible to model any given modulus-pressure or velocity-pressure profile with the appropriate distribution of crack aspect ratios (Warren, 1977; Zimmerman, 1991), or with a function describing the average aspect ratio (Sun and Goldberg, 1997) or fracture density (Meglis et al., 1996) with pressure. It is also possible to bound the aspect ratio of the cracks that will close to produce velocity increases up to a certain pressure (Jackson and Paterson, 1987). Nevertheless, this distribution depends significantly on the assumed crack shape and so any such aspect-ratio distribution or crack-density function will be highly non-unique (Mavko and Nur, 1978). The result is that for a given sample these models can be used to produce any velocity-pressure relationship or sensitivity-pressure relationship by selecting the appropriate set of crack shapes or crack aspect ratios.

OBSERVATIONS OF VELOCITY-PRESSURE SENSITIVITY WITH PRESSURE

A dataset of ultrasonic velocity measurements collected over a wide range of pressures was compiled for a wide variety of rocks and sediments, including unconsolidated sands (Chapter 3), consolidated shales and sandstones (Han, 1986; Jizba, 1991), and crystalline limestones, dolomites, and granites (Nur and Simmons, 1969). The sensitivity was calculated from the difference between each neighboring pair of velocity measurements for each sample, and plotted against the average pressure at which the two measurements were made. Figure 7.1 shows the compiled pressure sensitivity data plotted against the effective pressure for all the measurements on dry samples, while the compilation for the water-saturated samples is shown in Figure 7.2. All of these data are from measurements made at room temperature, so that no mineral transitions occur, and under hydrostatic loading conditions, so no shear failure or sample dilation occurs. The velocity measurements were all made at ultrasonic frequencies, above 100 kHz. The figure also shows the pressure sensitivity data for pure mineral aggregates of olivine (Zaug et al., 1993), and for plagioclase and orthoclase feldspars (Galdin, 1977).

The key observation is that the pressure sensitivity data for all of the rocks and sediments lie along a single continuous trend for each of the velocities, with relatively limited scatter about this trend. This is in contrast to the large variability and discontinuities in the trends of the actual velocities with the pressure and of the sensitivities with the velocities, as shown in Figure 7.3. The trend of the pressure sensitivity data is approximately linear in the log-log plots shown in Figure 7.1, though with a slight bend in the trend at approximately 50 MPa. The highest pressure data approach the low sensitivities demonstrated by the pure mineral moduli.

COMPARISON OF MODEL PREDICTIONS TO OBSERVED PRESSURE SENSITIVITIES

The consistency of the pressure sensitivities between the various rock types indicates that the coefficients of the empirical forms given in Equations 7.2 and 7.4 should be similar for a wide range of rock types. This implies that the significant variation of the individual parameters, as demonstrated in Table 7.1 and Table 3.4, is not likely to be truly independent. The interdependence, as demonstrated in Figure 7.4, especially for the *n* and *S* coefficients from Equation 7.2, and to a lesser degree for the *B* and *K* coefficients from Equation 7.4, is a product of sympathetic fitting of the parameters when the data are

A
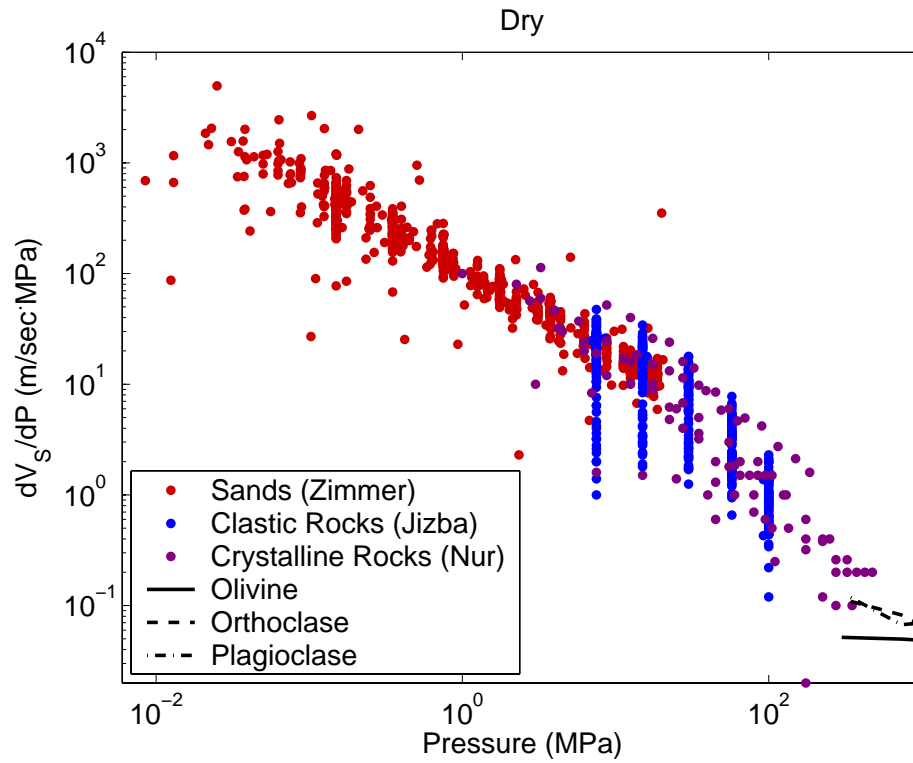
B
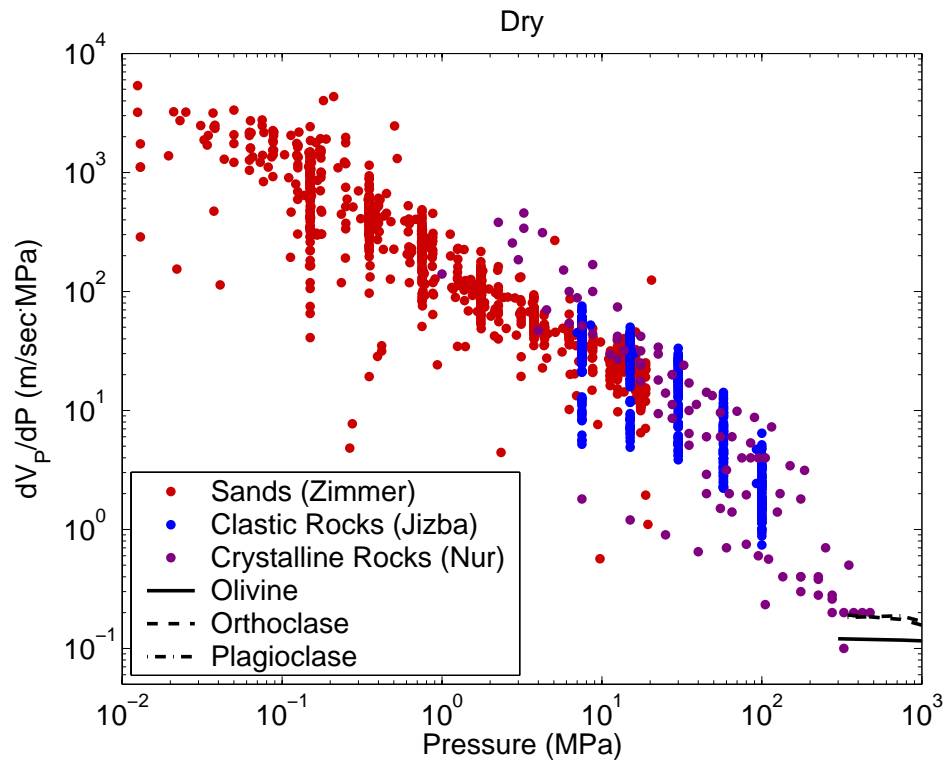
Figure 7.1. Compilation of pressure sensitivity data plotted against pressure for dry rocks: A) shear-wave velocity sensitivity, and B) compressional-wave velocity sensitivity.

A
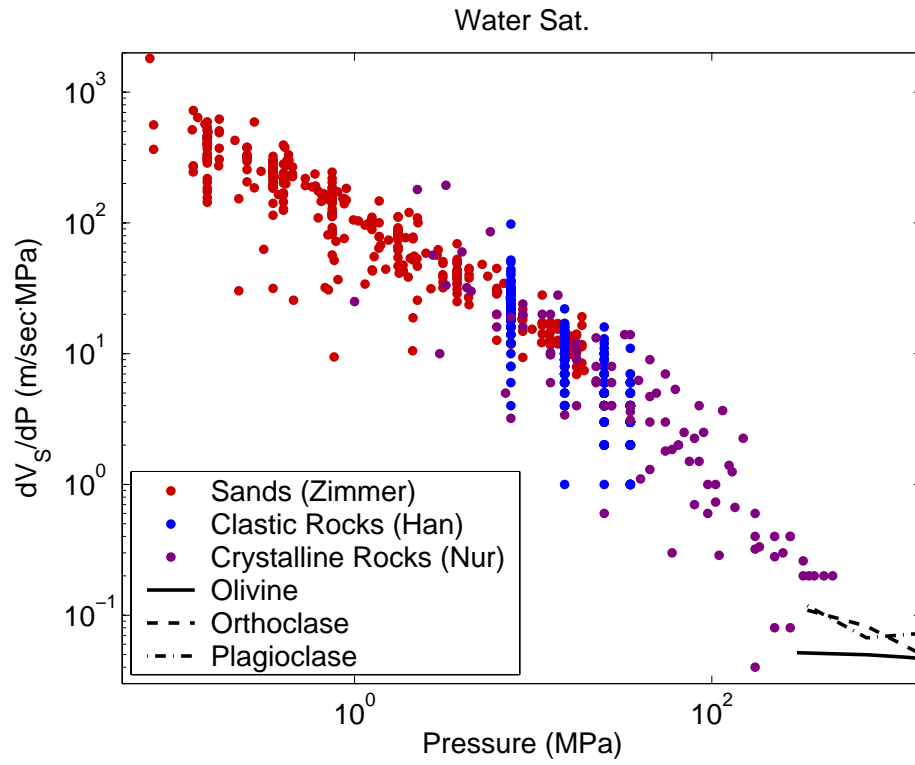
B
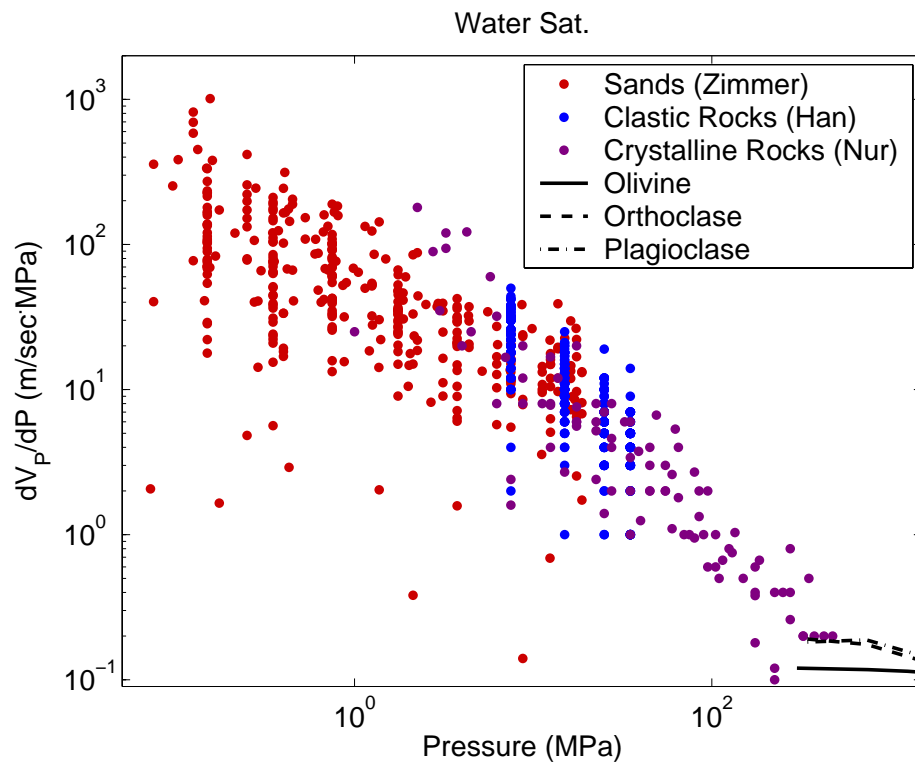
Figure 7.2: Compilation of pressure sensitivity data plotted against pressure for water-saturated rocks: A) shear-wave velocity sensitivity, and B) compressional-wave velocity sensitivity.

A
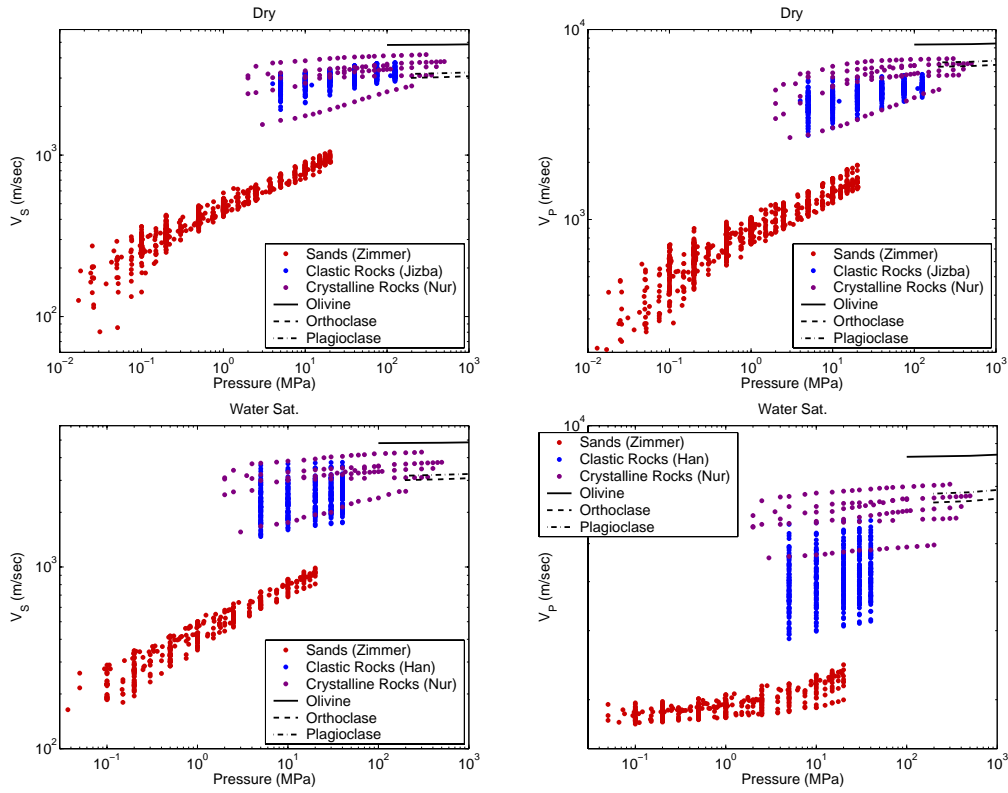
B
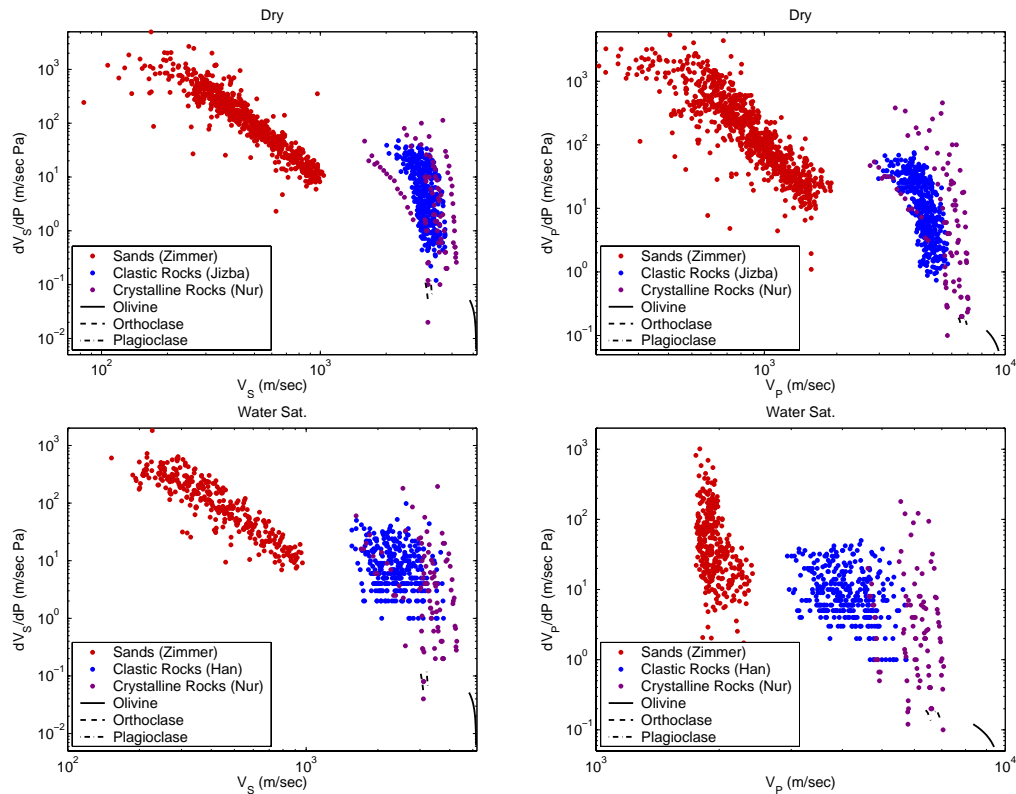
Figure 7.3: A) Velocity measurements plotted against pressure and B) sensitivity data plotted against velocity.

A

B
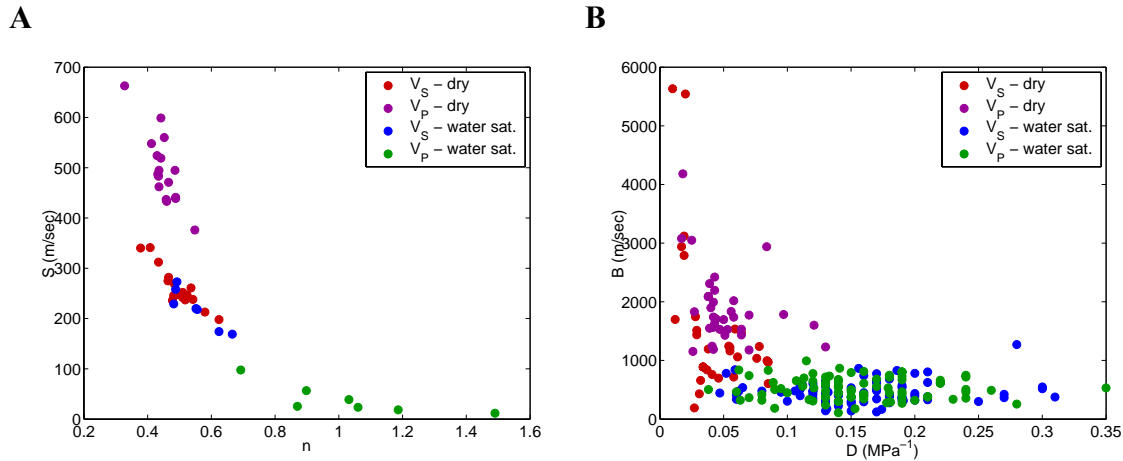
Figure 7.4: Comparison of empirical coefficients A) *S* versus *n* from Equation 7.1 and B) *B* versus *D* from Equation 7.2.
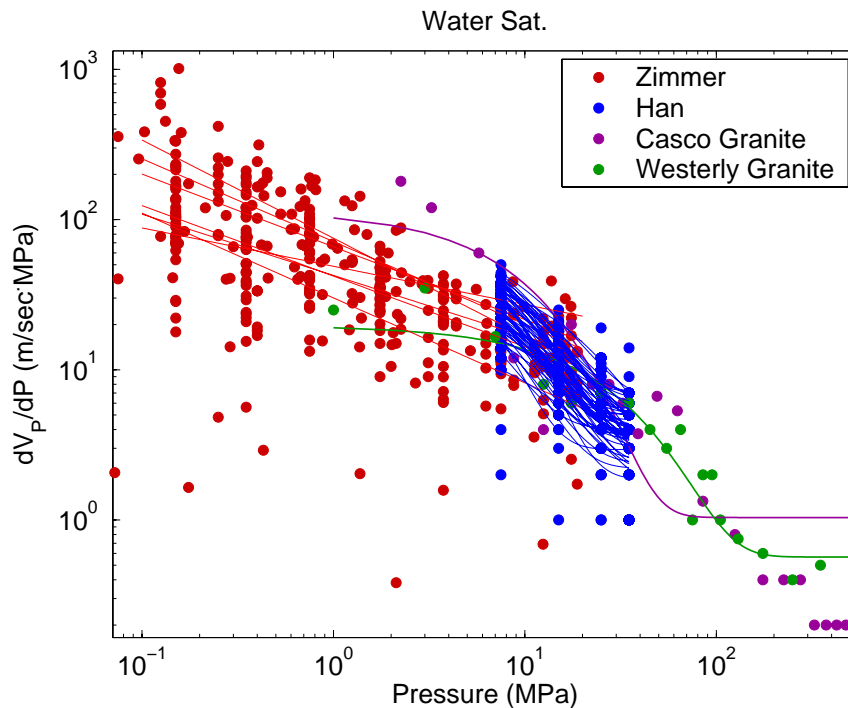
Figure 7.5: Comparison of pressure sensitivity data from Chapter 3, Han (1986), and Nur and Simmons (1969), to the sensitivity calculated from derivatives of the empirical fits calculated from the coefficients from Table 3.4, Eberhart-Phillips et al. (1989), and Stierman et al. (1979).

not perfectly described by the power-law or exponential form. Figure 7.5 shows a comparison of the sensitivity data for the compressional waves in water-saturated samples from Chapter 3, Han (1986), and Nur and Simmons (1969) to the sensitivity calculated from the derivatives of the empirical forms (Equations 7.2 and 7.4) with fit coefficients from Table 3.4, Eberhart-Phillips et al. (1989), and Stierman et al. (1979).

For the unconsolidated data, fit with the power-law form, the measured sensitivities compare well with those calculated with the derivatives of the empirical form. On the contrary, the good fit of the exponential form to the velocity data does not carry over to a good fit of the sensitivities calculated from Equation 7.4 with the same coefficients to the sensitivity data, as shown in Figure 7.5. This is especially apparent for the granite samples, while a close inspection of the erratic behavior of the empirical lines for the individual samples of Han's data also indicates that this form does not accurately predict the sensitivity. This is likely because the velocities are not described exactly by the exponential empirical form in Equation 7.3. The fit optimizes all the parameters, including the *A* parameter which is eliminated with the derivative, to minimize the error between the fit and the velocities, without honoring the sensitivities. Unfortunately these observations provide little physical understanding of the reason for the similarities of the sensitivities, but demonstrate that the exponential form does not preserve the velocity-pressure sensitivities demonstrated by the actual data.

To test whether the contact models or crack models might provide some insight into the similarities in the pore spaces between these very different sediment and rock types that result in this approximately universal pressure sensitivity trend, I compared the contact number and crack density distributions derived from individual samples of each rock type from each of these models. The inversions for these distribution were perform for four samples that were representative of the consistent sensitivity trend of the dry velocities, but were of very different characters (the Pomponio Beach sand, a sandstone and shale from the B.F. Phillips well from the Jizba dataset, and the Westerly Granite). The mineral moduli input into the models for the Pomponio Beach sand and Westerly granite were calculated as the Voigt-Reuss-Hill average bulk and shear mineral moduli using the mineralogic compositions given in Chapter 3 and Brace et al., 1965, respectively. The Poisson's ratios were then calculated from the average moduli. As only the clay content for the sandstone and shale is given by Jizba (1991), I assumed that the non-clay component had the same proportional mineralogic content as the Pomponio sand.

Contact Models

For samples with known porosity and constituent-mineral bulk and shear moduli, the Hertz-Mindlin-based contact models can be used to invert the measured bulk and shear moduli for the average coordination number in the sample at each measurement. The contact-model derivation of Walton (1987) gives two independent equations between the contact number and the shear modulus for a hydrostatic stress state, depending on whether one assumes infinite or zero friction at the grain contacts. It also gives a third equation between the coordination number and the bulk modulus that is the same in both cases (Mavko et al., 1998; Chapter 3). The results of the inversion for the coordination number for the four samples are shown in Figure 7.6. This inversion obviously produces non-physical, excessively large results for the coordination number with pressure for the stiffer rocks.

It is also possible to modify the assumption that the particles are perfectly spherical to allow the average radius of curvature, which affects the contact stiffnesses, to differ from the radius of the grains. A larger contact radius to grain radius ratio is analogous to assuming that the grains have flatter faces that are arranged to be in contact, as might be envisioned for highly consolidated clastic rocks and crystalline rocks. By assuming a constant coordination number, the contact models can be used to invert for this contact-to-grain radius ratio for each of the samples, yielding reasonable values of from 0.3 or 0.4 for the unconsolidated samples and from 4 and 8 for the consolidated clastic and crystalline rocks. Nevertheless, the model predictions of the velocities based on the values inverted from this version of the model do not furnish an acceptable match to the data, especially for the more consolidated rocks, which do not have velocities that go to zero at low pressures as predicted by the model (Figure 7.6B). Likewise, this model does not produce sensitivities that are continuous between the various samples with pressure (Figure 7.6C), but demonstrates an order of magnitude jump between the sensitivities of the unconsolidated sediments and the consolidated rocks.

A

B

C
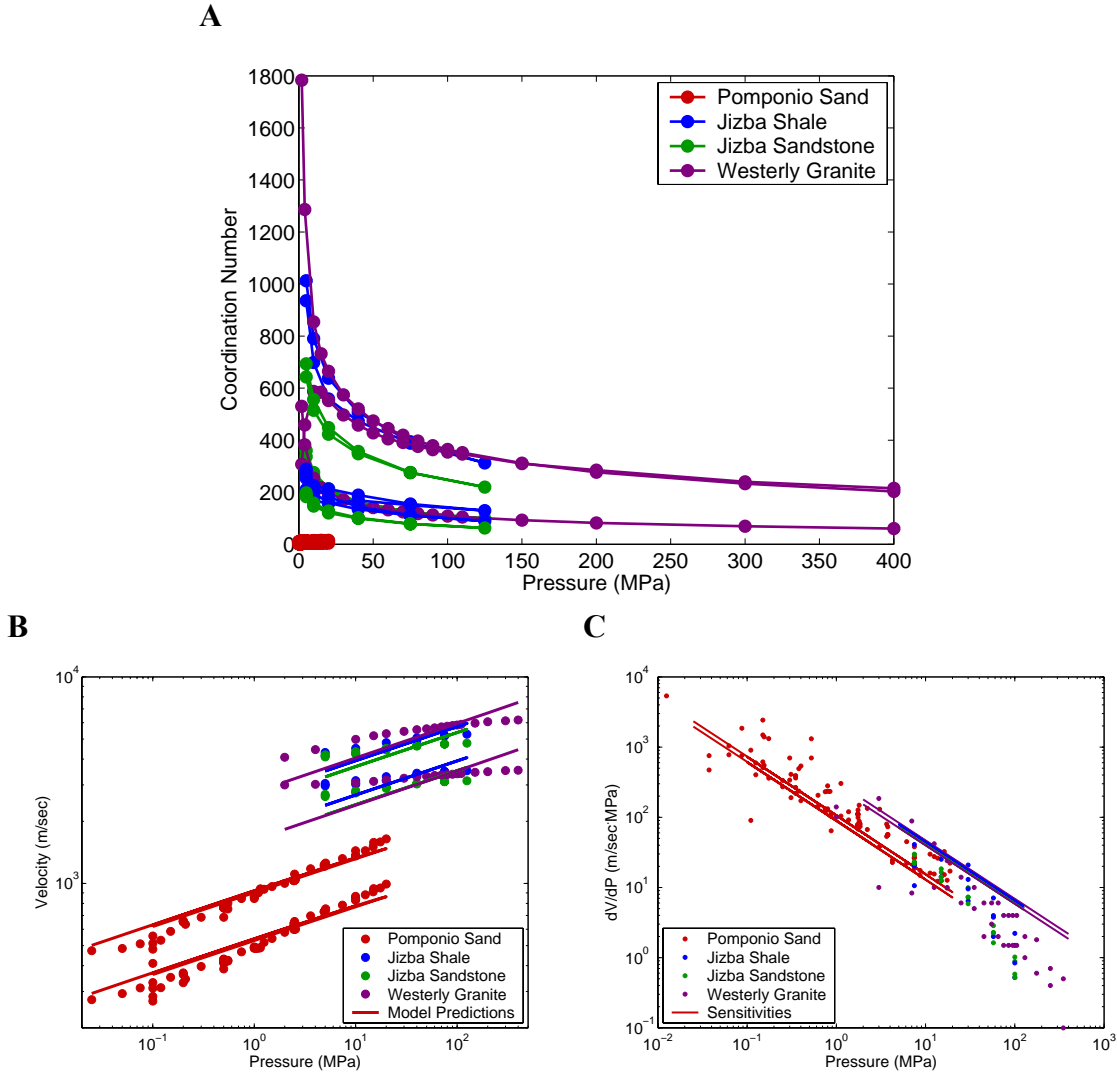
Figure 7.6: A) Coordination numbers inverted for each of the four samples from Walton's (1987) contact based models. B) The velocities and C) pressure sensitivities calculated from each of the contact radius functions derived from the contact models.

Crack Models

To investigate how crack-based theoretical models might account for the continuous sensitivity trend in the different rocks, the self-consistent model of O'Connell and Budiansky (1974) was used to invert for the crack density parameter, a dimensionless parameter describing the number of cracks per unit volume of rock. This theory is generally used to predict the moduli of a cracked solid of known constituent-mineral moduli with a given crack density. If the cracks are assumed to have an aspect ratio that approaches zero, this theory yields two expressions between the crack density parameter and the bulk moduli, shear moduli, and Poisson's ratios of the crack-filled rock and pure

mineral (Mavko et al., 1998). This inversion was performed on the same four samples as the contact model inversion, with the crack density parameter predicted independently for each of the samples from the bulk modulus and shear modulus data. The resultant predictions are shown in Figure 7.7. These predictions vary widely between the two predictions for each sample. They are also highly dependent on the average mineral modulus used. The estimates of the crack density parameter yield a negative value whenever the measured moduli exceed the average mineral moduli for the rock, which occurs for the values inverted from the shear modulus of the Westerly granite. This implies that there are errors either in the measurements or in the commonly accepted values of the pure mineral moduli. While this model does recreate the velocities and pressure sensitivities of the velocities perfectly if the different crack densities are used to calculate the moduli from which they were inverted, it fails for the non-crystalline rocks if a single crack density vs. pressure function is used to calculate both the bulk and shear moduli (Figure 7.7B,C). Additionally, this sort of model does not provide a very satisfying analogy for the unconsolidated sediments and sandstones, which contain a significant amount of porosity with high (near 1) aspect ratios.

In neither the crack-density model nor the contact model analyses is there any indication that the crack density, the coordination number, or the radius of curvature represents a significant, continuous property of the rocks. Likewise, the change in these parameters with pressure does not appear to be consistent between the samples.

DISCUSSION

The configuration of the pore space in the various rocks from which the velocity data is presented here is of course significantly different. Nevertheless, all of the various rock types demonstrate similar increases in velocity for a given increase in pressure, at a given effective pressure. This suggests that the incremental change in the pore space resulting from this pressure increment is similar in all rock types. The significant disparities between the various rock types for most of the factors that control the velocities, including the mineral moduli, density, and porosity, implies that none of these factors influence the pressure sensitivity to the first order. On the contrary, the pressure sensitivity demonstrates a continuous trend with pressure. This would indicate that a universal expression for the velocity would be of the form:

$$V = f(K_{min}, \mu_{min}, \phi, \rho) + g(P) + O^2 , \tag{7.5}$$

where the function *g* includes some as yet undetermined common characteristics of the pore geometry. Thus the derivative with respect to the pressure is essentially independent of everything but some characteristics of the pore geometry, and their change with pressure. Neither contact-mechanics-based models nor crack-density-based models have demonstrated an ability to capture the behavior of both the velocities and the velocity sensitivities for the full range of samples, indicating that their idealized pore space descriptions are not capturing the general behavior of all of the rock types. At present, it is not clear what characteristics of the pore space produce this continuous trend.
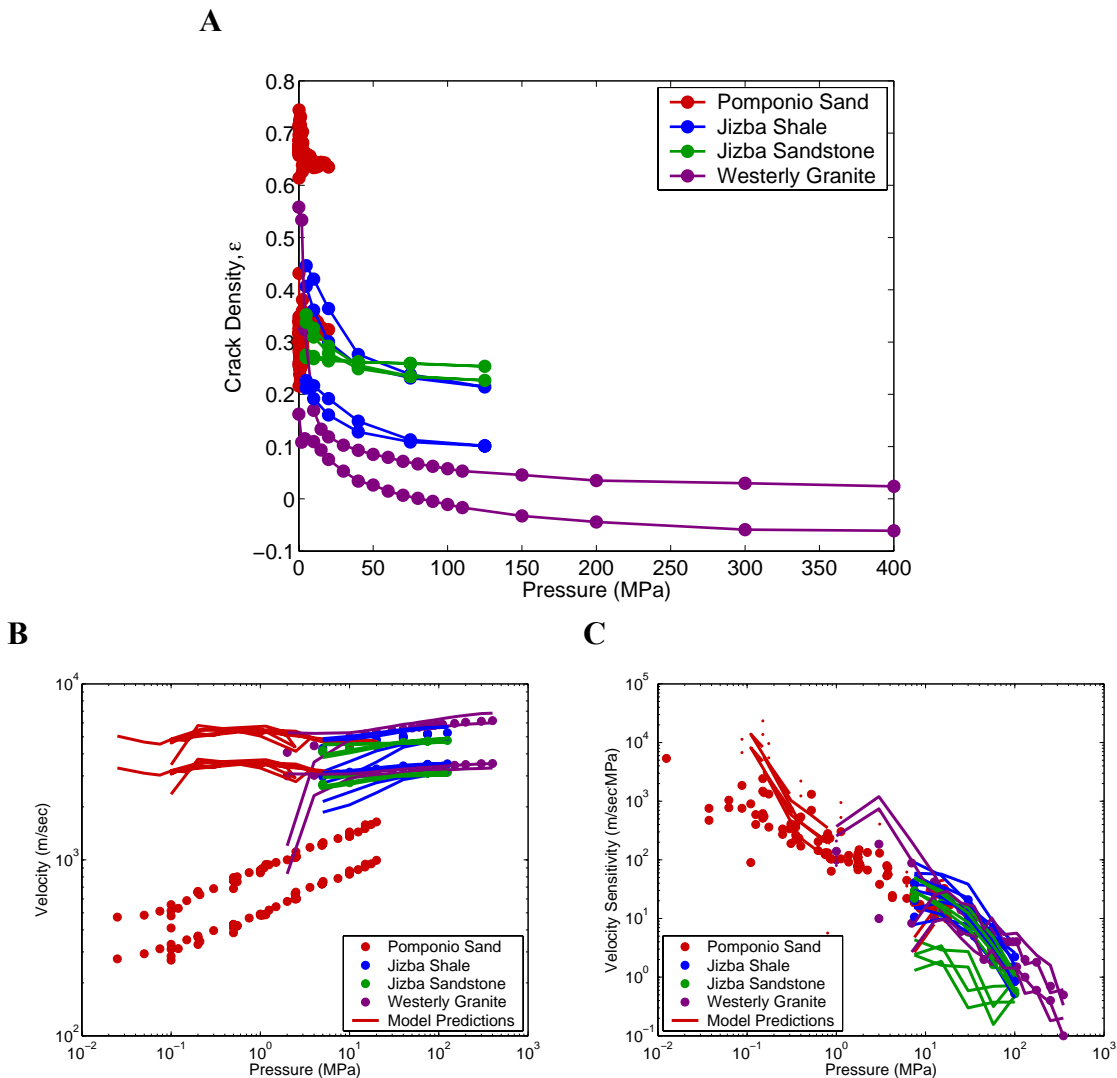
Figure 7.7: A) Crack densities inverted for each of the four samples from O'Connell and Budiansky's (1974) self consistent model. B) The velocities and C) pressure sensitivities calculated from each of the crack density functions in A).

Nevertheless, the observation that the pressure sensitivities of both the compressional- and shear-wave velocities demonstrate a universal trend for a wide variety of dry and water-saturated rocks, over a large pressure range, indicates that measurements of the pressure sensitivity *in situ* could be useful indicators of the effective pressure at depth. As the sensitivities demonstrate a range of values for a given pressure, the most robust use of this trend would be to use the lower end of the range as a bound on the lowest value of the effective pressure likely to correspond to a given measured sensitivity. As this correlation has been developed for samples under hydrostatic stress states, in areas of large stress anisotropy this correlation might not be valid, especially for shear-wave velocities which have been shown to be highly dependant on the stresses in directions other than the direction of propagation. Likewise, all of these measurements were made on rocks with low pore pressures, so the confining pressure is very close to the effective pressure. In low-porosity rocks, the effective pressure can be larger than the difference between the confining and pore pressures (Christensen and Wang, 1985; Prasad and Manghnani, 1997), so the calculation of the pore pressure from the effective pressure and overburden pressure should take into account the non-unique relationship between them. A final caveat is that these are all laboratory measurements made at high frequencies, so scale and frequency effects should also be considered before applying these results to sensitivities measured *in situ*.

CONCLUSIONS

The pressure sensitivity of the compressional- and shear-wave velocities of a wide variety of rocks was observed to demonstrate a consistent, approximately universal trend with respect to the effective pressure over a wide range of pressures. This observation was based on a compilation of data taken from laboratory measurements made at ultrasonic frequencies under hydrostatic pressure conditions. This trend could be used to place a bound on the effective pressure experienced *in situ* from measurements of the pressure sensitivities of the velocities.

No single parameterization of the Hertzian contact-based models or of O'Connell and Budiansky's self-consistent crack model is capable of capturing both the velocity and pressure sensitivity behavior of all of the samples. The fact that the velocities, porosities, densities, and mineralogies of the various samples vary widely indicates that the

156

controlling factor in the behavior of the pressure sensitivity is most likely some as yet undetermined commonality in their pore space geometries and in the changes in these geometries with pressure.

CHAPTER 8:
CONCLUSIONS

This dissertation has presented measurements of the compressional- and shear-wave velocities in a series of unconsolidated granular samples at pressures from below 100 kPa to 20 MPa. This chapter will review the conclusion drawn from this dataset in the previous six chapters and will discuss the progress that these combined observations represent in understanding the controls on the seismic velocities in unconsolidated sands. It will also suggest some areas of further research that might be beneficial in advancing our ability to remotely characterize unconsolidated sediments.

MAIN RESULTS

The development of the apparatus described in Chapter 2 has allowed compressional- and shear-wave velocities to be measured in unconsolidated sediments over a wide range of effective pressures, corresponding to depths from less than 10 m up to 2 km. The main innovations that make these measurements possible include the use of lower frequency (200 kHz) piezoelectric crystals to produce and record the ultrasonic signals and of low-impedance transducer face-plates to reduce the amount of energy reflected at the transducer faces. The apparatus also permits measurements of the static strain to monitor volume and porosity changes in the samples with pressure.

This apparatus was used to make more than 3300 independent velocity measurements on 21 different unconsolidated sand or glass bead samples over pressures from 100 kPa to 20 MPa under normally consolidated conditions and after loading to preconsolidation pressures up to 20 MPa. These data, presented in Chapter 3, demonstrate that the pressure dependences of the seismic velocities in sands are consistent over this entire pressure range. This pressure dependence averages close to the fourth root of the effective pressure, $p'^{1/4}$, for the shear-wave velocity, and between $p'^{1/4}$ and $p'^{1/5}$ for the compressional-wave velocities. The sands exhibit only a marginal increase in the velocities and decrease in the pressure dependence with preconsolidation, with both effects being slightly larger for the compressional-wave velocities.

The power law trend observed in the moduli of all of the samples indicates that contact mechanics are the principle control on the wave speeds. The consistent pressure dependence over the entire pressure range measured suggests that the controlling

mechanics are also consistent over the entire pressure range. The $p'^{1/3}$ dependence of the dry velocities predicted by Hertz-Mindlin contact theory is matched by only a single sample of all those tested, the largest grained glass-bead sample. Likewise, the magnitude of the velocities for all of the samples is fit by the contact theories only when zero-friction between the grains is assumed. These observations demonstrate that for truly unconsolidated granular media, the contact-theory assumptions of no slip at the contacts and of no rotation of the grains are invalid. The fact that the sand and fine- or mixed-grained glass bead samples demonstrate pressure dependences larger than those predicted by the Hertz-Mindlin models, and that the porosity changes observed in the samples are not large enough to support the coordination number changes required to produce these pressure dependences, suggests that changes in the amount of slip and grain rotation at the contacts are a likely cause of the higher pressure dependences observed in the measurements.

In Chapter 4, a subset of these data is presented to demonstrate the velocity-porosity trends associated with sorting- and compaction-induced porosity variations. The measurements on these reconstituted sand and glass bead samples with controlled grain-size distributions and consistent textures demonstrate that the sorting has a very limited effect on either the shear-wave or dry compressional-wave velocities at a given pressure. This trend is similar to the porosity-velocity trend produced by the Reuss bound (a harmonic average between the moduli of the highest porosity sample and the moduli of quartz). On the contrary, water-saturated velocities modeled with Gassmann fluid substitution demonstrate a significant increase in the compressional-wave velocity with decreasing porosity. This porosity-velocity trend is also similar to that of the harmonic average between the moduli of quartz and those of the highest porosity sample. The effect of compaction on the velocities of a given sample is slightly larger than the sorting-induced porosity effect at the higher pressures, but very similar at the lower pressures.

The sorting has no significant, systematic effect on the pressure dependences of the velocities or moduli. The porosity dependence of the water-saturated, compressional-wave velocities does appear to be mostly contained in the initial modulus of the bulk or P-wave moduli. An effective porosity correction for the water-saturated moduli consists of correcting for the difference between this initial modulus at the actual porosity and at a

reference porosity. The application of this porosity correction to the compressional-wave velocities does not reduce the scatter in the water-saturated V_P-V_S ratio, as most of this scatter is from non-systematic variations in the shear-wave velocities and not from the systematic porosity dependence of the compressional-wave velocities. The primary sensitivity of the water-saturated V_P-V_S ratio to the shear-wave velocity suggests that an approximate transform between the V_P-V_S ratio and the shear modulus might be generally valid.

Chapter 5 compares the velocities measured in water-saturated samples of four natural sands to theoretical predictions of the fluid-induced velocity dispersion based on velocity measurements in similarly prepared dry samples. The water-saturated, compressional-wave velocities show significant dispersion relative to velocities predicted by Gassmann fluid substitution. The velocity dispersion does not demonstrate any significant change with compaction of the samples. This indicates that the associated porosity reduction does not significantly change the pore geometry responsible for the dispersion at this measurement frequency. Comparisons of the velocity data to Biot and Mavko-Jizba dispersion models indicate that the squirt mechanism is active in these sediments, while the Biot viscosity and inertial mechanisms are not.

In Chapter 6, measurements of the static and dynamic moduli of dry samples of these same four sands, as well as of one glass bead sample, demonstrate that the dynamic modulus remains 2 to 10 times larger than the static modulus for normally consolidated sediments. On the first unloading step following a loading cycle, the static modulus is approximately equal to the dynamic modulus for most of the samples. An adapted Preisach-Mayergoyz space analysis that accounts for the plastic deformation of the samples illustrates that the elastic static behavior of the samples is very similar, while there are very large variations in the plastic behavior. Due to the large uncertainty in the static modulus measurements, the P-M space analysis did not accurately predict the dynamic moduli of most of the samples. However, this analysis does demonstrate the degree to which both the strain magnitude dependence of the moduli and the occurrence of plastic strain contribute to the difference between the static and dynamic moduli. The plastic strain contributes to this difference only on the loading paths, while the strain magnitude dependence acts on both the loading and unloading paths.

Chapter 7 presents a compilation of laboratory velocity-pressure data from a wide variety of rocks and sediments and over a broad pressure range. The compiled dataset demonstrates remarkable consistency in the relationship between the pressure sensitivity of the velocities, $\partial V / \partial p'$, and the effective pressure, for both the compressional- and shear-wave velocities of both dry and water-saturated samples. This trend could be used to place a bound on the effective pressure experienced by rocks and sediments *in situ* from measurements of the pressure sensitivities of the velocities. No single parameterization of the Hertzian contact-based models or of O'Connell and Budiansky's self-consistent crack-density model is capable of capturing both the velocity and pressure sensitivity behavior of all of the samples. The fact that the velocities, porosities, densities, and mineralogies of the various samples vary widely indicates that the controlling factor in the behavior of the pressure sensitivity is most likely some as yet undefined commonality in the pore space geometry and the change in this geometry with pressure.

SIGNIFICANT CONTRIBUTIONS

The foremost unique contribution of the research presented here is the velocity data itself. Prior to this effort, there was no dataset for unconsolidated sands that included both compressional- and shear-wave velocities over such an extensive pressure range, from below 100 kPa to 20 MPa, for either dry or water-saturated samples.

The most significant overarching observations based on this dataset are that the shear-wave velocities and the dry compressional-wave velocities in unconsolidated sands are primarily sensitive to the pressure, and display relatively similar relationships to the pressure for various sorting qualities and compaction histories over this entire pressure range. The water-saturated compressional-wave velocity exhibits a much larger sensitivity to the porosity associated with both of these factors than do the dry velocities, and so requires a correction for these effects to produce an accurate pressure predictions in water-saturated sands.

The large velocity dispersion observed in the water-saturated compressional-wave velocities is interpreted to be caused by the squirt-flow mechanism acting at the grain contacts. The analyses presented here demonstrate the lack of a pressure-history effect on the velocity dispersion in sands.

On the contrary, the pressure-history is the dominant influence on the static strain behavior and static bulk modulus. Due to significant differences in the plastic strains exhibited by the various samples, under normally consolidated condition no clear, consistent relationship between the static and dynamic bulk moduli was found to hold universally for the natural sands analyzed. Nevertheless, the relationship between the static and dynamic moduli as a function of the effective pressure and loading history is very similar from sample to sample for overconsolidated conditions.

Finally, the approximately universal trend of the pressure sensitivity of the velocities with effective pressure for a wide variety of rocks is a novel and surprising observation that has the potential to permit estimates of the effective pressures throughout the brittle crust.

POTENTIAL APPLICATIONS AND SUGGESTED FUTURE RESEARCH

The strong correlations between the effective pressure and the velocities, and between the pressure and the pressure sensitivities of the velocities, indicate that these parameters could be used to produce quantitative *in situ* estimates of the effective pressure in sands. The shear-wave velocities or dry compressional-wave velocities measured with tomographic techniques or the corresponding impedances inverted from seismic reflection data could be used as direct indicators of the pressure. For water-saturated clays and shales, in which the large porosity loss with compaction reinforces the pressure effects on the velocities, the compressional-wave velocity may also be used as a pressure indicator, as has commonly been done in the petroleum industry for a number of years. In sands, the porosity variation due to different sorting qualities can easily exceed that caused by compaction. The significant sensitivity of the compressional-wave velocity of water-saturated sands to both the pressure and porosity requires that a correction be applied to account for the effects of one of these properties to allow the interpretation of the other from velocity data collected *in situ*. The large velocity dispersion observed even in these high-porosity sediments indicates that the application of trends developed from laboratory measurements to field scenarios involving water-saturated sediments is best done using Gassmann fluid substitution of dry velocity measurements, rather than directly applying trends based on high-frequency water-saturated measurements.

The velocity-pressure correlations presented here are primarily from small, reconstituted samples of natural and synthetic sands and glass beads. A number of other factors that were not investigated here, including the clay content, age, cementation, and depositional environment, are likely to lead to a larger variability in the velocities corresponding to a given effective pressure. The accurate quantitative use of the seismic velocities for pressure estimation or pressure monitoring requires calibrations of the velocity-pressure relationship on actual samples from the field site of concern. An alternative, more approximate approach would be to bound *in situ* pressures based on large datasets compiled from undisturbed samples measured in the lab over an appropriate range of pressures. A velocity measured in the field could then be compared to the entire distribution of velocity-pressure data to determine a statistical likelihood of various pressures being present *in situ*. As there is very limited velocity data publicly available for unconsolidated sediments at pressures above a few hundred kPa, the development of such a dataset would require significant new experimental efforts.

The strong relationship between the pressure sensitivities of the velocities and the effective pressure in the data compiled here suggests that it too might serve to produce either quantitative pressure predictions, given calibration on local samples, or statistical pressure likelihoods based on a large compiled dataset. The pressure sensitivity could be measured using either tidal stress variations, as suggested by Bokelmann et al. (2003), controlled loading by fluid withdrawal accompanied by *in situ* pore pressure measurements, or, for shallow depths, by surface loading with known loads. While the velocity changes associated with any of these loads could be measured accurately, an experimental design that permits accurate estimations of the pressure increment experienced over the ray path of the waves would require additional research.

Additional future research that might lead to improved characterizations of unconsolidated sediments could include measurements of the magnitude of the effects of other sedimentological properties on the seismic velocities of unconsolidated sediments, such as the clay content, age, cementation, and depositional environment. Are the greater pressure-history effects observed in the velocities of cohesive sediments only a result of the greater porosity loss on compaction, in which case they might fit into the same Reuss average framework as the sands, or do they demonstrate dramatically different porosity-

velocity trends than the sands? Another factor not discussed here, which could significantly impact the characterization of these unconsolidated sediments from the velocities, is the effect of the velocity anisotropy resulting from natural depositional processes and from non-isotropic stress states. The investigation of most of these properties would require measurements on undisturbed samples of different ages and environments. While this would involve an additional set of experimental difficulties, and would prevent the effective isolation of individual properties, accurate measurements on undisturbed samples will be essential to understanding how many of these factors influence the seismic velocities in unconsolidated sediments and to being able to successfully apply the laboratory results to the field.

APPENDIX: DATA TABLES

This appendix contains tables of all the velocity, length, radius, volume, density, and porosity data at each pressure step for each of the samples discussed in this dissertation, corrected as discussed in Chapter 4.

Table A.1: Galveston Beach Sand, dry

Pressure (MPa)	V_P (m/sec)	V_S (m/sec)	Length (cm)	Radius (cm)	Volume (mL)	Density (g/cm^3)	Porosity
0	214		2.747	1.879	30.742	1.520	0.4287
0.025	294	203	2.747	1.878	30.727	1.521	0.4284
0.043	325	217	2.747	1.878	30.723	1.521	0.4283
0.057	349	233	2.747	1.877	30.704	1.522	0.4280
0.074	372	252	2.746	1.877	30.694	1.522	0.4278
0.098	405	275	2.746	1.876	30.682	1.523	0.4276
0.146	443	299	2.744	1.876	30.656	1.524	0.4271
0.198	524	321	2.743	1.876	30.632	1.525	0.4266
0.3	544	346	2.741	1.875	30.607	1.526	0.4261
0.17	528	329	2.741	1.875	30.605	1.527	0.4261
0.3	586	356	2.740	1.875	30.583	1.528	0.4257
0.5	670	398	2.737	1.874	30.535	1.530	0.4248
0.75	699	437	2.733	1.874	30.481	1.533	0.4238
1	766	469	2.730	1.873	30.441	1.535	0.4230
1.5	829	516	2.724	1.872	30.358	1.539	0.4214
2	866	549	2.721	1.872	30.307	1.542	0.4205
2.5	921	578	2.718	1.871	30.256	1.544	0.4195
1	810	486	2.722	1.873	30.341	1.540	0.4211
0.5	691	419	2.726	1.874	30.404	1.537	0.4223
0.2	586	353	2.729	1.875	30.461	1.534	0.4234
0.1	513	320	2.730	1.875	30.483	1.533	0.4238
0.076	517	301	2.730	1.875	30.486	1.533	0.4239
0.15	531	322	2.730	1.875	30.490	1.532	0.4239
0.203	548	344	2.730	1.875	30.479	1.533	0.4237
0.5	678	400	2.728	1.875	30.442	1.535	0.4230
1	769	469	2.724	1.873	30.372	1.538	0.4217
2.45	920	577	2.715	1.871	30.216	1.546	0.4187
3.75	1007	640	2.710	1.869	30.118	1.551	0.4168
4.9	1067	687	2.704	1.868	30.029	1.556	0.4151
7.5	1174	753	2.694	1.866	29.886	1.563	0.4123
9.85	1238	798	2.687	1.864	29.757	1.570	0.4098
5	1106	708	2.693	1.866	29.876	1.564	0.4121
2.5	983	605	2.699	1.868	29.986	1.558	0.4143
1	812	494	2.706	1.870	30.099	1.552	0.4165
0.5	717	423	2.710	1.871	30.170	1.549	0.4178
0.2	586	350	2.714	1.872	30.237	1.545	0.4191
0.1	522	304	2.716	1.873	30.266	1.544	0.4197
0.128	534	319	2.715	1.873	30.262	1.544	0.4196
0.2	557	338	2.715	1.873	30.260	1.544	0.4196
0.5	674	397	2.713	1.872	30.221	1.546	0.4188
1	781	468	2.709	1.871	30.160	1.549	0.4176
2.5	943	585	2.702	1.869	30.032	1.556	0.4152
5	1104	698	2.695	1.867	29.905	1.562	0.4127

Table A.1, cont.: Galveston Beach Sand, dry

Pressure	V_P	V_S	Length	Radius	Volume	Density	Porosity
(MPa)	(m/sec)	(m/sec)	(cm)	(cm)	(mL)	(g/cm^3)	
10	1260	806	2.683	1.862	29.687	1.574	0.4084
12.5	1314	844	2.677	1.861	29.589	1.579	0.4064
15	1371	877	2.671	1.859	29.491	1.584	0.4044
17.5	1414	904	2.665	1.858	29.391	1.590	0.4024
20	1448	928	2.659	1.856	29.296	1.595	0.4005
15	1395	888	2.662	1.858	29.355	1.592	0.4017
10	1291	820	2.667	1.859	29.444	1.587	0.4035
5	1145	720	2.674	1.862	29.574	1.580	0.4061
2.5	996	608	2.681	1.864	29.688	1.574	0.4084
1	838	493	2.688	1.866	29.807	1.567	0.4107
0.5	716	425	2.692	1.867	29.880	1.564	0.4122
0.51	740	435	2.693	1.867	29.884	1.563	0.4123
0.2	614	349	2.697	1.868	29.955	1.560	0.4137
0.1	520	299	2.699	1.869	29.991	1.558	0.4144
0	399	220	2.701	1.869	30.019	1.556	0.4149

Table A.2: Galveston Beach Sand, water saturated

Pressure	V_P	V_S	Length	Radius	Volume	Density	Porosity
(MPa)	(m/sec)	(m/sec)	(cm)	(cm)	(mL)	(g/cm^3)	
0			2.713	1.900	30.828	1.937	0.4354
0.1			2.712	1.899	30.799	1.938	0.4348
0.2			2.711	1.898	30.759	1.939	0.4341
0.2			2.710	1.897	30.726	1.940	0.4335
0.1			2.710	1.897	30.730	1.940	0.4336
0.198			2.709	1.897	30.712	1.941	0.4332
0.1			2.710	1.897	30.714	1.941	0.4333
0.1	1734	197	2.710	1.897	30.733	1.940	0.4336
0.15	1775	233	2.709	1.896	30.694	1.941	0.4329
0.2	1774	259	2.708	1.895	30.652	1.943	0.4321
0.3	1772	288	2.706	1.895	30.622	1.944	0.4316
0.5	1821	332	2.702	1.894	30.566	1.945	0.4306
0.8	1796	375	2.697	1.893	30.505	1.947	0.4294
1.3	1828	427	2.691	1.892	30.411	1.950	0.4276
1.8	1828	464	2.687	1.892	30.351	1.952	0.4265
2.3	1837	491	2.684	1.891	30.294	1.954	0.4254
0.5	1797	369	2.692	1.893	30.442	1.949	0.4282
0.2	1774	298	2.695	1.894	30.491	1.948	0.4292
0.1	1771	258	2.696	1.895	30.520	1.947	0.4297
0.2	1778	290	2.696	1.895	30.521	1.947	0.4297
0.5	1790	349	2.694	1.894	30.478	1.948	0.4289
1	1807	406	2.690	1.893	30.410	1.950	0.4276
2.5	1830	503	2.681	1.890	30.243	1.955	0.4245
3.75	1850	543	2.674	1.889	30.148	1.958	0.4226
5	1876	590	2.669	1.888	30.062	1.961	0.4210
7.5	1908	640	2.659	1.886	29.904	1.966	0.4179
10	1908	686	2.651	1.884	29.768	1.971	0.4153
7.5	1918	649	2.653	1.884	29.813	1.969	0.4162
5	1880	617	2.658	1.886	29.888	1.967	0.4176
3.75	1856	567	2.660	1.886	29.936	1.965	0.4186

Table A.2, cont.: Galveston Beach Sand, water saturated

Pressure	V_P	V_S	Length	Radius	Volume	Density	Porosity
(MPa)	(m/sec)	(m/sec)	(cm)	(cm)	(mL)	(g/cm^3)	
2.5	1845	523	2.664	1.887	29.995	1.963	0.4197
1	1800	426	2.671	1.889	30.123	1.959	0.4222
0.5	1780	351	2.677	1.891	30.225	1.956	0.4241
0.2	1754	287	2.680	1.892	30.272	1.954	0.4250
0.1	1757	236	2.682	1.892	30.308	1.953	0.4257
0.2	1759	273	2.682	1.892	30.303	1.953	0.4256
0.5	1778	332	2.679	1.892	30.258	1.955	0.4248
1	1799	392	2.675	1.890	30.191	1.957	0.4235
2.5	1848	508	2.667	1.888	30.058	1.961	0.4209
5	1864	602	2.659	1.886	29.915	1.966	0.4182
10	1910	695	2.647	1.881	29.676	1.974	0.4135
12.5	1935	731	2.642	1.879	29.581	1.977	0.4116
15	1960	760	2.635	1.878	29.471	1.980	0.4094
17.5	1978	785	2.627	1.876	29.354	1.984	0.4070
20	1998	806	2.620	1.874	29.230	1.988	0.4045
15	1966	772	2.623	1.876	29.290	1.986	0.4057
10	1940	708	2.628	1.877	29.381	1.983	0.4076
5	1874	599	2.636	1.880	29.518	1.979	0.4103
2.5	1848	505	2.642	1.882	29.634	1.975	0.4126
1	1807	407	2.650	1.884	29.760	1.971	0.4151
1.29	1846	417	2.649	1.884	29.752	1.971	0.4150
1	1831	389	2.650	1.884	29.765	1.971	0.4152
0.5	1792	333	2.654	1.885	29.832	1.969	0.4165
0.3	1806	300	2.657	1.885	29.875	1.967	0.4174
0.2	1764	275	2.658	1.886	29.896	1.966	0.4178
0.1	1774	235	2.660	1.886	29.937	1.965	0.4186
0.05	1772	216	2.662	1.887	29.969	1.964	0.4192
0			2.665	1.888	30.009	1.963	0.4200

Table A.3: Gulf of Mexico Sand, dry

Pressure	V_P	V_S	Length	Radius	Volume	Density	Porosity
(MPa)	(m/sec)	(m/sec)	(cm)	(cm)	(mL)	(g/cm^3)	
0		114	3.418	1.883	38.374	1.504	0.4305
0.017	207	126	3.418	1.883	38.371	1.504	0.4304
0.025	233	141	3.418	1.882	38.351	1.505	0.4301
0.037	263	159	3.419	1.881	38.326	1.506	0.4297
0.05	279	174	3.419	1.880	38.300	1.507	0.4293
0.075	311	195	3.419	1.878	38.247	1.509	0.4286
0.1	350	214	3.418	1.875	38.159	1.512	0.4272
0.15	384	242	3.416	1.874	38.102	1.514	0.4264
0.2	434	259	3.413	1.872	38.036	1.517	0.4254
0.15	419	255	3.413	1.872	38.032	1.517	0.4253
0.1	404	239	3.414	1.873	38.041	1.517	0.4255
0.2	438	259	3.413	1.872	38.026	1.517	0.4252
0.3	513	298	3.408	1.871	37.946	1.521	0.4240
0.5	577	338	3.399	1.870	37.793	1.527	0.4217
0.2	506	299	3.400	1.870	37.830	1.525	0.4223
0.1	442	256	3.401	1.871	37.852	1.524	0.4226
0.1	444	254	3.401	1.871	37.855	1.524	0.4226
0.2	479	288	3.401	1.871	37.852	1.524	0.4226

Table A.3, cont.: Gulf of Mexico Sand, dry

Pressure (MPa)	V_P (m/sec)	V_S (m/sec)	Length (cm)	Radius (cm)	Volume (mL)	Density (g/cm³)	Porosity
0.5	576	343	3.397	1.868	37.743	1.529	0.4209
0.75	634	384	3.390	1.867	37.626	1.533	0.4191
1	747	416	3.383	1.866	37.518	1.538	0.4175
0.5	624	370	3.385	1.867	37.568	1.536	0.4182
0.2	512	304	3.388	1.868	37.648	1.533	0.4195
0.1	470	256	3.390	1.869	37.688	1.531	0.4201
0.2	474	287	3.389	1.869	37.679	1.531	0.4199
0.5	595	355	3.387	1.868	37.616	1.534	0.4190
1	742	419	3.380	1.865	37.475	1.540	0.4168
1	756	421	3.379	1.865	37.466	1.540	0.4166
1.5	773	461	3.371	1.864	37.332	1.546	0.4145
2	856	500	3.363	1.862	37.189	1.552	0.4123
2.5	895	530	3.356	1.861	37.081	1.556	0.4106
1.75	844	501	3.358	1.861	37.119	1.554	0.4112
1	768	442	3.361	1.863	37.193	1.551	0.4124
0.5	625	381	3.365	1.864	37.279	1.548	0.4137
0.2	510	303	3.370	1.866	37.367	1.544	0.4151
0.1	436	254	3.372	1.867	37.421	1.542	0.4159
0.2	465	283	3.372	1.866	37.412	1.542	0.4158
0.5	599	351	3.369	1.865	37.351	1.545	0.4149
1	755	425	3.364	1.864	37.248	1.549	0.4132
1	768	430	3.363	1.863	37.239	1.549	0.4131
2.5	935	535	3.351	1.859	36.989	1.560	0.4091
3.75	1001	597	3.337	1.857	36.776	1.569	0.4057
5	1061	649	3.325	1.854	36.570	1.578	0.4024
3.75	1017	619	3.327	1.855	36.614	1.576	0.4031
2.5	981	568	3.331	1.856	36.683	1.573	0.4042
1	778	452	3.338	1.858	36.824	1.567	0.4065
0.5	634	386	3.343	1.860	36.922	1.563	0.4081
0.2	509	305	3.348	1.862	37.025	1.558	0.4097
0.1	436	262	3.351	1.862	37.074	1.556	0.4105
0.2	465	286	3.350	1.862	37.069	1.557	0.4104
0.5	608	373	3.346	1.861	36.986	1.560	0.4091
1	751	431	3.342	1.860	36.910	1.563	0.4079
2.5	957	553	3.333	1.857	36.731	1.571	0.4050
5	1069	658	3.320	1.852	36.475	1.582	0.4008
7.5	1182	726	3.302	1.849	36.186	1.595	0.3960
10	1276	786	3.283	1.845	35.888	1.608	0.3910
7.5	1224	750	3.286	1.846	35.940	1.605	0.3919
5	1134	692	3.290	1.848	36.021	1.602	0.3932
2.5	993	593	3.297	1.850	36.156	1.596	0.3955
1	787	468	3.306	1.852	36.306	1.589	0.3980
0.5	659	399	3.311	1.854	36.410	1.585	0.3997
0.2	512	321	3.317	1.855	36.512	1.580	0.4014
0.1	434	267	3.320	1.856	36.576	1.578	0.4024
0.2	466	287	3.320	1.856	36.570	1.578	0.4024
0.5	602	368	3.315	1.855	36.486	1.581	0.4010
1	751	442	3.310	1.854	36.394	1.585	0.3995
2.5	939	573	3.301	1.851	36.231	1.593	0.3968
5	1101	684	3.293	1.848	36.070	1.600	0.3941
10	1304	797	3.277	1.842	35.743	1.614	0.3885

Table A.3, cont.: Gulf of Mexico Sand, dry

Pressure (MPa)	V_P (m/sec)	V_S (m/sec)	Length (cm)	Radius (cm)	Volume (mL)	Density (g/cm^3)	Porosity
12.5	1354	843	3.265	1.840	35.567	1.622	0.3855
15	1439	888	3.251	1.838	35.357	1.632	0.3819
10	1339	825	3.256	1.840	35.442	1.628	0.3833
5	1159	711	3.264	1.842	35.595	1.621	0.3860
2.5	1006	606	3.271	1.844	35.727	1.615	0.3882
1	806	484	3.279	1.847	35.879	1.608	0.3908
0.5	747	407	3.285	1.848	35.986	1.603	0.3927
0.2	530	323	3.291	1.850	36.089	1.599	0.3944
0.1	425	263	3.295	1.851	36.161	1.596	0.3956
0.2	459	290	3.295	1.851	36.159	1.596	0.3956
0.5	603	371	3.290	1.850	36.066	1.600	0.3940
1	776	450	3.284	1.848	35.972	1.604	0.3924
2.5	958	585	3.276	1.846	35.815	1.611	0.3898
5	1141	703	3.267	1.843	35.663	1.618	0.3872
10	1335	826	3.257	1.840	35.467	1.627	0.3838
15	1455	909	3.243	1.835	35.189	1.640	0.3789
17.5	1512	952	3.235	1.833	35.060	1.646	0.3766
20	1571	990	3.224	1.832	34.892	1.654	0.3736
15	1503	942	3.227	1.833	34.954	1.651	0.3747
10	1381	852	3.232	1.834	35.047	1.646	0.3764
5	1194	725	3.240	1.837	35.202	1.639	0.3791
2.5	1033	621	3.247	1.839	35.335	1.633	0.3815
1	837	494	3.256	1.841	35.483	1.626	0.3840
0.5	758	413	3.261	1.843	35.583	1.622	0.3858
0.2	519	321	3.269	1.845	35.715	1.616	0.3880
0.1	422	256	3.274	1.846	35.806	1.611	0.3896
0.2	429	284	3.273	1.846	35.797	1.612	0.3894
0.5	603	372	3.267	1.845	35.693	1.617	0.3877
1	782	456	3.261	1.843	35.590	1.621	0.3859
2.5	999	602	3.252	1.840	35.426	1.629	0.3831
5	1162	715	3.244	1.838	35.279	1.636	0.3805
10	1358	845	3.234	1.835	35.086	1.645	0.3771
15	1491	941	3.225	1.832	34.926	1.652	0.3742
20	1581	1009	3.215	1.829	34.724	1.662	0.3706
15	1527	961	3.218	1.830	34.786	1.659	0.3717
10	1399	873	3.222	1.831	34.875	1.654	0.3733
5	1209	739	3.230	1.834	35.025	1.647	0.3760
2.5	1046	630	3.238	1.836	35.154	1.641	0.3783
1	847	505	3.246	1.838	35.301	1.635	0.3809
0.5	749	420	3.251	1.840	35.395	1.630	0.3825
0.2	516	323	3.258	1.842	35.524	1.624	0.3847
0.1	421	249	3.264	1.843	35.627	1.620	0.3865
0.05	283	210	3.267	1.844	35.673	1.617	0.3873
0.025		201	3.267	1.844	35.668	1.618	0.3872
0	313	202	3.267	1.844	35.672	1.618	0.3873

Table A.4: Gulf of Mexico Sand, water saturated

Pressure	V_P	V_S	Length	Radius	Volume	Density	Porosity
(MPa)	(m/sec)	(m/sec)	(cm)	(cm)	(mL)	(g/cm^3)	
0			4.284	1.886	48.180	1.940	0.4269
0.025			4.283	1.885	48.152	1.940	0.4266
0.0375			4.283	1.884	48.130	1.941	0.4263
0.05			4.283	1.884	48.102	1.941	0.4260
0.075			4.283	1.882	48.039	1.943	0.4253
0.1			4.282	1.880	47.979	1.944	0.4245
0.15			4.277	1.879	47.878	1.946	0.4233
0.2			4.273	1.878	47.816	1.947	0.4226
0.2			4.263	1.873	47.532	1.953	0.4191
0.1			4.263	1.873	47.529	1.953	0.4191
0.2			4.263	1.873	47.535	1.953	0.4192
0.1			4.264	1.874	47.549	1.952	0.4193
0.1			4.264	1.874	47.551	1.952	0.4194
0.1			4.263	1.874	47.547	1.952	0.4193
0.045			4.263	1.874	47.548	1.952	0.4193
0.1	1756		4.263	1.874	47.540	1.952	0.4192
0.15	1760	180	4.261	1.872	47.474	1.954	0.4184
0.2	1760	195	4.257	1.866	47.224	1.959	0.4153
0.3	1782	233	4.250	1.865	47.127	1.961	0.4141
0.4	1786	259	4.244	1.865	47.033	1.963	0.4130
0.5	1793	286	4.238	1.864	46.945	1.965	0.4119
0.3	1789	257	4.240	1.865	46.983	1.964	0.4123
0.2	1781	224	4.241	1.865	47.020	1.963	0.4128
0.1	1770	191	4.243	1.866	47.072	1.962	0.4135
0.2	1782	213	4.242	1.866	47.059	1.962	0.4133
0.5	1795	287	4.236	1.864	46.908	1.965	0.4114
0.75	1807	314	4.228	1.862	46.774	1.968	0.4097
1	1811	349	4.220	1.861	46.650	1.971	0.4082
0.5	1798	303	4.224	1.863	46.746	1.969	0.4094
0.2	1783	233	4.228	1.864	46.845	1.967	0.4106
0.1	1774	193	4.231	1.865	46.916	1.965	0.4115
0.2	1785	224	4.230	1.865	46.900	1.965	0.4113
0.5	1795	301	4.225	1.863	46.768	1.968	0.4096
1	1816	359	4.216	1.860	46.579	1.972	0.4073
1.5	1832	406	4.206	1.859	46.420	1.975	0.4052
2	1856	444	4.196	1.857	46.253	1.979	0.4031
2.5	1867	467	4.187	1.856	46.118	1.982	0.4013
1.5	1856	428	4.191	1.857	46.199	1.980	0.4024
1	1830	384	4.195	1.858	46.276	1.978	0.4034
0.5	1810	311	4.200	1.860	46.393	1.976	0.4049
0.2	1796	239	4.207	1.862	46.535	1.973	0.4067
0.1	1788	193	4.211	1.864	46.635	1.971	0.4080
0.2	1794	223	4.210	1.863	46.612	1.971	0.4077
0.5	1809	301	4.205	1.862	46.502	1.974	0.4063
1	1830	361	4.198	1.859	46.347	1.977	0.4043
1.75	1853	436	4.190	1.857	46.177	1.981	0.4021
2.5	1878	475	4.183	1.855	46.030	1.984	0.4002
3.75	1892	537	4.167	1.852	45.778	1.989	0.3969
5	1938	592	4.149	1.850	45.493	1.995	0.3931
2.5	1905	505	4.157	1.852	45.654	1.992	0.3952
1	1850	388	4.167	1.855	45.847	1.988	0.3978

Table A.4, cont.: Gulf of Mexico Sand, water saturated

Pressure	V_P	V_S	Length	Radius	Volume	Density	Porosity
(MPa)	(m/sec)	(m/sec)	(cm)	(cm)	(mL)	(g/cm^3)	
0.5	1864	310	4.174	1.857	45.989	1.985	0.3996
0.2	1805	237	4.181	1.859	46.138	1.981	0.4016
0.1	1788	192	4.187	1.860	46.245	1.979	0.4030
0.2	1795	210	4.185	1.860	46.223	1.980	0.4027
0.5	1816	300	4.179	1.858	46.098	1.982	0.4011
1	1845	382	4.171	1.856	45.944	1.986	0.3991
2.5	1886	502	4.158	1.852	45.680	1.991	0.3956
5	1923	595	4.144	1.847	45.352	1.998	0.3912
7.5	1965	667	4.123	1.844	45.009	2.006	0.3866
10	2024	721	4.099	1.840	44.616	2.015	0.3812
5	1969	618	4.108	1.842	44.800	2.011	0.3837
2.5	1917	513	4.117	1.845	44.978	2.007	0.3862
1	1864	401	4.127	1.847	45.181	2.002	0.3889
0.5	1833	307	4.135	1.849	45.318	1.999	0.3908
0.2	1810	222	4.145	1.852	45.517	1.995	0.3934
0.1	1789	191	4.156	1.855	45.738	1.990	0.3963
0.2	1799	208	4.153	1.854	45.684	1.991	0.3956
0.5	1818	298	4.144	1.852	45.499	1.995	0.3932
1	1853	381	4.135	1.849	45.332	1.999	0.3909
2.5	1906	513	4.122	1.846	45.076	2.005	0.3875
5	1962	623	4.109	1.843	44.831	2.010	0.3841
10	2019	733	4.090	1.836	44.415	2.019	0.3784
12.5	2055	776	4.076	1.834	44.184	2.025	0.3751
15	2103	814	4.060	1.831	43.925	2.031	0.3714
17.5	2137	848	4.043	1.829	43.667	2.037	0.3677
20	2169	889	4.026	1.826	43.399	2.043	0.3638
15	2135	839	4.030	1.827	43.478	2.041	0.3650
10	2082	765	4.037	1.829	43.611	2.038	0.3669
5	1994	634	4.047	1.832	43.807	2.034	0.3697
2.5	1942	531	4.057	1.834	43.990	2.029	0.3724
1	1889	405	4.068	1.837	44.189	2.025	0.3752
0.5	1843	303	4.077	1.839	44.368	2.021	0.3777
0.2	1823	206	4.091	1.842	44.625	2.015	0.3813
0.1			4.111	1.847	44.988	2.006	0.3863
0.06			4.111	1.847	44.988	2.006	0.3863
0			4.112	1.847	44.996	2.006	0.3864

Table A.5: Merritt Sand, dry

Pressure	V_P	V_S	Length	Radius	Volume	Density	Porosity
(MPa)	(m/sec)	(m/sec)	(cm)	(cm)	(mL)	(g/cm^3)	
0			5.411	1.883	60.726	1.678	0.3722
0.025			5.411	1.883	60.726	1.678	0.3722
0.05			5.409	1.882	60.693	1.679	0.3718
0.052			5.409	1.882	60.691	1.679	0.3718
0.075			5.408	1.882	60.653	1.680	0.3714
0.1			5.405	1.881	60.598	1.682	0.3708
0.15			5.399	1.879	60.454	1.686	0.3693
0.2			5.394	1.878	60.363	1.688	0.3684
0.1			5.395	1.878	60.372	1.688	0.3685
0.2			5.394	1.878	60.347	1.689	0.3682

Table A.5, cont.: Merritt Sand, dry

Pressure	V_P	V_S	Length	Radius	Volume	Density	Porosity
(MPa)	(m/sec)	(m/sec)	(cm)	(cm)	(mL)	(g/cm^3)	
0.3		426	5.385	1.876	60.168	1.694	0.3663
0.4		442	5.380	1.875	60.052	1.697	0.3651
0.5		443	5.375	1.874	59.937	1.700	0.3639
0.3		442	5.376	1.874	59.955	1.700	0.3641
0.2		425	5.377	1.874	59.978	1.699	0.3643
0.1	592	362	5.379	1.875	60.031	1.698	0.3649
0.2	594	423	5.379	1.875	60.023	1.698	0.3648
0.3		426	5.377	1.874	59.995	1.699	0.3645
0.5		443	5.374	1.873	59.907	1.701	0.3636
0.75	912	496	5.363	1.870	59.676	1.708	0.3611
1	878	584	5.354	1.868	59.461	1.714	0.3588
0.5	906	493	5.356	1.868	59.508	1.713	0.3593
0.2	691	425	5.361	1.869	59.606	1.710	0.3604
0.1	600	360	5.364	1.870	59.684	1.707	0.3612
0.2	599	421	5.364	1.870	59.674	1.708	0.3611
0.5	881	441	5.359	1.869	59.582	1.710	0.3601
1	1011	583	5.352	1.867	59.417	1.715	0.3583
1.5	1124	615	5.339	1.864	59.147	1.723	0.3554
2	1170	596	5.330	1.862	58.954	1.729	0.3533
1.33	1124	622	5.332	1.862	58.993	1.728	0.3537
2	1201	597	5.329	1.862	58.924	1.730	0.3530
2.5	1221	619	5.322	1.860	58.773	1.734	0.3513
1.75	1190	594	5.323	1.860	58.808	1.733	0.3517
1	1021	523	5.327	1.861	58.897	1.730	0.3527
0.5	881	441	5.333	1.863	59.014	1.727	0.3540
0.2	704	374	5.339	1.864	59.147	1.723	0.3554
0.1	591	330	5.343	1.865	59.232	1.721	0.3563
0.2	599	360	5.342	1.865	59.220	1.721	0.3562
0.29	709	383	5.339	1.864	59.149	1.723	0.3554
0.5	766	416	5.338	1.864	59.133	1.723	0.3553
1	1000	487	5.332	1.863	59.001	1.727	0.3538
2.5	1220	620	5.318	1.858	58.653	1.738	0.3500
3.75	1322	676	5.303	1.855	58.352	1.746	0.3466
5	1371	725	5.290	1.851	58.072	1.755	0.3435
2.5	1223	622	5.296	1.853	58.208	1.751	0.3450
1	1015	488	5.305	1.855	58.405	1.745	0.3472
0.5	775	418	5.311	1.857	58.530	1.741	0.3486
0.2	606	347	5.317	1.859	58.675	1.737	0.3502
0.1	526	306	5.325	1.861	58.839	1.732	0.3520
0.2	537	329	5.322	1.860	58.775	1.734	0.3513
0.5	716	375	5.317	1.859	58.682	1.737	0.3503
1	890	449	5.311	1.857	58.541	1.741	0.3487
2.5	1215	593	5.300	1.854	58.292	1.748	0.3459
5	1397	730	5.286	1.849	57.932	1.759	0.3419
7.5	1531	798	5.268	1.845	57.579	1.770	0.3379
10	1601	851	5.251	1.842	57.242	1.780	0.3340
5	1375	732	5.259	1.844	57.427	1.775	0.3361
2.5	1154	589	5.268	1.846	57.618	1.769	0.3383
1	995	468	5.277	1.849	57.831	1.762	0.3407
0.5	776	404	5.284	1.851	57.970	1.758	0.3423
0.2	605	334	5.291	1.852	58.113	1.754	0.3439

Table A.5, cont.: Merritt Sand, dry

Pressure	V_P	V_S	Length	Radius	Volume	Density	Porosity
(MPa)	(m/sec)	(m/sec)	(cm)	(cm)	(mL)	(g/cm^3)	
0.1		305	5.295	1.853	58.199	1.751	0.3449
0.2	515	313	5.295	1.853	58.213	1.751	0.3451
0.5	680	364	5.291	1.852	58.131	1.753	0.3441
1	884	439	5.284	1.851	57.981	1.758	0.3424
2.5	1117	569	5.273	1.848	57.737	1.765	0.3397
5	1337	711	5.262	1.845	57.496	1.772	0.3369
10	1643	863	5.244	1.838	57.012	1.788	0.3313
12.5	1688	899	5.232	1.835	56.790	1.795	0.3286
15	1756	939	5.218	1.832	56.510	1.803	0.3253
10	1645	875	5.223	1.834	56.637	1.799	0.3268
2.5	1162	599	5.242	1.839	57.057	1.786	0.3318
1	982	475	5.252	1.842	57.273	1.779	0.3343
0.5	867	405	5.259	1.844	57.418	1.775	0.3360
0.2	600	327	5.267	1.846	57.594	1.769	0.3380
0.1	522	280	5.271	1.847	57.692	1.766	0.3392
0.2	534	304	5.270	1.847	57.676	1.767	0.3390
0.5	676	366	5.266	1.846	57.575	1.770	0.3378
1	886	445	5.259	1.844	57.422	1.775	0.3360
2.5	1152	576	5.248	1.841	57.192	1.782	0.3334
5	1321	715	5.237	1.838	56.951	1.789	0.3306
7.62	1549	828	5.225	1.835	56.683	1.798	0.3274
10	1647	867	5.224	1.834	56.653	1.799	0.3270
15	1801	949	5.211	1.829	56.294	1.810	0.3227
17.5	1864	981	5.201	1.827	56.099	1.817	0.3204
20	1927	1010	5.190	1.824	55.868	1.824	0.3176
15	1820	967	5.194	1.825	55.959	1.821	0.3187
10	1617	870	5.201	1.827	56.114	1.816	0.3206
5	1356	728	5.211	1.830	56.356	1.808	0.3235
2.5	1196	600	5.220	1.833	56.545	1.802	0.3257
1	995	472	5.230	1.836	56.778	1.795	0.3285
0.5	867	406	5.237	1.837	56.924	1.790	0.3302
0.2	603	329	5.244	1.839	57.081	1.785	0.3321
0.1	521	280	5.249	1.841	57.184	1.782	0.3333
0.2	570	308	5.247	1.840	57.154	1.783	0.3329
0.5	687	372	5.243	1.839	57.065	1.786	0.3319
1	930	448	5.237	1.837	56.921	1.790	0.3302
2.5	1165	585	5.225	1.834	56.674	1.798	0.3273
5	1320	713	5.215	1.832	56.455	1.805	0.3247
10	1623	860	5.203	1.828	56.173	1.814	0.3213
10	1619	868	5.202	1.828	56.161	1.815	0.3211
15	1813	953	5.193	1.825	55.948	1.822	0.3185
20	1931	1015	5.182	1.821	55.646	1.831	0.3149
15	1837	974	5.186	1.822	55.738	1.828	0.3160
10	1643	878	5.191	1.824	55.880	1.824	0.3177
5	1359	734	5.202	1.827	56.122	1.816	0.3207
2.5	1183	607	5.210	1.830	56.317	1.810	0.3230
1	985	473	5.221	1.832	56.543	1.802	0.3257
0.5	866	404	5.227	1.834	56.689	1.798	0.3275
0.2	521	289	5.242	1.838	57.004	1.788	0.3312
0.1	456	248	5.244	1.838	57.036	1.787	0.3315
0			5.249	1.840	57.160	1.783	0.3330

Table A.6: Merritt Sand, water saturated

Pressure (MPa)	V_P (m/sec)	V_S (m/sec)	Length (cm)	Radius (cm)	Volume (mL)	Density (g/cm^3)	Porosity
0			5.133	1.925	59.360	2.102	0.3414
0.025			5.134	1.925	59.365	2.102	0.3415
0.017			5.133	1.925	59.364	2.102	0.3414
0.05			5.134	1.925	59.364	2.102	0.3414
0.075			5.134	1.925	59.366	2.102	0.3415
0.1			5.132	1.925	59.338	2.102	0.3412
0.15			5.123	1.925	59.230	2.104	0.3400
0.2			5.115	1.925	59.140	2.106	0.3389
0.2			5.114	1.925	59.130	2.106	0.3388
0.147			5.114	1.925	59.129	2.106	0.3388
0.1			5.114	1.925	59.131	2.106	0.3388
0.1	1801	187	5.114	1.925	59.130	2.106	0.3388
0.1	1792	186	5.114	1.925	59.132	2.106	0.3389
0.15	1821	199	5.113	1.925	59.120	2.106	0.3387
0.2	1817	231	5.109	1.925	59.072	2.107	0.3382
0.3	1837	251	5.100	1.925	58.970	2.109	0.3370
0.5	1835	285	5.085	1.925	58.781	2.113	0.3349
0.2	1828	251	5.085	1.925	58.787	2.113	0.3350
0.1	1810	199	5.087	1.925	58.808	2.112	0.3352
0.2	1837	230	5.087	1.925	58.804	2.112	0.3352
0.5	1846	285	5.077	1.925	58.685	2.115	0.3338
0.75	1867	329	5.065	1.924	58.531	2.117	0.3321
1	1867	368	5.053	1.923	58.361	2.121	0.3301
0.5	1853	325	5.057	1.924	58.405	2.120	0.3306
0.2	1829	269	5.061	1.924	58.454	2.119	0.3312
0.1	1832	229	5.065	1.924	58.505	2.118	0.3318
0.2	1841	249	5.065	1.924	58.501	2.118	0.3317
0.5	1847	323	5.059	1.924	58.434	2.119	0.3310
0.076	1841		5.065	1.924	58.504	2.118	0.3318
0.5	1859	325	5.056	1.924	58.397	2.120	0.3305
1	1865	368	5.047	1.923	58.288	2.122	0.3293
1.5	1927	423	5.034	1.922	58.082	2.126	0.3269
2	1924	478	5.022	1.921	57.898	2.130	0.3248
2.5	1933	491	5.010	1.919	57.692	2.134	0.3224
1.75	1922	477	5.013	1.919	57.728	2.133	0.3228
1	1925	366	5.018	1.920	57.800	2.132	0.3236
0.5	1867	324	5.026	1.920	57.900	2.130	0.3248
0.2	1859	267	5.030	1.920	57.962	2.128	0.3255
0.1	1856	228	5.033	1.920	58.004	2.128	0.3260
0.2	1850	261	5.033	1.920	58.004	2.128	0.3260
0.5	1872	325	5.026	1.920	57.913	2.129	0.3249
1	1907	366	5.020	1.920	57.824	2.131	0.3239
1	1916	367	5.016	1.920	57.775	2.132	0.3233
2.5	1947	494	4.998	1.916	57.444	2.139	0.3194
3.75	1978	557	4.982	1.915	57.184	2.144	0.3163
5	2015	613	4.963	1.912	56.848	2.151	0.3123
2.5	1962	551	4.971	1.912	56.960	2.148	0.3137
1	1934	413	4.980	1.913	57.105	2.145	0.3154
0.5	1883	326	4.987	1.914	57.196	2.144	0.3165

Table A.6, cont.: Merritt Sand, water saturated

Pressure	V_P	V_S	Length	Radius	Volume	Density	Porosity
(MPa)	(m/sec)	(m/sec)	(cm)	(cm)	(mL)	(g/cm^3)	
0.1	1857	227	4.999	1.915	57.379	2.140	0.3187
0.2	1858	258	4.997	1.915	57.351	2.140	0.3183
0.5	1892	326	4.989	1.914	57.231	2.143	0.3169
1	1933	418	4.980	1.913	57.105	2.145	0.3154
2.5	1970	539	4.966	1.912	56.899	2.149	0.3129
5	2032	616	4.949	1.907	56.482	2.158	0.3078
7.5	2100	729	4.927	1.903	56.092	2.166	0.3030
10	2158	752	4.898	1.898	55.557	2.177	0.2963
5	2101	645	4.907	1.899	55.715	2.174	0.2983
2.5	2007	548	4.916	1.900	55.857	2.171	0.3001
1	1957	418	4.927	1.901	56.029	2.167	0.3022
0.5	1944	361	4.937	1.903	56.203	2.164	0.3044
0.2	1913	292	4.941	1.903	56.256	2.163	0.3051
0.1	1899	263	4.943	1.903	56.290	2.162	0.3055
0.2	1932	278	4.942	1.903	56.281	2.162	0.3054
0.5	1934	360	4.937	1.903	56.205	2.164	0.3044
1	1980	417	4.931	1.902	56.107	2.166	0.3032
2.5	2016	547	4.920	1.901	55.918	2.170	0.3009
5	2095	651	4.907	1.899	55.718	2.174	0.2983
10	2197	764	4.887	1.894	55.294	2.183	0.2930
12.5	2221	834	4.870	1.891	54.971	2.190	0.2888
15	2319	877	4.850	1.887	54.584	2.198	0.2838
10	2238	794	4.855	1.888	54.685	2.196	0.2851
5	2163	678	4.865	1.889	54.858	2.192	0.2873
2.5	2057	550	4.875	1.891	55.014	2.189	0.2894
1	2004	469	4.884	1.892	55.178	2.185	0.2915
0.5	1958	359	4.891	1.893	55.294	2.183	0.2930
0.25	1927	318	4.898	1.894	55.397	2.181	0.2943
0.2	1940	316	4.898	1.894	55.411	2.180	0.2945
0.1	1917	275	4.903	1.894	55.487	2.179	0.2954
0.2	1924	291	4.903	1.894	55.484	2.179	0.2954
1	1993	480	4.892	1.893	55.300	2.183	0.2930
2.5	2053	551	4.880	1.891	55.100	2.187	0.2905
5	2131	724	4.868	1.890	54.907	2.191	0.2880
10	2232	829	4.852	1.887	54.639	2.197	0.2845
15	2320	887	4.838	1.883	54.292	2.205	0.2799
17.5	2350	919	4.825	1.880	54.052	2.210	0.2767
20	2383	967	4.811	1.877	53.773	2.216	0.2730
15	2335	897	4.815	1.878	53.846	2.215	0.2740
10	2275	837	4.822	1.879	53.967	2.212	0.2756
5	2194	723	4.831	1.880	54.137	2.208	0.2779
2.5	2103	601	4.841	1.882	54.301	2.204	0.2800
1	2059	483	4.851	1.884	54.484	2.200	0.2825
0.5	2008	408	4.857	1.885	54.588	2.198	0.2838
0.2	1963	320	4.865	1.886	54.724	2.195	0.2856
0.1	1947	261	4.870	1.886	54.807	2.193	0.2867
0.2	1946	315	4.870	1.886	54.802	2.193	0.2866
0.5	2009	357	4.864	1.886	54.698	2.196	0.2853
1	2050	480	4.856	1.884	54.573	2.198	0.2836
2.5	2128	598	4.846	1.883	54.401	2.202	0.2814
1.24	2070	543	4.851	1.884	54.481	2.201	0.2824

Table A.6, cont.: Merritt Sand, water saturated

Pressure	V_P	V_S	Length	Radius	Volume	Density	Porosity
(MPa)	(m/sec)	(m/sec)	(cm)	(cm)	(mL)	(g/cm^3)	
2.5	2122	603	4.846	1.883	54.393	2.202	0.2813
5	2195	728	4.835	1.881	54.207	2.207	0.2788
10	2296	857	4.821	1.879	53.959	2.212	0.2755
15	2371	918	4.809	1.877	53.753	2.217	0.2727
20	2455	987	4.797	1.872	53.441	2.224	0.2685
15	2344	942	4.801	1.873	53.518	2.222	0.2695
10	2313	855	4.807	1.874	53.624	2.220	0.2710
5	2186	730	4.817	1.876	53.804	2.216	0.2734
2.5	2168	627	4.826	1.877	53.963	2.212	0.2755
2.86	2171	638	4.825	1.877	53.958	2.212	0.2755
1	2060	495	4.836	1.879	54.138	2.208	0.2779
0.5	2010	410	4.842	1.880	54.248	2.206	0.2793
0.2	1979	334	4.850	1.881	54.386	2.203	0.2812
0.1	1963	289	4.855	1.882	54.468	2.201	0.2822
0.05	1945	260	4.858	1.883	54.527	2.200	0.2830
0	1917		4.864	1.884	54.634	2.197	0.2844

Table A.7: Pomponio Beach Sand, dry

Pressure	V_P	V_S	Length	Radius	Volume	Density	Porosity
(MPa)	(m/sec)	(m/sec)	(cm)	(cm)	(mL)	(g/cm^3)	
0	338		2.652	1.895	30.012	1.637	0.3997
0.025	473	274	2.651	1.895	30.007	1.637	0.3996
0.05	484	293	2.650	1.894	29.988	1.638	0.3992
0.075	510	312	2.650	1.894	29.979	1.639	0.3990
0.1	557	331	2.649	1.894	29.972	1.639	0.3989
0.15	586	351	2.648	1.894	29.952	1.640	0.3985
0.2	652	369	2.647	1.893	29.932	1.641	0.3981
0.3	686	396	2.645	1.893	29.903	1.643	0.3975
0.5	794	431	2.643	1.892	29.855	1.646	0.3966
0.75	845	467	2.640	1.891	29.804	1.648	0.3955
1	861	492	2.637	1.890	29.758	1.651	0.3946
1.25	937	518	2.635	1.889	29.714	1.653	0.3937
1.5	967	541	2.633	1.889	29.683	1.655	0.3930
2	1001	580	2.629	1.888	29.623	1.658	0.3918
2.45	1031	640	2.627	1.887	29.579	1.661	0.3909
1.05	892	486	2.631	1.889	29.656	1.657	0.3925
0.55	752	420	2.635	1.890	29.714	1.653	0.3937
0.5	686	385	2.639	1.891	29.790	1.649	0.3952
0.12	531	313	2.640	1.891	29.801	1.649	0.3954
0.1	513	311	2.640	1.891	29.811	1.648	0.3957
0.2	662	362	2.638	1.891	29.785	1.649	0.3951
0.5	780	428	2.636	1.890	29.747	1.652	0.3943
1	844	489	2.633	1.889	29.688	1.655	0.3932
2.5	1035	655	2.625	1.885	29.521	1.664	0.3897
3.6	1178	697	2.620	1.884	29.431	1.669	0.3878
4.9	1208	729	2.615	1.883	29.357	1.674	0.3863
7.4	1320	785	2.606	1.881	29.209	1.682	0.3832
9.95	1358	829	2.598	1.879	29.074	1.690	0.3803
5	1224	737	2.604	1.880	29.178	1.684	0.3826
2.55	1046	600	2.609	1.882	29.269	1.679	0.3845

Table A.7, cont.: Pomponio Beach Sand, dry

Pressure	V_P	V_S	Length	Radius	Volume	Density	Porosity
(MPa)	(m/sec)	(m/sec)	(cm)	(cm)	(mL)	(g/cm^3)	
1.15	942	488	2.614	1.884	29.362	1.673	0.3864
0.55	802	424	2.620	1.886	29.465	1.667	0.3886
0.21	634	344	2.623	1.886	29.510	1.665	0.3895
0.1	480	284	2.625	1.887	29.546	1.663	0.3902
0.5	760	419	2.620	1.886	29.473	1.667	0.3887
1	875	485	2.617	1.885	29.419	1.670	0.3876
2.45	1037	599	2.611	1.883	29.316	1.676	0.3854
4.9	1233	730	2.605	1.881	29.205	1.682	0.3831
10	1366	842	2.595	1.876	28.978	1.695	0.3783
12.45	1439	881	2.588	1.874	28.867	1.702	0.3759
14.9	1503	911	2.582	1.872	28.769	1.708	0.3738
17.5	1588	951	2.573	1.870	28.626	1.716	0.3706
20	1643	993	2.561	1.868	28.449	1.727	0.3667
15	1580	944	2.564	1.869	28.494	1.724	0.3677
9.95	1441	866	2.567	1.870	28.563	1.720	0.3693
5.05	1255	754	2.573	1.872	28.670	1.714	0.3716
2.5	1110	609	2.579	1.874	28.767	1.708	0.3737
1.1	902	486	2.584	1.876	28.867	1.702	0.3759
0.5	761	410	2.589	1.877	28.952	1.697	0.3777
0.2	652	331	2.594	1.879	29.039	1.692	0.3796
0.1	410	269	2.597	1.880	29.088	1.689	0.3806
5	1245	765	2.575	1.873	28.710	1.711	0.3725
9.95	1421	879	2.568	1.871	28.575	1.719	0.3695
15	1584	955	2.562	1.868	28.462	1.726	0.3670
20	1698	1042	2.550	1.863	28.239	1.740	0.3620
20	1750	1048	2.549	1.863	28.221	1.741	0.3616
20	1734	1052	2.548	1.863	28.203	1.742	0.3612
20	1754	1053	2.544	1.863	28.161	1.745	0.3603
20.05	1761	1057	2.547	1.862	28.182	1.743	0.3607
20	1774	1060	2.546	1.862	28.169	1.744	0.3604
20	1745	1062	2.545	1.862	28.152	1.745	0.3600
20	1736	1062	2.545	1.862	28.151	1.745	0.3600
20	1786	1065	2.544	1.862	28.132	1.746	0.3596
20	1804	1069	2.544	1.861	28.122	1.747	0.3594
20	1803	1069	2.543	1.861	28.110	1.748	0.3591
20	1763	1071	2.543	1.861	28.107	1.748	0.3590
20	1778	1073	2.542	1.861	28.090	1.749	0.3586
20	1763	1073	2.541	1.861	28.072	1.750	0.3582
15	1685	1010	2.543	1.862	28.119	1.747	0.3593
10.05	1570	924	2.546	1.863	28.183	1.743	0.3607
7.55	1448	865	2.548	1.864	28.226	1.741	0.3617
5.05	1333	792	2.553	1.866	28.309	1.736	0.3636
2.6	1208	646	2.557	1.867	28.390	1.731	0.3654
2.5	1176	647	2.558	1.867	28.396	1.730	0.3655
1	973	513	2.562	1.869	28.476	1.725	0.3673
0.5	893	449	2.566	1.870	28.544	1.721	0.3688
0.25	797	371	2.570	1.871	28.616	1.717	0.3704
0.1	511	292	2.574	1.872	28.669	1.714	0.3716
0			2.600	1.880	29.126	1.687	0.3814

Table A.8: Pomponio Beach Sand, water saturated

Pressure	V_P	V_S	Length	Radius	Volume	Density	Porosity
(MPa)	(m/sec)	(m/sec)	(cm)	(cm)	(mL)	(g/cm^3)	
0			3.136	1.899	35.617	2.040	0.3978
0			3.137	1.899	35.627	2.040	0.3980
0.024			3.137	1.899	35.613	2.040	0.3977
0.05			3.136	1.899	35.605	2.040	0.3976
0.075			3.135	1.899	35.590	2.041	0.3973
0.1			3.134	1.899	35.581	2.041	0.3972
0.15			3.133	1.899	35.559	2.042	0.3968
0.2			3.131	1.898	35.529	2.043	0.3963
0.2			3.131	1.898	35.532	2.042	0.3964
0.2			3.131	1.898	35.522	2.043	0.3962
0.2			3.130	1.898	35.513	2.043	0.3960
0.2			3.129	1.898	35.499	2.043	0.3958
0.2			3.128	1.898	35.475	2.044	0.3954
0.173			3.128	1.897	35.473	2.044	0.3954
0.068			3.129	1.898	35.490	2.044	0.3957
0.147			3.128	1.897	35.470	2.044	0.3953
0.129			3.128	1.897	35.479	2.044	0.3955
0.203			3.127	1.897	35.454	2.045	0.3950
0.291			3.126	1.897	35.433	2.045	0.3947
0.1			3.127	1.897	35.460	2.045	0.3951
0.073			3.127	1.897	35.453	2.045	0.3950
0.114			3.127	1.897	35.456	2.045	0.3951
0.108			3.127	1.897	35.458	2.045	0.3951
0.205			3.125	1.897	35.428	2.046	0.3946
0.1	1884	226	3.127	1.897	35.450	2.045	0.3950
0.1	1861	226	3.126	1.897	35.445	2.045	0.3949
0.15	1896	240	3.125	1.897	35.427	2.046	0.3946
0.2	1891	264	3.124	1.896	35.409	2.046	0.3943
0.25	1876	272	3.124	1.896	35.396	2.046	0.3940
0.3	1878	301	3.123	1.896	35.382	2.047	0.3938
0.4	1897	305	3.121	1.895	35.344	2.048	0.3932
0.5	1916	328	3.119	1.895	35.319	2.049	0.3927
0.3	1896	303	3.121	1.896	35.347	2.048	0.3932
0.2	1878	266	3.122	1.896	35.367	2.047	0.3935
0.1	1884	226	3.124	1.896	35.396	2.046	0.3940
0.2	1875	266	3.122	1.896	35.371	2.047	0.3936
0.3	1890	304	3.121	1.896	35.351	2.048	0.3933
0.5	1923	329	3.119	1.895	35.303	2.049	0.3925
0.41	1919	327	3.119	1.895	35.303	2.049	0.3924
0.75	1912	391	3.115	1.894	35.239	2.051	0.3913
1	1920	410	3.112	1.893	35.186	2.053	0.3904
0.5	1904	382	3.115	1.894	35.234	2.051	0.3913
0.3	1900	303	3.117	1.894	35.271	2.050	0.3919
0.2	1887	272	3.118	1.895	35.298	2.049	0.3924
0.1	1877	226	3.121	1.895	35.336	2.048	0.3930
0.2	1884	271	3.119	1.895	35.310	2.049	0.3926
0.3	1909	302	3.118	1.895	35.294	2.050	0.3923
0.5	1916	342	3.116	1.894	35.257	2.051	0.3916
1	1933	407	3.111	1.893	35.164	2.053	0.3900
1.5	1960	460	3.105	1.892	35.081	2.056	0.3886
2	1964	491	3.102	1.891	35.023	2.058	0.3876

Table A.8: Pomponio Beach Sand, water saturated

Pressure	V_P	V_S	Length	Radius	Volume	Density	Porosity
(MPa)	(m/sec)	(m/sec)	(cm)	(cm)	(mL)	(g/cm^3)	
2.5	2008	546	3.099	1.890	34.962	2.059	0.3865
1.75	2008	489	3.101	1.891	35.000	2.058	0.3872
1	1901	430	3.105	1.892	35.064	2.056	0.3883
0.5	1893	352	3.109	1.893	35.148	2.054	0.3898
0.3	1889	304	3.111	1.893	35.178	2.053	0.3903
0.2	1881	271	3.112	1.894	35.204	2.052	0.3907
0.1	1868	225	3.115	1.894	35.246	2.051	0.3915
0.2	1878	271	3.113	1.894	35.225	2.052	0.3911
0.3	1879	303	3.113	1.894	35.209	2.052	0.3908
0.5	1885	359	3.110	1.893	35.169	2.053	0.3901
1	1913	430	3.106	1.892	35.099	2.055	0.3889
1.75	1914	488	3.101	1.891	35.009	2.058	0.3874
2.5	1978	547	3.098	1.889	34.934	2.060	0.3860
3.75	2021	595	3.091	1.888	34.820	2.064	0.3840
5	2017	625	3.085	1.886	34.709	2.067	0.3821
2.5	2001	553	3.091	1.888	34.816	2.064	0.3839
1	1949	431	3.097	1.890	34.932	2.060	0.3860
0.5	1895	359	3.101	1.891	35.009	2.058	0.3873
0.2	1888	270	3.107	1.892	35.101	2.055	0.3890
0.1	1865	225	3.109	1.893	35.134	2.054	0.3895
0.2	1873	270	3.107	1.892	35.113	2.055	0.3892
0.5	1926	359	3.104	1.892	35.058	2.057	0.3882
1	1915	431	3.100	1.891	34.985	2.059	0.3869
2.5	2015	552	3.092	1.888	34.840	2.063	0.3844
5	2019	636	3.082	1.884	34.633	2.070	0.3807
7.5	2045	715	3.073	1.882	34.459	2.075	0.3776
10	2066	764	3.059	1.878	34.228	2.082	0.3734
5	2039	655	3.066	1.880	34.358	2.078	0.3757
2.5	1989	557	3.073	1.882	34.485	2.074	0.3780
1	1951	430	3.079	1.884	34.602	2.071	0.3801
0.5	1901	357	3.083	1.885	34.658	2.069	0.3811
0.2	1892	269	3.089	1.887	34.777	2.065	0.3833
0.1	1884	226	3.094	1.888	34.867	2.062	0.3848
0.2	1897	270	3.091	1.888	34.818	2.064	0.3840
0.5	1902	359	3.086	1.886	34.728	2.067	0.3824
1	1997	432	3.081	1.885	34.639	2.069	0.3808
2.5	1989	560	3.073	1.883	34.484	2.074	0.3780
5	2063	667	3.064	1.880	34.326	2.079	0.3751
7.5	2077	742	3.058	1.878	34.211	2.083	0.3730
10	2097	791	3.052	1.873	34.014	2.089	0.3694
12.5	2130	834	3.045	1.871	33.890	2.093	0.3671
15	2160	874	3.032	1.868	33.690	2.099	0.3633
17.5	2234	904	3.019	1.865	33.475	2.107	0.3593
20	2251	932	3.002	1.862	33.199	2.116	0.3539
20	2217	933	3.001	1.862	33.178	2.116	0.3535
20	2222	935	2.999	1.861	33.153	2.117	0.3530
15	2209	896	3.002	1.862	33.209	2.115	0.3541
10	2134	846	3.005	1.864	33.282	2.113	0.3556
5	2077	691	3.012	1.866	33.414	2.109	0.3581
2.5	2054	560	3.018	1.868	33.522	2.105	0.3602
1	1983	425	3.025	1.870	33.650	2.101	0.3626

Table A.8, cont.: Pomponio Beach Sand, water saturated

Pressure	V_P	V_S	Length	Radius	Volume	Density	Porosity
(MPa)	(m/sec)	(m/sec)	(cm)	(cm)	(mL)	(g/cm^3)	
0.5	1966	354	3.030	1.871	33.738	2.098	0.3643
0.2	1915	264	3.035	1.873	33.831	2.095	0.3660
0.1	1918	222	3.039	1.874	33.894	2.093	0.3672
0			3.055	1.878	34.178	2.084	0.3724

Table A.9: Santa Cruz Aggregate, dry, 1 (Dry 1)

Pressure	V_P	V_S	Length	Radius	Volume	Density	Porosity
(MPa)	(m/sec)	(m/sec)	(cm)	(cm)	(mL)	(g/cm^3)	
0			2.750	1.864	30.461	1.522	0.4161
0.029			2.750	1.862	30.422	1.524	0.4154
0.055	321		2.745	1.861	30.355	1.527	0.4141
0.099	417	256	2.741	1.861	30.298	1.530	0.4130
0.148	503	277	2.738	1.861	30.257	1.532	0.4122
0.206	530	303	2.736	1.860	30.222	1.534	0.4115
0.35	603	341	2.731	1.859	30.151	1.537	0.4101
0.51	639	374	2.729	1.859	30.110	1.539	0.4093
0.28	633	338	2.730	1.859	30.126	1.539	0.4096
0.053	438		2.733	1.861	30.197	1.535	0.4110
0.111	503	253	2.732	1.861	30.190	1.535	0.4109
0.22	535	312	2.731	1.860	30.159	1.537	0.4103
0.53	646	379	2.727	1.858	30.074	1.541	0.4086
0.76	699	410	2.724	1.857	30.022	1.544	0.4076
1	773	434	2.721	1.856	29.978	1.546	0.4067
0.21	610	318	2.727	1.859	30.104	1.540	0.4092
0.5	658	377	2.724	1.858	30.046	1.543	0.4080
0.76	717	414	2.722	1.857	30.004	1.545	0.4072
1	745	437	2.720	1.856	29.965	1.547	0.4064
1.26	797	457	2.718	1.856	29.924	1.549	0.4056
1.51	818	472	2.716	1.855	29.892	1.551	0.4050
2.03	866	500	2.711	1.854	29.826	1.554	0.4037
2.5	893	522	2.708	1.854	29.772	1.557	0.4026
1.55	834	478	2.711	1.855	29.831	1.554	0.4038
0.8	755	418	2.715	1.857	29.917	1.549	0.4055
0.2	619	313	2.721	1.859	30.030	1.543	0.4077
0.5	678	376	2.718	1.858	29.976	1.546	0.4067
0.45	672	377	2.717	1.858	29.958	1.547	0.4063
1.1	764	449	2.713	1.856	29.885	1.551	0.4049
1.79	837	491	2.710	1.855	29.815	1.555	0.4035
2.53	909	531	2.705	1.852	29.721	1.560	0.4016
3.3	942	592	2.701	1.852	29.651	1.563	0.4002
4.15	999	614	2.695	1.850	29.564	1.568	0.3984
5.03	1038	630	2.690	1.849	29.475	1.573	0.3966
2.61	936	536	2.696	1.851	29.601	1.566	0.3991
1.08	813	448	2.704	1.854	29.743	1.558	0.4020
0.21	626	312	2.712	1.858	29.902	1.550	0.4052
1.05	804	519	2.705	1.855	29.780	1.556	0.4028
2.04	909	516	2.700	1.853	29.685	1.561	0.4008
3	956	585	2.697	1.852	29.609	1.565	0.3993
4.02	1025	620	2.692	1.850	29.523	1.570	0.3976
5.01	1052	633	2.688	1.848	29.443	1.574	0.3959

Table A.9, cont.: Santa Cruz Aggregate, dry, 1 (Dry 1)

Pressure	V_P	V_S	Length	Radius	Volume	Density	Porosity
(MPa)	(m/sec)	(m/sec)	(cm)	(cm)	(mL)	(g/cm^3)	
6.25	1090	657	2.683	1.847	29.364	1.578	0.3943
7.53	1135	675	2.677	1.846	29.278	1.583	0.3925
5.96	1103	668	2.678	1.846	29.290	1.582	0.3928
7.6	1174	691	2.667	1.842	29.085	1.594	0.3885
8.75	1213	706	2.666	1.842	29.066	1.595	0.3881
10.07	1223	719	2.663	1.841	29.021	1.597	0.3871
12.54	1301	754	2.651	1.839	28.840	1.607	0.3833
14.98	1399	788	2.640	1.836	28.658	1.617	0.3794
17.54	1516	871	2.625	1.833	28.432	1.630	0.3745
20.35	1473	905	2.606	1.829	28.163	1.646	0.3685
20.45	1486	907	2.605	1.829	28.138	1.647	0.3679
15.08	1425	865	2.609	1.830	28.211	1.643	0.3695
10.12	1306		2.613	1.832	28.297	1.638	0.3715
4.2	1153		2.622	1.835	28.450	1.629	0.3748
0.64	835	490	2.646	1.842	28.862	1.606	0.3838
0.32	712	413	2.651	1.844	28.947	1.601	0.3856
0			2.686	1.854	29.542	1.569	0.3979

Table A.10: Santa Cruz Aggregate, dry, 2 (Dry 2)

Pressure	V_P	V_S	Length	Radius	Volume	Density	Porosity
(MPa)	(m/sec)	(m/sec)	(cm)	(cm)	(mL)	(g/cm^3)	
0		156	2.749	1.865	30.481	1.474	0.4344
0.026		173	2.749	1.865	30.473	1.474	0.4342
0.024		163	2.749	1.862	30.414	1.477	0.4331
0.052	267	174	2.749	1.863	30.426	1.477	0.4333
0.076	319	210	2.746	1.863	30.395	1.478	0.4328
0.101	370	237	2.744	1.863	30.361	1.480	0.4321
0.126	421	254	2.741	1.862	30.329	1.481	0.4315
0.15	437	274	2.740	1.862	30.307	1.482	0.4311
0.176	483	287	2.738	1.862	30.284	1.484	0.4307
0.201	531	298	2.737	1.862	30.269	1.484	0.4304
0.3	648	331	2.733	1.861	30.213	1.487	0.4294
0.4	633	348	2.731	1.861	30.173	1.489	0.4286
0.5	679	368	2.728	1.860	30.135	1.491	0.4279
0.73	799	402	2.723	1.859	30.062	1.495	0.4265
0.44	686	369	2.724	1.860	30.089	1.493	0.4270
0.79	797	411	2.721	1.859	30.039	1.496	0.4261
1.02	826	437	2.718	1.858	29.989	1.498	0.4251
1.28	854	461	2.715	1.858	29.941	1.501	0.4242
1.52	862	481	2.712	1.857	29.895	1.503	0.4233
2	918	510	2.707	1.856	29.818	1.507	0.4218
2.46	987	535	2.702	1.855	29.750	1.510	0.4205
3.66	1064	589	2.693	1.853	29.603	1.518	0.4176
5.03	1150	634	2.684	1.852	29.471	1.525	0.4150
6.35	1215	672	2.676	1.850	29.353	1.531	0.4126
7.52	1231	698	2.669	1.848	29.239	1.537	0.4103
9.97	1314	753	2.656	1.845	29.019	1.548	0.4059
9.49	1314	760	2.652	1.844	28.958	1.552	0.4046
12.54	1396	855	2.641	1.840	28.765	1.562	0.4006
15.05	1463	872	2.628	1.837	28.559	1.573	0.3963

Table A.10, cont.: Santa Cruz Aggregate, dry, 2 (Dry 2)

Pressure	V_P	V_S	Length	Radius	Volume	Density	Porosity
(MPa)	(m/sec)	(m/sec)	(cm)	(cm)	(mL)	(g/cm^3)	
17.54	1514	900	2.615	1.834	28.350	1.585	0.3919
19.96	1567	931	2.601	1.831	28.157	1.596	0.3877
18.79	1566	919	2.601	1.831	28.154	1.596	0.3876
16.42	1531	898	2.603	1.832	28.185	1.594	0.3883
13.85	1489	863	2.605	1.833	28.222	1.592	0.3891
10.85	1416	814	2.608	1.834	28.274	1.589	0.3902
8.75	1337	751	2.610	1.835	28.318	1.587	0.3912
6.35	1264	691	2.613	1.836	28.374	1.583	0.3924
3.88	1152	611	2.618	1.838	28.459	1.579	0.3942
1.83	971	511	2.625	1.840	28.576	1.572	0.3967
1.09	920	460	2.628	1.841	28.642	1.569	0.3981
0.65	849	393	2.633	1.842	28.714	1.565	0.3996
0.22	663	280	2.639	1.844	28.819	1.559	0.4018
0.143	353	213	2.645	1.846	28.919	1.554	0.4038
0.112	286	186	2.647	1.846	28.960	1.551	0.4047
0		145	2.681	1.856	29.528	1.522	0.4161
0		146	2.681	1.856	29.533	1.521	0.4162

Table A.11: Santa Cruz Aggregate, water saturated, 1 (Wet 3)

Pressure	V_P	V_S	Length	Radius	Volume	Density	Porosity
(MPa)	(m/sec)	(m/sec)	(cm)	(cm)	(mL)	(g/cm^3)	
0			1.994	1.886	22.432	1.954	0.4057
0.027			1.994	1.883	22.389	1.956	0.4046
0.052			1.992	1.882	22.339	1.958	0.4032
0.066	1752		1.988	1.881	22.275	1.961	0.4015
0.111	1748		1.985	1.880	22.238	1.963	0.4005
0.2	1838		1.978	1.880	22.152	1.966	0.3982
0.36	1877	343	1.973	1.879	22.096	1.969	0.3967
0.5	1878	386	1.967	1.879	22.009	1.973	0.3943
0.325	1885	351	1.967	1.879	22.020	1.972	0.3946
0.329	1876	343	1.968	1.879	22.030	1.972	0.3949
0.292	1883	341	1.968	1.879	22.034	1.972	0.3950
0.41	1875	365	1.966	1.879	22.004	1.973	0.3942
0.65	1901	411	1.962	1.878	21.951	1.975	0.3927
0.889	1941	424	1.958	1.878	21.895	1.978	0.3912
0.481	1913	410	1.960	1.878	21.935	1.976	0.3923
0.947	1944	425	1.956	1.877	21.863	1.979	0.3903
0.67	1900	415	1.958	1.877	21.887	1.978	0.3909
0.75	1911	421	1.954	1.876	21.821	1.981	0.3891
1.049	1927	476	1.953	1.876	21.817	1.981	0.3890
1.527	1968	502	1.949	1.875	21.767	1.984	0.3876
2.032	1965	523	1.944	1.875	21.702	1.987	0.3857
2.499	1986	570	1.941	1.874	21.663	1.988	0.3846
3.734	2034	620	1.933	1.873	21.545	1.994	0.3813
4.947	2074	652	1.927	1.872	21.455	1.998	0.3786
6.197	2117	701	1.920	1.870	21.362	2.002	0.3760
7.52	2111	747	1.915	1.869	21.291	2.006	0.3739
9.792	2198	789	1.903	1.866	21.101	2.015	0.3682
12.507	2208	821	1.896	1.864	21.004	2.019	0.3653
15.017	2257	853	1.888	1.862	20.878	2.025	0.3615

Table A.11, cont.: Santa Cruz Aggregate, water saturated, 1 (Wet 3)

Pressure	V_P	V_S	Length	Radius	Volume	Density	Porosity
(MPa)	(m/sec)	(m/sec)	(cm)	(cm)	(mL)	(g/cm^3)	
17.526	2294	884	1.879	1.860	20.749	2.032	0.3575
19.992	2298	913	1.869	1.857	20.600	2.039	0.3529
18.602	2360	902	1.868	1.857	20.581	2.040	0.3523
16.192	2296	880	1.869	1.857	20.603	2.039	0.3530
13.872	2244	852	1.870	1.858	20.619	2.038	0.3535
10.994	2242	815	1.873	1.859	20.663	2.036	0.3549
8.734	2182	780	1.874	1.859	20.682	2.035	0.3554
6.327	2144	752	1.876	1.860	20.720	2.033	0.3566
4.049	2114	642	1.880	1.861	20.785	2.030	0.3586
1.754	2028	512	1.886	1.863	20.864	2.026	0.3611
0.983	2017	463	1.889	1.863	20.914	2.024	0.3626
0.624	1951	400	1.893	1.865	20.977	2.021	0.3645
0.073	1885		1.902	1.867	21.103	2.015	0.3683
0.26	1901	285	1.899	1.866	21.065	2.016	0.3672
0.562	1951	367	1.895	1.865	21.014	2.019	0.3656
0.79	1987	403	1.894	1.865	20.986	2.020	0.3648
1.008	1966	435	1.892	1.865	20.970	2.021	0.3643
4.87	2117	677	1.880	1.861	20.776	2.030	0.3584
9.997	2187	813	1.871	1.858	20.646	2.037	0.3543
14.857	2293	883	1.865	1.857	20.553	2.042	0.3514
19.371	2332	934	1.857	1.854	20.426	2.048	0.3474
13.722	2281	876	1.859	1.855	20.463	2.046	0.3485
8.783	2228	794	1.863	1.856	20.520	2.043	0.3503
3.857	2127	648	1.869	1.858	20.619	2.038	0.3535
1.164	2023	490	1.877	1.861	20.744	2.032	0.3574
0.559	1992	397	1.882	1.862	20.808	2.029	0.3593
0.255	1896	282	1.886	1.863	20.880	2.025	0.3616
0.6	1957	397	1.883	1.862	20.827	2.028	0.3599
0.3	1895	329	1.885	1.863	20.856	2.027	0.3608
0	1874		1.891	1.864	20.943	2.022	0.3635

Table A.12: Santa Cruz Aggregate, water saturated, 2 (Wet 4)

Pressure	V_P	V_S	Length	Radius	Volume	Density	Porosity
(MPa)	(m/sec)	(m/sec)	(cm)	(cm)	(mL)	(g/cm^3)	
0		141	2.585	1.890	29.165	1.936	0.4171
0.037		164	2.571	1.890	29.007	1.941	0.4140
0.106		289	2.565	1.890	28.941	1.943	0.4126
0.197		334	2.560	1.890	28.877	1.945	0.4113
0.094	1822	275	2.561	1.890	28.892	1.945	0.4116
0.05	1822		2.563	1.890	28.909	1.944	0.4120
0.156	1863	305	2.559	1.890	28.870	1.946	0.4112
0.109	1842	275	2.560	1.890	28.879	1.945	0.4114
0.319	1867	365	2.554	1.890	28.810	1.948	0.4100
0.547	1900	418	2.548	1.890	28.741	1.950	0.4085
0.8	1911	460	2.543	1.890	28.683	1.952	0.4073
0.737	1920	459	2.540	1.890	28.648	1.953	0.4066
0.837	1928	466	2.540	1.890	28.645	1.953	0.4065
0.5	1887	416	2.542	1.890	28.674	1.952	0.4072
0.34	1876	368	2.544	1.890	28.692	1.952	0.4075
0.21	1862	344	2.546	1.890	28.715	1.951	0.4080

Table A.12, cont.: Santa Cruz Aggregate, water saturated, 2 (Wet 4)

Pressure	V_P	V_S	Length	Radius	Volume	Density	Porosity
(MPa)	(m/sec)	(m/sec)	(cm)	(cm)	(mL)	(g/cm^3)	
0.1	1855		2.548	1.890	28.740	1.950	0.4085
0.2	1878	344	2.546	1.890	28.717	1.951	0.4081
0.51	1902	414	2.542	1.890	28.675	1.952	0.4072
0.79	1913	461	2.540	1.890	28.644	1.953	0.4065
1.18	1940	502	2.534	1.890	28.583	1.955	0.4053
1.81	1990	530	2.529	1.890	28.525	1.957	0.4041
2.23	1996	581	2.524	1.889	28.463	1.959	0.4028
2	1999	578	2.524	1.889	28.467	1.959	0.4028
1.51	1969	524	2.526	1.889	28.487	1.958	0.4033
1	1942	502	2.528	1.889	28.508	1.958	0.4037
0.5	1911	417	2.531	1.889	28.548	1.956	0.4045
0.2	1868	346	2.535	1.889	28.591	1.955	0.4054
1.01	1956	501	2.529	1.889	28.517	1.957	0.4039
1.51	1970	523	2.526	1.889	28.487	1.958	0.4033
2	1992	565	2.524	1.889	28.460	1.959	0.4027
2.31	1999	582	2.522	1.889	28.442	1.960	0.4023
2.16	2005	574	2.523	1.889	28.449	1.960	0.4025
1.59	1987	550	2.524	1.889	28.466	1.959	0.4028
0.83	1973	473	2.528	1.889	28.511	1.958	0.4038
0.23	1882	342	2.535	1.889	28.591	1.955	0.4054
0.12	1863		2.537	1.889	28.610	1.954	0.4058
0.2	1893	333	2.535	1.889	28.589	1.955	0.4054
0.097	1859		2.537	1.889	28.613	1.954	0.4059
0.192	1862	314	2.536	1.889	28.595	1.955	0.4055
0	1814		2.545	1.890	28.701	1.951	0.4077

Table A.13: Santa Cruz Aggregate, large fraction, dry (Sa Big)

Pressure	V_P	V_S	Length	Radius	Volume	Density	Porosity
(MPa)	(m/sec)	(m/sec)	(cm)	(cm)	(mL)	(g/cm^3)	
0			2.934	1.891	33.127	1.538	0.4098
0.024	283	186	2.933	1.891	33.108	1.539	0.4095
0.05	365	227	2.932	1.890	33.089	1.540	0.4091
0.075	419	258	2.931	1.890	33.071	1.541	0.4088
0.1	457	280	2.930	1.890	33.055	1.541	0.4085
0.147	523	311	2.929	1.889	33.030	1.543	0.4081
0.2	560	333	2.928	1.889	33.008	1.544	0.4077
0.1	517	302	2.928	1.889	33.020	1.543	0.4079
0.2	565	334	2.927	1.889	33.001	1.544	0.4076
0.3	616	365	2.925	1.888	32.945	1.547	0.4066
0.5	720	403	2.922	1.887	32.898	1.549	0.4057
0.2	613	354	2.924	1.888	32.935	1.547	0.4064
0.1	554	314	2.925	1.888	32.962	1.546	0.4069
0.2	596	344	2.924	1.888	32.943	1.547	0.4065
0.5	717	404	2.922	1.887	32.893	1.549	0.4056
0.75	771	441	2.918	1.886	32.827	1.552	0.4044
0.75	785	441	2.918	1.886	32.827	1.552	0.4044
1	809	470	2.915	1.885	32.776	1.555	0.4035
0.5	747	423	2.918	1.886	32.827	1.552	0.4044
0.2	673	362	2.921	1.887	32.891	1.549	0.4056
0.1	561	320	2.923	1.888	32.922	1.548	0.4061

Table A.13, cont.: Santa Cruz Aggregate, large fraction, dry (Sa Big)

Pressure	V_P	V_S	Length	Radius	Volume	Density	Porosity
(MPa)	(m/sec)	(m/sec)	(cm)	(cm)	(mL)	(g/cm^3)	
0.2	641	350	2.922	1.888	32.906	1.548	0.4059
0.5	732	411	2.919	1.887	32.853	1.551	0.4049
1	833	472	2.914	1.885	32.758	1.555	0.4032
1.5	889	515	2.910	1.884	32.686	1.559	0.4019
2	968	551	2.906	1.883	32.621	1.562	0.4007
2.5	1001	580	2.903	1.882	32.570	1.564	0.3997
1	919	498	2.908	1.884	32.664	1.560	0.4014
0.5	778	438	2.912	1.885	32.731	1.557	0.4027
0.2	664	367	2.915	1.886	32.799	1.553	0.4039
0.1	565	319	2.918	1.887	32.842	1.551	0.4047
0.199	647	349	2.916	1.887	32.822	1.552	0.4043
0.5	745	419	2.914	1.886	32.771	1.555	0.4034
1	835	485	2.910	1.885	32.700	1.558	0.4021
2.5	1000	584	2.901	1.881	32.519	1.567	0.3988
3.75	1076	654	2.895	1.879	32.413	1.572	0.3968
5	1139	684	2.889	1.878	32.323	1.576	0.3951
2.5	1051	616	2.895	1.880	32.426	1.571	0.3971
1	926	513	2.901	1.882	32.536	1.566	0.3991
0.5	797	445	2.905	1.883	32.606	1.563	0.4004
0.2	686	368	2.909	1.884	32.684	1.559	0.4018
0.1	572	320	2.911	1.885	32.718	1.557	0.4024
0.2	669	348	2.910	1.885	32.700	1.558	0.4021
0.5	758	424	2.907	1.884	32.647	1.561	0.4011
1	867	492	2.903	1.883	32.582	1.564	0.3999
2.5	1045	599	2.896	1.880	32.444	1.570	0.3974
5	1146	682	2.887	1.877	32.280	1.578	0.3943
7.5	1256	768	2.878	1.875	32.119	1.586	0.3913
10	1313	812	2.869	1.872	31.970	1.594	0.3885
5	1185	705	2.876	1.875	32.103	1.587	0.3910
2.5	1065	625	2.882	1.877	32.211	1.582	0.3930
1	913	509	2.889	1.879	32.336	1.576	0.3954
0.5	809	435	2.893	1.880	32.414	1.572	0.3968
0.2	690	350	2.898	1.881	32.495	1.568	0.3983
0.2	686	350	2.898	1.881	32.495	1.568	0.3983
0.1	561	298	2.900	1.882	32.537	1.566	0.3991
0.2	685	333	2.899	1.882	32.519	1.567	0.3988
0.5	776	416	2.895	1.881	32.455	1.570	0.3976
1	890	491	2.892	1.880	32.394	1.573	0.3965
2.5	1050	604	2.885	1.878	32.262	1.579	0.3940
5	1180	697	2.878	1.875	32.133	1.586	0.3916
10	1343	824	2.866	1.870	31.892	1.598	0.3870
12.5	1404	859	2.860	1.869	31.783	1.603	0.3849
15	1440	892	2.851	1.867	31.639	1.610	0.3821
10	1371	835	2.855	1.868	31.729	1.606	0.3838
5	1219	709	2.863	1.871	31.868	1.599	0.3865
2.5	1074	620	2.869	1.873	31.978	1.593	0.3886
1	907	503	2.876	1.875	32.104	1.587	0.3910
0.5	803	425	2.880	1.876	32.175	1.584	0.3924
0.2	673	335	2.885	1.878	32.266	1.579	0.3941
0.1	554	285	2.888	1.879	32.319	1.576	0.3951
0.2	676	319	2.886	1.878	32.295	1.578	0.3946

Table A.13, cont.: Santa Cruz Aggregate, large fraction, dry (Sa Big)

Pressure	V_P	V_S	Length	Radius	Volume	Density	Porosity
(MPa)	(m/sec)	(m/sec)	(cm)	(cm)	(mL)	(g/cm^3)	
0.5	762	409	2.882	1.877	32.225	1.581	0.3933
1	885	484	2.879	1.876	32.162	1.584	0.3921
2.5	1048	598	2.872	1.874	32.036	1.590	0.3897
5	1183	706	2.865	1.872	31.910	1.597	0.3873
10	1370	844	2.855	1.868	31.722	1.606	0.3837
15	1474	906	2.846	1.865	31.544	1.615	0.3802
17.5	1510	931	2.840	1.863	31.434	1.621	0.3780
20	1565	955	2.832	1.861	31.306	1.627	0.3755
15	1481	913	2.835	1.863	31.365	1.624	0.3767
10	1390	849	2.839	1.864	31.452	1.620	0.3784
5	1236	717	2.846	1.867	31.590	1.613	0.3811
2.5	1086	617	2.853	1.869	31.705	1.607	0.3833
1	955	499	2.859	1.871	31.827	1.601	0.3857
1	944	500	2.861	1.871	31.852	1.600	0.3862
0.5	822	423	2.864	1.872	31.905	1.597	0.3872
0.2	682	332	2.869	1.873	31.988	1.593	0.3888
0.1	544	281	2.872	1.874	32.040	1.590	0.3898
0.2	660	313	2.870	1.874	32.022	1.591	0.3894
0.5	788	406	2.866	1.873	31.951	1.595	0.3881
1	953	483	2.863	1.872	31.887	1.598	0.3869
2.5	1071	600	2.856	1.870	31.761	1.604	0.3844
5	1229	719	2.849	1.868	31.635	1.611	0.3820
10	1385	861	2.840	1.865	31.465	1.619	0.3786
15	1501	924	2.832	1.862	31.329	1.626	0.3759
20	1572	972	2.824	1.858	31.139	1.636	0.3721
15	1518	932	2.827	1.859	31.203	1.633	0.3734
10	1406	866	2.831	1.861	31.290	1.628	0.3752
5	1269	730	2.838	1.863	31.421	1.622	0.3778
2.5	1102	622	2.844	1.865	31.536	1.616	0.3800
1	950	505	2.851	1.867	31.653	1.610	0.3823
0.5	821	428	2.855	1.869	31.730	1.606	0.3838
0.2	694	329	2.861	1.870	31.830	1.601	0.3858
0.1	546	273	2.864	1.871	31.884	1.598	0.3868
0.05	423	222	2.867	1.872	31.935	1.595	0.3878
0	262		2.872	1.874	32.026	1.591	0.3895

Table A.14: Santa Cruz Aggregate, 65% large and 35% small fractions, dry (Sa 35% Small)

Pressure	V_P	V_S	Length	Radius	Volume	Density	Porosity
(MPa)	(m/sec)	(m/sec)	(cm)	(cm)	(mL)	(g/cm^3)	
0	248	142	2.589	1.887	29.147	1.617	0.3794
0	252	142	2.589	1.887	29.146	1.617	0.3794
0.026	281	173	2.589	1.887	29.135	1.618	0.3791
0.05	338	200	2.588	1.886	29.122	1.619	0.3789
0.075	392	225	2.588	1.886	29.107	1.620	0.3785
0.1	415	243	2.587	1.886	29.092	1.620	0.3782
0.15	497	273	2.585	1.885	29.065	1.622	0.3776
0.2	521	307	2.583	1.885	29.033	1.624	0.3769
0.1	486	274	2.584	1.885	29.045	1.623	0.3772
0.2	529	308	2.583	1.885	29.033	1.624	0.3770
0.31	595	336	2.581	1.884	28.997	1.626	0.3762

Table A.14, cont.: Santa Cruz Aggregate, 65% large and 35% small fractions, dry (Sa 35% Small)

Pressure	V_P	V_S	Length	Radius	Volume	Density	Porosity
(MPa)	(m/sec)	(m/sec)	(cm)	(cm)	(mL)	(g/cm^3)	
0.5	655	374	2.578	1.883	28.941	1.629	0.3750
0.2	626	320	2.579	1.884	28.967	1.627	0.3755
0.1	495	277	2.581	1.884	28.995	1.626	0.3761
0.2	534	311	2.580	1.884	28.979	1.627	0.3758
0.5	671	376	2.577	1.883	28.926	1.630	0.3747
0.75	721	413	2.574	1.882	28.875	1.633	0.3735
1	773	441	2.571	1.881	28.818	1.636	0.3723
0.5	689	388	2.573	1.882	28.856	1.634	0.3731
0.2	588	320	2.576	1.883	28.905	1.631	0.3742
0.1	489	277	2.577	1.883	28.934	1.629	0.3748
0.2	546	313	2.576	1.883	28.917	1.630	0.3744
0.5	667	377	2.574	1.882	28.877	1.632	0.3736
1	774	443	2.570	1.880	28.797	1.637	0.3718
1.5	846	487	2.565	1.879	28.721	1.641	0.3702
2	888	521	2.561	1.878	28.653	1.645	0.3687
2.5	939	551	2.557	1.877	28.588	1.649	0.3673
1	833	458	2.561	1.879	28.666	1.644	0.3690
0.5	703	393	2.564	1.880	28.723	1.641	0.3702
0.2	582	319	2.568	1.881	28.785	1.638	0.3716
0.1	486	273	2.570	1.882	28.818	1.636	0.3723
0.2	529	304	2.569	1.881	28.807	1.636	0.3721
0.5	670	379	2.566	1.881	28.763	1.639	0.3711
1	820	448	2.563	1.879	28.701	1.642	0.3697
2.5	941	555	2.555	1.876	28.554	1.651	0.3665
3.75	1027	611	2.548	1.875	28.445	1.657	0.3641
5	1088	658	2.541	1.873	28.319	1.665	0.3612
2.5	967	571	2.545	1.874	28.398	1.660	0.3630
1	820	464	2.551	1.876	28.491	1.655	0.3651
0.5	704	394	2.554	1.877	28.554	1.651	0.3665
0.2	576	316	2.558	1.878	28.626	1.647	0.3681
0.1	484	271	2.560	1.879	28.660	1.645	0.3688
0.2	519	299	2.559	1.879	28.649	1.645	0.3686
0.5	676	377	2.556	1.878	28.598	1.648	0.3675
1	800	455	2.553	1.877	28.537	1.652	0.3661
2.5	969	563	2.546	1.875	28.421	1.659	0.3635
5	1113	669	2.538	1.872	28.269	1.668	0.3601
7.5	1210	752	2.527	1.869	28.082	1.679	0.3558
10	1301	804	2.514	1.866	27.887	1.690	0.3514
5	1144	697	2.520	1.868	27.982	1.685	0.3536
2.5	1006	583	2.525	1.869	28.069	1.679	0.3556
1	844	466	2.531	1.871	28.171	1.673	0.3579
0.5	739	394	2.534	1.872	28.236	1.670	0.3594
0.2	582	308	2.539	1.874	28.312	1.665	0.3611
0.1	484	259	2.541	1.874	28.356	1.662	0.3621
0.2	519	288	2.541	1.874	28.344	1.663	0.3618
0.5	673	374	2.537	1.873	28.282	1.667	0.3604
1	858	456	2.533	1.872	28.223	1.670	0.3591
2.5	989	572	2.527	1.870	28.120	1.676	0.3567
5	1171	685	2.521	1.868	28.003	1.683	0.3540
10	1326	818	2.509	1.864	27.786	1.697	0.3490
12.5	1391	855	2.502	1.862	27.661	1.704	0.3460

Table A.14, cont.: Santa Cruz Aggregate, 65% large and 35% small fractions, dry (Sa 35% Small)

Pressure	V_P	V_S	Length	Radius	Volume	Density	Porosity
(MPa)	(m/sec)	(m/sec)	(cm)	(cm)	(mL)	(g/cm^3)	
15	1475	889	2.492	1.860	27.514	1.713	0.3426
10	1335	827	2.495	1.861	27.575	1.710	0.3440
5	1201	711	2.501	1.863	27.676	1.703	0.3464
2.5	1040	591	2.506	1.865	27.766	1.698	0.3485
1	873	469	2.512	1.866	27.865	1.692	0.3508
0.5	743	396	2.516	1.868	27.935	1.688	0.3525
0.2	581	303	2.521	1.869	28.020	1.682	0.3544
0.1	486	252	2.524	1.870	28.071	1.679	0.3556
0.2	512	280	2.523	1.870	28.055	1.680	0.3552
0.5	693	373	2.519	1.869	27.994	1.684	0.3538
1	821	452	2.515	1.867	27.928	1.688	0.3523
2.5	1004	579	2.509	1.866	27.817	1.695	0.3497
5	1183	705	2.503	1.864	27.714	1.701	0.3473
10	1373	835	2.494	1.861	27.563	1.710	0.3437
15	1491	904	2.485	1.858	27.403	1.720	0.3399
17.5	1562	934	2.480	1.857	27.325	1.725	0.3380
20	1567	963	2.472	1.855	27.198	1.733	0.3349
15	1506	916	2.474	1.856	27.241	1.731	0.3360
10	1395	839	2.477	1.857	27.304	1.727	0.3375
5	1212	718	2.483	1.859	27.400	1.720	0.3398
2.5	1059	594	2.488	1.861	27.487	1.715	0.3419
1	891	474	2.494	1.862	27.592	1.708	0.3444
0.5	767	399	2.498	1.863	27.653	1.705	0.3458
0.2	586	302	2.503	1.865	27.744	1.699	0.3480
0.1	489	244	2.506	1.866	27.797	1.696	0.3492
0.2	523	280	2.505	1.865	27.772	1.697	0.3487
0.5	686	371	2.501	1.865	27.717	1.701	0.3474
1	837	452	2.497	1.863	27.652	1.705	0.3458
2.5	1041	582	2.491	1.862	27.544	1.711	0.3433
5	1197	713	2.485	1.860	27.442	1.718	0.3408
10	1373	847	2.477	1.857	27.310	1.726	0.3376
15	1500	921	2.471	1.855	27.197	1.733	0.3349
20	1600	984	2.463	1.852	27.059	1.742	0.3315
15	1521	936	2.466	1.853	27.102	1.739	0.3326
10	1402	857	2.469	1.854	27.162	1.735	0.3340
5	1224	731	2.474	1.856	27.262	1.729	0.3365
2.5	1076	604	2.479	1.858	27.346	1.724	0.3385
1	889	475	2.485	1.860	27.441	1.718	0.3408
0.5	769	399	2.489	1.861	27.506	1.714	0.3424
0.2	581	302	2.494	1.862	27.593	1.708	0.3444
0.1	444	236	2.498	1.863	27.658	1.704	0.3460
0.05			2.503	1.865	27.741	1.699	0.3479
0			2.520	1.869	28.020	1.682	0.3544

Table A.15: Glass beads, large fraction, dry (GB Big)

Pressure	V_P	V_S	Length	Radius	Volume	Density	Porosity
(MPa)	(m/sec)	(m/sec)	(cm)	(cm)	(mL)	(g/cm^3)	
0	408	220	3.286	1.900	37.320	1.524	0.3813
0.026	415	203	3.286	1.900	37.324	1.524	0.3814
0.018	414	192	3.286	1.900	37.325	1.524	0.3814
0.051	482	233	3.286	1.900	37.327	1.524	0.3815
0.076	550	295	3.287	1.900	37.329	1.524	0.3815
0.101	588	317	3.286	1.900	37.328	1.524	0.3815
0.151	655	337	3.286	1.900	37.324	1.524	0.3814
0.201	705	359	3.285	1.900	37.313	1.525	0.3812
0.3	742	394	3.284	1.899	37.288	1.526	0.3808
0.5	863	475	3.282	1.899	37.256	1.527	0.3803
0.2	758	418	3.283	1.899	37.265	1.527	0.3804
0.1	712	361	3.283	1.899	37.272	1.526	0.3805
0.2	746	414	3.283	1.899	37.262	1.527	0.3804
0.5	902	481	3.281	1.899	37.243	1.528	0.3801
0.76	948	515	3.279	1.898	37.199	1.529	0.3793
1.01	971	540	3.278	1.897	37.171	1.530	0.3789
0.5	904	486	3.279	1.898	37.194	1.530	0.3792
0.201	898	419	3.280	1.898	37.217	1.529	0.3796
0.1	711	346	3.281	1.898	37.225	1.528	0.3798
0.2	752	375	3.280	1.898	37.216	1.529	0.3796
0.5	924	476	3.279	1.898	37.200	1.529	0.3793
1	983	539	3.277	1.897	37.158	1.531	0.3786
1.51	1065	577	3.274	1.896	37.099	1.533	0.3777
2	1089	604	3.271	1.896	37.057	1.535	0.3769
2.5	1135	628	3.269	1.895	37.014	1.537	0.3762
2.18	1134	627	3.268	1.895	37.005	1.537	0.3761
1.01	1012	538	3.272	1.896	37.069	1.535	0.3771
0.5	934	474	3.274	1.896	37.106	1.533	0.3778
0.2	867	396	3.276	1.897	37.141	1.532	0.3783
0.1	731	329	3.277	1.897	37.154	1.531	0.3786
0.2	753	380	3.277	1.897	37.150	1.531	0.3785
0.5	921	470	3.275	1.897	37.126	1.532	0.3781
1	964	532	3.273	1.896	37.091	1.534	0.3775
2.5	1175	627	3.267	1.895	36.980	1.538	0.3757
3.74	1199	674	3.263	1.893	36.900	1.542	0.3743
5	1266	709	3.259	1.893	36.835	1.544	0.3732
2.5	1150	624	3.264	1.894	36.922	1.541	0.3747
1	996	528	3.269	1.895	37.011	1.537	0.3762
0.5	971	461	3.272	1.896	37.062	1.535	0.3770
0.2	791	394	3.274	1.896	37.098	1.534	0.3776
0.1	731	273	3.275	1.896	37.110	1.533	0.3778
0.2	753	393	3.274	1.896	37.107	1.533	0.3778
0.5	887	461	3.273	1.896	37.081	1.534	0.3774
1	964	525	3.271	1.896	37.051	1.535	0.3768
0.53	895	476	3.272	1.896	37.071	1.535	0.3772
2.5	1143	614	3.265	1.894	36.942	1.540	0.3750
5	1309	705	3.259	1.891	36.799	1.546	0.3726
7.5	1335	765	3.253	1.890	36.692	1.550	0.3707
10	1424	812	3.247	1.888	36.579	1.555	0.3688
5	1263	705	3.254	1.890	36.717	1.549	0.3712
2.5	1145	618	3.260	1.892	36.828	1.545	0.3731

Table A.15, cont.: Glass beads, large fraction, dry (GB Big)

Pressure	V_P	V_S	Length	Radius	Volume	Density	Porosity
(MPa)	(m/sec)	(m/sec)	(cm)	(cm)	(mL)	(g/cm^3)	
1.8	1095	580	3.264	1.893	36.902	1.542	0.3743
1	997	517	3.266	1.894	36.940	1.540	0.3750
0.5	884	453	3.269	1.894	36.990	1.538	0.3758
0.2	779	387	3.271	1.895	37.033	1.536	0.3766
0.102	738	272	3.271	1.895	37.041	1.536	0.3767
0.2	754	388	3.271	1.895	37.035	1.536	0.3766
0.5	863	456	3.270	1.895	37.012	1.537	0.3762
1	1026	521	3.268	1.894	36.977	1.539	0.3756
2.5	1120	612	3.262	1.893	36.868	1.543	0.3738
5	1248	698	3.256	1.891	36.758	1.548	0.3719
10	1399	806	3.247	1.886	36.535	1.557	0.3680
12.5	1452	841	3.243	1.885	36.465	1.560	0.3668
15	1515	873	3.240	1.884	36.400	1.563	0.3657
10	1402	802	3.245	1.886	36.510	1.558	0.3676
5	1252	699	3.253	1.889	36.664	1.552	0.3703
2.5	1144	611	3.259	1.891	36.782	1.547	0.3723
1	1000	514	3.264	1.893	36.891	1.542	0.3741
1.06	949	517	3.266	1.893	36.923	1.541	0.3747
0.5	898	448	3.268	1.894	36.957	1.539	0.3753
0.2	763	349	3.270	1.894	36.998	1.538	0.3760
0.103	693	301	3.270	1.894	37.008	1.537	0.3761
0.2	744	343	3.270	1.894	37.002	1.538	0.3760
0.5	852	452	3.268	1.894	36.978	1.538	0.3756
1	1023	518	3.266	1.893	36.939	1.540	0.3750
2.5	1103	607	3.261	1.892	36.831	1.545	0.3731
5	1248	693	3.255	1.890	36.712	1.550	0.3711
10	1426	797	3.247	1.887	36.541	1.557	0.3681
15	1502	865	3.240	1.882	36.361	1.565	0.3650
17.51	1557	902	3.237	1.881	36.299	1.567	0.3639
19.96	1575	930	3.234	1.880	36.235	1.570	0.3628
15	1522	865	3.238	1.882	36.326	1.566	0.3644
10.13	1474	805	3.243	1.884	36.434	1.561	0.3663
5	1253	696	3.251	1.887	36.607	1.554	0.3693
2.5	1129	607	3.257	1.890	36.735	1.549	0.3715
1	993	513	3.263	1.892	36.849	1.544	0.3734
0.5	948	454	3.266	1.892	36.906	1.541	0.3744
0.201	771	348	3.268	1.893	36.960	1.539	0.3753
0.1	674	302	3.269	1.894	36.972	1.539	0.3755
0.2	750	339	3.269	1.894	36.970	1.539	0.3755
0.5	870	410	3.267	1.893	36.938	1.540	0.3749
1	944	520	3.265	1.892	36.897	1.542	0.3742
2.5	1099	608	3.260	1.890	36.785	1.547	0.3723
2.65	1112	618	3.259	1.890	36.774	1.547	0.3722
5	1218	692	3.254	1.888	36.665	1.552	0.3703
10	1385	795	3.246	1.885	36.492	1.559	0.3673
15	1514	860	3.239	1.883	36.355	1.565	0.3649
19.97	1567	922	3.234	1.879	36.194	1.572	0.3621
15	1515	861	3.238	1.880	36.288	1.568	0.3637
10	1403	797	3.243	1.883	36.409	1.563	0.3659
5	1255	693	3.251	1.886	36.584	1.555	0.3689

Table A.15, cont.: Glass beads, large fraction, dry (GB Big)

Pressure	V_P	V_S	Length	Radius	Volume	Density	Porosity
(MPa)	(m/sec)	(m/sec)	(cm)	(cm)	(mL)	(g/cm^3)	
2.5	1116	606	3.257	1.889	36.706	1.550	0.3710
1.43	1003	548	3.262	1.890	36.809	1.546	0.3728
1	965	512	3.263	1.891	36.829	1.545	0.3731
0.5	924	399	3.266	1.892	36.889	1.542	0.3741
0.2	745	346	3.268	1.893	36.937	1.540	0.3749
0.1	683	298	3.268	1.893	36.943	1.540	0.3750
0	476	201	3.268	1.893	36.946	1.540	0.3751

Table A.16: Glass beads, small fraction, dry (GB Small)

Pressure	V_P	V_S	Length	Radius	Volume	Density	Porosity
(MPa)	(m/sec)	(m/sec)	(cm)	(cm)	(mL)	(g/cm^3)	
0	183		3.004	1.890	33.898	1.450	0.4117
0.026	228	118	3.005	1.890	33.904	1.449	0.4118
0.013	210		3.005	1.890	33.901	1.449	0.4117
0.052	284	160	3.004	1.889	33.881	1.450	0.4114
0.075	321	184	3.004	1.889	33.863	1.451	0.4111
0.101	367	206	3.003	1.888	33.842	1.452	0.4107
0.15	433	244	3.001	1.888	33.809	1.453	0.4101
0.197	524	272	2.999	1.888	33.784	1.455	0.4097
0.25	582	302	2.998	1.888	33.761	1.456	0.4093
0.3	582	322	2.997	1.887	33.744	1.456	0.4090
0.4	646	349	2.995	1.887	33.717	1.457	0.4085
0.5	713	370	2.993	1.887	33.697	1.458	0.4082
0.74	810	419	2.991	1.886	33.650	1.460	0.4073
1	876	459	2.988	1.886	33.608	1.462	0.4066
0.5	884	403	2.990	1.886	33.642	1.461	0.4072
0.202	697	324	2.992	1.887	33.672	1.459	0.4077
0.101	564	274	2.992	1.887	33.687	1.459	0.4080
0.096	572	275	2.992	1.887	33.688	1.459	0.4080
0.201	590	302	2.992	1.887	33.686	1.459	0.4080
0.5	749	382	2.990	1.886	33.649	1.460	0.4073
1	915	460	2.987	1.885	33.580	1.463	0.4061
1.5	913	520	2.984	1.884	33.525	1.466	0.4051
1.98	974	548	2.981	1.884	33.481	1.468	0.4044
2.5	1009	575	2.978	1.883	33.432	1.470	0.4035
3.75	1080	627	2.974	1.882	33.354	1.473	0.4021
5	1142	666	2.970	1.881	33.294	1.476	0.4010
2.5	1026	581	2.975	1.882	33.379	1.472	0.4025
1.01	886	482	2.980	1.884	33.475	1.468	0.4042
0.86	883	479	2.981	1.884	33.486	1.467	0.4044
0.51	741	381	2.983	1.885	33.525	1.466	0.4051
0.2	700	300	2.986	1.886	33.580	1.463	0.4061
0.1	554	259	2.987	1.886	33.596	1.463	0.4064
0.2	589	291	2.986	1.886	33.591	1.463	0.4063
0.5	737	360	2.984	1.885	33.551	1.465	0.4056
0.99	866	448	2.981	1.884	33.498	1.467	0.4047
2.49	995	566	2.975	1.882	33.388	1.472	0.4027
5	1148	665	2.969	1.880	33.258	1.478	0.4004
7.49	1248	724	2.963	1.878	33.149	1.482	0.3984
10	1301	771	2.958	1.877	33.061	1.486	0.3968

Table A.16, cont.: Glass beads, small fraction, dry (GB Small)

Pressure	V_P	V_S	Length	Radius	Volume	Density	Porosity
(MPa)	(m/sec)	(m/sec)	(cm)	(cm)	(mL)	(g/cm^3)	
12.46	1348	809	2.954	1.876	32.987	1.490	0.3954
15.01	1404	847	2.950	1.874	32.913	1.493	0.3941
17.5	1435	868	2.947	1.873	32.842	1.496	0.3928
20	1473	904	2.943	1.872	32.778	1.499	0.3916
15	1412	851	2.948	1.873	32.858	1.496	0.3930
10	1317	766	2.953	1.875	32.964	1.491	0.3950
5	1154	655	2.961	1.878	33.120	1.484	0.3979
2.53	1055	570	2.967	1.880	33.242	1.478	0.4001
1.03	870	468	2.973	1.882	33.342	1.474	0.4019
0.5	767	389	2.976	1.883	33.406	1.471	0.4030
0.2	655	298	2.980	1.884	33.466	1.468	0.4041
0.102	586	260	2.980	1.884	33.480	1.468	0.4043
0.051	543	226	2.981	1.884	33.484	1.468	0.4044
0.025	478	174	2.980	1.884	33.481	1.468	0.4043
0		172	2.980	1.884	33.482	1.468	0.4044

Table A.17: Glass beads, tiny fraction, dry (GB Tiny)

Pressure	V_P	V_S	Length	Radius	Volume	Density	Porosity
(MPa)	(m/sec)	(m/sec)	(cm)	(cm)	(mL)	(g/cm^3)	
0			3.098	1.870	34.459	1.424	0.4222
0.026		114	3.097	1.870	34.447	1.424	0.4220
0.052	257	141	3.098	1.869	34.433	1.425	0.4218
0.075	293	165	3.098	1.868	34.413	1.426	0.4214
0.101	330	187	3.098	1.867	34.390	1.427	0.4210
0.15	383	219	3.096	1.866	34.358	1.428	0.4205
0.2	457	250	3.094	1.866	34.322	1.429	0.4199
0.3	654	299	3.090	1.866	34.274	1.431	0.4191
0.5	733	361	3.086	1.865	34.214	1.434	0.4180
0.34	728	366	3.086	1.866	34.218	1.434	0.4181
0.5	733	370	3.085	1.865	34.197	1.435	0.4178
0.74	790	412	3.082	1.865	34.148	1.437	0.4169
1	840	448	3.078	1.864	34.100	1.439	0.4161
1.51	935	506	3.073	1.864	34.027	1.442	0.4149
1.99	989	550	3.070	1.863	33.978	1.444	0.4140
2.5	1024	579	3.067	1.862	33.929	1.446	0.4132
1	939	505	3.070	1.864	34.005	1.443	0.4145
0.5	860	414	3.073	1.865	34.066	1.440	0.4155
0.2	689	343	3.075	1.866	34.108	1.438	0.4163
0.1	629	298	3.076	1.866	34.123	1.438	0.4165
0.2	663	327	3.075	1.866	34.119	1.438	0.4164
0.57	843	406	3.074	1.866	34.089	1.439	0.4159
1	892	469	3.072	1.865	34.041	1.441	0.4151
2.51	1011	582	3.065	1.862	33.889	1.448	0.4125
3.69	1111	638	3.060	1.861	33.811	1.451	0.4111
5	1157	675	3.055	1.859	33.734	1.454	0.4098
5.14	1195	695	3.054	1.859	33.707	1.455	0.4093
7.51	1243	736	3.049	1.857	33.603	1.460	0.4075
10	1321	784	3.043	1.855	33.498	1.465	0.4056
5	1180	683	3.049	1.858	33.636	1.459	0.4081
2.5	1026	581	3.055	1.860	33.755	1.453	0.4101

Table A.17, cont.: Glass beads, tiny fraction, dry (GB Tiny)

Pressure	V_P	V_S	Length	Radius	Volume	Density	Porosity
(MPa)	(m/sec)	(m/sec)	(cm)	(cm)	(mL)	(g/cm^3)	
0.6	850	437	3.063	1.863	33.915	1.447	0.4129
0.2	692	334	3.066	1.865	33.973	1.444	0.4139
0.1	640	295	3.066	1.865	33.983	1.444	0.4141
0.2	658	327	3.066	1.865	33.976	1.444	0.4140
0.5	731	375	3.065	1.865	33.967	1.444	0.4138
1	845	450	3.063	1.863	33.910	1.447	0.4128
2.5	996	571	3.057	1.861	33.787	1.452	0.4107
5	1160	672	3.050	1.858	33.650	1.458	0.4083
10	1332	794	3.040	1.854	33.433	1.467	0.4045
12.49	1373	818	3.036	1.853	33.361	1.471	0.4032
15	1425	849	3.032	1.851	33.280	1.474	0.4017
17.49	1462	875	3.029	1.850	33.219	1.477	0.4006
20	1492	910	3.025	1.849	33.156	1.480	0.3995
15	1459	868	3.029	1.851	33.236	1.476	0.4009
10	1317	776	3.034	1.853	33.354	1.471	0.4031
5	1151	659	3.043	1.857	33.527	1.463	0.4061
2.5	1028	573	3.049	1.859	33.652	1.458	0.4083
1	939	470	3.055	1.861	33.778	1.452	0.4105
0.5	821	394	3.058	1.862	33.837	1.450	0.4116
0.2	689	329	3.061	1.863	33.884	1.448	0.4124
0.1	648	290	3.061	1.864	33.897	1.447	0.4126
0.046	582	255	3.061	1.863	33.892	1.448	0.4125
0	457	161	3.061	1.863	33.888	1.448	0.4125

Table A.18: Glass beads, 65% large and 35% small fractions, dry (GB 35% Small)

Pressure	V_P	V_S	Length	Radius	Volume	Density	Porosity
(MPa)	(m/sec)	(m/sec)	(cm)	(cm)	(mL)	(g/cm^3)	
0	311		3.222	1.871	35.872	1.683	0.3171
0.051	306	85	3.222	1.868	35.801	1.686	0.3158
0.031	304	81	3.223	1.875	35.975	1.678	0.3191
0.075	302	133	3.220	1.868	35.761	1.688	0.3150
0.1	358	142	3.219	1.867	35.738	1.689	0.3145
0.151	417	246	3.216	1.867	35.704	1.691	0.3139
0.2	493	272	3.213	1.867	35.669	1.692	0.3132
0.3	670	334	3.208	1.867	35.612	1.695	0.3121
0.5	745	382	3.203	1.866	35.541	1.698	0.3108
0.196	652	293	3.204	1.866	35.546	1.698	0.3108
0.097	541	246	3.204	1.867	35.551	1.698	0.3109
0.197	688	288	3.204	1.866	35.550	1.698	0.3109
0.5	759	382	3.201	1.866	35.513	1.700	0.3102
0.75	852	443	3.197	1.866	35.461	1.702	0.3092
1	907	469	3.194	1.865	35.409	1.705	0.3082
0.5	835	386	3.196	1.866	35.438	1.703	0.3088
0.2	672	291	3.197	1.866	35.471	1.702	0.3094
0.101	589	247	3.197	1.867	35.476	1.701	0.3095
0.201	706	289	3.197	1.866	35.470	1.702	0.3094
0.5	771	382	3.195	1.866	35.428	1.704	0.3086
0.99	919	465	3.191	1.864	35.343	1.708	0.3069
1.51	987	513	3.188	1.864	35.318	1.709	0.3064
2	1065	565	3.184	1.864	35.256	1.712	0.3052

Table A.18, cont.: Glass beads, 65% large and 35% small fractions, dry (GB 35% Small)

Pressure (MPa)	V_P (m/sec)	V_S (m/sec)	Length (cm)	Radius (cm)	Volume (mL)	Density (g/cm^3)	Porosity
2.5	1146	593	3.181	1.863	35.215	1.714	0.3044
1.01	936	493	3.185	1.865	35.299	1.710	0.3060
0.51	803	380	3.189	1.866	35.377	1.706	0.3076
0.2	715	292	3.191	1.867	35.413	1.704	0.3083
0.103	629	247	3.191	1.867	35.422	1.704	0.3084
0.202	692	289	3.191	1.867	35.422	1.704	0.3084
0.5	772	378	3.189	1.866	35.383	1.706	0.3077
1	903	464	3.186	1.865	35.319	1.709	0.3064
2.5	1113	597	3.178	1.862	35.160	1.717	0.3033
3.75	1193	653	3.174	1.861	35.088	1.720	0.3018
5	1276	709	3.170	1.860	35.007	1.724	0.3002
2.5	1126	591	3.174	1.862	35.098	1.720	0.3021
1	949	488	3.179	1.864	35.197	1.715	0.3040
0.5	860	378	3.182	1.865	35.273	1.711	0.3055
0.201	703	292	3.185	1.866	35.330	1.708	0.3066
0.102	597	247	3.186	1.866	35.343	1.708	0.3069
0.105	602	255	3.184	1.866	35.324	1.709	0.3065
0.201	669	289	3.184	1.866	35.324	1.709	0.3065
0.51	805	381	3.183	1.865	35.289	1.710	0.3058
1	953	457	3.180	1.864	35.224	1.714	0.3045
2.5	1103	591	3.174	1.862	35.096	1.720	0.3020
5	1261	703	3.167	1.859	34.952	1.727	0.2991
7.5	1387	780	3.161	1.857	34.841	1.732	0.2969
10	1470	845	3.156	1.855	34.743	1.737	0.2949
5	1274	701	3.162	1.858	34.877	1.731	0.2976
2.51	1106	586	3.167	1.860	34.989	1.725	0.2999
1	921	486	3.172	1.862	35.093	1.720	0.3020
0.5	873	381	3.175	1.863	35.155	1.717	0.3032
0.2	723	291	3.179	1.865	35.228	1.713	0.3046
0.105	608	262	3.179	1.865	35.233	1.713	0.3047
0.1	612	262	3.179	1.865	35.235	1.713	0.3048
0.202	674	290	3.179	1.865	35.232	1.713	0.3047
0.5	774	379	3.177	1.864	35.192	1.715	0.3039
0.99	931	456	3.174	1.863	35.133	1.718	0.3027
2.51	1105	591	3.168	1.861	35.011	1.724	0.3003
5.01	1248	698	3.162	1.858	34.885	1.730	0.2978
10	1453	832	3.153	1.853	34.670	1.741	0.2934
12.53	1498	888	3.150	1.852	34.608	1.744	0.2922
15	1562	919	3.147	1.852	34.554	1.747	0.2911
15	1562	922	3.146	1.851	34.540	1.748	0.2908
9.99	1467	838	3.150	1.853	34.630	1.743	0.2926
5.02	1262	694	3.157	1.856	34.770	1.736	0.2955
2.5	1129	583	3.162	1.858	34.885	1.730	0.2978
1	923	488	3.167	1.860	34.997	1.725	0.3000
0.5	828	380	3.170	1.862	35.057	1.722	0.3012
0.2	704	291	3.174	1.863	35.121	1.719	0.3025
0.099	623	268	3.175	1.863	35.150	1.717	0.3031
0.201	711	289	3.174	1.863	35.143	1.718	0.3029
0.5	801	381	3.172	1.862	35.100	1.720	0.3021
1	991	458	3.169	1.861	35.042	1.723	0.3009
2.51	1114	590	3.164	1.859	34.927	1.728	0.2986

Table A.18, cont.: Glass beads, 65% large and 35% small fractions, dry (GB 35% Small)

Pressure	V_P	V_S	Length	Radius	Volume	Density	Porosity
(MPa)	(m/sec)	(m/sec)	(cm)	(cm)	(mL)	(g/cm^3)	
5	1254	694	3.158	1.857	34.808	1.734	0.2962
10.01	1463	828	3.150	1.854	34.639	1.743	0.2928
15	1588	922	3.145	1.850	34.479	1.751	0.2895
17.51	1619	948	3.142	1.849	34.429	1.753	0.2885
20	1658	963	3.139	1.848	34.383	1.756	0.2875
20.04	1657	977	3.139	1.848	34.381	1.756	0.2875
14.99	1600	922	3.143	1.850	34.456	1.752	0.2890
10	1433	826	3.147	1.852	34.554	1.747	0.2911
5	1265	689	3.153	1.855	34.696	1.740	0.2940
2.52	1118	583	3.159	1.857	34.817	1.734	0.2964
1	928	453	3.164	1.859	34.924	1.728	0.2986
0.51	891	382	3.167	1.860	34.992	1.725	0.2999
0.2	706	289	3.171	1.862	35.076	1.721	0.3016
0.1	605	252	3.173	1.862	35.098	1.720	0.3020
0.201	728	290	3.172	1.862	35.096	1.720	0.3020
0.5	818	383	3.169	1.861	35.030	1.723	0.3007
1	984	462	3.166	1.860	34.977	1.726	0.2996
2.5	1089	590	3.161	1.858	34.858	1.732	0.2972
5	1243	693	3.155	1.856	34.744	1.737	0.2949
10	1435	827	3.148	1.852	34.581	1.745	0.2916
15	1608	917	3.142	1.850	34.457	1.752	0.2891
20	1658	990	3.138	1.847	34.347	1.757	0.2868
15	1575	917	3.141	1.849	34.422	1.754	0.2883
9.99	1433	825	3.145	1.851	34.525	1.748	0.2905
5	1253	688	3.151	1.854	34.659	1.742	0.2932
2.51	1091	583	3.157	1.856	34.775	1.736	0.2956
1	995	454	3.162	1.858	34.889	1.730	0.2979
0.5	873	378	3.165	1.860	34.951	1.727	0.2991
0.201	730	291	3.169	1.861	35.036	1.723	0.3008
0.1	633	246	3.169	1.861	35.030	1.723	0.3007
0	299		3.171	1.862	35.064	1.721	0.3014

Table A.19: Glass beads, 65% large and 35% tiny fractions, dry, 1 (GB 35% Tiny)

Pressure	V_P	V_S	Length	Radius	Volume	Density	Porosity
(MPa)	(m/sec)	(m/sec)	(cm)	(cm)	(mL)	(g/cm^3)	
0	309		3.121	1.901	35.495	1.734	0.2961
0.026	338		3.121	1.901	35.495	1.734	0.2961
0.049	394		3.121	1.901	35.486	1.735	0.2960
0.076	449	233	3.121	1.901	35.472	1.735	0.2957
0.102	506	244	3.120	1.900	35.459	1.736	0.2954
0.15	587	272	3.119	1.900	35.428	1.738	0.2948
0.2	632	300	3.118	1.899	35.409	1.739	0.2944
0.22	719	340	3.117	1.898	35.372	1.740	0.2937
0.31	720	354	3.117	1.898	35.355	1.741	0.2933
0.51	838	390	3.115	1.897	35.314	1.743	0.2925
0.51		390	3.115	1.897	35.314	1.743	0.2925
0.75	889	443	3.113	1.896	35.271	1.745	0.2917
1	961	481	3.111	1.895	35.223	1.748	0.2907
1.52	1080	549	3.107	1.894	35.157	1.751	0.2894
2.01	1148	592	3.105	1.893	35.110	1.753	0.2884

Table A.19, cont.: Glass beads, 65% large and 35% tiny fractions, dry, 1 (GB 35% Tiny)

Pressure	V_P	V_S	Length	Radius	Volume	Density	Porosity
(MPa)	(m/sec)	(m/sec)	(cm)	(cm)	(mL)	(g/cm^3)	
2.49	1184	624	3.103	1.893	35.075	1.755	0.2877
1	978	505	3.107	1.895	35.173	1.750	0.2897
0.51	817	396	3.110	1.897	35.247	1.747	0.2912
0.201	647	300	3.113	1.898	35.318	1.743	0.2926
0.099	531	246	3.114	1.899	35.349	1.741	0.2932
0.202	639	291	3.113	1.899	35.335	1.742	0.2929
0.5	855	395	3.111	1.898	35.286	1.745	0.2920
1	978	482	3.109	1.896	35.220	1.748	0.2906
2.51	1190	630	3.103	1.892	35.040	1.757	0.2870
3.72	1350	712	3.099	1.890	34.965	1.761	0.2855
5.01	1404	766	3.095	1.889	34.897	1.764	0.2841
7.5	1501	849	3.090	1.887	34.791	1.769	0.2819
10	1623	908	3.085	1.886	34.702	1.774	0.2800
5	1392	764	3.090	1.888	34.827	1.768	0.2826
2.5	1182	612	3.095	1.891	34.938	1.762	0.2849
1	965	471	3.100	1.894	35.065	1.756	0.2875
0.49	835	392	3.104	1.895	35.144	1.752	0.2891
0.2	664	303	3.107	1.897	35.210	1.748	0.2904
0.1	578	262	3.108	1.897	35.236	1.747	0.2910
0.2	706	300	3.107	1.897	35.228	1.747	0.2908
0.51	892	393	3.105	1.896	35.184	1.750	0.2899
1.01	942	475	3.103	1.895	35.126	1.753	0.2887
2.51	1164	617	3.097	1.892	34.990	1.759	0.2860
5	1397	757	3.092	1.890	34.877	1.765	0.2837
7.52	1487	844	3.088	1.887	34.774	1.770	0.2815
10	1579	902	3.085	1.883	34.646	1.777	0.2789
12.51	1644	952	3.082	1.882	34.578	1.780	0.2775
15	1705	991	3.079	1.881	34.522	1.783	0.2763
17.45	1764	1021	3.076	1.880	34.463	1.786	0.2750
20.01	1812	1049	3.073	1.879	34.408	1.789	0.2739
15	1705	987	3.076	1.881	34.481	1.785	0.2754
10.01	1556	886	3.080	1.883	34.577	1.780	0.2774
5.01	1389	741	3.086	1.887	34.732	1.772	0.2807
2.51	1166	605	3.091	1.889	34.853	1.766	0.2832
1	954	474	3.096	1.892	34.973	1.760	0.2856
0.5	844	396	3.100	1.893	35.053	1.756	0.2873
0.2	693	313	3.103	1.895	35.123	1.753	0.2887
0.1	596	269	3.104	1.895	35.150	1.751	0.2892
0.051	528	230	3.104	1.896	35.160	1.751	0.2894
0			3.104	1.896	35.156	1.751	0.2893

Table A.20: Glass beads, 65% large and 35% tiny fractions, dry, 2 (GB 35% Tiny 2)

Pressure	V_P	V_S	Length	Radius	Volume	Density	Porosity
(MPa)	(m/sec)	(m/sec)	(cm)	(cm)	(mL)	(g/cm^3)	
0	299		2.948	1.901	33.519	1.827	0.2585
0.027	371		2.948	1.901	33.522	1.827	0.2586
0.049	427		2.948	1.901	33.515	1.827	0.2584
0.076	505		2.947	1.901	33.503	1.828	0.2582
0.099	514	223	2.943	1.901	33.462	1.830	0.2573
0.149	518	252	2.935	1.901	33.373	1.835	0.2553
0.158	553	255	2.929	1.901	33.304	1.839	0.2537
0.201	553	267	2.929	1.901	33.301	1.839	0.2537
0.31	628	269	2.924	1.901	33.243	1.842	0.2524
0.5	700	308	2.914	1.901	33.121	1.849	0.2496
0.75	903	332	2.910	1.900	33.069	1.852	0.2484
0.74	867	363	2.905	1.900	33.017	1.855	0.2472
1	860	381	2.905	1.900	33.001	1.856	0.2469
1.51	967	465	2.899	1.899	32.908	1.861	0.2448
2	1006	509	2.893	1.899	32.839	1.865	0.2431
2.23	1084	541	2.892	1.898	32.803	1.867	0.2423
2.5	1062	549	2.892	1.897	32.794	1.867	0.2421
1	846	374	2.895	1.898	32.843	1.865	0.2433
0.5	657	296	2.899	1.898	32.887	1.862	0.2443
0.199	430	244	2.902	1.898	32.929	1.860	0.2452
0.1	358	208	2.904	1.898	32.949	1.859	0.2457
0.2	430	243	2.903	1.898	32.940	1.859	0.2455
0.5	659	311	2.900	1.898	32.906	1.861	0.2447
1	916	417	2.897	1.898	32.862	1.864	0.2437
2.63	1114	573	2.890	1.897	32.764	1.869	0.2414
3.75	1197	634	2.886	1.896	32.695	1.873	0.2398
5	1309	692	2.882	1.895	32.639	1.876	0.2385
7.5	1387	767	2.877	1.894	32.545	1.882	0.2363
10	1501	835	2.873	1.893	32.474	1.886	0.2347
5	1272	675	2.878	1.893	32.541	1.882	0.2362
2.5	1047	531	2.882	1.894	32.602	1.878	0.2377
0.97	769	388	2.887	1.894	32.676	1.874	0.2394
0.5	666	328	2.891	1.895	32.732	1.871	0.2407
0.2	511	253	2.895	1.895	32.784	1.868	0.2419
0.1	357	220	2.897	1.896	32.813	1.866	0.2426
0.2	522	247	2.896	1.896	32.802	1.867	0.2423
0.5	702	323	2.893	1.895	32.762	1.869	0.2414
1	915	417	2.890	1.895	32.720	1.872	0.2404
2.5	1067	555	2.884	1.894	32.633	1.877	0.2384
5	1304	703	2.878	1.893	32.550	1.881	0.2364
10	1502	836	2.872	1.891	32.436	1.888	0.2338
12.5	1583	895	2.869	1.891	32.382	1.891	0.2325
15	1629	944	2.867	1.890	32.336	1.894	0.2314
17.5	1724	979	2.864	1.889	32.302	1.896	0.2306
20.01	1765	1030	2.862	1.889	32.266	1.898	0.2297
15	1634	974	2.865	1.889	32.300	1.896	0.2305
10	1492	831	2.867	1.890	32.344	1.893	0.2316
5	1299	690	2.873	1.891	32.428	1.888	0.2336
2.5	1104	543	2.877	1.892	32.495	1.885	0.2351
1	875	424	2.882	1.892	32.567	1.880	0.2368
0.5	696	327	2.886	1.893	32.622	1.877	0.2381

Table A.20, cont: Glass beads, 65% large and 35% tiny fractions, dry, 2 (GB 35% Tiny 2)

Pressure	V_P	V_S	Length	Radius	Volume	Density	Porosity
(MPa)	(m/sec)	(m/sec)	(cm)	(cm)	(mL)	(g/cm^3)	
0.199	558	283	2.891	1.894	32.701	1.873	0.2400
0.098	424	225	2.893	1.894	32.718	1.872	0.2404
0.05	356		2.894	1.894	32.740	1.870	0.2409
0	288		2.895	1.894	32.749	1.870	0.2411

Table A.21: Glass beads, broad size distribution, dry (GB Broad)

Pressure	V_P	V_S	Length	Radius	Volume	Density	Porosity
(MPa)	(m/sec)	(m/sec)	(cm)	(cm)	(mL)	(g/cm^3)	
0	332	161	3.334	1.927	38.582	1.629	0.3389
0.024	350	191	3.334	1.927	38.585	1.629	0.3389
0.031	401	226	3.334	1.927	38.587	1.629	0.3390
0.052	405	233	3.334	1.927	38.591	1.629	0.3390
0.076	410	243	3.334	1.927	38.587	1.629	0.3390
0.101	428	251	3.334	1.927	38.590	1.629	0.3390
0.15	483	274	3.333	1.927	38.581	1.629	0.3389
0.2	505	285	3.333	1.927	38.571	1.629	0.3387
0.3	609	311	3.331	1.927	38.547	1.630	0.3383
0.5	723	338	3.328	1.927	38.514	1.632	0.3377
0.75	747	372	3.324	1.927	38.474	1.634	0.3370
1	776	399	3.321	1.926	38.438	1.635	0.3364
1.5	841	441	3.315	1.926	38.358	1.639	0.3350
2	869	462	3.310	1.926	38.281	1.642	0.3337
2.51	916	485	3.308	1.925	38.246	1.643	0.3331
1	729	360	3.312	1.925	38.304	1.641	0.3341
0.3	570	277	3.316	1.925	38.354	1.639	0.3349
0.2	501	257	3.318	1.926	38.369	1.638	0.3352
0.1	421	226	3.318	1.926	38.378	1.638	0.3354
0.201	505	269	3.319	1.926	38.380	1.638	0.3354
0.5	686	329	3.316	1.925	38.352	1.639	0.3349
1	758	376	3.313	1.925	38.310	1.641	0.3342
2.5	948	494	3.305	1.925	38.210	1.645	0.3324
3.76	991	546	3.300	1.923	38.101	1.650	0.3305
5	1071	576	3.296	1.922	38.038	1.652	0.3294
7.5	1140	639	3.289	1.921	37.912	1.658	0.3272
10	1229	706	3.259	1.900	37.023	1.698	0.3110
5	1021	544	3.266	1.902	37.156	1.692	0.3135
2.31	919	439	3.271	1.904	37.267	1.686	0.3155
1	750	340	3.277	1.906	37.378	1.681	0.3176
0.5	575	288	3.281	1.906	37.440	1.679	0.3187
0.2	490	235	3.283	1.907	37.490	1.676	0.3196
0.1	490	215	3.284	1.907	37.505	1.676	0.3199
0.201	493	259	3.283	1.907	37.494	1.676	0.3197
0.5	712	321	3.281	1.907	37.451	1.678	0.3189
1	775	386	3.278	1.906	37.394	1.681	0.3179
2.5	951	509	3.271	1.904	37.259	1.687	0.3154
5	1094	613	3.264	1.902	37.136	1.692	0.3131
10	1273	733	3.255	1.899	36.939	1.701	0.3095
12.5	1322	767	3.252	1.897	36.879	1.704	0.3084
15	1404	801	3.249	1.896	36.819	1.707	0.3072
17.51	1453	831	3.246	1.896	36.764	1.710	0.3062

Table A.21, cont.: Glass beads, broad size distribution, dry (GB Broad)

Pressure	V_P	V_S	Length	Radius	Volume	Density	Porosity
(MPa)	(m/sec)	(m/sec)	(cm)	(cm)	(mL)	(g/cm^3)	
20	1473	856	3.243	1.895	36.716	1.712	0.3053
15	1362	784	3.247	1.896	36.790	1.708	0.3067
10	1231	708	3.251	1.898	36.885	1.704	0.3085
5	1071	568	3.259	1.900	37.030	1.697	0.3112
2.5	953	469	3.265	1.902	37.149	1.692	0.3134
1	747	352	3.271	1.904	37.271	1.686	0.3156
0.5	634	301	3.275	1.905	37.335	1.683	0.3168
0.2	493	242	3.279	1.906	37.404	1.680	0.3181
0.1	414	213	3.280	1.906	37.426	1.679	0.3185
0.05	392	202	3.280	1.906	37.433	1.679	0.3186
0	340	160	3.280	1.906	37.426	1.679	0.3185

REFERENCES

Avseth, P., Dvorkin, J., Mavko, G., and Rykkje, J., 2000, Rock physics diagnostic of North Sea sands; link between microstructure and seismic properties. *Geophys. Res. Lett.*, **27**(17):2761-2764.

Ball, V., and Batzle, M., 1994, Contrasting stress dependence of compressional and shear velocities; implications for laboratory, logging, and seismic measurements. *SEG Annual Meeting Expanded Technical Program Abstracts with Biographies*, **64**:1065-1068.

Beard, D.C., and Weyl, P.K., 1973, Influence of texture on porosity and permeability of unconsolidated sand. *Am. Assoc. Petroleum Geol. Bull.*, **57**(2):349-369.

Berryman, J.G., 1981, Elastic wave propagation in fluid-saturated porous media. *J. Acoust. Soc. Am.*, **69**:416-424.

Biot, M.A., 1956a, Theory of propagation of elastic waves in a fluid saturated porous solid. I. Low frequency range. *J. Acoust. Soc. Am.*, **28**(2):169-178.

Biot, M.A., 1956b, Theory of propagation of elastic waves in a fluid saturated porous solid. II. Higher-frequency range. *J. Acoust. Soc. Am.*, **28**(2):179-191.

Birch, A.F, 1960, The velocity of compressional waves in rocks to 10 kilobars. Part 1. *J. Geophys. Res.*, **65**(4):1083-1102.

Birch, A.F., 1961, The velocity of compressional waves in rocks to 10 kilobars. Part 2. *J. Geophys. Res.*, **66**(7):2199-2224.

Birch, A.F., and Bancroft, D., 1938, The effect of pressure on the rigidity of rocks. *J. Geol.*, **46**(1, Part 2):59-87.

Blake, W.D., and Gilbert, R.B., 1997, Investigation of possible relationships between undrained shear strength and shear wave velocity for normally consolidated clays. *Proc. 27th Offshore Technology Conference*, paper OTC 8325, pp. 411-419.

Bokelmann, G., Nur, A., Zimmer, M., Beroza, G., Zoback, M., and Baisch, S., 2003, How to constrain crustal pore pressure from surface seismic observations. *European Geophys. Soc., Geophys. Res. Abstracts*, **5**:07873.

Bolton, M.D., and Wilson, J.M.R., 1989. An experimental and theoretical comparison between static and dynamic torsional soils tests. *Geotechnique*, **39**(4):585-599.

Bowers, G. L., 1995, Pore pressure estimation from velocity data: Accounting for pore pressure mechanisms besides undercompaction. *Soc. Petroleum Eng. Drilling and Completion*, June, pp. 89-95.

Brace, W.F., Orange, A.S., Madden, T.R., 1965, The effect of pressure on the electrical resistivity of water-saturated crystalline rocks. *J. Geophys. Res.*, **70**(22):5669-5698.

Brace, W.F., 1965; Some new measurements of linear compressibility of rocks. *J. Geophys. Res.*, **70**(2):391-398.

Cannadey, F.X., 1964, Modulus of elasticity of a rock determined by four different methods, U.S. Bureau of Mines Rept. Invest. 6533.

Carlson, R.L., and Gangi, A.F., 1985, Effect of cracks on the pressure dependence of P wave velocities in crystalline rocks. *J. Geophys. Res., B*, **90**(10):8675-8684.

Cheng, C.H., and Johnston, D.H., 1981, Dynamic and static moduli. *Geophys. Res. Lett.*, **8**(1):39-42.

Christensen, N.I., 1965, Compressional wave velocities in metamorphic rocks at pressures to 10 kilobars. *J. Geophys. Res.*, **70**(24):6147-6164.

Christensen, N.I,, 1974, Compressional wave velocities in possible mantle rocks to pressures of 30 kilobars. *J. Geophys. Res.*, **79**(2):407-412.

Christensen, N.I., and Wang, H.F., 1985, The influence of pore pressure and confining pressure on dynamic elastic properties of Berea Sandstone. *Geophysics*, **50**(2):207-213.

Cook, N.G.W., and Hodgson, K., 1965, Some detailed stress-strain curves for rock. *J. Geophys. Res.*, **70**(12):2883-2888.

Cumberland, D. J., and R. J. Crawford, 1987, The Packing of Particles. Elsevier Science Publishers, Amsterdam.

Digby, P. J., 1981, The effective elastic moduli of porous granular rocks. *J. Appl. Mech.*, **48**:803-808.

Domenico, S.N., 1977, Elastic properties of unconsolidated porous sand reservoirs. *Geophysics*, **42**:1339-1368.

Duffy, J., and Mindlin, R.D., 1957, Stress-strain relations and vibrations of a granular medium. *J. Appl. Mech. (ASME)*, **24**:585-593.

Dvorkin, J. and Nur, A., 1996, Elasticity of high porosity sandstones: Theory for two North Sea datasets. *Geophysics*, **61**(5):1363-1370.

Eberhart-Phillips, D., Han, D.-H., and Zoback, M.D., 1989. Empirical relationships among seismic velocity, effective pressure, porosity, and clay content in sandstone. *Geophysics*, **54**(1):82-89.

Eissa, E.A., and Kazi, A., 1988, Relation between static and dynamic Young's moduli of rocks. *Int. J. Rock Mech. Mining Sci. & Geomech. Abstracts*, **25**(6):479-482.

Estes, C.A., Mavko, G., Yin, H., and Cadoret, T., 1994, Measurements of velocity, porosity, and permeability on unconsolidated granular materials. *SRB Annual Report*, **55**(B):G1-1 – G1-9.

Fam, M., and Santamarina, J.C., 1997, A study of consolidation using mechanical and electromagnetic waves. *Geotechnique*, **47**(2):203-219.

Fjaer, E., 1999, Static and dynamic moduli of weak sandstones. In Amadei, B., Kranz, R.L., Scott, G.A, and Smeallie, P.H. (eds.), Rock mechanics for industry; *Proc. - Symposium on Rock Mechanics*, **37**(2):675-681.

Freund, D., 1992; Ultrasonic compressional and shear velocities in dry clastic rocks as a function of porosity, clay content, and confining pressure. *Geophys. J. Int.*, **108**(1):125-135.

Galdin N.Ye, 1977, Elastic parameters of feldspars and quartz at high pressures. *Int. Geol. Rev.*, **19**(5):569-576.

Gassmann, F., 1951, Uber die Elastizitat poroser Medien. *Vier. Der Natur. Gesellschaft in Zurich*, **96**:1-23.

Goddard, J. D., 1990, Nonlinear elasticity and pressure-dependent wave speeds in granular media. *Proc. Royal Soc. Lond., Series A*, **430**:105-131.

Greenfield, R.J., and Graham, E.K., 1994, A convenient functional form, consistent with elasticity theory, for fitting the velocities of rocks containing cracks. *Eos, Transactions, American Geophys. Union*, **75**(16,Suppl.):337.

Guyer, R.A., McCall, K.R., Boitnott, G.N., Hilbert, L.B. Jr., and Plona, T.J., 1997, Quantitative implementation of Preisach-Mayergoyz space to find static and dynamic elastic moduli in rock. *J. Geophys. Res., B*, **102**(3):5281-5293.

Hagin, P., 2003, Application of Viscoelastic, Viscoplastic, and Rate-and-State Friction Constitutive Laws to the Deformation of Unconsolidated Sands. Ph.D. dissertation, Stanford University.

Han, D-H. Nur, A., and Morgan, D., 1986, The effects of porosity and clay content on wave velocities in sandstones. *Geophysics*, **51**(11):2093-2107.

Han, D.-H., 1986, Effects of Porosity and Clay Content on Acoustic Properties of Sandstones and Unconsolidated Sediments. Ph.D. dissertation, Stanford University.

Hardin, B.O., 1980; Anisotropic shear modulus due to stress anisotropy. *J. Geotech. Eng. Div.*, *ASCE*, **106**(GT8):956-958.

Hardin, B.O.. and Black, W.L., 1969 Vibration modulus of normally consolidated clay ; closure. *J. Soil Mech. Found. Div., ASCE*, **95**(SM6):1531-1537.

Hardin, B. O., and Blandford, G. E., 1989, Elasticity of particulate materials. *J. Geotech. Eng.*, **115**(6):788-805.

Hardin B. O., and Drnevich V. P., 1972, Shear modulus and damping in soils: design equations and curves. *J. Soil Mech. Found. Div., ASCE*, **98**(SM7):667-692.

Hardin, B.O., and Richart, F.E., Jr., 1963, Elastic wave velocities in granular soils. *J. Soil Mech. Found. Div., ASCE*, **89**(SM1):33-65.

Hashin, Z., and Shtrikman, S., 1963, A variational approach to the elastic behavior of multiphase materials. *J. Mech. Phys. Solids*, **11**:127-140.

Hilbert, L.B., Kwong, T.K., Cook, N.G.W., Nihei, K.T., and Myer, L.R., 1994, Effects of strain amplitude on the static and dynamic non-linear deformation of Berea sandstone. *Proc. the 1st North American Rock Mechanics Symposium*, **1**:497-502.

Hottman, C. E., and Johnson, R. K., 1965, Estimation of formation pressures from log-derived shale properties. *J. Petr. Tech.*, June, pp. 717 – 722.

Hryciw, R. D., and Thomann, T. G., 1993, Stress-history-based model for G^e of cohesionless soils. *J. Geotech. Eng.*, **119**(7):1073-1093.

Hudson, J.A., 1981, Wave speeds and attenuation of elastic waves in material containing cracks. *Geophys. J. Royal Astronom. Soc.*, **64**:133-150.

Huffman, A. R., and Castagna, J. P., 2001, The petrophysical basis for shallow-water flow prediction using multicomponent seismic data. *Leading Edge*, **20**(9):1030-1052.

Ide, J.M., 1936, Comparison of statically and dynamically determined Young's modulus of rocks. *Proc. Nat. Acad. Sci. U.S.A.*, **22**(2):81-92.

Jackson, I., and Paterson, M.S., 1987 Shear modulus and internal friction of calcite rocks at seismic frequencies; pressure, frequency and grain size dependence. *Phys. Earth & Planetary Interiors*, **45**(4):349-367.

Jaime, A., and Romo, M.P., 1988, Correlations between dynamic and static properties of Mexico City clay. *Earthquake Spectra*, **4**(4):787-804.

Jenkins, J.T., 1997, Inelastic behavior of random arrays of identical spheres. In: Fleck, N.A., and Cocks, A.C.F. (eds.), IUTAM Symposium on Mechanics of Granular and Porous Materials, Kluwer Academic Publishers, Dordrecht, the Netherlands, pp. 11-22.

Jizba, D.L., 1991, Mechanical and Acoustical Properties of Sandstones and Shales. Ph.D. dissertation, Stanford University.

Jones, S.M., 1995, Velocities and quality factors of sedimentary rocks at low and high effective pressures. *Geophys. J. Int.*, **123**:774-780.

Kern, H, and Tubia, J.M., 1993; Pressure and temperature dependence of P- and S-wave velocities, seismic anisotropy and density of sheared rocks from the Sierra Alpujata Massif (Ronda peridotites, southern Spain). *Earth & Planetary Sci. Lett.*, **119**(1-2):191-205.

Kern, H., Popp, T., Gorbatsevich, F., Zharikov, A., Lobanov, K.V., Smirnov, Y.P., 2001, Pressure and temperature dependence of V_P and V_S in rocks from the superdeep well and from surface analogues at Kola and the nature of velocity anisotropy. *Tectonophysics*, **338**(2):113-134.

Khaksar, A., Griffiths, C.M., and McCann, C., 1999, Compressional- and shear-wave velocities as a function of confining stress in dry sandstones. *Geophys. Prospecting*, **47**(4):487-508.

Khaksar, A., and Griffiths, C., 1998; Acoustic velocities as a function of effective pressure in low to moderate porosity shaly sandstones; Part 1, Experimental results. *Exploration Geophysics*, **29**(3-4):447-455.

King, M.S., 1966, Wave velocities in rocks as a function of change in overburden pressure and pore fluid saturants. *Geophysics*, **31**(1):50-73.

King, M.S., 1970, Static and dynamic elastic moduli of rocks under pressure. *Rock mechanics, theory and practice; 11th symposium on Rock mechanics, Proc.*, pp.329-351.

King, M.S., 1983, Static and dynamic elastic properties of rocks from the Canadian Shield. *Int. J. Rock Mech. Mining Sci. & Geomech. Abstracts*, **20**(5):237-241.

Knight, R., Dvorkin, J., and Nur, A., 1998, Acoustic signatures of partial saturation. *Geophysics*, **63**(1):132-138.

Kuster, G.T., and Toksoz, M.N., 1974, Velocity and attenuation of seismic waves in two-phase media. *Geophysics*, **39**:587-618.

Marion, D., Nur, A., Yin, H., and Han, D.-H., 1992, Compressional velocity and porosity in sand-clay mixtures. *Geophysics*, **57**(4):554-563.

Mavko, G., and Jizba, D., 1991, Estimating grain-scale fluid effects on velocity dispersion in rocks. *Geophysics*, **56**(12):1940-1949.

Mavko, G., Mukerji, T., and Dvorkin, J., 1998, The Rock Physics Handbook; Tools for Seismic Analysis in Porous Media. Cambridge University Press, Cambridge, 329 pp.

Mavko, G., and Nur, A., 1978, The effect of nonelliptical cracks on the compressibility of rocks. *J. Geophys. Res., B*, **83**(B9):4459-4468.

Mayergoyz, J.D., 1985, Hysteresis models from the mathematical and control theory points of view. *J. Appl. Phys.*, **57**:3803.

McCall, K.R., and Guyer, R.A., 1994, A new theoretical paradigm to describe hysteresis, discrete memory and nonlinear elastic wave propagation in rock. *Nonlinear Processes Geophys.*, **3**(2):89-101.

Meglis, I.L., Greenfield, R.J., Engelder, T., and Graham, E.K., 1996, Pressure dependence of velocity and attenuation and its relationship to crack closure in crystalline rocks. *J. Geophys. Res., B*, **101**(8):17,523-17,533.

Mindlin, R. D., 1949, Compliance of elastic bodies in contact. *J. Appl. Mech.*, **16**:259-268.

Moos, D., 1983, Velocity, Attenuation, and Natural Fractures in Shallow Boreholes. Ph.D. dissertation, Stanford University.

Murphy, W.F., III., 1982, Effects of Microstructure and Pore Fluids on the Acoustic Properties of Granular Sedimentary Materials. Ph.D. dissertation, Stanford University.

Nur, A., and Simmons, G., 1969, The effect of saturation on velocity in low porosity rocks. *Earth & Planetary Sci. Lett.*, **7**(2):183-193.

O'Connell, R.J., and Budiansky, B., 1974, Seismic velocities in dry and saturated cracked solids. *J. Geophys. Res.*, **79**:5412-5426.

Palmer, I.D., and Taviola, M.L., 1980, Attenuation by squirt flow in undersaturated gas sands. *Geophysics*, **45**(12):1780-1792.

Pennebaker, E. S. Jr., 1970, A drilling engineering interpretation of seismic field data. *Soc. Petr. Eng., Am. Inst. Min., Metall. Petr. Eng. Meeting*, SPE paper 2165.

Pilbeam, C.C., and Vaisnys, J.R., 1973, Acoustic velocities and energy losses in granular aggregates. *J. Geophys. Res.*, **78**(5):810-824.

Pilkington, P. E., 1988, Uses of pressure and temperature data in exploration and new developments in overpressure detection: *J. Petr. Tech.*, **40**, 543 – 549.

Plona, T.J., and Cook, J.M., 1995; Effects of stress cycles on static and dynamic Young's moduli in Castlegate Sandstone. *Proc. - Symposium on Rock Mechanics*, **35**:155-160.

Prasad, M., 2002, Acoustic measurements in sands at low effective pressure and overpressure detection. *Geophysics*. **67**(2):405-412.

Prasad, M., and Manghnani, M.H., 1997, Effects of pore and differential pressure on compressional wave velocity and quality factor in Berea and Michigan sandstones. *Geophysics*, **62**(4):1163-1176.

Prasad, M., and Meissner, R., 1992, Attenuation mechanisms in sands: Laboratory versus theoretical (Biot) data. *Geophysics*, **57**:710-719.

Preisach, F.,1935, Uber die magnetische Nachwirkung. *Z. Phys.*, **94**:277.

Reasenberg, P., and Aki, K., 1974, A Precise, Continuous Measurement of Seismic Velocity for Monitoring In Situ Stress. *J. Geophys. Res.*, **79**(2):399-406.

Robertson, P. K., Sasitharan, S., Cunning, J. C., and Sego, D. C., 1995, Shear-wave velocity to evaluate in-situ state of Ottawa sand. *J. Geotech. Eng.*, **121**(3):262-273.

Roesler, S.K., 1979, Anisotropic shear modulus due to stress anisotropy. *J. Geotech. Eng. Div., ASCE*, **105**(GT7):871-880.

Santamarina, J. C., and Cascante, G., 1996, Stress anisotropy and wave propagation: a micromechanical view. *Can. Geotech. J.*, **33**:770-782.

Sayers, C. M., Johnson, G. M., Denyer, G., 2000, Pore pressure prediction from seismic tomography. *Proc. - Offshore Technology Conference*, **32**(1):173-179.

Simmons, G., and Brace, W.F., 1965, Comparison of static and dynamic measurements of compressibility of rocks. *J. Geophys. Res.*, **70**(22):5649-5656.

Stierman, D.J., Healy, J.H., and Kovach, R.L., 1979, Pressure-induced velocity gradient; an alternative to a Pg refractor in the Gabilan Range, central California. *Bull. Seis. Soc. Am.*, **69**(2):397-415.

Stiller, H., Wagner, F.K., and Vollstaedt, H., 1980, The dependence of elastic-wave propagation velocity on the pressure in fractured rock and its relation to forerunners of earthquakes. *Phys. Solid Earth*, **16**(1):34-40.

Sun, Y.F. and Goldberg, D, 1997, Estimation of aspect-ratio changes with pressure from seismic velocities. In Lovell, M.A., and Harvey, P.K., *Developments in petrophysics. Geological Society Special Publications*, **122**:131-139.

Sutherland, R.B., 1963, Some dynamic and static properties of rock. In C. Fairhurst (ed.), Rock Mechanics, Pergamon Press, London, pp. 473-491.

Timoshenko, S.P., and Goodier, J.N., 1970, Theory of Elasticity. McGraw-Hill Book Company, New York.

Tosaya, C., and Nur, A., 1982; Effects of diagenesis and clays on compressional velocities in rocks. *Geophys. Res. Lett.*, **9**(1):5-8.

Walsh, J.B., 1965a, The effect of cracks on the compressibility of rock. *J. Geophys. Res.*, **70**(2):381-389.

Walsh, J.B., 1965b, The effect of cracks on the uniaxial elastic compression of rocks. *J. Geophys. Res.*, **70**(2):399-411.

Walton, K., 1987, The effective elastic moduli of a random packing of spheres. *J. Mech. Phys. Solids*, **35**:213-226.

Warren, N., 1977, Characterization of modulus-pressure systematics of rocks; dependence on microstructure. In Heacock, J.G., Keller, G.V., Oliver, J.E., and Simmons, G., The Earth's crust; its nature and physical properties. *Geophysical Monograph*, **20**:119-148.

Williams, K.L., D.R. Jackson, E.I. Thorsos, D. Tang, and S.G. Schock, 2002, Comparison of sound speed and attenuation measured in a sandy sediment to predictions on the Biot theory or porous media. *IEEE J. Oceanic Eng.* **27**:413-428.

Winkler, K.W., 1983, Contact stiffness in granular porous materials: Comparison between theory and experiment. *Geophys. Res. Lett.*, **10**:1073-1076.

Winkler, K.W., 1985, Dispersion analysis of velocity and attenuation in Berea Sandstone. *J. Geophys. Res.*, **90**(B8):6793-6800.

Wyllie, M.R.J., Gregory, A.R., and Gardner, G.H.F., 1958, An experimental investigation of factors affecting elastic wave velocities in porous media. *Geophysics*, **23**(2):459-493.

Yale, D.P., and Jamieson, W.H., Jr., 1994; Static and dynamic rock mechanical properties in the Hugoton and Panoma fields, Kansas. *Proc.; Mid-continent gas symposium, Soc. Petroleum Eng.*, pp. 209-219.

Yamamura, K., Sano, O., Utada, H., Fukao, Y., Nakao, S., and Yasuko, T., 2002, Long-term observation of tidal variations of in situ seismic velocity and attenuation. *J. Geodetic Soc. Japan*, **47**(1):482-487.

Yin, H., 1992, Acoustic Velocity and Attenuation of Rocks: Isotropy, Intrinsic Anisotropy, and Stress Induced Anisotropy. Ph.D. dissertation, Stanford University.

Youd, T.L., and Idriss, I.M., 1997, Proceedings of the NCEER Workshop on Evaluation of Liquefaction Resistance of Soils. Technical Report NCEER-97-0022. National Center for Earthquake Engineering Research, Buffalo, NY.

Yu, P., and Richart, F. E., Jr., 1984, Stress ratio effects on shear modulus of dry sands. *J. Geotech. Eng.*, **110**(3):331-345.

Zaug, J.M., Abramson, E.H., Brown, J.M., and Slutsky, L.J., 1993, Sound velocities in olivine at earth mantle pressures. *Science*, **260**(5113):1487-1489.

Zimmerman, R.W., 1991, Compressibility of Sandstones. Developments in Petroleum Series, Elsevier, Amsterdam.

Zisman, W.A., 1933, Comparison of statically and seismologically determined elastic constants of rocks. *Proc. Natl. Acad. Sci., U.S.*, **19**:680-686.